# Constitutive Mixed Mode Behavior of Cracks in Concrete

## - Experimental Investigations and Material Modeling

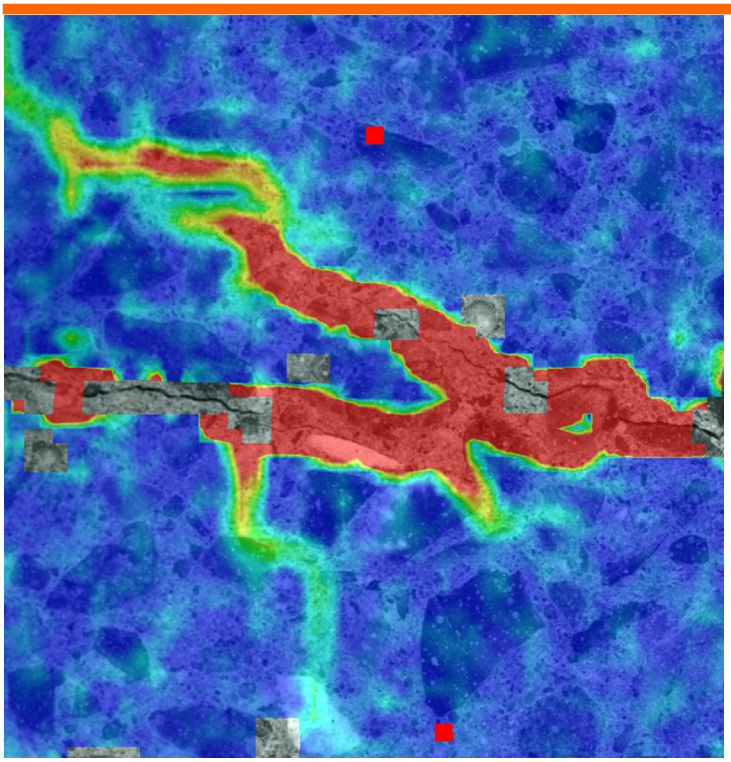

**Jonas Sejersbøl Jacobsen**

**PhD Thesis**

**Department of Civil Engineering**

2012

DTU Civil Engineering Report R-263 (UK)
May 2012

DTU Civil Engineering
Department of Civil Engineering

# Constitutive Mixed Mode Behavior of Cracks in Concrete

- **Experimental Investigations and Material Modeling**

**Jonas Sejersbøl Jacobsen**

PhD Thesis

Department of Civil Engineering
Technical University of Denmark

2012

Constitutive Mixed Mode Behavior of Cracks in Concrete
-Experimental Investigations and Material Modeling



Cover illustration: Photogrammetric registration of the crack development during a concrete experiment.

Printed by Rosendahls - Schultz Grafisk
Department of Civil Engineering
Technical University of Denmark

ISBN: 9788778773463
ISSN: 1601-2917

# Preface

This thesis is submitted as a partial fulfillment of the requirements for the Danish PhD degree. The majority of the work summarized herein has been carried out at the Department of Civil Engineering, Technical University of Denmark (DTU) between September 2008 and April 2012 under the joint supervision of Associate Professor Peter Noe Poulsen and Associate Professor John Forbes Olesen. During January and April 2011, I worked with Associate Professor Kristian Krabbenhøft at the Centre for Geotechnical and Materials Modelling, University of Newcastle, NSW, Australia. The PhD project has been financed through a DTU PhD scholarship.

The thesis is divided into a number of chapters. The first six chapters introduce the background and motivation for the research, give a detailed presentation of the work and conclude the major findings. The last chapter is a collection of two papers presenting the most important topics of the research undertaken.

Kgs. Lyngby, April 30, 2012

Jonas Sejersbøl Jacobsen

# Acknowledgements

First and foremost, I would like to thank my two supervisors Associate Professor Peter Noe Poulsen and Associate Professor John Forbes Olesen both from Department of Civil Engineering, DTU. They are the ones who guided me all the way through and provided me with numerous useful advices and feedbacks along with many fruitful discussions.

Furthermore, I would like to thank Jørgen Bjørnbak Hansen, Christian Peter Rasmussen, Lars Kokholm Andersen and Keld Plougmann from the department for Laboratories and Workshops at the Department of Civil Engineering, DTU, for their help, ideas and inspiration during the experimental part of PhD project.

A special thank to Associate Professor Kristian Krabbenhøft for the many inspiring ideas and an exciting collaboration in relation to the research stay at the Centre for Geotechnical and Materials Modelling, University of Newcastle, NSW, Australia. I am grateful for the support and hospitality of the people in and around the Centre for Geotechnical and Materials Modelling, who all contributed to the warm, welcoming atmosphere and made the external stay indeed memorable.

The external stay could not have been realized without the founding from Larsen & Nielsen Fonden, Berg-Nilsens Legat, Oticon Fonden and the support from the Centre for Geotechnical and Materials Modelling, University of Newcastle. Otto Mønsteds Fond is acknowledged for the support to the participation in the FraMCoS 7 international conference.

I have had the pleasure to share office with Christian Skodborg Hansen, with whom I have had an endless number of discussions on all technical and non-technical matters; and who has provided me with moral and scientific support. Additionally, I would like to thank Johannes Due-Hansen, Jacob Jacobsen and Lise Keinicke for proof reading the manuscript and for their constructive feedback.

Sincere thanks to my fellow PhD students at the department for the always social and enjoyable atmosphere. Finally, I would like to thank all the people in and around the section for Structural Engineering, Department of Civil Engineering, DTU, for the supportive and helpful working environment.

# Abstract

Cracks are a natural part of concrete and concrete structures. The cracks influence the general structural behavior in terms of e.g. the stress distribution and the stiffness. A direct inclusion of the cracks in the design will result in a more precise description of the structural behavior and a better basis for the assessment of the service life of the structure. The constitutive relation between Mode I crack opening and the normal stresses across the crack is well described through the Fictitious Crack Model (FCM) and related models. However, after a crack in concrete is initiated, the crack may open in mixed mode, i.e. a combination of opening and sliding. To get a thorough description of the structural consequences it is important to include the stress transferring effects related to the mixed mode opening.

The existing constitutive mixed mode models either have a rather extensive model formulation or are based on one or more model parameters which are difficult to conceive and give a mechanical interpretation. To some extent this may be explained by the sparse experimental basis for the mixed mode cracking in concrete. In this thesis a series of new mixed mode experiments are presented. An experimental basis for the interpretation of the mixed mode crack behavior is achieved through the experimental results. Based on an elasto-plastic model a constitutive mixed mode model is formulated. By a direct inclusion of the actual crack topography, the model gives a consistent and purely mechanical based interpretation of the crack behavior.

A stiff biaxial test set-up is applied to the mixed mode measurements. The relative opening and sliding of the crack is used as the control signals in a new enhanced closed control loop. The opening and the sliding of the crack are measured by clip gauges using a pair of custom made orthogonal gauge rails mounted on the specimen. The precise orthogonal gauge rails entail a direct interpretation of the mixed mode crack opening process, ensuring that the achieved response over the ligament is equal to the prescribed mixed mode displacement. After a crack is initiated in a double notch specimen, the crack is exposed to mixed mode opening. The experiments may be used in a direct interpretation of the mixed mode behavior.

The elliptic yield surface in the associated elasto-plastic material model is controlled by two hardening parameters, which represent the actual compressive and tensile strength of the concrete, respectively. The constitutive behavior is based on the relation between normal opening and normal traction. For an opening of the crack the material softens, for a closure the material hardens, and for a large closure the material crushes described as a softening. The crack surface is measured through an optical laser scan-

ner. In the model, the included topographic description consists of a series of average contour lines describing the average trends of the topography.

Compared with experiments and without any tuning the constitutive model based on the plasticity model and the topographic description gives a convincing description of both Mode I opening, crushing and mixed mode cracking. The experimental investigations, and the topographic description together with the constitutive model provide an interpretation of the mixed mode crack behavior.

# Resumé

Revner er en naturlig del af beton og betonkonstruktioner. De har indflydelse på den generelle strukturelle opførsel fx med hensyn til spændingsfordelingen og stivhedsfordelingen. Såfremt revnerne medtages direkte i konstruktionsdesignet vil der kunne opnås en mere præcis beskrivelse af den strukturelle opførsel samt dannes et bedre grundlag for levetidsundersøgelser. Den konstitutive relation mellem Mode I revneåbning og normalspændingerne på tværs af revnen er velbeskrevet gennem the Fictitious Crack Model (FCM) og tilsvarende modeller. En Mode I beskrivelse af revnen er dog ikke tilstrækkelig. Efter revneinitieringen kan revnen nemlig åbne i mixed mode, dvs. en kombination af åbning og forskydning. For at få en præcis beskrivelse af den strukturelle opførsel er det nødvendigt at medtage de spændingsoverførende effekter relateret til mixed mode.

Nuværende konstitutive mixed mode modeller har enten en omfattende modelformulering eller er baseret på en eller flere modelparametre, der er vanskelige at tilskrive en mekanisk fortolkning. Den manglende mekaniske fortolkning kan til dels forklares ud fra det lave antal af eksperimentelle undersøgelser af mixed mode revner i beton. Denne afhandling præsenterer en serie nye mixed mode eksperimenter. De eksperimentelle resultater danner en basis for forståelsen af revneopførslen i mixed mode. En konstitutiv mixed mode model er dannet med udgangspunkt i en elasto-plastisk modelformulering. Ved direkte at inddrage den aktuelle revnetopografi, giver modellen en konsistent og rent mekanisk baseret fortolkning af revneopførslen.

En stiv bi-aksial forsøgsopstilling benyttes til mixed mode forsøgene, hvor den relative åbning og forskydning af revnen anvendes som styresignaler. Ved hjælp af et par nydesignede ortogonale gauge-skinner monteret på prøveemnet måles åbningen og forskydningen af revnen med clips gauges. De nøjagtige ortogonale gauge-skinner resulterer i en direkte fortolkning af mixed mode revneåbningen, og sikrer samtidig at den opnåede åbning over ligamentet er lig med den foreskrevne mixed mode åbning. Efter at en revne er initieret i det dobbelt-kærvede prøveemne åbnes revnen i mixed mode. Forsøgene kan efterfølgende anvendes i en direkte fortolkning af mixed mode opførslen.

I den tilhørende elasto-plastiske materialemodel styres den elliptiske flydeflade af to hærdeparametre, der hhv. repræsenterer den aktuelle tryk- og trækstyrke af betonen. Den konstitutive opførsel er baseret på forholdet mellem normalåbning og normalspændinger. Ved revneåbning soft'ner materialet, ved revnelukning hærder materialet, og for en stor revnelukning knuses materialet, hvilket beskrives som en soft'ning. En optisk laser er anvendt til at opmåle revnefladen. Revnetopografien er beskrevet gennem en

række gennemsnitlige konturlinier, der beskriver tendenserne over fladen.

Sammenlignet med eksperimenter og uden nogen form for tuning giver den konstitutive model baseret på plasticitetsmodellen og den topografiske beskrivelse en overbevisende beskrivelse af både Mode I åbning, knusning og mixed mode åbning. I fællesskab beskriver og fortolker forsøgene, den topografiske beskrivelse og den konstitutive model mixed mode opførslen af en revne i beton.

# Contents

## Additional work (not included in the thesis)

[1] *Measurement and Characterization of Mixed Mode Fracture in Concrete*
J.S. Jacobsen, P.N. Poulsen & J. F. Olesen
Published in: *B.H.Oh et al., editor, Fracture Mechanics of Concrete and Concrete Structures - Recent Advances in Fracture Mechanics of Concrete, pages 717–723. Korea Concrete Institute, Seoul, 2010*

[2] *A Mixed Mode Model for Fracture in Concrete*
L.O. Nielsen, J.F. Mougaard, J.S. Jacobsen & P.N. Poulsen
Published in: *B.H.Oh et al., editor, Fracture Mechanics of Concrete and Concrete Structures - Recent Advances in Fracture Mechanics of Concrete, pages 231–237. Korea Concrete Institute, Seoul, 2010*

[3] *Experimental Basis for Mixed Mode Constitutive Modeling of Cracks in Concrete*
J.S. Jacobsen, P.N. Poulsen & J. F. Olesen
Published in: *8th fib International PhD Symposium in Civil Engineering, pages 171–176. 2010*

# Chapter 1

# Introduction

Encyclopædia Britannica (2012): **Concrete and reinforced concrete**, *structural material consisting of a hard, chemically inert particulate substance, known as aggregate (usually sand and gravel), that is bonded together by cement and water. Plain concrete does not easily withstand tensile and shear stresses caused by wind, earthquakes, vibrations, and other forces and is therefore unsuitable in most structural applications. In reinforced concrete, the tensile strength of steel and the compressive strength of concrete work together to allow the member to sustain these stresses over considerable spans.*

The era of modern concrete started with the patent for Portland cement by Joseph Aspdin in 1824 and the patent for a reinforcement system for garden tubs by Joseph Monier in 1868. Unreinforced concrete structures have been used for more than two thousand years, e.g. are the Roman aqueducts and Pantheon in Rome build with concrete-like materials. Since the introduction of reinforced concrete as a construction material 150 years ago, the technique has been developed and refined. Worldwide concrete is today the most extensively used man-made construction material. The annual consumption of concrete is over 10 billion tons, or more than one ton per year per person in the world. Compared to other materials concrete has the obvious advantages that the components like cement, aggregates and reinforcement can be found and prepared all around the world, the components are easy to transport and can together with water be mixed and casted directly at the construction site. With the proper form work, the concrete can be constructed in almost any kind of shapes and sets and it hardens at room temperature. Concrete is used in a great variety of applications like building structures, bridges, on- and off-shore foundations and as a base for roads and railways and if designed and constructed properly the structures can survive for centuries.

Normally the uniaxial compressive strength for concrete is placed in the interval 20-60 MPa whereas the tensile strength is less than one tenth of the compressive. For structures kept in compression pure concrete is suited as construction material but if, as in most cases, there can be expected some tensile forces in the structure the concrete may need to be reinforced. Normally steel rebars are used as reinforcement, but also fibers (e.g. steel or carbon fibers) or different kinds of pre-stressing systems may be used. Dependent on the desired ductility of the structure and the choice of reinforcement,

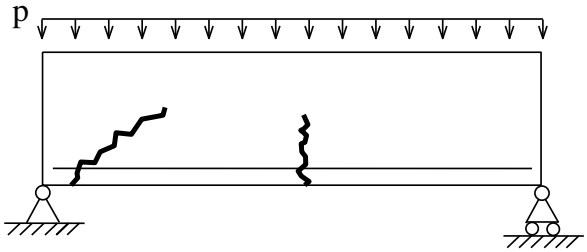


**Figure 1.1**: *Simple supported, uniformly loaded beam with an illustration of a mid span bending crack and a shear crack near the support.*

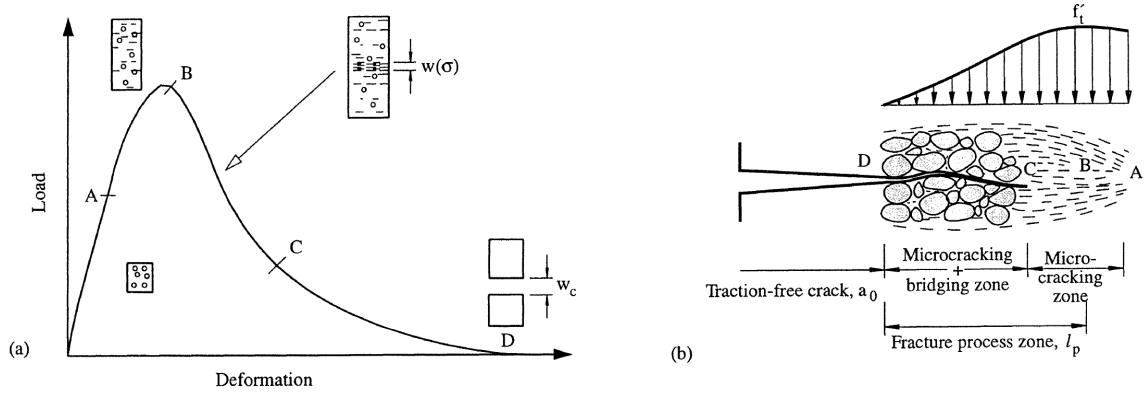


**Figure 1.2**: ***(a)*** *Typical tensile load-deformation response for a concrete specimen;* ***(b)*** *illustration of the fracture process zone around the traction free crack. Micro cracks are formed in the pre-peak tensile hardening region (AB); the micro cracks coalesce into a macro crack in the post-peak tensile softening region (BC); continued opening of the macro crack (CD). From Karihaloo (1995).*

an activation of the reinforcement causes load induced cracks to initiate and propagate in the concrete and between the concrete and the reinforcement. In general cracks in concrete will initiate and propagate if the stresses in the concrete exceed the tensile capacity. This implies that cracks can be found not only in relation to the reinforcement but also directly related to the loading, for instance for a simply supported and uniformly loaded beam as mid span bending cracks or shear cracks over the supports as illustrated in Figure 1.1. Cracks are therefore a natural part of concrete and concrete structures and the effects of cracks ought to be taken into consideration in the design of the structures. Most building codes incorporate the effects of cracks in an indirect manner e.g. by the prescription of extra safety in the design. But since the cracks influence the general structural behavior in terms of e.g. the stress distribution and the stiffness, a direct inclusion of the cracks in the design would result in a more precise description of the structural behavior.

## 1.1 Mixed Mode Cracks in Concrete

Concrete are usually characterized as a quasi-brittle material having a tensile load-deformation response as illustrated in Figure 1.2a with a long post-peak tensile softening response. For an increasing tensile load the elastic behavior changes to a nonlinear response (A) and the loading results in the formation of micro cracks. At some point after the peak during the tensile softening region (BC) the micro cracks coalesce into the formation of a macro crack. A continued opening will primarily open the now established macro crack. For a single crack the crack evolution is shown in Figure 1.2b, relating the micro cracking and bridging over the crack as a consequence of e.g. aggregate interlock to the different crack opening stages (A-D). Thus, the cracking in concrete takes place at different scales and can consequently be modeled at different scales. The heterogeneous nature of concrete can be modeled at the micro scale, but in terms of computational resources a micro scale model, modeling aggregates, mortar and interlayer, is very demanding. In the modeling of real size structures, it is therefore advantageous to use a macro scale model where the concrete can be considered homogeneous and for instance the micro cracking effects are included in the larger cracks through the constitutive description. The macro crack (hereafter called crack) behavior is illustrated in Figure 1.3. The initiation is assumed to take place in pure Mode I opening, perpendicular to the largest principal stress. However, after the initiation the established crack can open in a combination of crack opening (Mode I) and crack sliding (Mode II), i.e. a mixed mode opening. In the linear elastic fracture theory the mixed mode cracking is related to the crack initiation and crack propagation through a body. To distinguish the mixed mode cracking in concrete from the linear elastic fracture theory and to emphasize the premise for mixed mode cracking in concrete, it is defined as:

- The initiation takes place perpendicular to the largest principal stress, i.e. a pure Mode I crack initiation.

- The established crack can open in mixed mode, i.e. a combination of crack opening and crack sliding.

For the simply supported and uniformly loaded beam in Figure 1.1 the mid span bending crack opens almost entirely in Mode I whereas the shear crack over the support after the initiation will open in mixed mode.

The different aggregate sizes in the concrete composition will, as a consequence of a Mode I crack initiation, introduce a rough and irregular crack surface. For a sliding between the crack surfaces, the irregular crack surface introduces a lateral expansion of the crack, the dilation. If the dilation is prevented, a crack with a small opening is capable of transferring considerable shear stresses across the crack. This frictional capacity decreases with crack opening but increases with crack closure. Based on the frame work of the cohesive fracture mechanics, for concrete introduced with the fictitious crack model (FCM) by Hillerborg et al. (1976), the concrete cracking can be

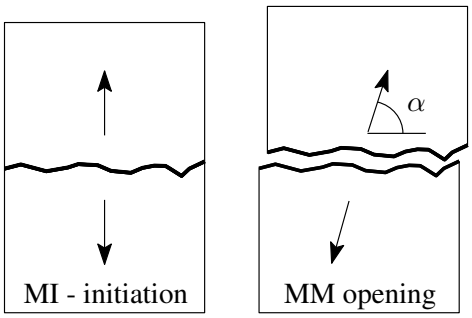


**Figure 1.3***: The macro crack initiates in a pure Mode I opening (MI), perpendicular to the largest principal stress. After the initiation the crack can open in mixed mode (MM). The ratio between crack opening and crack sliding is described by the mixed mode angle* $\alpha$*.*

considered as a discrete phenomenon. The constitutive relation between Mode I crack opening and the normal stresses across the crack is well described through the FCM and related models, whereas in most constitutive crack models the mixed mode effects are ignored. However, to get a thorough description of the structural consequences in terms of the stress distribution, the stiffness and the crack distribution and –openings as a result of concrete cracking, it is important to include the mixed mode effects. Besides a more realistic model for the general structural loading response, details about crack distribution and crack openings will provide a more complete basis for a durability analysis including detailed deterioration conditions concerning the structure. All together the establishment of a detailed computational model would lead to a more reliable prediction of the structural behavior and thereby a better and more economical usage of concrete.

## 1.2 Constitutive Modeling of Concrete Cracking

The establishment of a detailed computational model can be divided into a number of steps and disciplines, see Figure 1.4. First there is the realization of the need for a model. Most likely this is triggered by structural observations or experiments of a given phenomenon, e.g. cracks in concrete. From the experimental knowledge the constitutive behavior may then be sought explained through a suited theory. However, often in the model development process there is a need for further experimental investigations so the physical basis for the model can be verified. Dependent on the character of the modeled problem a proper numerical tool may be developed before the constitutive relation can be used to model the structural behavior. On the other hand, the available numerical tools may also dictate the framework in which the constitutive model is formulated.

A conceptual example, though not directly related to concrete, is Griffith (Griffith, 1921) who sought an explanation for the divergence between the predicted elastic

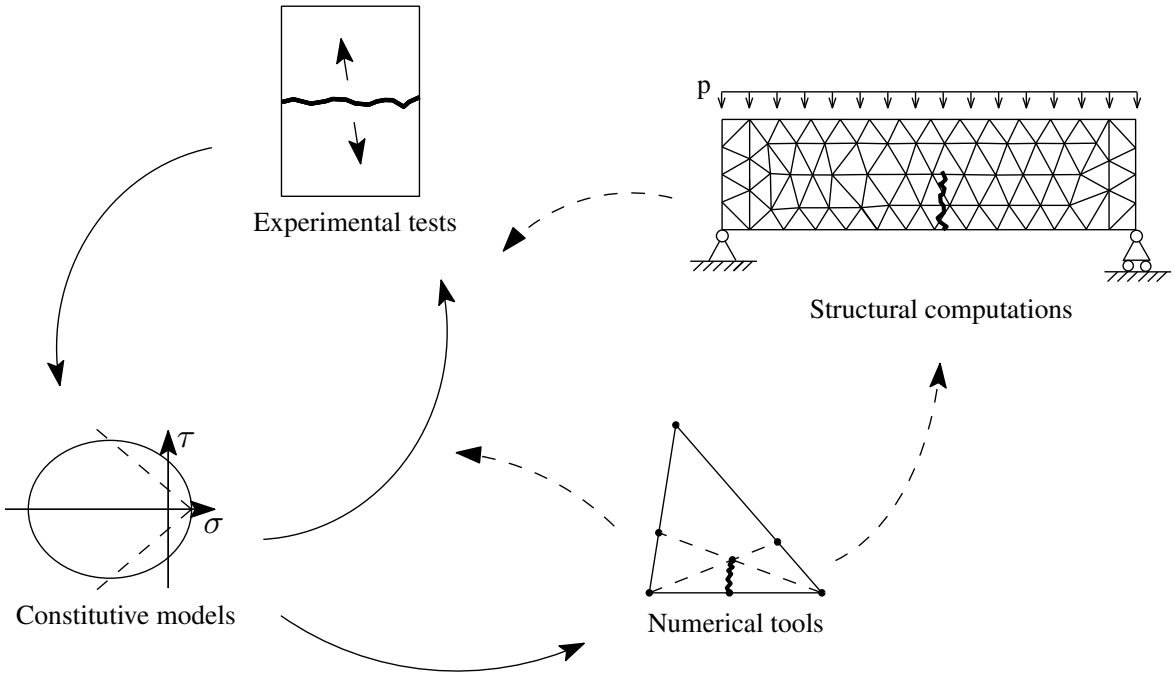


**Figure 1.4***: The process in the formulation of a detailed computational structural model and the relation between experiments, theory and numerical tools.*

strength and the observed strength of some metallic machine parts. Griffith found an explanation through a series of experiments with glass panels and consequently described the base for the theory of linear elastic fracture mechanics (see more about the history of fracture mechanics in Chapter 2.1). For concrete, the FCM (Hillerborg et al., 1976) is another example of the coherence between experiments, theory and the development of numerical tools. The model formulation has paved the way for a wide range of experimental research of cracks in concrete and the development of numerical methods to deal with concrete cracking.

For cracks in concrete, and in particular the mixed mode cracking, the following gives a survey of the three steps in the formulation of a detailed computational structural model; experimental investigations, constitutive modeling and numerical tools.

### 1.2.1 Experimental Investigations of Concrete Cracking

The most direct and precise experimental method to determine the Mode I behavior of a crack in concrete (the tensile softening curve in Figure 1.2) is to use a double notch plate specimen in a stiff uniaxial tensile set-up like the ones proposed by Cornelissen et al. (1986) and Hassanzadeh (1992). Together with a closed control loop over the crack measuring the crack opening the uniaxial tensile set-up ensures a stable crack growth (Gettu et al., 1996). However, such a set-up may be difficult to construct and troublesome to use, therefore some alternative methods have been developed. In RILEM (1985) the Mode I behavior is proposed to be determined from tests on three

point bending beams or the Mode I behavior can be interpreted through the wedge splitting test (Brühwiler and Wittmann, 1990). Both the three point bending test and the wedge splitting test give an indirect determination of the Mode I behavior and to determine the fracture mechanical properties the results need to go through an inverse analysis. In Østergaard (2003) the three different methods are investigated in details.

As a supplement to the Mode I behavior it has been proposed to investigate the Mode II behavior to constitute the basis for the mixed mode cracking. Reinhardt et al. (1997) and Reinhardt and Xu (2000) suggest a method for Mode II testing in pure concrete. A shear stress state is established by loading one side of a double notch specimen in compression, parallel to the notch direction, while the other side is unsupported. However, the reported crack patterns indicate that the crack initiates in Mode I and the measured fracture properties cannot alone be prescribed to the Mode II behavior. It is questionable if it is possible to determine pure Mode II properties for a material point in concrete. As mentioned in Section 1.1 it is the assumption that a crack in concrete initiates under pure Mode I conditions perpendicular to the largest principal stress. The assumption is consolidated by observations of crack patterns by Hassanzadeh (1992), Nooru-Muhamed (1992), Carpinteri et al. (1993) and Østergaard et al. (2007).

Thus, instead of combining the Mode I behavior with the other more questionable extremity, the Mode II behavior, pre-notched beams in three point bending (see e.g. Carpinteri and Brighenti (2010)) and four point bending (see e.g. Gálvez et al. (1998)) have been used to characterize cracks in concrete under mixed mode loading. The level of mixed mode is dictated by the position of the notch with respect to the supports/loadings. The beam tests give the beam response to the applied loading but it is very difficult to interpret the mixed mode material behavior of the crack, and the test can only provide an indirect crack interpretation.

The most direct method to determine the mixed mode crack behavior is based on a development of the uniaxial tensile set-up with a second shear axis. With a double notch concrete specimen in a bi-axial set-up with a closed control loop it is possible to impose both normal and shear loads on a given crack surface and at the same time possible to ensure a stable crack growth. Nooru-Muhamed (1992) and Hassanzadeh (1992) investigate cracks in concrete using set-ups as the mentioned. However, the actual mixed mode behavior is blurred by lacking stiffness in the set-ups or experiments focusing more on the crack initiation under different loading cases than the behavior of an already established crack. The set-ups by Nooru-Muhamed (1992) and Hassanzadeh (1992) are described in Chapter 2.3. They provide a basis for the development of a stiff bi-axial set-up and from their results it is possible to establish a more focused test program centered on the mixed mode behavior.

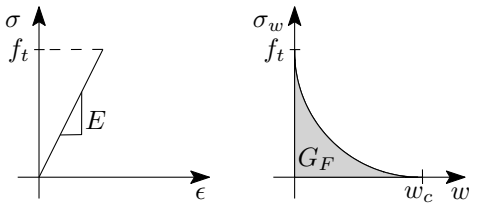


**Figure 1.5***: The tensile load-deformation behavior of concrete is in terms of the FCM divided into an elastic part and a tensile softening part.*

### 1.2.2 Constitutive Crack Models

The Mode I behavior of concrete can be modeled using a cohesive fracture model. In the fictitious crack model (FCM) the tensile load-deformation response for concrete displayed in Figure 1.2 is divided into a linear elastic part and a tensile softening part, see Figure 1.5. The linear elastic part is characterized by the Youngs Modulus, $E$, and the tensile strength, $f_t$. The softening part is described through $f_t$, the fracture energy, $G_F$, and the critical crack opening, $w_c$. $G_F$ is the area under the softening curve whereas $w_c$ corresponds to the crack opening at the end of the fictitious crack where the crack becomes stress free (point D in Figure 1.2). The softening response are often described through a bi-linear, multi-linear or exponential relation where $f_t$ and $G_F$ usually are kept constant between the relations and $w_c$ differs. Since a crack in concrete initiates under pure Mode I conditions perpendicular to the largest principal stress some beam experiments under mixed loading can be modeled using only a Mode I model (Cendón et al. (2000), Bocca et al. (1991), Lens et al. (2009)). However, as shown with the model work in Lens et al. (2009) and consistent with the mixed mode experiments by Nooru-Muhamed (1992) and Hassanzadeh (1992) the crack path in other experiments exhibit both normal and shear loadings. Generally, to model the correct crack behavior a constitutive mixed mode model is essential.

Some simple mixed mode models are based on a tensile and a frictional softening curve with associated fracture energies and a coupled expression for normal and sliding displacements for a given combination of Mode I and II fracture, see Högberg (2006) and Walter and Olesen (2008). For mixed mode fracture, the models are not able to determine all the cracking mechanisms and they are based on the somehow artificial Mode II fracture energy, a parameter which seems very difficult to determine in direct experiments. A macro elasto-plastic constitutive model by Lourenço and Rots (1997) is able to describe both tensile softening, slipping and crushing, all desirable effects in a model for concrete cracking. The model requires a number of parameters, which are experimentally hard to determine. Two elasto-plastic damage interface models are presented by Spada et al. (2009) and Alfano and Sacco (2006). The first one has a rather extensive thermodynamical formulation, the second one lacks dilatational effects and both lack a compressive failure cut off. In Carol et al. (1997) a softening elasto-plastic constitutive model for the mixed mode behavior is presented. The constitutive model is Coulomb-like and uses a fracture energy-based damage parameter as the control variable for the yield surface contraction. A modified version of the model with an added compression limitation of the elastic region is presented in Dick-Nielsen

(2007). Again a Mode II fracture energy quantity is part of the model. By Lens et al. (2009) another elasto-plastic mixed model is presented. The model is based on a similar Coulomb-like yield surface and a non-associated plastic potential as in Carol et al. (1997). The surface is controlled through a tensile-softening response controlling the actual tensile and cohesive strengths. The inelastic opening and sliding is coupled through a coupling factor which lacks a physical interpretation and is fitted against experiments. The model by Nielsen et al. (2010) is based on a new Coulomb-like yield surface. The model is elasto-plastic with damage and has a cohesional and a frictional part. The frictional part includes deformation state dependency, where the friction decreases with crack opening and is restored with crack closure. The models by Carol et al. (1997) and Nielsen et al. (2010) are described in Chapter 2.2 and together they provide inspiration for the formulation of a simple mixed mode crack model.

### 1.2.3 Finite Element Methods for Concrete Cracking

To model structural members the constitutive model is used in combination with a suited numerical tool. Often the numerical tool is established in relation to the Finite Element Method (FEM).

In smeared crack models (see e.g. Bažant and Oh (1983) and de Borst and Nauta (1985)) the cracking in a given material point is the result of the micro and macro cracking in a given volume surrounding the point. The smeared approach is e.g. used in relation to the crack band model (Bažant and Oh, 1983). The smeared models tend to show some mesh dependencies and the smeared manner makes it difficult to interpret the actual crack width and the exact location of a macro crack in an element.

The FCM was developed to be implemented in a FEM discrete crack modeling. Tools like interface elements, embedded elements or the extended finite element method may be used for the discrete crack modeling. In interface crack models the crack can develop along predefined paths; in 2D the path is a line and in 3D it is a plane. As examples the interface approach has been used for 2D mixed mode modeling of the bond between steel and concrete (Walter and Olesen, 2008) and at the micromechanical scale to model the bond between aggregates and mortar and internal in the mortar, Carol et al. (2001), López et al. (2008a) and López et al. (2008b). For a structural modeling with general unknown crack paths the predefinition of the crack path is disadvantageous but this can be overcome using re-meshing techniques, see e.g. Yang and Chen (2005). However, in relation to a structural modeling the re-meshing is computationally expensive.

With embedded crack models strain or displacement discontinuities are embedded into standard finite elements. In most embedded crack models the parameters representing the discontinuity are element local and do not like other degrees of freedom have to be treated as global unknowns. However, the treatment at local level does not necessarily ensure that a discontinuity path in one element fits together with the discontinuity

path in a neighboring element. A review of embedded crack models is given in e.g. Jirásek (2000).

In the eXtended Finite Element Method (XFEM) proposed by Belytschko and Black (1999) and Moës et al. (1999) an enrichment of the elemental basis functions allows the displacement field to be decomposed into a continuous and a discontinuous part. The discontinuous part can then represent a discontinuity like a crack in a discrete manner and the direction of the crack and the crack propagation are independent of the element mesh. With the use of XFEM cohesive Mode I cracking in concrete has been considered by e.g. Asferg et al. (2007) and mixed mode cracking by Mougaard et al. (2010). Even though the elemental enrichment gives an increased demand in respect to computational power, the XFEM seems to be an effective tool for modeling concrete structures.

## 1.3 Objective and Overview of the Thesis

A simple and precise macro scale formulated constitutive model for a mixed mode crack in concrete, which is well founded on physical observations, is a cornerstone in the establishment of a detailed computational model for the structural behavior of concrete structures. As it appears from the survey in the previous section the proposed models are insufficient either in regard to simplicity or in the physical interpretation of the model. A great deal of this can be explained by the sparse experimental basis for the mixed mode cracking in concrete. The objectives of the present work are to establish an experimental basis for the mixed mode cracking and to formulate a simple, but mechanically well founded mixed mode crack model.

A double notch concrete specimen is used to investigate the mixed mode concrete behavior. For the testing a stiff biaxial testing machine, capable of imposing both normal and shear loads on a given crack surface, is applied. A custom made orthogonal gauge is used to measure the opening and sliding components of the mixed mode displacement, and the measurements are used directly in the closed control loop. The high stiffness of the set-up together with the closed control loop ensure a stable crack initiation followed by a controllable mixed mode opening. The results from the experiments cover a range of mixed mode angles together with the effect of a varying initial Mode I opening of the crack.

Based on the experimental results a constitutive mixed mode model for concrete cracking is formulated. The model is formulated at macro level but includes the most important micro scale effects. A simple, associated plasticity model inspired by the modified Cam clay model is established. The hardening is based on the softening in Mode I crack opening and Mode I crushing, and the micro effects are included through a topographic description of the crack surface.

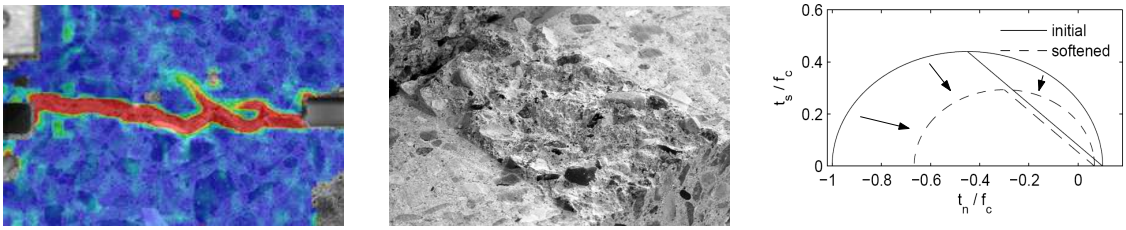


(a) (b) (c)

**Figure 1.6***: Illustrations of the different topics related to the thesis.* ***(a)*** *Photogrammetric registration of the crack development during a mixed mode test.* ***(b)*** *View of the crack topography.* ***(c)*** *Yield surface evolution for a constitutive mixed mode model.*

Figure 1.6 gives a glimpse of the content of the work included in this thesis. Chapter 3 presents the mixed mode experiments; illustrated in Figure 1.6(a) by the crack evolution during a mixed mode experiment. As illustrated in Figure 1.6(b), Chapter 4 investigates and characterizes the crack topography, whereas Chapter 5 describes the constitutive crack modeling; in Figure 1.6(c) exemplified by a yield surface contraction.

Before the three mentioned chapters, Chapter 2 gives a survey of the fracture mechanics theory with the focus on the aspects concerning fracture in concrete. The survey is followed by a more detailed description of the constitutive mixed mode models by Carol et al. (1997) and Nielsen et al. (2010) and the experimental set-ups by Nooru-Muhamed (1992) and Hassanzadeh (1992).

The bi-axial set-up which is used to capture the experimental basis for the mixed mode cracking is presented and discussed in Chapter 3. The Mode I results provide a basis for the determination of material values, whereas the mixed mode results display the cracking mechanisms for varying initial opening and varying mixed mode angle. The experimental results are supplemented by photogrammetric measures monitoring the crack development during the experiments. Together with Paper I, *Characterization of Mixed Mode Crack Opening in Concrete* (Jacobsen et al., 2012a) Chapter 3 presents the experimental work regarding the mixed mode behavior.

A detailed description of the concrete crack topography has proven to give a better physical understanding of the mixed mode crack behavior. In Chapter 4 the method used and the characterization of the topography is presented. Besides a characterization of the crack surface the topography gives a qualitative description of the crack surface obtained through the mixed mode experiments.

The simple mixed mode material model is introduced in Chapter 5. The model consists of an associated plasticity model which together with the topographic description gives an interpretation of the mechanisms behind the mixed mode cracking. The plasticity frame work is presented and the implementation with the topography is exemplified. Besides Chapter 4 and Chapter 5 the plasticity model and the principles behind the

topography are presented in Paper II, *Constitutive Mixed Mode Model for Cracks in Concrete*, (Jacobsen et al., 2012b).

In Chapter 6 the findings from the experimental work and the modeling are summarized and the work is concluded. The chapter ends with ideas and suggestions for the future research.

# Chapter 2

# Discrete Mixed Mode Cracking

For the last half century a debate has existed as how to properly describe and model cracks in concrete. By now, it is generally agreed that the quasi-brittle behavior of concrete can be described through a non linear fracture mechanics theory like the FCM (Hillerborg et al., 1976). The following section gives a brief survey of the fracture mechanics theory, beginning with the linear elastic fracture theory and ending with a number of nonlinear fracture models for concrete. The section focuses more on the conceptual mechanisms described through the fracture theory than the mathematical framework behind it. The fracture mechanics theory section is followed by a presentation of two constitutive mixed mode models and two mixed mode set-ups. Both the models and the set-ups represent contributions in the development of a simple mixed mode model.

## 2.1 Survey of the Fracture Mechanics

The fracture mechanics theory has been developed over the last century, first with the formulation of the linear elastic fracture theory followed by nonlinear fracture theories. A broad view of the development of the linear elastic fracture theory is given in Sanford (2003) whereas fracture mechanics models especially for concrete are presented and analyzed in Karihaloo (1995). The following presents some of the important findings in the development of the fracture mechanics theory for concrete.

Generally regarded, **Inglis (1913)** is the first paper that addressed the stress fields around a crack tip. Inglis found the stress intensities around a crack by solving the elasticity problem concerning an elliptical hole in a uniformly loaded plate, see Figure 2.1. Letting the elliptic aspect ratio go towards zero, the problem gives the stress intensities for a crack-like defect.

**Griffith (1921)** observed that the actual strength under fatigue for some metallic machine parts were significant lower than predicted by elastic theory. This triggered some investigations of the difference between the theoretic and measured tensile strength of some glass panels. Based on the mathematical work by Inglis (1913) the low measured

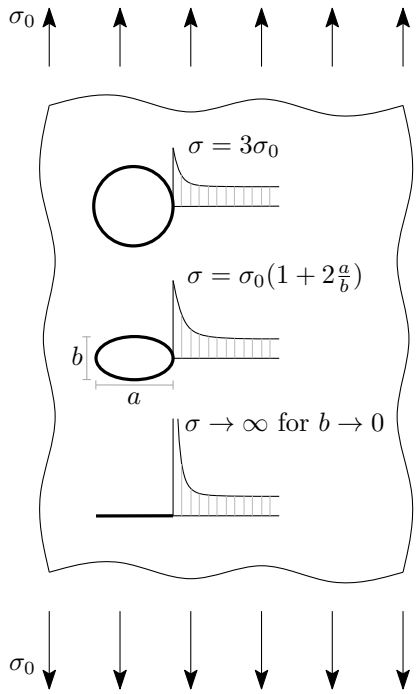


**Figure 2.1***: Stress distributions close to a circular hole, an elliptic hole and a crack in an infinitely large plate subjected to the uniform stress* $\sigma_0$*. After Petersson (1981).*

strength was postulated to be caused by high stress levels around microscopic cracks. Near the crack tips the stresses tend to infinity regardless of the size of the applied stress, while the stress field away from the crack is undisturbed. Instead of using a strength criterion the investigations led to a theory of fracture for brittle materials based on the surface energy.

**Irwin (1957)** noted that around a sharp crack tip the different stress components have the same singular asymptotic behavior, regardless of the applied load, the boundary conditions or the shape of the elastic body. Since the fracture process takes place around the crack tip these observations led to the introduction of the stress intensity factors and the local stress criterion for fracture of brittle materials, important aspects in the development of the Linear Elastic Fracture Mechanics (LEFM). The singular stress behavior at the crack tip is illustrated in Figure 2.2. It can be shown that the local stress criterion at the crack tip is identical to the global energy based criterion by Griffith, (Karihaloo, 1995). The stress intensity factors are determined by the geometry and the loading of the whole body, but stress intensity factors for a number of problems have been computed and can be found in handbooks like Tada et al. (2000).

The paper by **Prandtl (1933)**, originally in German, is the first to suggest a cohesive description of the pre peak behavior of brittle fracture. In the model the material on the two sides of the crack is represented by two beams. The cohesion is described by linear elements or springs. When a weak point is introduced in the material the succeeding springs will for a certain elongation start to fail and a crack will begin to propagate. Prandtl suggests that for heterogeneous materials like concrete the model

may explain the observed weakening of the material as a consequence of repeated loadings.

In the LEFM the assumption is that the stresses and strains at the crack tip have a singular asymptotic behavior and that during the fracture process energy only dissipates at the crack tip. For truly brittle materials the LFEM works, but if the material has a limited ductility the concept of small scale yielding may be introduced. By the small scale yielding concept a small plastic zone is introduced at the crack tip but enclosed by sufficient elastic material to keep the plastic zone within the singularity dominated zone. This implies that large cohesive forces, approaching the tensile strength, act in the plastic zone and give a smooth crack closure, while the failure law of LEFM still can be used. **Barenblatt (1962)** and **Dugdale (1960)** present two such cohesive crack models. Barenblatt assumed that smooth closure was achieved due to a generally unknown distribution of large cohesive forces acting over the small plastic zone (or fracture process zone) near the crack-tip. Based on experiments for steel sheets, Dugdale proposed a cohesive crack model giving the relation between the applied load and the extent of the plastic yielding. In the Dugdale model the distribution of cohesive stresses is known and constant, and unlike the model by Barenblatt the extent of the cohesive zone is not restricted to a small plastic zone. In the limiting case of small scale yielding both Barenblatt's and Dugdale's model reproduces the results of LEFM.

The first nonlinear fracture mechanics model for concrete is the fictitious crack model (FCM) by **Hillerborg et al. (1976)**. In continuation of the concept of the cohesive models by Barenblatt and Dugdale the FCM has closing stresses acting near the crack tip which ensure a smooth crack closure. The term fictitious is used to underline the fact that the real, stress free part of the crack is ending in an artificial crack. Over the artificial crack stresses are transferred giving the smooth crack closure, illustrated in Figure 2.2. In terms of principal stresses the crack initiation takes place for $\sigma_I = f_t$, where $f_t$ is the concrete tensile strength. Unlike the Dugdale model, the closing stresses in the process zone are not constant. From zero at the tip of the stress free part the closing stresses increase to the tensile strength of the material at the tip of the fictitious crack. In the model there is no assumptions regarding the size of the process zone and therefore the distribution of the cohesive stresses near the crack tip must be known. Normally the cohesive stress relation is termed the $\sigma_w$-relation, see Figure 1.5, where $\sigma_w$ is the cohesive stress and $w$ is the crack opening. As for Barenblatt's and Dugdale's models in the limiting case of small process zone, for instance in the case of a crack in a large structure, the FCM is reduced to LEFM.

In concrete the fracture process takes place on different scales ranging from the separation of atomic bonds to fracture related to aggregate bridging on the largest length scale. **Needleman (1990)** proposed the concept that a cohesive law introduces a length scale through a characteristic crack opening; the concept is named bridged crack models. For an absolute analysis of the concrete fracture all the cohesive laws related to the different scales would have to be considered; however, that would require an impracticable detailed computational model. Thus, for bridged crack models the

energy corresponding to length scales smaller than a certain scale is assembled into a single point corresponding to applying LEFM to scales smaller than this certain scale. The cohesive law is then applied for the larger scales. As illustrated in Figure 2.2 the general bridged crack model assembles LEFM and the cohesive crack behavior. Cohesive crack models with smooth crack closure and no stress intensity at the crack-tip like Barenblatt's, Dugdale's and FCM may be considered as a special case of the general bridged crack model, (Cox and Marshall (1991), Cox and Marshall (1994)). For a computational analysis, the ratio between the fracture energy associated with stress singularity at the crack tip, $G_{K_I}$, and the fracture energy associated with the cohesive law, $G_{\sigma_w}$, determines whether a cohesive crack model or a more general bridged crack model may be used. The influence of using FCM compared with a bridged crack model in respect to the fracture energy ratio is investigated in Stang et al. (2007). Based on a semi-analytic model Stang et al. shows that for concrete the FCM gives a reasonable description of fracture.

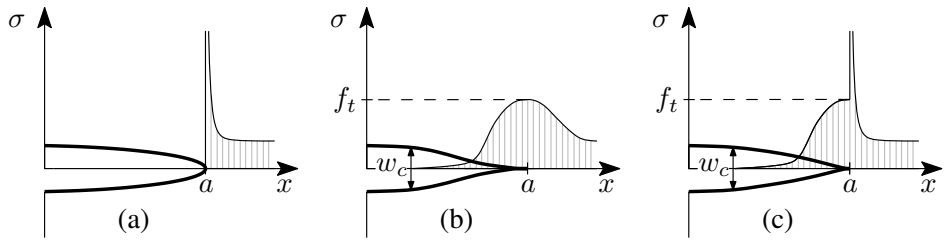


**Figure 2.2**: *Sketch showing the stress distribution in the vicinity of the crack tip in the case of:* ***(a)*** *linear elastic fracture mechanics,* ***(b)*** *the fictitious crack model and* ***(c)*** *a general bridged crack model. After Stang et al. (2007).*

## 2.2 Mixed Mode Models

Figure 2.3 represents a schematic presentation of the elasto-plastic constitutive model by Carol et al. (1997). In tension the elasto-plastic model is associated whereas in compression it is non-associated. The hyperbolic yield surface is asymptotic to a Coulomb-friction model with the cohesion $c$. As mentioned in Section 1.2.2 the yield surface is controlled by a fracture energy-based damage parameter, $W^{cr}$. The tensile strength vanish for $W^{cr} = G_f^I$ and the cohesion vanish for $W^{cr} = G_f^{IIa}$. $G_f^I$ is the fracture energy related to a regular Mode I crack opening, equivalent to the fracture energy in the FCM. $G_f^{IIa}$ is the fracture energy related to a sliding crack established under high confinement and no dilation, where the crack propagates through both cement paste and aggregates, see Figure 2.3(b). Even though a test method leading to $G_f^{IIa}$ has been proposed (Montenegro et al., 2007), the fracture energy is still difficult to conceive. Figure 2.3(c) shows the effect on the yield surface for a Mode I opening and for a Mode IIa sliding, respectively. For a Mode I opening the tensile strength $\chi$ vanish, the cohesion $c$ is reduced and the yield surface shrinks from the initial state (0) to the new state (1). For a Mode IIa sliding the yield surface is reduced from (0) to (2) equivalent to a pure Coulomb friction model. Figure 2.3(d) and (e) shows the

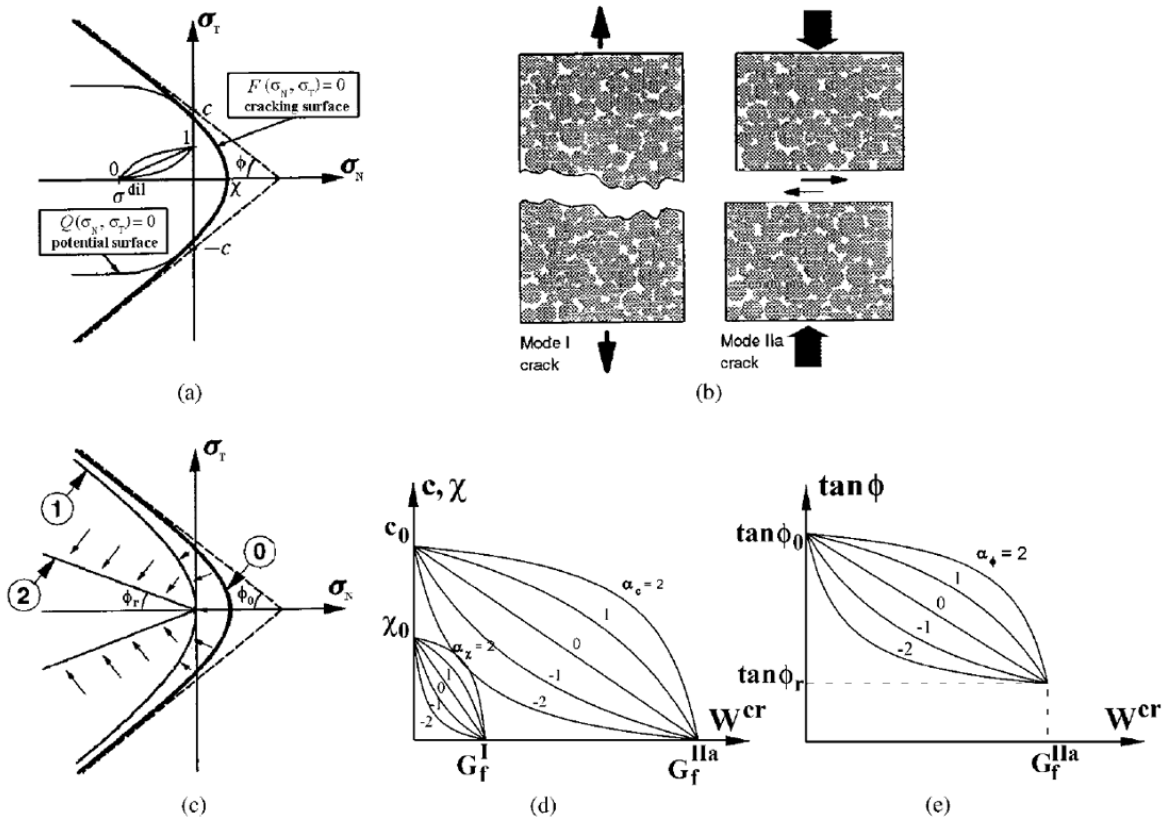


**Figure 2.3**: *Crack laws:* ***(a)*** *hyperbolic cracking surface F and plastic potential Q;* ***(b)*** *fundamental modes of fracture;* ***(c)*** *evolution of cracking surface;* ***(d)*** *softening laws for $\chi$ and c; and* ***(e)*** *softening law for tan($\phi$). From Carol et al. (2001).*

exponential softening laws for $\chi$, $c$ and the friction angle $\tan(\phi)$, the latter was added in Carol et al. (2001).

In Nielsen et al. (2010) another elasto-plastic concrete crack model is presented. The model is based on the observations that for a mixed mode crack opening both the cohesive and the frictional capacity are weakened. However, when the cohesion is exhausted, some frictional capacity is still left between the crack faces and for a crack closure the frictional capacity is rebuild. This suggests that the strength capacity for a cracked material point may be composed of a cohesional and a frictional contribution, hence, the model consists of a cohesional and a frictional submodel. The cohesive submodel is an elastic, perfectly plastic material with damage and dominates the total model response in tension. In the uniaxial tensile case the model response is only affected by the cohesive submodel, see Figure 2.4. The exponential damage function is based on an effective strain measure described by the displacement change of the mixed mode crack opening, giving an exponential degradation of the tensile strength similar to the concrete behavior described in Section 1.1. The unloading stiffness is deformation dependent; for a crack opening the stiffness is reduced, whereas, for a crack closure the stiffness is regained. When the cohesion is exhausted, the friction generated stiffness and strength still remain in the material. For increasing crack opening these

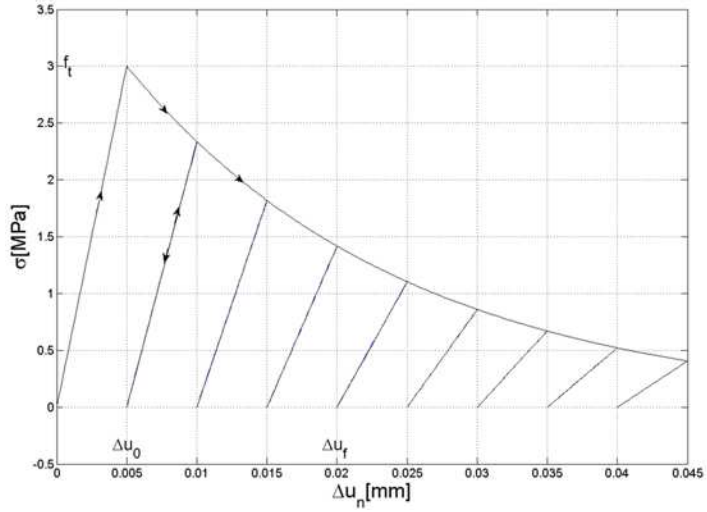


**Figure 2.4***: Uniaxial tension with un/reload of the cohesional submodel. From Nielsen et al. (2010).*

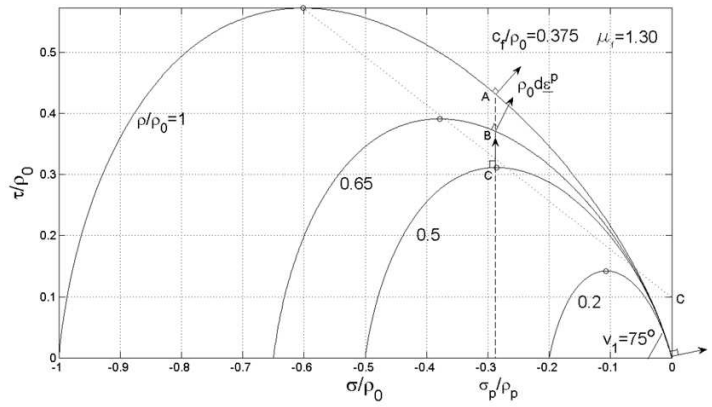


**Figure 2.5***: Upper half of the deformation state dependent yield surface for the frictional submodel. From Nielsen et al. (2010).*

properties decrease, but since they are increasing with decreasing crack opening, the friction capacity is modeled as reversible. The frictional submodel is a non-hardening elasto-plastic material with deformation state dependence and an associated flow rule. The yield surface is a hyperbolic Mohr-Coulomb surface controlled by a deformation state parameter $\rho$, which describes the uniaxial compressive yield stress. In Figure 2.5 the yield surface is displayed for four different deformation states. For a compression stress which is not too small, the top points are approximately placed on a straight line (dotted in Figure 2.5), which is related to a modified Coulomb model.

The experiments by Hassanzadeh (1992) have been used to verify the models by Carol et al. (1997) and by Nielsen et al. (2010). Both models are able to simulate similar characteristics as found from the experiments. Further, the model by Nielsen et al. (2010) is compared to experiments by Jacobsen et al. (2010) and the model is able to simulate some of the same characteristics as found in the experiments. However, the model by Carol et al. (1997) is based on a difficult obtainable fracture energy and the

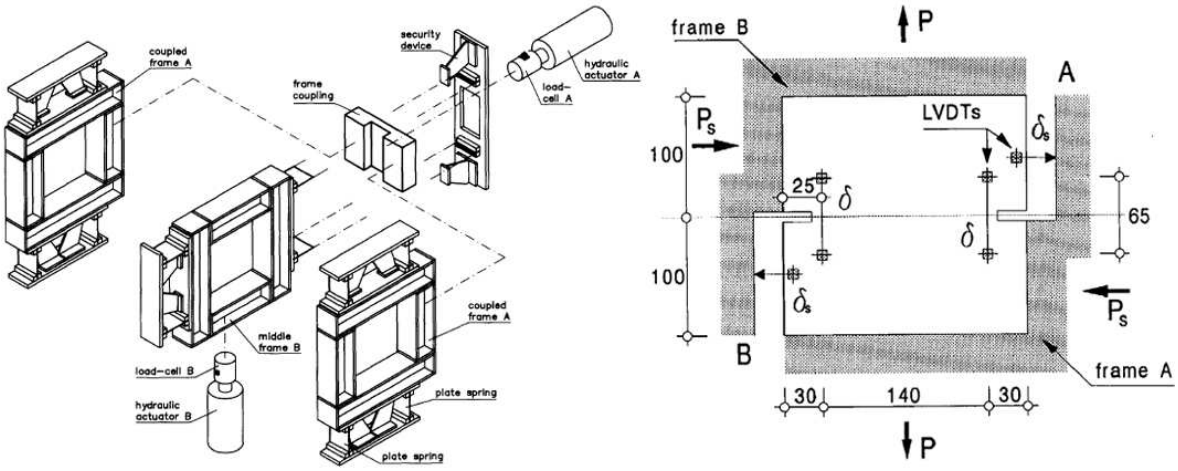


**Figure 2.6**: *Left: exploded view of the loading frames. The outer double frame is named A, the inner frame is named B. Right: Schematic view of the boundary conditions. From Nooru-Muhamed (1992).*

model formulation by Nielsen et al. (2010) is rather comprehensive and introduces a number of new material parameters. This suggests that a new, simple mixed mode model may be established on the foundation of the experimental work included in this thesis.

## 2.3 Mixed Mode Experimental Set-ups

Nooru-Muhamed (Nooru-Muhamed, 1992) developed a setup in which three frames were used to induce the mixed mode loading condition. As displayed in Figure 2.6 the lower part of the double notch specimen is attached to the outer double frame (A) and the upper part to the inner frame (B). The specimen is glued to the loading frames and frame B can only move vertically and frame A only horizontally. In the majority of the tests the experiments are displacement controlled using the average vertical opening from four strain gauges near the notches (LVDTs in Figure 2.6, two at the front and two at the back) and the average horizontal displacement between the upper and lower specimen part, where the distance to the frames is used as reference. Nooru-Muhamed reports that the crack initiation for a vertical load starts at the left notch indicating that the set-up has some build in eccentricity. The rigidity between the two sets of frames is also questionable which might have affected the horizontal displacement measuring.

The set-up is established with the objective to investigate mixed mode fracture in concrete, not in accordance with the definition in Section 1.1, but fracture initiation under mixed mode loading conditions. Moreover is the shear strength of partially opened cracks investigated, however, the introduced shear displacement of the established crack introduces secondary cracking. Over all, the crack patterns reported by

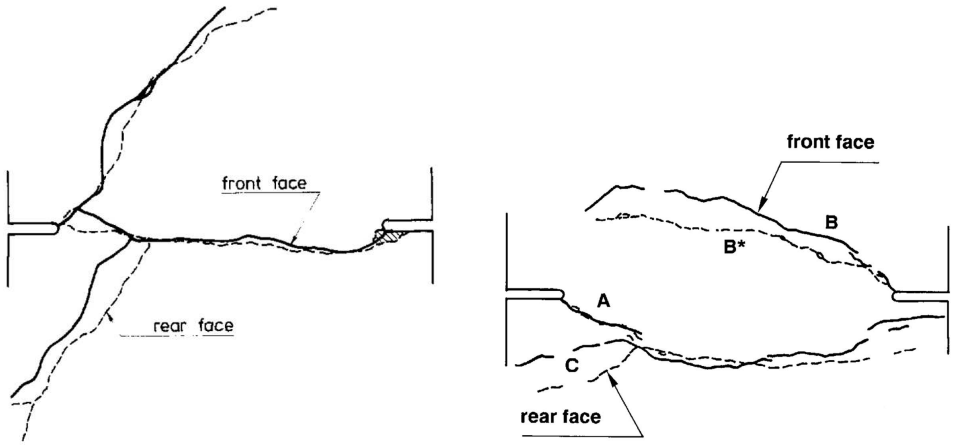


(a) (b)

**Figure 2.7***: Crack patterns reported by Nooru-Muhamed (1992).* ***(a)*** *After an initial opening the specimen is shear loaded at a constant crack opening.* ***(b)*** *An initial shear load is introduced and succeeded by an opening at a constant shear deformation.*

Nooru-Muhamed mainly consist of either cracks which initiate from each notch and propagate in a curved pattern without joining into a single crack or of a tensile crack between the notches followed by secondary cracking as a consequence of the horizontal load, see Figure 2.7. Such crack patterns may only form an indirect basis for the determination of the mixed mode behavior of an already established crack.

Unlike Nooru-Mohamed the objective for Hassanzadeh (Hassanzadeh, 1992) is to determine "the behavior of a fracture process zone in concrete, formed under pure tensile stress conditions, which later becomes subjected to simultaneously imposed normal and shear displacement", i.e. the mixed mode crack behavior. In the tests when the applied tensile stress reaches the tensile strength, the fracture process zone is considered established and the mixed mode displacement starts. Hassanzadeh developed a set-up suited for mounting in a standard testing machine, see Figure 2.8, were the vertical load is imposed through the two holes located above and below the specimen. The mixed mode loading condition is established with a separate second axis and the used specimen is notched at all four vertical faces and glued into the set-up. The tests are controlled through the relative average opening and sliding between the two specimen halves measured with two pairs of clip gauges. Hassanzadeh reports that the rotational stiffness of the set-up is too low. The lack of stiffness affects some of the experiments, seen by sudden variations or humps on the descending branches. From the tensile level equal to the tensile strength the mixed mode behavior has been explored for a variation of linear and parabolic relations between opening and sliding. In the linear cases for a relatively high amount of sliding, $\alpha = 30°, 40°$ ($\alpha$ is the inclination between the horizontal plane and the displacement path - see Section 1.1), some secondary cracking is reported. However, since the final crack pattern corresponds to the ones obtained for a pure tensile case, the results are considered valid to describe the mixed mode crack behavior of the fracture process zone established under tensile conditions.

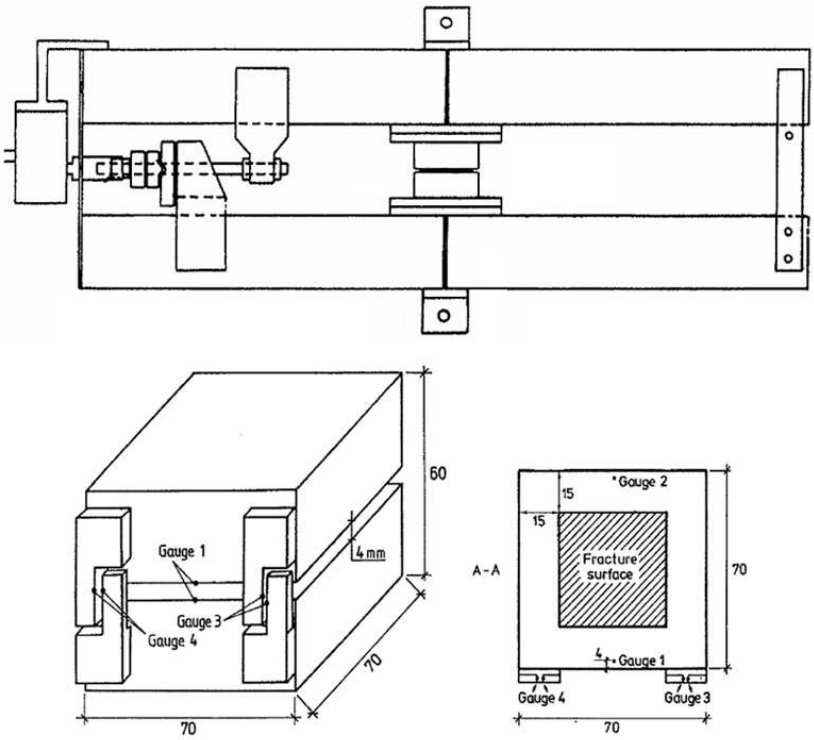


**Figure 2.8**: *Above: sketch of bi-axial test set-up. Below: sketch of specimen and attachment of strain gauges. From Hassanzadeh (1992).*

The experiences obtained from the bi-axial set-ups by Nooru-Mohamed and Hassanzadeh provides a basis for the development of a stiffer set-up for the mixed mode investigations. Besides the ideas for the set-up the comprehensive description by both Nooru-Mohamed and Hassanzadeh yield ideas for the design of the test specimens and useful knowledge in the design of the orthogonal gauge rail for the closed control loop. Their results provide a basis for the establishment of a more focused test program, centered on the mixed mode crack behavior.

# Chapter 3

# Mixed Mode Experiments

The concrete crack behavior is characterized through a series of mixed mode experiments. Double notch concrete specimens displaced in a stiff bi-axial set-up with a closed control loop are used for the experiments. For a proper displacement path the experiments result in a plane crack between the notches. The intension is to investigate the material point behavior for a single crack in a pure concrete specimen under mixed mode opening conditions. Following the definition for mixed mode crack opening from Section 1.1 a crack in concrete is initiated in pure Mode I, perpendicular to the largest principal stress. After the initiation the crack can be exposed to both opening and sliding, i.e. mixed mode opening. By crack initiation is meant the cracking stage where the micro cracks have coalesced into an apparent macro crack. In the fictitious crack model by Hillerborg et al. (1976) the initiated macro crack is assumed to be formed when the largest principal stress over the fracture process zone reaches the tensile capacity. Hillerborg et al. states that actually the crack is still an accumulation of micro cracks and that the coalescence of micro cracks into a macro crack happens once the cohesion is exhausted. However, the macro crack is observed to be formed before the cohesion is exhausted. As stated in Hassanzadeh (1992) and observed in Østergaard et al. (2007) and in the present experiments the initial crack band, i.e. the macro crack, is established when the tension load has decreased to around 50% - 80 % of the maximum tensile capacity. Hence, to make a proper mixed mode crack test of and already established crack, the test may be divided into two steps as illustrated in Figure 3.1. The first step is the crack initiation under pure Mode I opening conditions until the macro crack is fully initiated, followed by the second step, the mixed mode opening.

In the following the set-up as well as the specimen design and the design of a orthogonal gauge rail used for the closed control loop are presented. The usability of the set-up is demonstrated through both Mode I and mixed mode experiments. Based on the Mode I results an interpretation of material values like the tensile strength and the fracture energy is suggested. The mixed mode results show some clear relations between the opening level and the incremental displacement ratio between opening and sliding, and the results form a basis for the determination of the mixed mode behavior. The interpretation of both the Mode I and the mixed mode results are supported by photogrammetric registrations of the crack development.

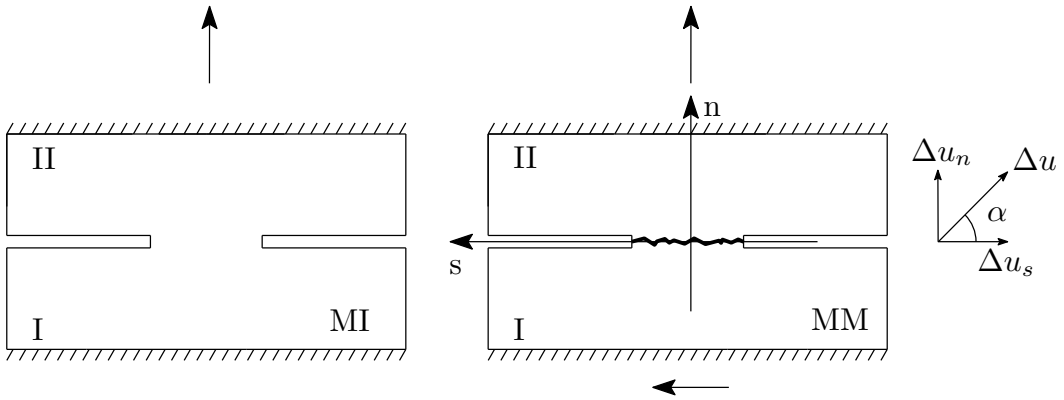


**Figure 3.1**: *The two test steps, the Mode I opening step (MI) and the mixed mode step (MM) together with the displacements directions. At the mixed mode step the local (n,s)-coordinate system and direction of positive relative displacements between the two specimen parts, I and II, are indicated and the mixed mode angle $\alpha$ is defined.*

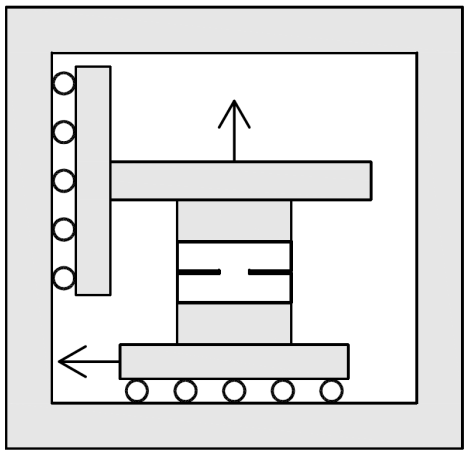

**Figure 3.2**: *The general principle of the set-up with the stiff frame supporting the motions of the two axes. Displacement directions are indicated.*

## 3.1 Set-up

The biaxial setup by Østergaard et al. (2007) has been enhanced with a new improved closed control loop and is modified to the present specimen dimensions, but the principle build up is the same. The set-up consists of a four column 5 MN universal testing machine and a built in second axis. The four column 5 MN testing machine ensures a stiff frame for the set-up as illustrated in Figure 3.2, and supports the motions in the two perpendicular directions. The support structure ensures that the two axes are geometrically independent, and the set-up has separate control valves for the hydraulic supply for the two axes.

The set-up consists of two independent actuators and is controlled by a multi-axial

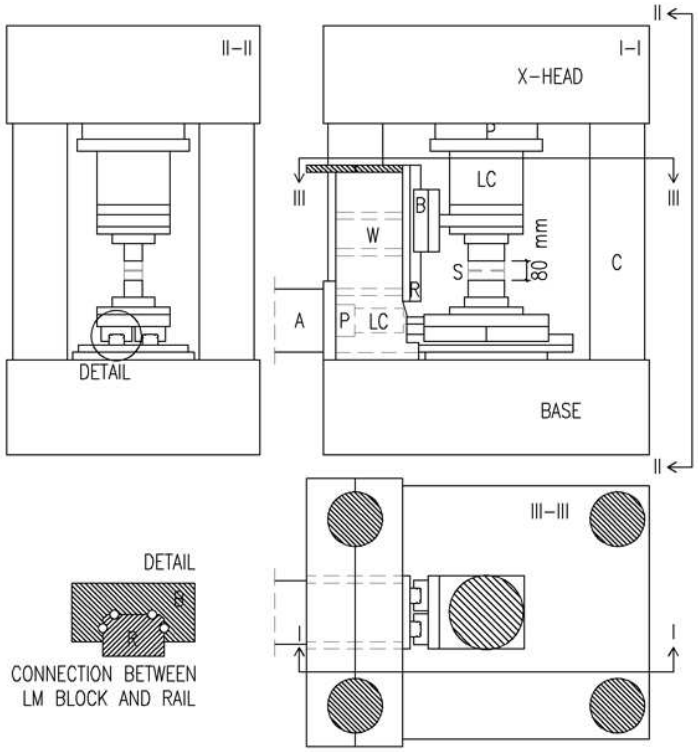


**Figure 3.3**: *Sketch of biaxial set-up. A = actuator, P = piston, LC = load cell, S = specimen, C = column, B = linear motion block (LM block), R = Rail, W = web. Some background details are left out for clarity.*

Instron 8800 control unit. The overall structure of the set-up is displayed in Figure 3.3. The four column Instron 5 MN universal testing machine is the basis of the set-up, giving a very stiff and fully functional vertical axis of loading. The horizontal axis is designed especially for the set-up and built into a very stiff support structure. This entails that the horizontal load is carried from the actuator through the specimen and back to the actuator through compression in the support structure. The support structure ensures that this custom made bi-axial hydraulic testing machine has a considerable rotational stiffness. The stiffness was measured by Østergaard et al. (2007) and is given as the translational stiffness $K_{m,t} = 500$ kN/mm and the rotational stiffness as $K_{m,r} = 8000$ kNm/rad. Compared to the actual maximum load used in the test, which is between 10-20 kN, the stiffness is considerable. Additionally, the set-up has a closed control loop, which ensures that the measuring length and thereby the impact from the elasticity of the set-up is negligible.

Figure 3.4 is a photo of the set-up with a glued in specimen but without attachment of the clip gauges used in the closed control loop. The motions of the test specimen are conducted through two slides, a horizontal and a vertical. The slides are constructed from low friction and high precision THK linear motion systems with oversized balls in the closed ball bearings. All bolted connections in the set-up are pre-stressed such that no slip between the steel plates can occur during the experiment. The specimen is glued into the set-up using sandblasted steel blocks. A rapid curing two component

**Figure 3.4**: *Test set-up with a glued in specimen. The photo shows the vertical load cell, the support structure and the slides in both vertical and horizontal direction.*

adhesive is used for the attachment. The attachment of the specimen is divided into two steps, the attachment of the bottom and the top surface of the specimen, respectively. During the gluing process the set-up is in load control, avoiding that stresses arise in the specimen during the hardening. A moderate vertical force of maximum 0.4 kN squeezes the specimen and the steel blocks together and the complete attachment takes around 25-30 minutes.

The control in the present set-up is improved to let the vertical and the horizontal axes be controlled independently by separate closed loop controls. Measurements of the opening and sliding are obtained by using specially designed gauge rails mounted on the specimen, see Section 3.1.2. In the vertical direction the load is measured using the load cell from the four column testing machine, while the horizontal load is measured by a load cell placed in immediate continuation of the horizontal slide, see Figure 3.3. The set-up has been designed for 500 kN in the vertical direction and 250 kN in the horizontal direction. In the present set-up however, the load cells limit the capacity to 100 kN and 50 kN in the vertical and horizontal direction, respectively, giving a better load resolution for the actual load interval.

### 3.1.1 Specimen

The set-up has been used in a number of different configurations. The crack initiation under mixed mode loading conditions has been investigated with the application

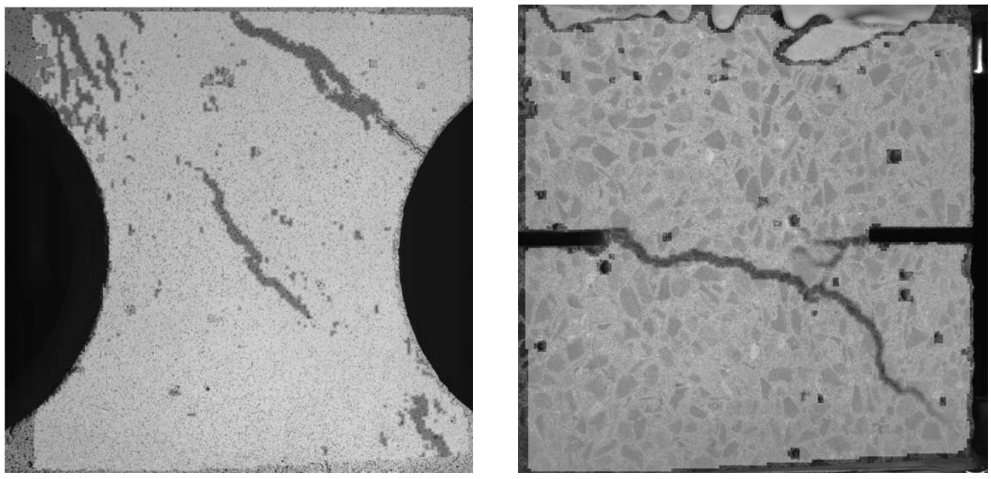

(a) (b)

**Figure 3.5***: Specimens used in the early applications of the mixed mode set-up.* ***(a)*** *Dogbone shaped specimen by Østergaard et al. (2007).* ***(b)*** *Double notch specimen tested by Jessen (2006) and presented in Østergaard et al. (2007).*

of un-notched, dogbone shaped specimens, (Østergaard et al., 2007). Figure 3.5(a) displays the specimen, were the crack initiation at the surface is shown by the use of photogrammetric techniques. Østergaard et al. (2007) report that the crack initiation occurs purely in Mode I, perpendicular to the largest principal stress. The first double notch concrete specimen had a side length and height of 150 mm and a depth of 100 mm, see Figure 3.5(b). The tests were displacement controlled using the piston motions as control variables, (Jessen, 2006). The relatively high specimen introduced a large amount of elastic energy in the set-up and together with the non-local displacement control, the larger elastic energy made the fracture initiation unstable and extremely difficult to control. Another effect of the non-local displacement control and the included elastic energy is that the obtained displacement of the crack differs from the prescribed. Hence, the actual crack opening and sliding has to be determined through an inverse analysis. Considering the double notch specimen in Figure 3.5(b) a crack between the notches has been initiated in Mode I until the tensile load is decreased to around $\frac{1}{2}f_t$, followed by a mixed mode opening with $\alpha \approx 40°$, i.e. a bit more sliding than opening. The mixed mode displacement has, as it appears from the figure, resulted in a final secondary crack pattern.

In an attempt to reduce the elastic stiffness in the set-up, the specimen dimensions were reduced by Petersen (2008) to the dimensions $150 \times 80 \times 75$ mm$^3$ with a notch depth of 37.5 mm, see Figure 3.6. The significant lower height reduced the amount of elastic energy resulting in a more stable crack growth. However, according to Petersen, the use of the piston displacements as the control signal still resulted in a large deviation between the prescribed mixed mode angle and the actual angle achieved. Besides the necessary inverse analysis, the large deviation made it difficult to control the test.

**Table 3.1**: *Mix design.*

| Mix | kg/m$^3$ |
|---|---|
| Cement (Portland Basis) | 290 |
| Water | 184 |
| Sand, 00-04 mm | 933.8 |
| Aggregates. 04-08 mm | 928.5 |

The specimen design by Petersen is used in the present experimental work as well. Here, the closed control loop ensures that the prescribed displacement corresponds to the displacement actually achieved. The specimen is used both in mixed mode experiments and in uniaxial tensile tests with repetitive loading (Madsen, 2009). However, for the mixed mode opening the specimen design results in curved crack paths, Figure 3.6(a), or even in unfortunate diagonal cracks, Figure 3.6(b). Since the crack propagates outside the measured area the diagonal crack is a challenge for the closed control loop. And the results from both the curved crack path and the diagonal crack may be considered as a structural response rather than the material point behavior for a crack in concrete. Therefore, a new specimen with deeper notches is introduced, giving the specimens dimensions $150 \times 80 \times 75$ mm$^3$ and a notch dept of 55 mm and a ligament area of $40 \times 75$ mm$^2$, see Figure 3.7(b). As shown in Figure 3.7(a) the deep notches ensure that a single plane crack develops between the two notches, which again ensures that the results may be considered as material point information.

The specimens are cut from a beam with a cross section of $150 \times 150$ mm$^2$ and a length of 600 mm. A 35 mm top and bottom layer are cut away from the beam, leaving a homogeneous, slender beam with minimal influence of the casting surfaces. The slender beam is sliced into concrete blocks with a thickness of 75 mm, and finally the 55 mm deep notches are introduced with a saw cut from the sides. The concrete has a maximum aggregate size of 8 mm and a predicted 28 days strength of 30 MPa, the mix design is shown in Table 3.1. The beams were de-molded after 24 h and then cured in 100 % humidity at 20 °C for 40 days. The testing was carried out between 45 to 65 days from the mixing day, and the compressive strength was measured in a standard cylinder test to 41 MPa, 42 days after the mixing. During the compressive test the Youngs modulus was measured to 31 GPa.

### 3.1.2 Closed Control Loop

As illustrated by Madsen (2009), who used a pair of clip gauges (CGs) mounted directly on the specimen, the test set-up is fully capable of performing full uniaxial opening histories and cyclic loading histories. But to perform stable mixed mode testing, both the measure of opening and the sliding over the fracture ligament are needed in the closed control loop. To do so, a pair of orthogonal gauges rail are designed. In Figure 3.1, the local (**n,s**)-coordinate system is introduced. Fracture in the ligament divides the specimen in two parts, I and II, respectively. Relative displacements between the two

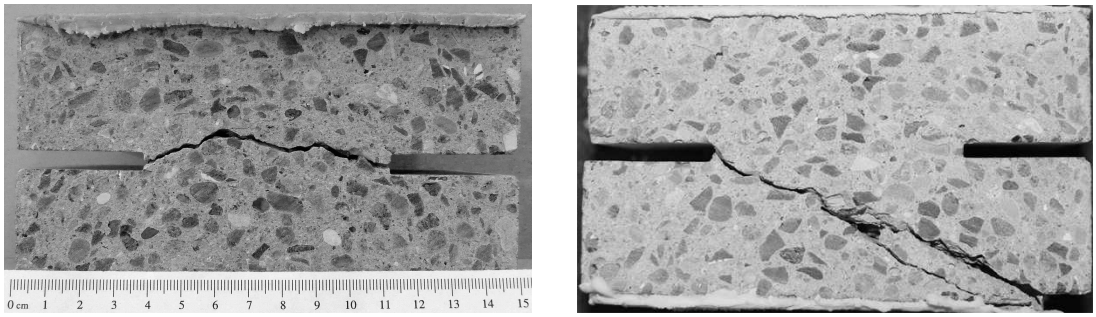

(a) (b)

**Figure 3.6***: Test specimen in the configuration with short notches.* ***(a)*** *Curved crack path between notches.* ***(b)*** *Diagonal failure.*

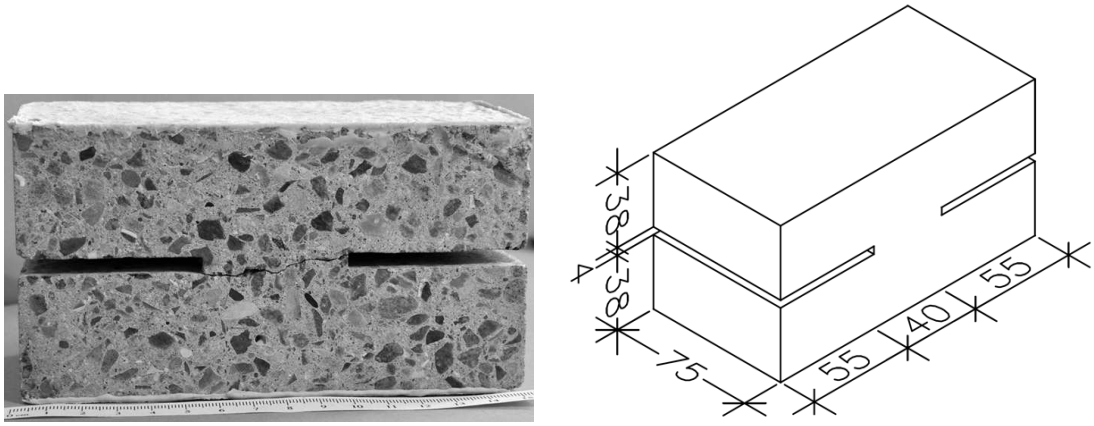


(a) (b)

**Figure 3.7***: Specimen design with deep notches.* ***(a)*** *Test specimen in the configuration with deep notches.* ***(b)*** *Sketch of test specimen with dimensions given in mm.*

parts, $\Delta u_n$ and $\Delta u_s$ in the **n** and the negative **s** direction, respectively, are defined as

$$\begin{aligned} \Delta u_n &= u_n^{II} - u_n^I \\ \Delta u_s &= u_s^I - u_s^{II} \end{aligned} \tag{3.1}$$

In the test the relative displacement $\Delta u$ is assumed to be constant along the ligament. The relative displacements are measured by four CGs mounted on the specimen using the two custom made orthogonal gauge rails placed across the two notches. In pair the CGs measure the deformation in vertical and horizontal direction, respectively. The CGs allow for independent control of the vertical and horizontal axis in the closed control loop using the mean signal in respective directions as the response signal.

Figure 3.8 shows the principle structure of the orthogonal gauge rails, and Figure 3.9 shows a two sided view of the gauge rails. The precision of the crack measures are crucial in order to obtain a stable crack growth. In each orthogonal gauge rail two small, high precision THK miniature Type LM Guides, THK (2008), are used. Low

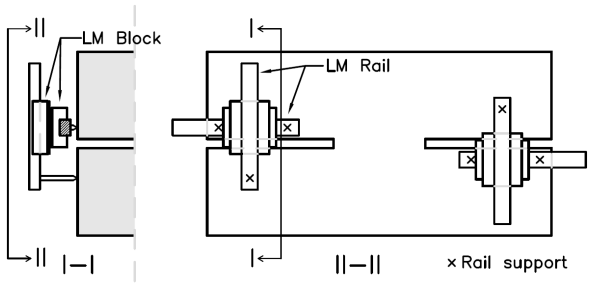


**Figure 3.8***: Principle sketch of gauges rails with Linear Motion (LM) rails, LM blocks and indication of rail supports.*

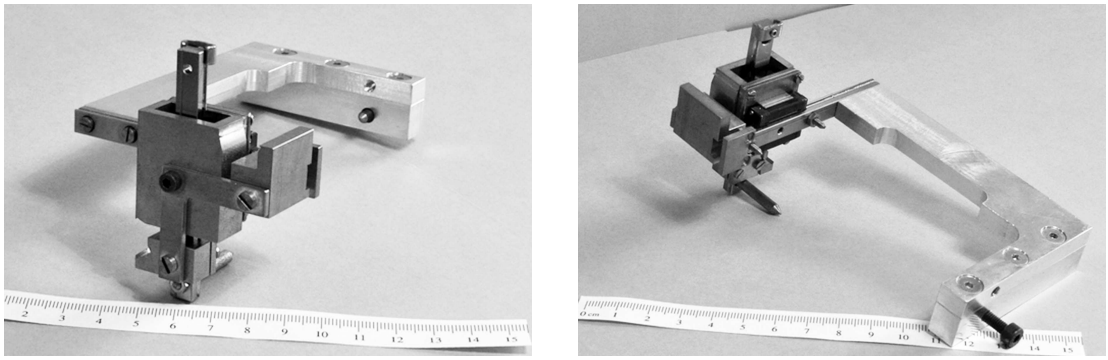

(a) (b)

**Figure 3.9***: Design of the gauges rails.* ***(a)*** *Front of gauges rail.* ***(b)*** *Rear side of gauges rail.*

friction oversized ball bearings together with the CGs allow for the determination of displacements smaller than 1 $\mu$m. The rails are assembled orthogonally through the blocks top on top, and a specially designed house around the blocks together with modified end blocks enables the attachment of CGs. At the front of the specimen the gauge rail has three supports, two at one side of the notch supporting the horizontal rail and one at the opposite side supporting the vertical rail. The two horizontal supports and the vertical support can move independently, allowing for the measuring of the relative displacement in both directions between the two parts of the specimen. The gauge rail is kept in place by an aluminum arm clamping around the specimen. At the back, the aluminum arm's point support is placed close to the centre of the triangle defined by the three front supports.

In the picture in Figure 3.9(a) a small angular metal piece, or distance piece, connects the two end blocks with the house around the two blocks. The distance piece ensures that in every test the CGs are attached with the same distance between the horizontal supports and the vertical support. In the design, the distance between the horizontal supports and the vertical support is sought minimized. At the mounting the distance is 33 mm, and the vertical center line between the horizontal supports and the vertical support is placed approximately 25 mm from the edge of the specimen. The ligament area is used to observe the crack development using the photogrammet-

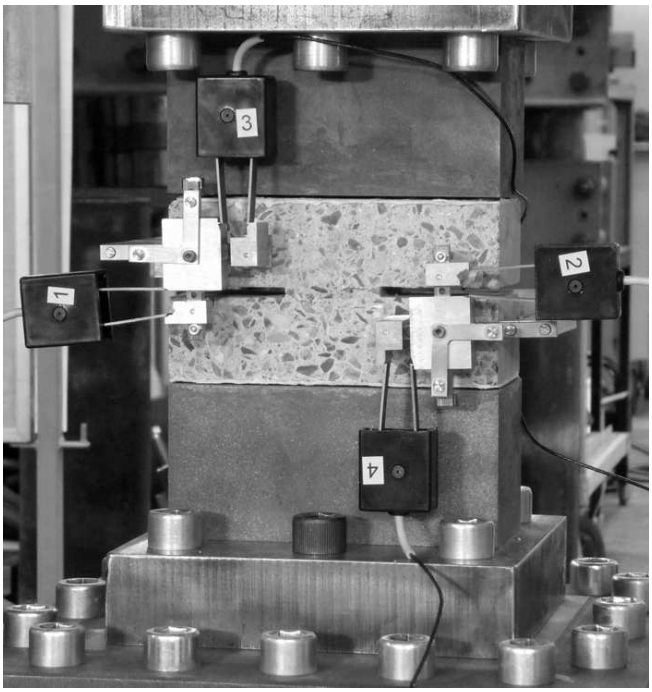


**Figure 3.10***: Close view of test specimen, gauges rails and clip gauges.*

ric equipment. If the gauges rails were mounted closer to the vertical center of the specimen, they would block the free view to the ligament area. Figure 3.10 shows the gauges rails with attached CGs mounted on the specimen.

### 3.1.3 Test Procedure and Test Program

Initially a crack is introduced between the notches by a pure Mode I opening, $\Delta u_s$= 0, and the crack is opened to a specified crack opening measured by the CGs. After the initiation of the crack the specimen can be exposed to both Mode I and II opening introducing a mixed mode opening of the crack. The mixed mode opening angle, $\alpha$ in Figure 3.1 is defined as the angle between the horizontal plane and the incremental relative displacement, i.e.

$$\tan(\alpha) = \frac{\Delta u_n}{\Delta u_s} \tag{3.2}$$

The initial, vertical displacement velocity is 0.1 $\mu$m/s, while the mixed mode opening pace is gradually increased to a final opening pace of 2.0 $\mu$m/s. Displacement velocity is set to ensure that the peak load corresponding to $f_t$ is captured in around 60 s and the test in total is finished in around 600 s. A similar displacement velocity history is used for the mixed mode experiments by Hassanzadeh (1990) and almost the same initial velocity is used in the uniaxial tensile tests by Cornelissen et al. (1986). Slow opening pace ensures a more stable crack initiation, while the total time is limited in an attempt to limit the influence of viscoelastic effects. The reported test program is listed in Table 3.2. It consists of 16 mixed mode experiments for the specimen with deep

**Table 3.2**: *Test Program, initial opening $\Delta u_n$ and mixed mode angle $\alpha$.*

| | $\Delta u_n$ [mm] | | | | |
|---|---|---|---|---|---|
| $\alpha$ | 0.015 | 0.020 | 0.025 | 0.040 | 0.100 |
| 40° | | | x | x | x |
| 45° | | | x | x | x |
| 50° | | x | x | x | x |
| 55° | | x | x | x | |
| 60° | x | x | x | | |
| 90° | 1 | 2 | 3 | 4 | |

notches (Figure 3.7(a)) with varying mixed mode angle $\alpha$ from 40° to 60° and varying initial Mode I openings $\Delta u_n$ from 0.015 mm to 0.100 mm. Besides these mixed mode experiments four uniaxial tensile tests are conducted on the same type of specimen.

### 3.1.4 Aramis

For a number of the experiments the displacement measures from the CGs are accompanied with displacements recorded by the high-resolution digital image correlation system Aramis by GOM mbH (GOM, 2005). The Aramis system is a 3D photogrammetric equipment. It employs digital stereo photographing and subsequent triangulation to determine 3D displacements on the observed surface of the specimen. The system enables determination of the displacement field in a close vicinity of the crack. The four megapixels picture, with the side lengths h×h, is divided into small regions called facets, which here consist of 15 × 15 pixels. During the analysis the movement and deformation of the facets are registered and assembled. The analysis gives a displacement field of the surface, which e.g. can be post-processed into a strain field. The discrete cracking in the experiments is then illustrated by the use of the largest principal strain registered on the surface. The notion of strain is normally not valid in combination with localized cracking, and the strain measure is only for visualization purposes. The strain calculation is based on the engineering strain determined from the relative displacement between the facets. The displacement resolution is approximately $h \times 10^{-5}$ and in the present case h equals 120 mm.

## 3.2 Noise in the Results

The nature of the crack surface introduces some scatter. At a given opening, the surface has a certain shear capacity. At a larger opening or caused by some damage in the crack surface, e.g. a rotating grain, the shear capacity may be exceeded. Exceeding the shear capacity introduces a sudden but limited drop in the load level, and this courses some scatter in the results. The scatter is most distinct in the mixed mode phase, however, since the crack is not completely plane, some frictional scatter is also present in Mode I. Figure 3.11 illustrates the size of the noise during the mixed mode for five different experiments, whereas the noise during the Mode I crack initiation is

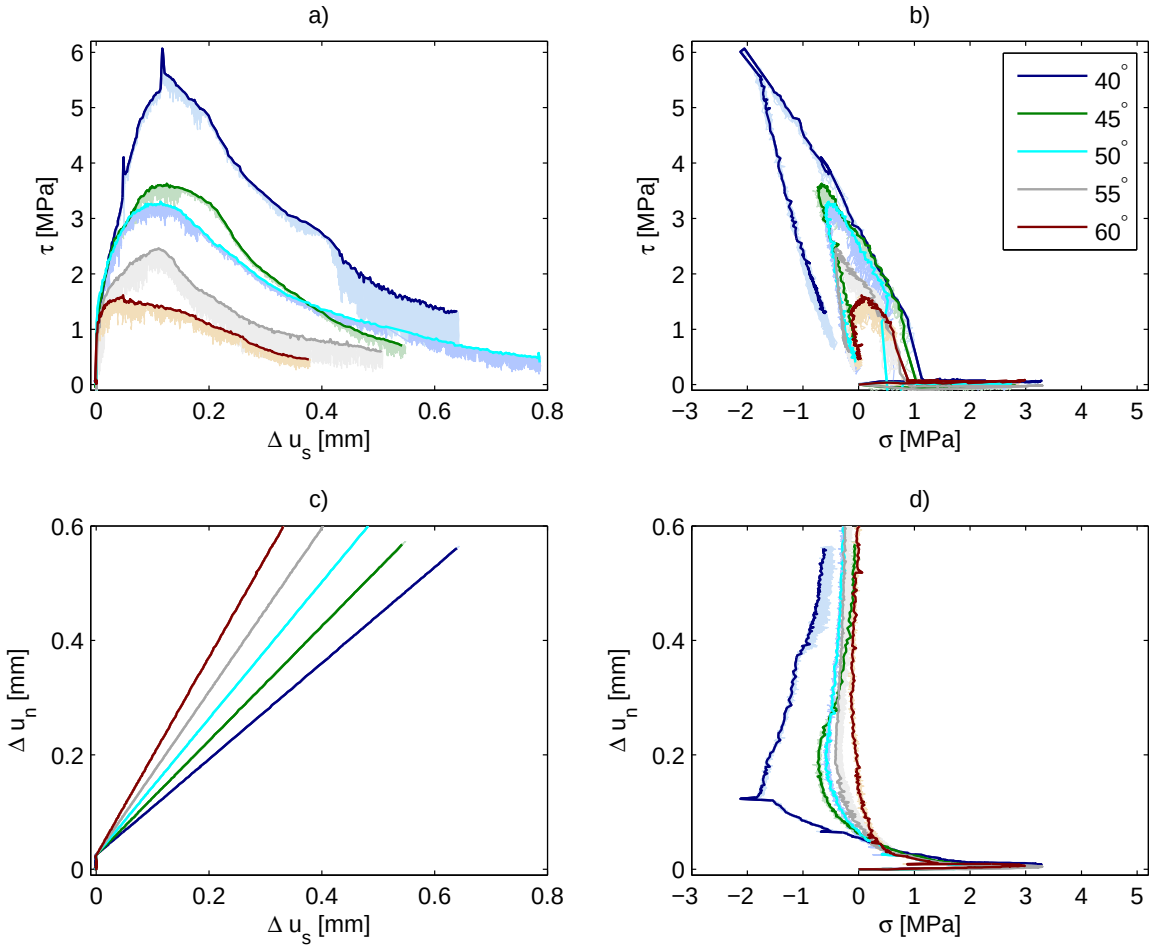


**Figure 3.11***: Mixed mode results for an initial opening of* $\Delta u_n = 0.025$ *mm. Measured data with some amount of noise shown together with the filtered representation.*

displayed in **Paper I**. The amount of noise changes during the experiments, but for all the experiments it is present at some stage, in the figure represented by the dusty colors. Figure 3.11 represents the relation between the average stresses $\sigma$ and $\tau$, defined as the measured normal and shear load divided by the ligament area, respectively, and the opening $\Delta u_n$ and the sliding $\Delta u_s$ for an initial opening of $(\Delta u_n, \Delta u_s) = (0.025, 0)$ mm followed by five different mixed mode angles from 40° to 60° controlled by the closed control loop. The mixed mode results are commented in detail in Section 3.4.

Besides the scatter related to friction some noise related to the operation of the set-up may also occur in the results. The two axes are hydraulically independent and connected only through the specimen. Noise recognized is primarily caused by tuning difficulties with the closed loop control. Stiffness of the specimen changes remarkably during the test, which makes it difficult to find a single tuning level for the entire test, and some noise is to be expected. For the mixed mode angles 40°, 45° and 50° the noise after the shear peak (see Figure 3.11(a)) is reduced. The reduction is a result of an increase in displacement rate and thereby an indirect change in the tuning of the closed control loop signal. In Figure 3.11 both the original test data and a filtered rep-

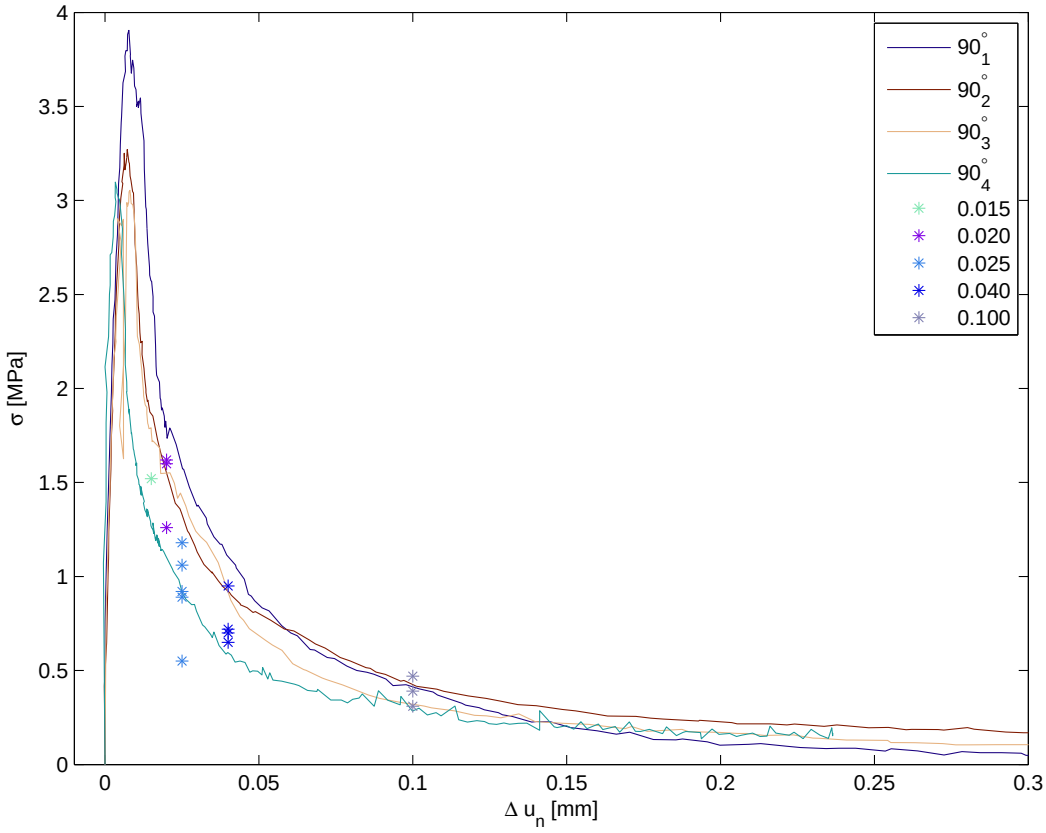


**Figure 3.12**: *Load-opening displacement results from four experiments. Normal stress $\sigma$ plotted as function of the opening displacement $\Delta u_n$.*

resentation is shown, where the filtered curves are bold and clear colored. The filtering is based on a running mean method, where the maximum shear load in an interval is found. The interval length corresponds to 20 data records of raw data, approximately equal to 2 seconds of testing time. These 20 data records are reduced to the one representing the maximum shear load. From the figure it is clear that the noise is most distinct for the shear load (Figure 3.11(a)), whereas for the normal load the scatter is in the same scale as the line thickness (Figure 3.11(d)). In the following the results have been filtered to emphasize the overall mixed mode behavior.

## 3.3 Mode I

The first experiments to be presented are four uniaxial tensile tests, where the test specimen is loaded in pure tension with respect to the ligament between the two notches, i.e. $\alpha = 90°$. The characteristic load-opening displacement responses are displayed in Figure 3.12, where the normal stress $\sigma$ is plotted as function of the opening displacement $\Delta u_n$. In three of the four tests the response during the initial loading, the peak and the tensile softening is well captured. In the last case, $90_3$, there is a stress drop around the peak. However, for an additional opening the response returns to the peak and continues with a smooth tensile softening response. Despite the fact that the

same type of specimen made of the same material is used in all four tests, there is a deviation between the result curves. Obviously, the deviation tells something about the precision of the test set-up, however, as presented with the mixed mode results in Section 3.4, the deviation may primarily be explained by the natural variation of concrete properties in the specimens. In addition to the results from the four opening tests, the normal stress level right at the end of the initial opening for the 16 mixed mode experiments are displayed in Figure 3.12. The results are placed in the same range as for the Mode I opening curves, consolidating the load opening response from the four uniaxial tensile tests. The measured load opening responses end for an opening between 0.25 mm – 0.55 mm, however, for $\Delta u_n > 0.25$ mm the inclination of the curves tend to zero, suggesting that the cohesion is exhausted.

The photogrammetric system Aramis is used to locate the crack pattern at the specimen surface, see Section 3.1.4 for details about Aramis. The crack initiation and development during the Mode I opening for a section of specimen $90_4$ is displayed in Figure 3.13. The section is approximately 50 mm wide ($\approx$ 40 mm between the notches) and the height corresponds to the 80 mm specimen height. Figure 3.13(a) shows the Aramis picture and the analyzed area. In the picture parts of the CG rails and the two horizontal CGs can be seen. In the succeeding Aramis pictures only the central part of the analyzed area are displayed. The section is focused on a 50 mm wide and 45 mm high area with a horizontal centerline corresponding to the two notches. Figure 3.13(f) shows the normal stress $\sigma$ as function of the normal opening displacement $\Delta u_n$ and the stress stages for the matching pictures are indicated. At the peak (a) the macro crack between the notches is not fully established. In fact a clear crack establishment is not obtained before the load is reduced to 30-50% of the peak load, corresponding to a stage in between pictures (b) and (c). In this case the macro crack establishment occurs at a rather large opening displacement. However, the pictures only show the fracture evolution at the surface and hence, the macro crack formation through the specimen may be more pronounced even for an earlier opening displacement stage. For an additional opening the crack pattern changes into the final pattern (pictures (d) and (e)), which consists of an apparent and plane macro crack between the two notches.

### 3.3.1 Comments on the Determination of $f_t$, $E$ and $G_f$

In the framework of the FCM (Figure 1.5), the results from the uniaxial tensile tests in Figure 3.12 can be divided into an elastic and an inelastic part. The elastic part is described by the Youngs modulus $E$ and the tensile strength $f_t$, whereas the inelastic part is described by the tensile softening curve normally denoted $\sigma_w$, where $\sigma_w$ is the tensile stress and $w$ the post peak inelastic deformations. For $w = 0$ the $\sigma_w$ is equal to the tensile strength $f_t$. For increasing crack opening $\sigma_w$ decreases until the critical crack opening $w_c$ is reach, where $\sigma_w = 0$.

Figure 3.14(a) displays a close view around the maximum tensile region. Besides the four tensile tests the measured tensile strengths from the mixed mode tests are indicated. The maximum points are scattered in the interval $\sigma = [2.7; 4.2]$ MPa with the mean value $f_t = 3.3$ MPa.

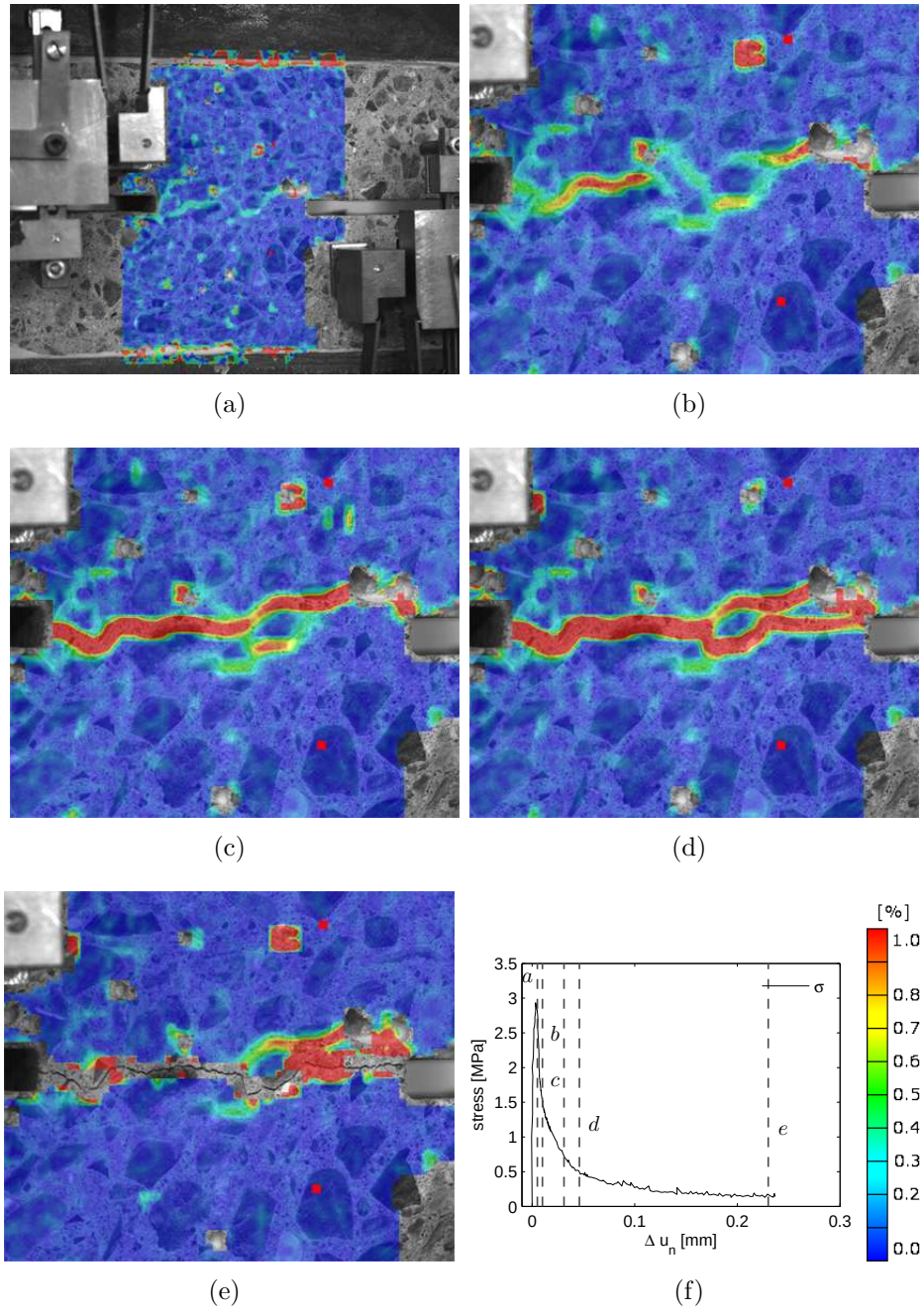


**Figure 3.13**: *Crack initiation and propagation during a Mode I opening, $\alpha = 90°$, for the specimen $90_4$.* ***(a)*** *Maximum tension, crack not fully initiated.* ***(b)*** *Tensile softening, crack initiation still in progress.* ***(c)*** *Crack fully localized.* ***(d)*** *Changing crack path.* ***(e)*** *Final crack pattern.* ***(f)*** *Stress opening relation indicating the test progress for* ***a-e***.

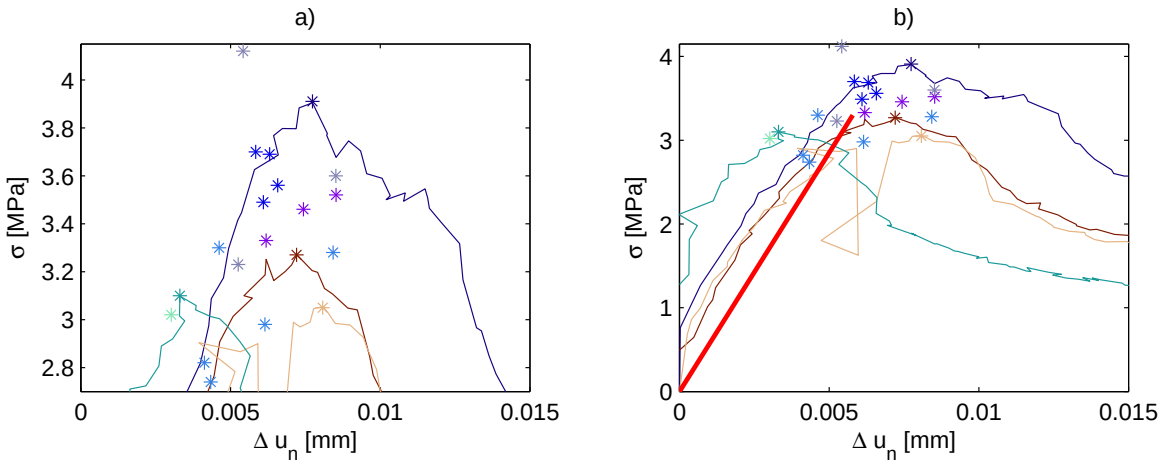


**Figure 3.14**: *Expanded view of the maximum tensile region for the uniaxial tensile tests in Figure 3.12 with indications of the maximum tensile stress for each experiment.* ***(a)*** *is centered around the tensile strength, while* ***(b)*** *displays the initial loading and the elastic response corresponding to* $E = 31$ *GPa (red line). The remaining labeling corresponds to Figure 3.12.*

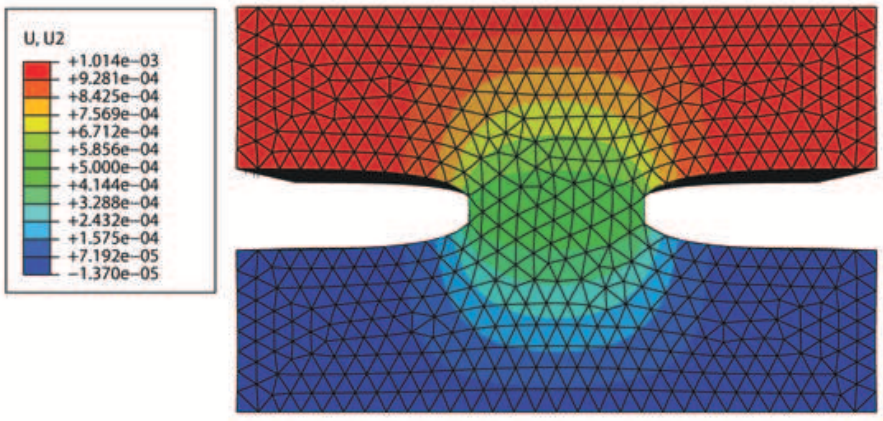


**Figure 3.15**: *Elastic FEM calculation for a Mode I displacement (perpendicular to the ligament area) of the specimen top surface. The figure displays the vertical displacements.*

The initial tensile curves, displayed for the four tensile uniaxial tests in Figure 3.14(b), are strongly non-linear which makes it rather difficult to determine the tensile Youngs modulus $E_t$ directly. Another complication in the determination of $E$ is that the deformations are measured not directly over the ligament but over the notches. The clip gauges (CGs) are attached to the gauges rails, and the location of the reference points on the two specimen halves is $\pm 33/2$ mm from the horizontal centerline and 25 mm from the vertical boundary of the specimen. To investigate the consequences of the location of the reference points and thereby the relation between the applied load and the measured displacements, an elastic FEM analysis is conducted in the commercial

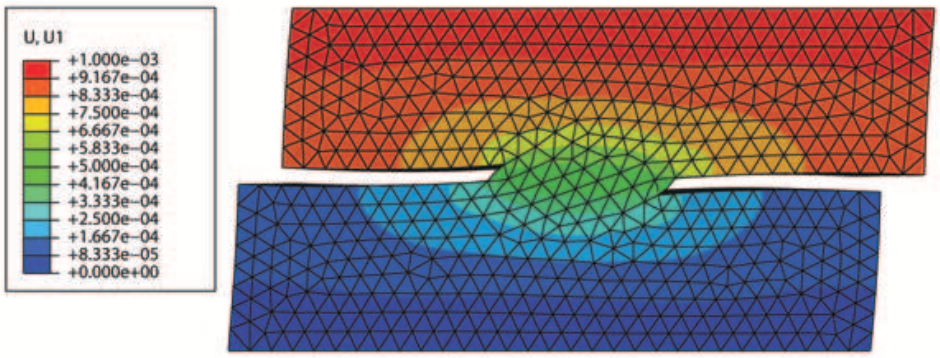


**Figure 3.16**: *Elastic FEM calculation for a sliding (parallel to the ligament area) of the specimen top surface. The figure displays the horizontal displacements.*

finite element program Abaqus. The uncertainties related to whether the specimen can be considered in plane stress or in plane strain is eliminated with a 3D modeling of the specimen. A rather fine mesh with 46.509 10-node linear strain tetrahedrons is established. The top and bottom surfaces of the specimen are rigid supported and as elastic properties the compressive measured $E_c = 31$ GPa and an assumed poison ratio $\nu = 0.22$ are used. In respect to the ligament area, the first computation is a pure Mode I displacement of the top surface of the specimen, see Figure 3.15. In this case 98% of the prescribed displacement is obtained between the reference points. Again with respect to the ligament area the second computation is a pure Mode II displacement of the top surface of the specimen, see Figure 3.16. Here 78% of the prescribed displacement is obtained between the reference points. Assuming that the prescribed displacement and the related reaction can be interpreted as the boundary conditions for the specimen in the set-up, the Mode I displacement can give the normal stiffness relation between the prescribed reaction and the measured displacement between the reference points. In a parallel fashion, the Mode II displacement can give the shear stiffness relation. In each case in order to determine the stiffness $D$, the reaction $P$ needed to introduce the displacement is divided by the ligament area $A$ and scaled by the percentage $\beta$ of the displacement reach between the reference points, i.e. $D = P/(A \times \beta)$. For $E = 31$ GPa and $\nu = 0.22$ the analyses give the elastic normal stiffness $D_n = 570$ GPa/m and the elastic shear stiffness $D_s = 380$ GPa/m. In Figure 3.14(b) the red line corresponds to $D_n = 570$ GPa/m, and the normal stiffness measured in compression seems to be a reasonable estimate for the tensile pre peak behavior.

Even with the limitation given by $f_t = 3.3$ MPa, $E = 31$ GPa and $w_c \approx 0.3$ mm, the inelastic post peak behavior $\sigma_w$ cannot accurately be determined from Figure 3.12. However, the results can give a sound estimate of the fracture energy $G_f$, which corresponds to the area under the inelastic tensile softening response. Based on a multi linear discretization of the lower and upper part of the softening response band, respectively, and with $f_t = 3.3$ MPa, $w_c = 0.3$ mm and $E = 31$ GPa the fracture energy is placed in the interval $G_f = [115 - 165]$ N/mm. Observing that over the entire displacement history none of the softening curves are placed neither in the upper nor

**Table 3.3**: *Mixed mode test program, initial opening $\Delta u_n$ and mixed mode angle $\alpha$.*

| | $\Delta u_n$ [mm] | | | | |
|---|---|---|---|---|---|
| $\alpha$ | 0.015 | 0.020 | 0.025 | 0.040 | 0.100 |
| 40° | *secondary* | | ⊣ | ⊣ | ⊣ |
| 45° | *cracking* | | ⊣ | ⊣ | ⊣ |
| 50° | | ⊣ | ⊣ | ⊣ | — |
| 55° | | ⊣ | ⊣ | — | |
| 60° | ⊣ | ⊣ | — | *pure opening* | |

— plane crack,
⊣ plane crack with local secondary cracking,
⊣ dominant secondary crack

in the lower part of the softening band interval, an average value seems to be a good estimate for the fracture energy. Summarized, in terms of the FCM the uniaxial tensile response can be described by $f_t \approx 3.3$ MPa, $E \approx 31$ GPa and $G_f \approx 140$ N/mm.

## 3.4 Mixed Mode

This section presents selected characteristic results for the mixed mode experiments. The effect of the different combinations of initial openings and mixed mode angles are illustrated and in addition to the results, the fracture development recorded with Aramis is reported for four of the experiments. The complete series of mixed mode results are presented in **Paper I**.

The test combinations of initial openings and mixed mode angles for the 16 mixed mode experiments are listed in Table 3.3. The combinations cover results ranging from an almost pure Mode I opening, ($\Delta u_n$,$\alpha$)=(0.100,60°), to an ending failure in one of the secondary cracks, ($\Delta u_n$,$\alpha$)=(0.015,60°). The secondary failure results in a new inclined primary crack, similar to the one shown in Figure 3.6(b), running away from the ligament area. For a larger initial opening the specimen can be displaced in a smaller mixed mode angle without introducing secondary cracks, while a smaller initial opening needs a larger mixed mode angle to avoid the secondary failure. The different tests indicate a band for combinations of interest, i.e. combinations where the mixed mode angle for the given initial opening is small enough to introduce some shear stresses and still high enough to avoid a secondary failure. The combinations (0.015,60°), (0.020,55°) and (0.025,45°) almost result in a secondary failure with (0.015,60°) actual changing from a ligament crack to a secondary fracture during the test. In the other end the dilation caused by the sliding is balanced by the simultaneous crack opening, so the combinations (0.025,60°), (0.040,55°) and (0.100,50°) almost do not encounter any build up of compression stresses.

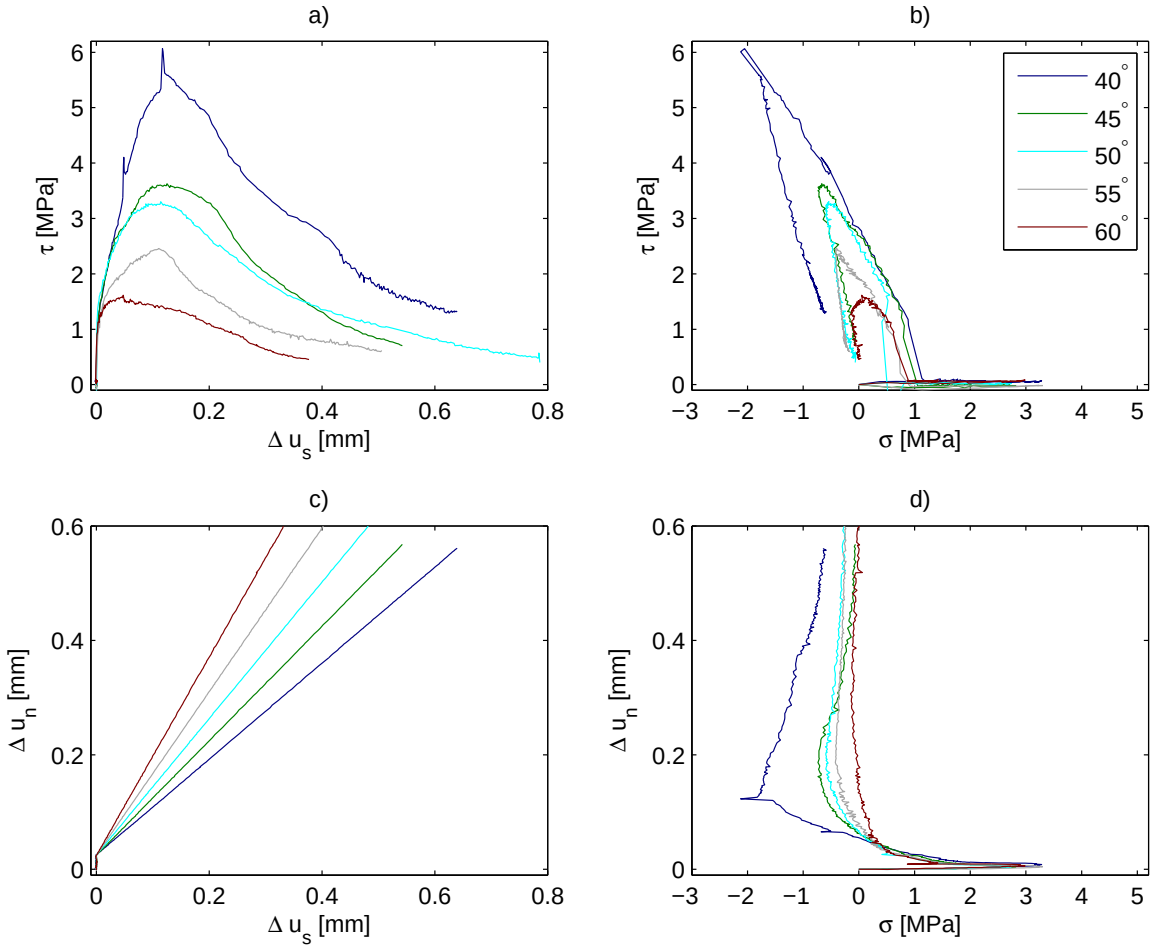


**Figure 3.17**: *Mixed mode test results for five different mixed mode angles with the same initial opening of* $\Delta u_n = 0.025$ *mm.*

### 3.4.1 Results for Constant Initial Opening

The filtered results from Figure 3.11 are presented in Figure 3.17. The figure shows the mixed mode behavior for five specimens with an initial opening of $\Delta u_n = 0.025$ mm followed by five different mixed mode angles ranging from 40° to 60° dictated by the closed control loop. In Figure 3.17(c) the initial opening of $(\Delta u_n, \Delta u_s) = (0.025, 0)$ mm in each test is recognized and after the opening the five different mixed mode angles can be read from the figure. Deformations in Figure 3.17(c) are measured by the CGs and are the actual responses to the demand. Figure 3.17(d) shows the load opening displacement similar to Figure 3.12 but with interchanged axes and a larger range of opening. In Figure 3.17(d) for the normal stress, there is a clear correlation between the level of compression and the size of the mixed mode angle. A lowered mixed mode angle is equal to a higher level of sliding and thereby intensified dilational effects, which in the displacement controlled test results in more compression. The 40° has the most compression followed by 45°, 50° and 55° while in the 60° test the compression level approaches zero. Responses for 45° and 50° are roughly identical, which probably is an effect of the natural variation of concrete properties. The spike

for 40° at maximum compression is caused by a change of fracture from a beginning shear crack away from the ligament to a more significant opening crack. Similar to Figure 3.17(d) for normal stress, the shear stress level, shown together with the shear displacement in Figure 3.17(a), increases for lowered mixed mode angle where the sliding starts to dominate. The displacement controlled test introduces some confinement over the ligament and the ligament can thereby transfer a considerable amount of shear stresses, in these tests up to twice as high as the tensile strength. Figure 3.17(b) combines the results from the three other plots and shows the shear stress, $\tau$, as function of the normal stress, $\sigma$. Despite the few tests there is a clear tendency in the mixed mode behavior, where the results exhibit almost straight lines in the stress-plot in both loading and unloading before and after the peak, respectively.

The fracture evolution at the surface is registered with the photogrammetric system Aramis for four of the five experiments in Figure 3.17. The pictures give an idea on how the primary crack between the notches develops and illustrates the amount of secondary fracture for varying mixed mode angles. In the Figures 3.18-3.21 the fracture evolution for the four specimens are displayed. All four specimens are displaced to an initial opening of $\Delta u_n = 0.025$ mm and then followed by the mixed mode angles $\alpha =$ 60°, 50°, 45° and 40° , respectively. In three of the four experiments the localization of a macro crack takes place between the peak and the beginning of mixed mode, i.e. between pictures (a) and (b), where the load normal load is reduced to 30-40 % of the peak load. For $\alpha = 40°$ in Figure 3.21 an actual primary crack is not localized until the end of the experiment, picture (e). For $\alpha = 60°$ in Figure 3.18 the final crack pattern consists of one primary crack between the notches and a second crack propagating parallel with the first one from the left notch towards the right notch. Even though the fractured area seems overwhelming, the extent perpendicular to the notch-line is in the range of the notch width (4 mm) and below the maximum aggregate size of 8 mm.

The tests are displacement controlled, so after some mixed mode loading the dilational effects will shift the normal load from tension to compression and thereby build up some confinement over the ligament area. Figure 3.19(c) for $\alpha = 50°$ is snapped directly at this transition and despite a clear, primary crack some secondary cracks tend to grow in crack planes inclined with respect to the ligament area. Figure 3.19(e) shows the final fracture development for loads returning to zero, where a clear fracture area is localized representing some secondary cracks and an distinct primary opening crack. The crack path is influenced by the aggregates and the current stress state. The sliding introduces some secondary cracks in one or more crack planes located outside the ligament area. If the sliding is dominant compared to the opening, one or more of the secondary cracks may end up being the primary one and the specimen may fail due to a secondary fracture. In this case the test has failed. But if the end state consists of a primary crack between the two notches, possibly with some local secondary cracking, the results are considered as the material information for a single, plane crack.

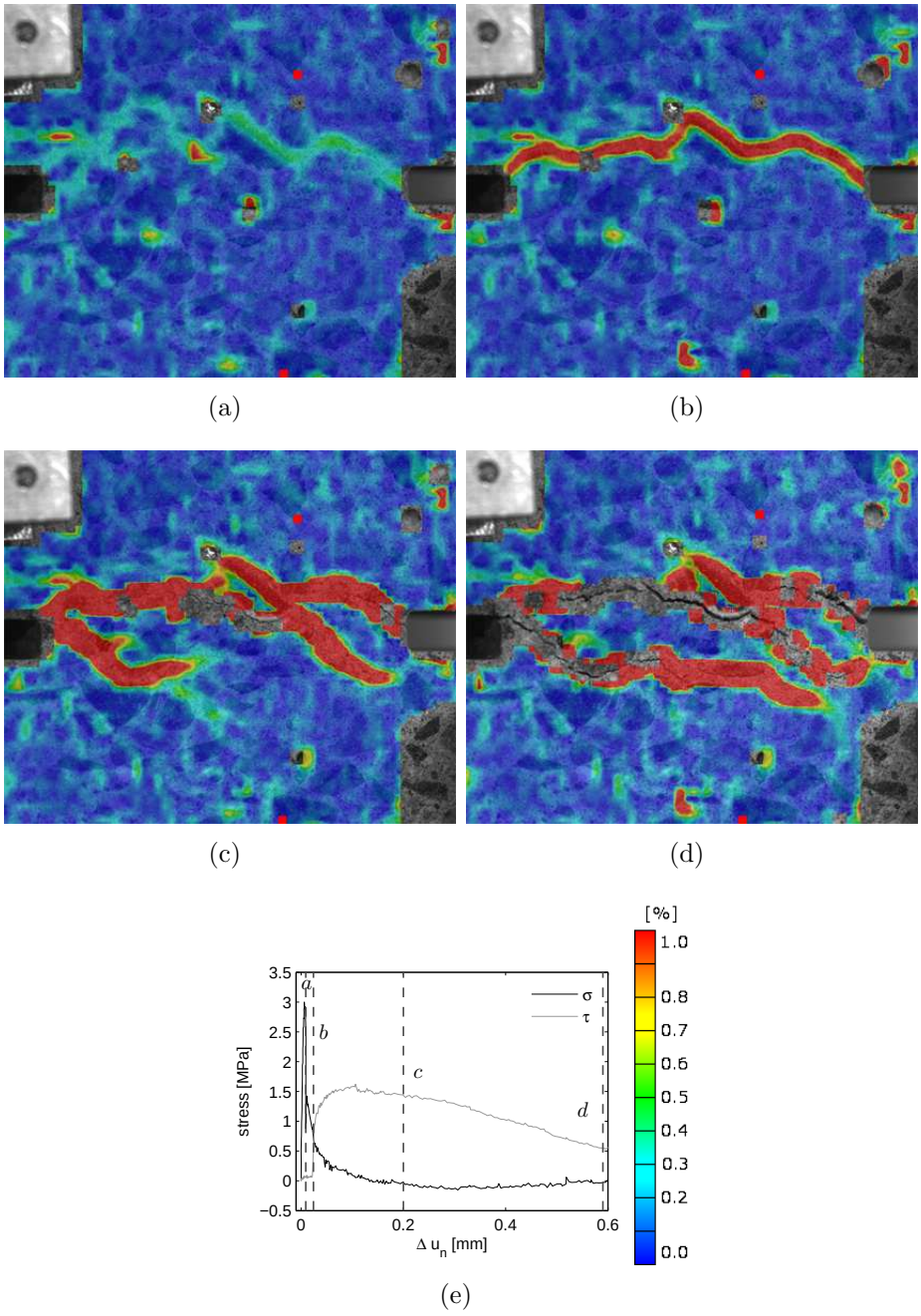


**Figure 3.18**: *Crack initiation and propagation during the mixed mode experiment with initial opening* $\Delta u_n = 0.025$ *mm and mixed mode angle* $\boldsymbol{\alpha}$**= 60°**. ***(a)*** *Maximum tension, crack not fully initiated.* ***(b)*** *Start of mixed mode, crack fully localized.* ***(c)*** *Fracture area propagates.* ***(d)*** *Final crack pattern.* ***(e)*** *Stress opening relation indicating the test progress for* ***a-d***.

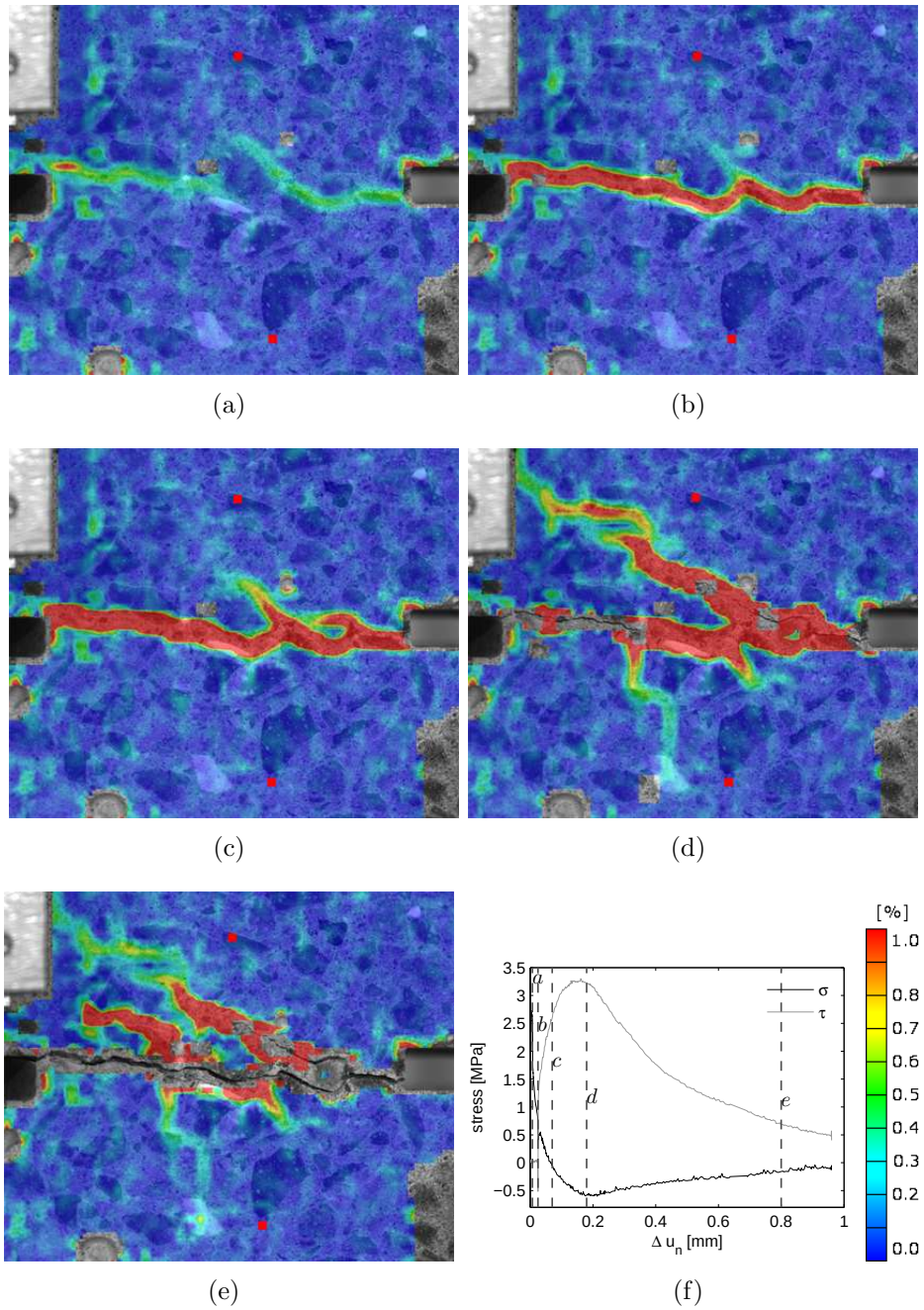


**Figure 3.19**: *Crack initiation and propagation during the mixed mode experiment with initial opening* $\Delta u_n = 0.025$ *mm and mixed mode angle* $\boldsymbol{\alpha}$**= 50°**. ***(a)*** *Maximum tension, crack not fully initiated.* ***(b)*** *Start of mixed mode, crack fully localized.* ***(c)*** *Normal stress changing from tension to compression, initiation of secondary cracks.* ***(d)*** *Maximum compression and shear. Propagating secondary cracks and visible opening crack.* ***(e)*** *Final crack pattern with clear primary crack and some secondary fracture primarily localized at the right notch.* ***(f)*** *Stress opening relation indicating the test progress for* ***a-e***.

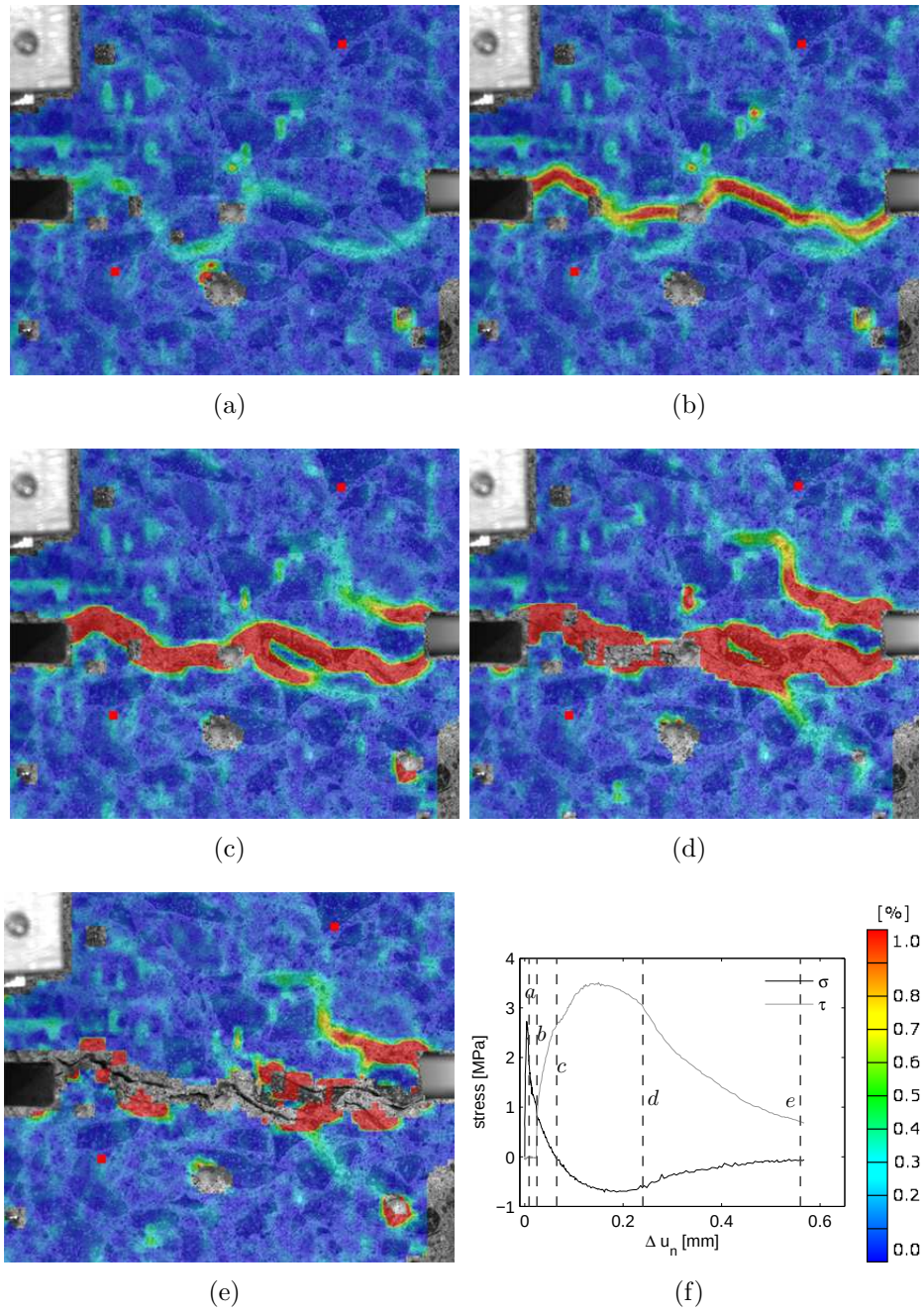


**Figure 3.20**: *Crack initiation and propagation during the mixed mode experiment with initial opening* $\Delta u_n = 0.025$ *mm and mixed mode angle* $\boldsymbol{\alpha}$**= 45°**. ***(a)*** *Maximum tension, crack not fully initiated.* ***(b)*** *Start of mixed mode, crack fully localized.* ***(c)*** *Normal stress changing from tension to compression, initiation of secondary cracks.* ***(d)*** *After maximum compression and shear. Propagating secondary cracks and visible opening crack.* ***(e)*** *Final crack pattern with a clear primary crack and only minor secondary fracture primarily localized at the right notch.* ***(f)*** *Stress opening relation indicating the test progress for* ***a-e***.

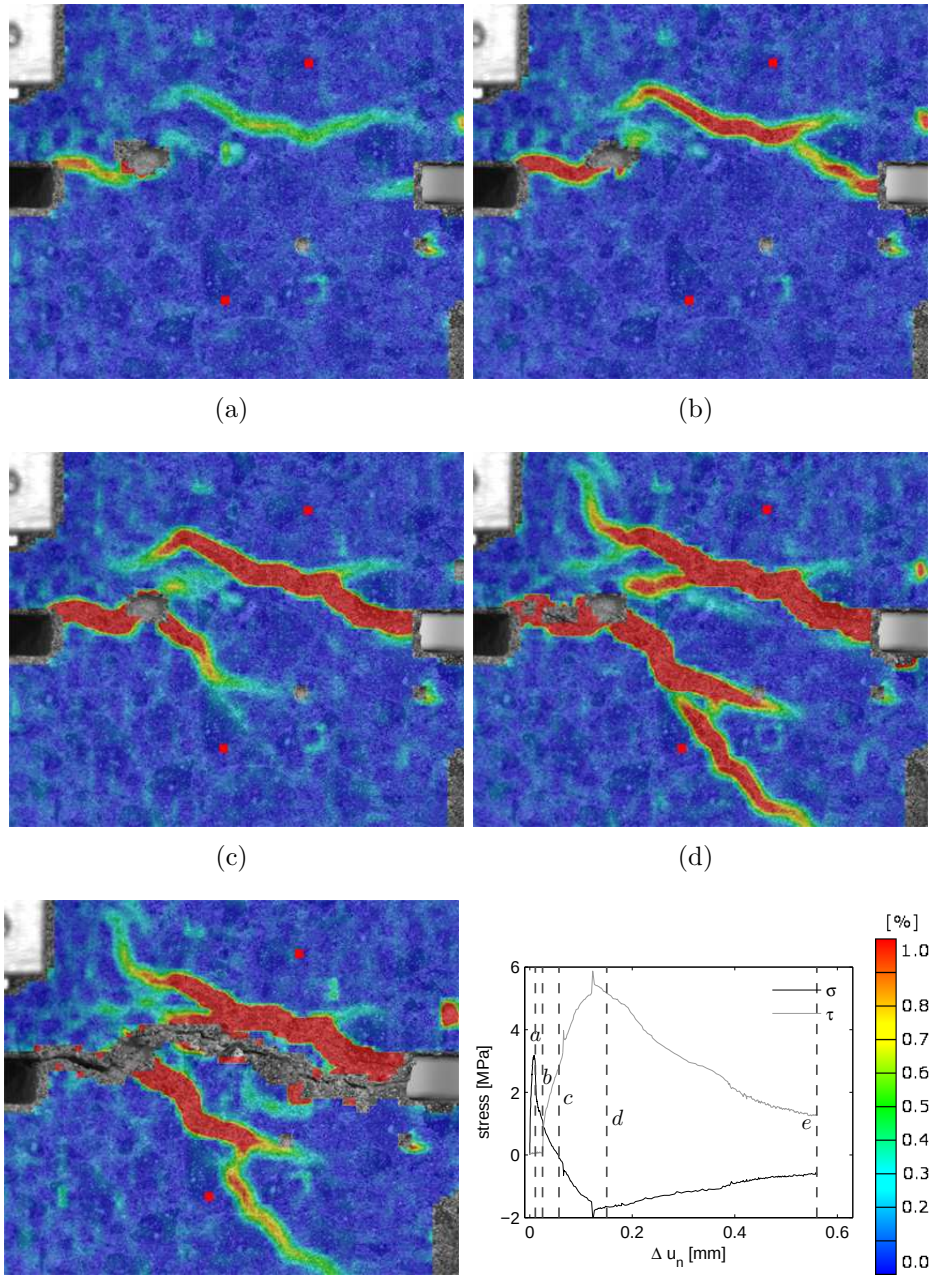


**Figure 3.21**: *Crack initiation and propagation during the mixed mode experiment with initial opening* $\Delta u_n = 0.025$ *mm and mixed mode angle* $\boldsymbol{\alpha}$**= 40°**. ***(a)*** *Maximum tension, crack not fully initiated.* ***(b)*** *Start of mixed mode, macro crack seems divided into three parts.* ***(c)*** *Normal stress changing from tension to compression, two crack paths.* ***(d)*** *Maximum compression and shear. Propagating secondary cracks.* ***(e)*** *Final crack pattern with a clear primary crack and some secondary fracture.* ***(f)*** *Stress opening relation indicating the test progress for* ***a-e***.

The secondary cracking seems less pronounced for $\alpha = 45°$ in Figure 3.20 and the experiment ends with a distinct primary crack between the notches and minor secondary cracking primarily localized at the right notch. The fracture development for $\alpha = 40°$ in Figure 3.21 consists of two cracks propagating from each notch. Only at a late stage the two cracks coalesce into a primary crack between the notches. As seen in Figures 3.18-3.21 the crack between the notches is not completely straight and the crack pattern also includes some secondary cracking. The secondary cracking seems more pronounced for lowered mixed mode angle. The Aramis pictures give a surface image with only an indication of how the underlying fracture surface develops. In Chapter 4 an investigation of the fracture surface is conducted.

### 3.4.2 Results for Constant Mixed Mode Angle

Figure 3.22 presents the mixed mode behavior for four specimens with varying initial openings from $\Delta u_n = 0.020$ mm to $\Delta u_n = 0.100$ mm. In all four cases the initial opening is followed by a mixed mode opening with a constant mixed mode angle $\alpha = 50°$ . From Figure 3.22(c) the different initial openings together with the constant mixed mode opening of 50° are recognized. From (a) and (d) it is clear that the highest level of shear and compression is obtained for the smallest initial opening, and that the stress level drops for increasing initial opening, with almost no compression for $\Delta u_n = 0.100$ mm. For the first 0.2 mm displacements the responses from $\Delta u_n = 0.020$ mm and $\Delta u_n = 0.025$ mm almost coincide. The small change in initial opening should introduce a larger difference. However, the scatter band for the opening tests in Figure 3.12 suggests that the almost coinciding curves probably are a consequence of the natural variation of concrete properties. Despite the few tests there is an apparent tendency in the mixed mode behavior presented in Figure 3.22(b). The stress level increases for decreasing initial opening, and again the lines in both loading and unloading before and after the peak in the stress-plot are almost straight.

For the tests with constant initial opening in Figure 3.17, the 40° test with the relative large amount of sliding almost results in a shear fracture. The 60° test with a relatively large amount of opening is almost without any mixed mode effects. Similar for the tests with constant mixed mode angle in Figure 3.22 the large initial opening of $\Delta u_n = 0.100$ mm is almost without any mixed mode effects, while it was impossible to conduct the same test for an initial opening of $\Delta u_n = 0.015$ mm. The five tested mixed mode angles for the chosen initial opening, and the four different initial openings for the same mixed mode angle, cover the relevant test area from nearly encountering a shear fracture to an almost pure Mode I opening. In the stress plots in Figure 3.17(b) and Figure 3.22(b) the stress paths in mixed mode have almost straight lines in both loading and unloading, a Coulomb-like behavior. In general there is a clear tendency that the shear level and the compression level raise for both decreasing initial opening and for decreasing mixed mode angle.

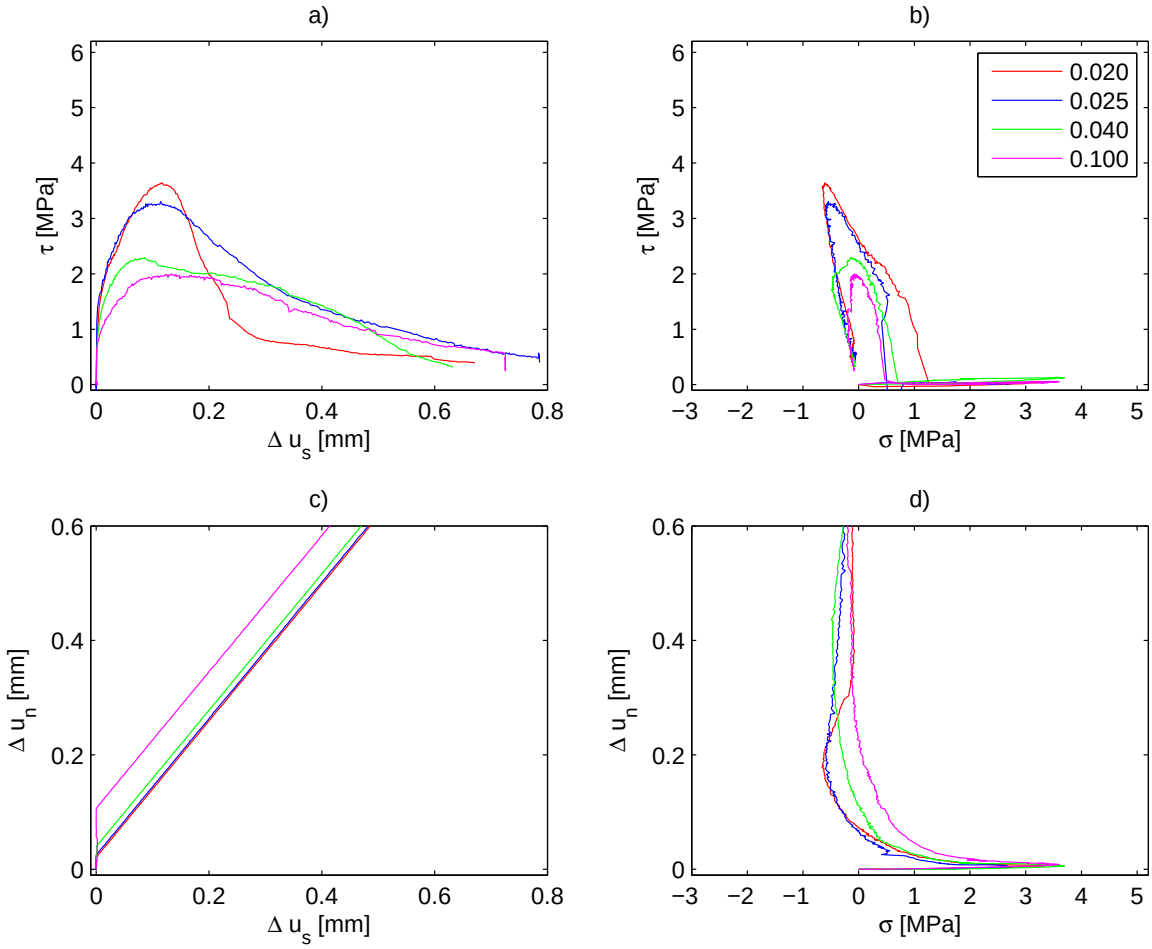


**Figure 3.22**: *Mixed mode test results for four different initial openings with the same mixed mode angle of* 50°.

## 3.5 Concluding Remarks

The biaxial set-up has obtained a new enhanced closed control loop with the relative opening and sliding of the crack as the control signals. The opening and the sliding of the crack are measured by clip gauges using two custom made orthogonal gauge rails mounted on the specimen. With a build in second axis, the set-up is to some extent equivalent to the one described in Hassanzadeh (1992). The present set-up is significantly stiffer and with the closed control loop it is possible to run stable Mode I and mixed mode experiments. The orthogonal gauge rails result in a direct interpretation of the mixed mode crack opening process, ensuring that the achieved response over the ligament is equal to the prescribed mixed mode angle. There are both pros and cons regarding the use of the 5 MN universal testing machine. It provides an extremely stiff vertical axis and a stiff support for the second, horizontal axis. The load resolution is improved by a smaller load cell; however, since the vertical axis is designed for loads up to 5 MN, the hydraulic supply may be oversized.

As a double notch rectangular specimen the specimen design follows the design line from Nooru-Muhamed (1992). Hassanzadeh (1992) used a specimen notched on all four vertical faces. However, with a sufficient out of plane stiffness the double notch specimen has the advantage that during the experiment it is possible to follow the fracture propagation. The deep notches of the present specimen ensures that the crack surface is even and governed by material aspects like aggregate size and concrete strength rather than structural effects. This even crack supports a direct interpretation of the mixed mode behavior, and the results may be considered to be the mixed mode material point behavior of a crack in concrete.

The Mode I crack behavior is well tested both in continuous opening and under open-closure conditions (Madsen, 2009). Despite some scatter between the Mode I results, the total response from the 20 experiments provide solid information on the tensile softening curve. The scatter indicates the natural variation in the concrete properties. The presented mixed mode results only represent the mixed mode behavior during continuous opening. However, the results show clear relations between the opening stage and the prescribed mixed mode angle. To conduct a successful mixed mode experiment a crack is initiated in the specimen. The experiments indicate that the crack is initiated or localized for an opening around $\Delta u_n > 0.015$ mm corresponding to a decrease of the normal load to 30-50% of the peak load. Smaller initial openings result in misfortunate secondary cracking failure. In the tested range of initial openings and mixed mode angles, $\alpha \approx 40^\circ$ seems to be a lower limit for the mixed mode angle. Smaller angles will most certainly result in a secondary and misfortune failure. On the other hand, experiments with $\alpha > 60^\circ$ seems to be an upper limit, where the mixed mode effects becomes less pronounced and the response resembles the Mode I response. Summarized, the set-up has proven adequate for mixed mode testing and the obtained results provide a basis for the understanding of cracks in mixed mode.

# Chapter 4

# Crack Topography

The photogrammetric registration of the test specimens with Aramis, Figure 3.13 and 3.18-3.21, gives a detailed insight into the fracture propagation at different stages during the mixed mode displacement. Despite the tendency to develop some secondary cracks the final crack pattern in all the Aramis examples consist of a distinct primary crack between the notches. The test specimens are casted from a concrete with varying aggregate size up to 8 mm, and the concrete properties is far from being homogenous. Therefore a completely straight crack path will not be possible. Nevertheless, the crack paths in the present tests are almost straight, with a variation smaller than or equal to the notch height of 4 mm. This fracture localization between the notches is a characteristic of the test specimen. Structural effects obtained with the old test specimen with short notches, Figure. 3.6(a), are avoided by the deeper notches. The Aramis pictures of the specimen surface give a qualitative estimate of the crack propagation all the way through the specimen. The heterogeneous nature of the concrete may affect the pictures though, so that they only tell a part of the fracture history. An example of this is the specimen with the initial opening $\Delta u_n = 0.025$ mm followed by a 40° mixed mode opening. Besides a distinct final crack between the notches the Aramis pictures in Figure 3.21 display a significant amount of secondary cracks. The result curves in Figure 3.17 with a high amount of shear and compression stresses support the picture

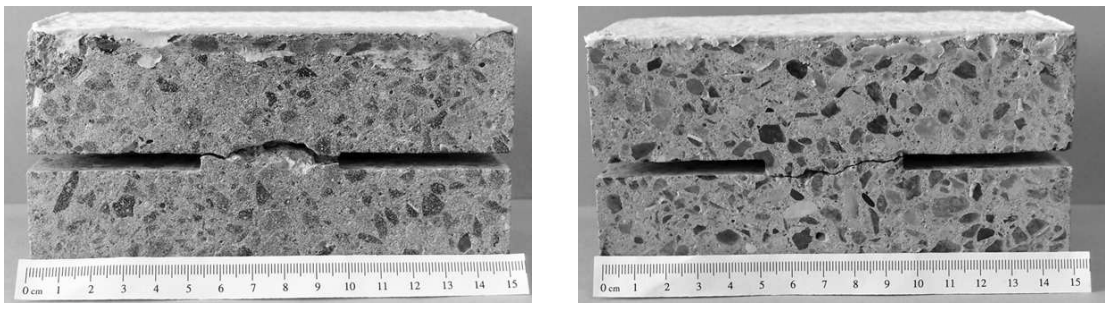

(a) Front, Aramis side.

(b) Back.

**Figure 4.1***: Final crack path for specimen initially opened to $\Delta u_n = 0.025$ mm followed by a 40° mixed mode opening. With the photogrammetric system Aramis the crack propagation during the test is followed in Figure 3.21.*

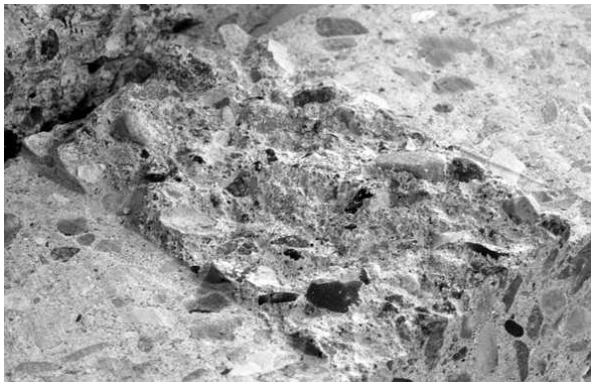

**Figure 4.2***: Close view of the crack surface for the specimen initially opened to* $\Delta u_n = 0.025$ *mm followed by a* $40^\circ$ *mixed mode opening.*

of an almost secondary failure mode. However, an investigation of the specimen after the experiment, see Figure 4.1(a), shows that at least some of the secondary cracking in the Aramis pictures in Figure 3.21 is caused by a loose piece of concrete in direct connection to the picture surface. The back side of the specimen in Figure 4.1(b) shows a more straight crack path. The closer view of the crack surface in Figure 4.2 supports the picture of a more straight crack path. Based on the Aramis pictures and the picture of the fracture surface in Figure 4.2, it can in general be stated that the fracture is localized between the aggregates and that the crack surface is influenced by the aggregate size, but without the earlier reported structural effects. Within the scope of macro cracking this plane fracture localization ensures that the mixed mode results in Chapter 3 and **Paper I** may be considered as material point information.

To some extent crack mechanisms like the cohesion, the dilatational effect, the stiffness degradation and the friction are related to the irregular and rough crack surface. When the mixed mode results are considered as the material point behavior for a crack in concrete, these crack mechanisms are a part of the material response. Hence, a constitutive crack modeling may also include these crack effects and thereby either directly or indirectly the roughness of the crack surface. Simplified for the plasticity models by Carol et al. (1997) and Nielsen et al. (2010) the friction and the dilatational effects are included through the yield surface and the plastic potential; the cohesional degradation is described through the yield surface shrinkage; and in Nielsen et al. (2010) the stiffness degradation is ensured by the damage submodel. The roughness may also be included in a more direct way by for instance damage-contact through a rough crack model as presented in Mihai and Jefferson (2011). Based on observations of concrete and cracks in concrete they establish a schematic saw-tooth crack surface which is used in a micro-mechanical modeling. Through a distribution of the inclinations and the height of the saw-teeth the surface represents the roughness and irregularities of a crack surface. The concept in Mihai and Jefferson (2011) follows the ideas of aggregate interlock from Walraven and Reinhardt (1981). In Walraven and Reinhardt (1981) the aggregates are simplified by spheres. Under the assumption that the fracture develops between aggregates and cement paste the crack surface is characterized by a plane surface and a number of spherical irregularities. As in the saw-teeth crack surface in Mihai


**Figure 4.3***: Hawk scanner and specimen half.*

and Jefferson (2011) the roughness of the crack surface is described by the spherical contact area for a shear displacement at a given opening.

If a more direct inclusion of the irregularities and roughness of the crack surface are sought, a surface description is needed. Figure 4.2 gives a visual impression of a crack surface and the observations may be used to characterize the surface roughness. However, a more quantified estimate of the surface may be obtained from an actual topographic measurement of the specimen halves and in particular the crack surface. In this chapter a laser measurement of the crack surface is presented. The result directly represents the crack topography. Based on the topographic measure the surface is characterized by a sequence of average contour lines. Thereafter the surface description can be used as input to the constitutive modeling in Chapter 5.

## 4.1 Laser Scanning

A description of the concrete crack surface topography is obtained by a measurement of the cracked specimen. The Nextec Hawk scanner (Hawk, 2000), which is a non-contact optical laser-scanner, is used for the crack surface registration, see Figure 4.3. As input to the scan a representative, rectangular area of the cracked surface is selected and the spacing in the plane between the scan points is dictated. For each scanning point at the crack surface the scan gives a $(x, y, z)$-coordinate data set representing latitude, longitude and height, respectively. Figure 4.4 illustrates a 3D plot of the measured rough crack surface and the adjacent plane, notched parts. A few of the exposed aggregates give an unfortunate reflection and some of the scan points are thereby unregistered. Though, as displayed in Figure 4.4 the scan does provide a convincing measure of the crack topography. As listed in Table 4.1 four different specimens have

**Table 4.1**: *Scan program.*

| Specimen | resolution [mm] | $\Delta z$ [mm] |
|---|---|---|
| $90_3^d$ | 0.08 | 9.55 |
| $90_3$ | 0.16 | 9.52 |
| $90_1$ | 0.16 | 10.55 |
| $90_2$ | 0.16 | 10.29 |
| $\Delta u_n = 0.040$ mm, $\alpha = 45°$ | 0.16 | 11.59 |

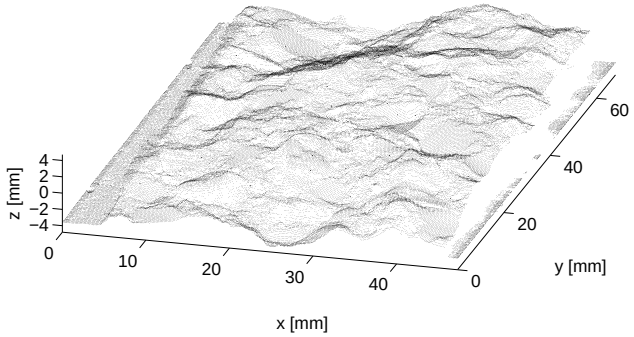


**Figure 4.4**: *Scan of the crack surface of specimen* $90_3$ *using the Nextec HAWK scanner.*

been measured. $90_1, 90_2$ and $90_3/90_3^d$ have only been exposed in a pure Mode I opening whilst the last one initially has been opened to $\Delta u_n = 0.040$ mm followed by a $\alpha = 45°$ mixed mode opening. The resolution or spacing dictates the distance between the scan points and is identical in both latitudinal and longitudinal directions. Specimen $90_3$ has been measured twice using two different spacing values 0.08 mm and 0.16 mm, the rest with a 0.16 mm spacing. Omitting the plane, notched parts of the scans the maximum vertical distance between all the scan points for each specimen is around $\Delta z = 10.5$ mm. This is in the same order of magnitude as the 8 mm maximum aggregate size supporting that the cracks as a result of the mixed mode openings are influenced by material aspects more than by structural aspects.

The surface description through the scan points may be used directly in a 3D micro modeling of the topographic measure. However, in a 2D macro crack model, the extensive topographic information needs to be simplified and organized. The information could for instance be used to describe a characteristic inner friction angle of the material or as basis for a simplified surface description. The latter is explained in the following.

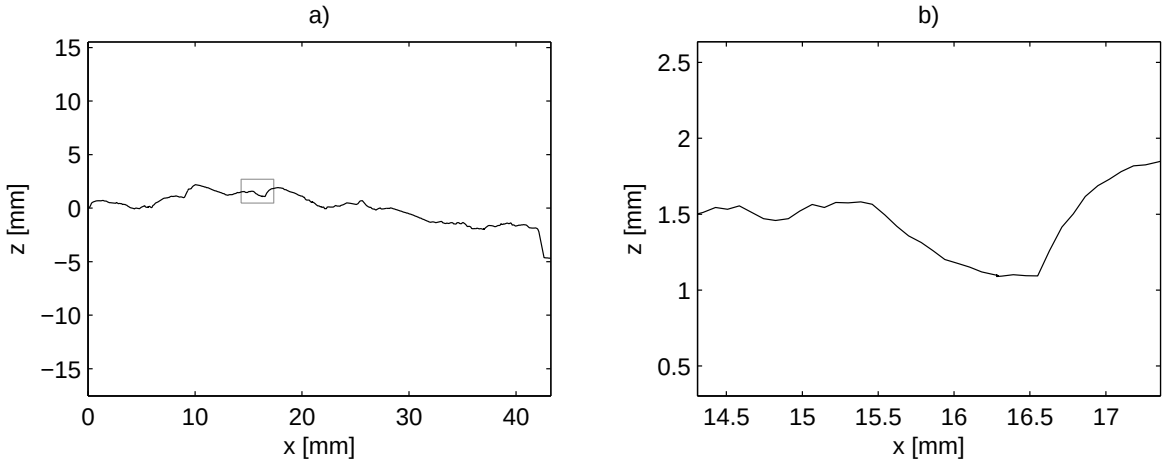


**Figure 4.5***: **(a)** A single contour line taken directly from the scan in Figure 4.4. **(b)** An enlargement of the contour line corresponding to the square in (a).*

## 4.2 Average Contour Lines

Provided with a constitutive model, which describes the relation between the displacements and tractions for a crack, the idea with the average contour lines is to relate a global displacement between the two specimen parts and the matching local displacements in the crack. A global displacement increment may be transformed into local displacements. At local level the local displacements and the constitutive model are used to determine the matching local tractions. To obtain the global response the local tractions are then summed over the surface using an appropriate discretization of the crack topography. This discretization of the crack topography can be obtained through the average contour lines.

For each xz-plane in the y-direction the scan-points located in the plane form a contour line. An arbitrary contour line from the scan in Figure 4.4 is displayed in Figure 4.5 together with an enlargement of a part of the line. Based on the contour line it is evident that in the crack a global displacement will result both in opening, sliding and maybe even crushing. For instance, for an inclined path of the crack surface a pure global opening locally results in a combined opening and sliding. Generally for a given global mixed mode displacement the local ratio between opening and sliding is dependent on the actual topography of the surface.

Based on the inclination of the line in a given point on the contour line it is possible to predict the most likely path of the succeeding contour line. In a point with the inclination of the contour line $\theta$, the succeeding line will probably continue in an average manner and then after some distance decline towards the horizontal plane. With the points $a$ and $b$ this is exemplified in Figure 4.6.

For every scan point a unique contour line can be establish. The contour line, $k_\theta$, proceeds from the actual scan point and includes a number of the succeeding points. These contour lines represents $x$- and $z$-coordinates for a line path running along the

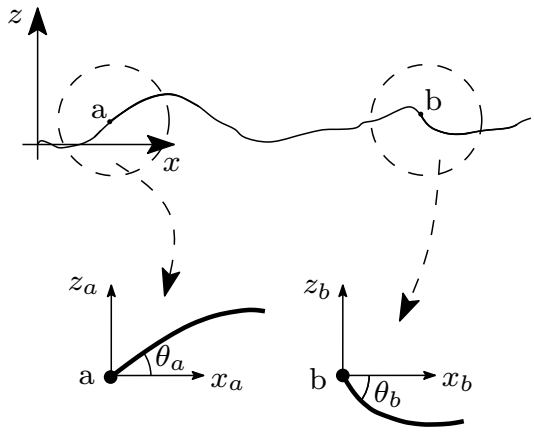


**Figure 4.6**: *Sketch of two points a and b on a contour line. Based on the inclination in the points $\theta_a$ and $\theta_b$, respectively, the most likely paths of the succeeding contour line may be found.*

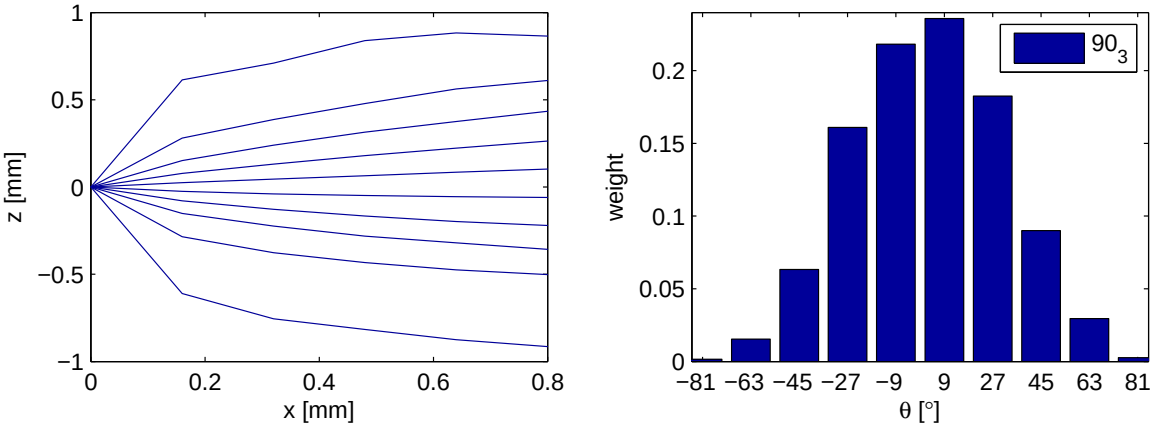


**Figure 4.7**: *Average contour lines representing the crack surface for specimen $90_3$ ordered from lowest to highest start inclination together with their weight of representation.*

crack surface. Like in Figure 4.6 each contour line can be characterized by its start inclination $\theta$, which is approximated by the inclination between the first and the second data point in the contour line in respect to the horizontal plane. A series of average contour lines are established by dividing the total angle interval covered by the start inclinations into a number of intervals, $\Delta\theta_i$. For a given $\Delta\theta_i$ the average contour line, $k_{\Delta\theta_i}$, then describes where the successive points in the contour line most likely will be situated with respect to the starting point.

To represent a crack surface, a contour line is established for each point in the scan, though neglecting points at the edges. By their start inclination $\Delta\theta_i$ the contour lines are assembled into average contour lines $k_{\Delta\theta_i}$. The weight of the interval is given as the number of contour lines in the interval with respect to the total amount of contour lines times $(\cos(\Delta\theta_i))^{-1}$ which represents the true length of the given interval. Figure 4.7 shows 10 average contour lines ordered from lowest to highest start inclination

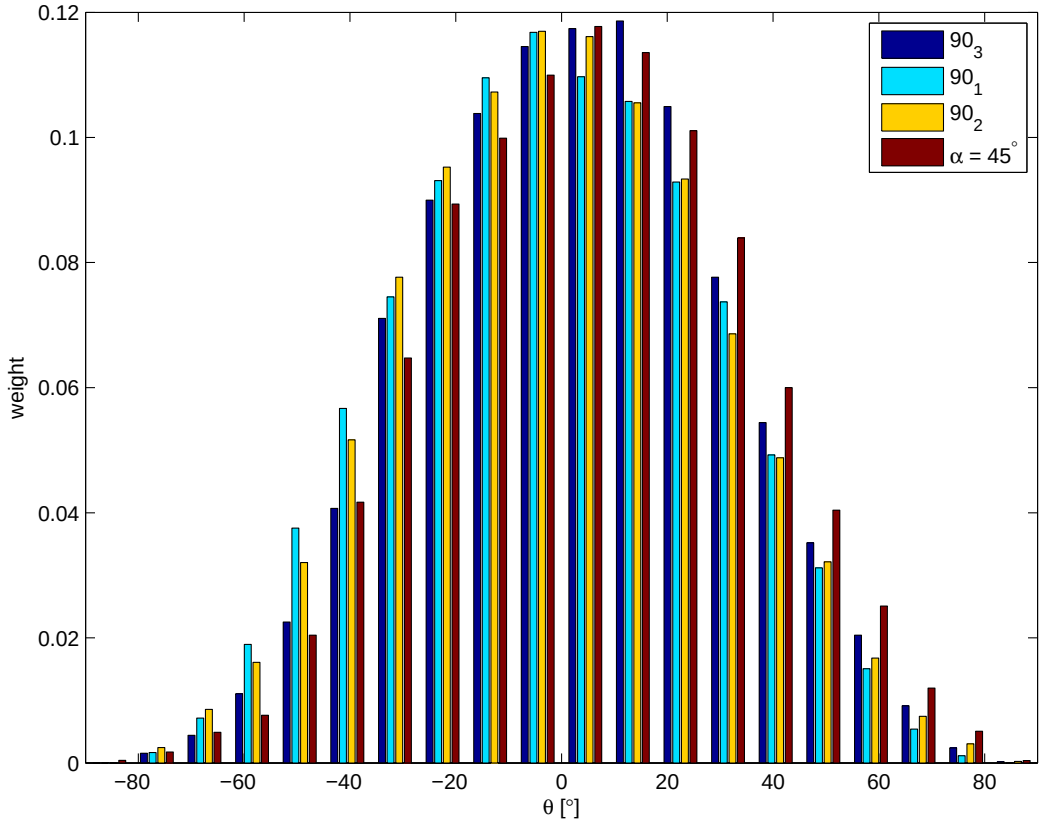


**Figure 4.8**: *Weights for the average contour lines for the surfaces for specimens* $90_3$, $90_1$, $90_2$ *and the one initially opened to* $\Delta u_n = 0.040$ *mm followed by a* $\alpha = 45°$ *mixed mode opening. The angle interval has been divided into* 20 *smaller intervals.*

and their weight all together representing the crack surface in Figure 4.4 for specimen $90_3$. The average contour lines are based on more than 63.000 contour lines. Almost half of these describe the two intervals around $\theta = 0°$ , while the two steepest intervals all together are based only on around 250 contour lines. The low representation explains the edged outer average contour lines whereas the inner average contour lines are smoother. Theoretic the scan of the $40 \times 75$ mm$^2$ crack surface could result in $\approx$ 120.000 scan points. The omission of the points at the edges together with the failure of some of the scan points due to reflection from the aggregates reduces the actual number of points till around 63.000 still covering a substantial part of the surface.

In Figure 4.8 the weights of representation for the average contour lines for the four specimens measured with a 0.16 mm spacing are compared. The angle interval from vertical downwards (-90°) to vertical upwards (90°) is divided into 20 smaller intervals. The weights are normal distributed around the horizontal plane with the majority of the weights $\approx$ 80-90% in the flat part between $\pm$ 40° and only insignificant weights for the most inclined parts. The figure shows the weights for three specimens opened in Mode I and for one specimen displaced in mixed mode. The mixed mode specimen ($\alpha$= 45°) tends to have more positive weight than negative, though, for instance specimen $90_1$ has a similar tendency just the other way around with more negative than positive

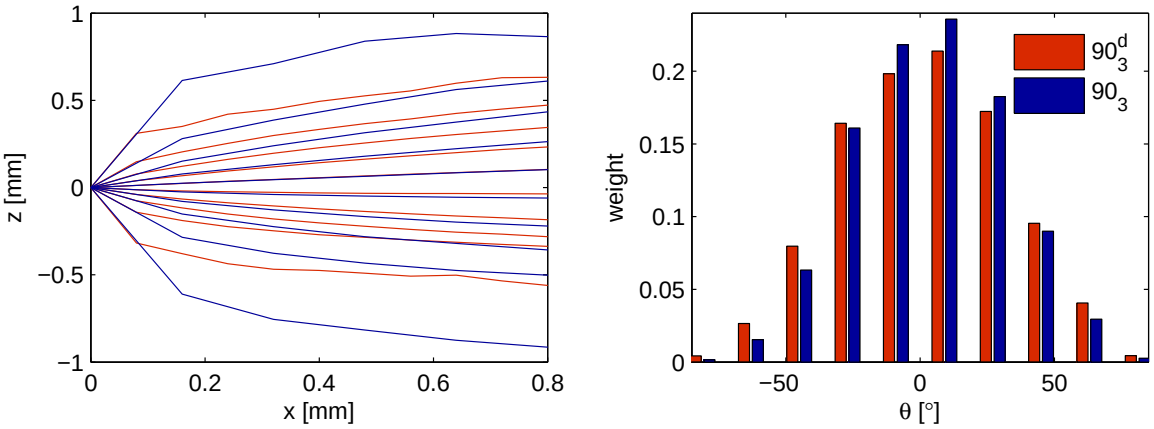


**Figure 4.9**: *The average contour lines representing the crack surface for specimen* $90_3$ *and* $90_3^d$ *with the dense spacing and their corresponding weights of representation.*

intervals. Thus, for the given spacing distance the mixed mode displacement of the crack has not introduced measurable damage to the crack surface.

Figure 4.9 compares the average contour lines and matching weights for a scan of the same specimen with two different spacing values 0.16 mm and 0.08 mm named $90_3$ and $90_3^d$, respectively. The normal distribution of the weights for the dense spacing tends to be smaller around 0° and higher for the steeper inclinations. This means that the fine scan detects more inclined parts, which the coarse scan steps past. When the scan detects more inclined parts over a smaller distance the succeeding contour line should be flatter compared to the equivalent contour line for the coarse scan. However, since the start inclination for the fine scan is followed over a smaller spacing the spread of the contour lines is naturally narrower. Looking closer at the contour lines after the first kink the succeeding paths are flatter for the fine scan when compared to the coarse scan. From the plot of the weights there is the trend that the positive start inclinations are more pronounced, a trend which can also be found from the contour lines where the lines tend to have higher positive $z$-deflection than negative. Thus, the fine scan tends to reduce the imbalance.

### 4.2.1 Local Displacements

For a given direction of motion the topographic effects may be included as follows. A given global displacement increment is transformed into a local displacement for each of the average contour lines. The local coordinate system is defined from the start inclination line, see Figure 4.10. For each of the average contour lines the local traction response may then be computed and the weighted result is transformed back to global scale and added together with the global results from the other average contour lines.

The introduction of the contour lines results in a new measure of the crack opening $\tilde{u}_{ng}$. $\tilde{u}_{ng}$ is given as the opening between the global displacement and the contour line, see Figure 4.10. The relations between global and local displacements are summarized

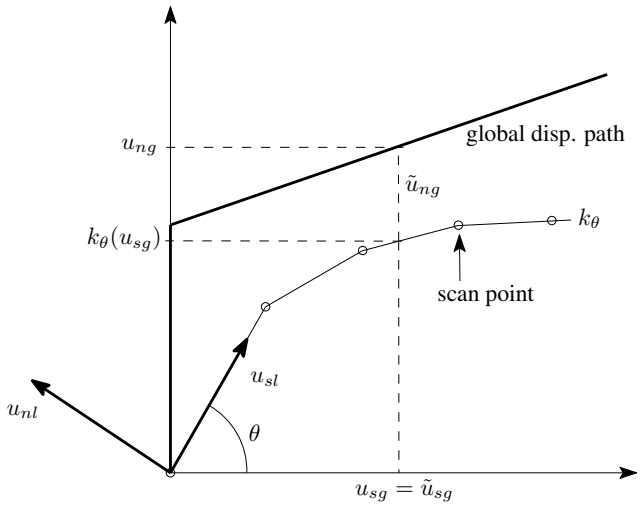


**Figure 4.10***: Global and local coordinate system. Indications of the global displacement path, $k_\theta$ and scan points.*

as

$$\tilde{u}_{ng} = u_{ng} - k_\theta(u_{sg})$$

$$\tilde{u}_{sg} = u_{sg} \tag{4.1}$$

$$[\![\mathbf{u}]\!]_l = \mathbf{T}[\![\tilde{\mathbf{u}}]\!]_g$$

where $\mathbf{T}$ gives the transformation between global and local scale.

## 4.3 Concluding Remarks

The topographic measure provides information about the crack surface, which is used to understand the cracking mechanisms. The topographic measures of some of the crack surfaces belonging to the experiments in Chapter 3 show that the surfaces are influenced by material properties more than structural aspects. Furthermore, the topography is used as basis for the average contour lines, which give a simplified description of the crack surface. The random contour line in Figure 4.5 illustrates that for a given mixed mode opening, the surface locally experiences both opening, friction and crushing. However, referring to Figure 4.8 the very steep paths of the contour lines have a very low weight of representation in the overall result. For the given scan spacing, the average contour lines and their weight characterize the topography of the concrete crack surface for small crack openings. In Chapter 5 the topography is combined with a plasticity model to describe the constitutive crack behavior in concrete. The surface description by the average contour lines gives a direct inclusion of the roughness of the crack surface in the constitutive model.

# Chapter 5

# Constitutive Modeling

Through the last decades it has been discussed whether it is reasonable to talk about Mode II initiated cracks in concrete. Based on a series of experiments with notched beams loaded in shear Bažant and Pfeiffer (1986) states that "shear fracture, i.e. Mode II fracture, of concrete exists". A few years later in Carpinteri et al. (1993) single notched beams are tested under mixed loadings. Their results can be reproduced numerically entirely based on a Mode I formulation, which leads to the indicative question and title of the paper "Is Mode II Fracture Energy a Real Material Property?". In Reinhardt et al. (1997) and Reinhardt and Xu (2000) a method for Mode II fracture in concrete is suggested. However, the reported crack patterns indicate that the cracks initiate in Mode I. Similar observations under mixed loadings are obtained by Hassanzadeh (1992), Nooru-Muhamed (1992) and Østergaard et al. (2007) where the crack initiation takes place perpendicular to the largest principal stress, i.e. a Mode I initiation. The alternative Mode IIa fracture introduced in the crack model by Carol et al. (1997) is related to sliding under high compression. The quantity seems difficult to measure, and with the needed compression the fracture energy measure is a mix of Mode I and II properties. As it appears from the foregoing the Mode II fracture energy is difficult to conceive. The quantity is questionable and if it is introduced as a material parameter the definition needs to be clarified and related to suitable experiments.

Simple mixed mode models like Högberg (2006) and Lens et al. (2009) are based on a relation between Mode I and Mode II fracture. Despite the uncertainty about the Mode II fracture it is doubtful if the mixed mode behavior in concrete can be treated this simple. The concrete mixed mode behavior seems to be path dependent, a behavior which by simple means is difficult to describe by two independent parameters. In this chapter an incremental mixed mode crack model is presented. The model consists of an associated elasto-plastic model and a description of the crack topography, the latter presented in the previous chapter, Chapter 4. The elasto-plastic model is inspired by the modified Cam clay model which originates from the work by Roscoe and Burland (1968), Wood (1990). The modified Cam clay model is simple and normally used to model the strength and deformation properties of soil. The model includes hardening/softening and compaction/dilatational behavior and is described by few material parameters (de Borst and Groen, 2000). The model describes the relation between mean and deviatoric stresses and volumetric and deviatoric strains. It has an elliptic

yield surface controlled by a critical state line running from origo to the top of the ellipse. A stress state on the critical state line is characterized as having no change in either stress or volume. The advantage of the modified Cam clay model lies in its apparent simplicity.

For the present elasto-plastic model the normality of the flow and the elliptic yield surface is kept, see Figure 5.2. The model describes the relation between normal and shear tractions at the crack faces and the related normal and sliding displacements between the crack faces. The cohesional behavior is added to the model formulation and the hardening functions are completely new. For an opening of the crack the material softens, for a closure the material hardens, and for a large closure the material crushes described as a softening. In the tensile region the elliptic yield surface is shaped and behaves similar compared to the yield surfaces in the models by Carol et al. (1997) and Nielsen et al. (2010). Further, the elliptic surface provides a simple compressive-shear relation. When the plasticity model is used together with the topographic description the model (called the topographic model) is able to represent both the crack initiation, the evolution in Mode I and the mixed mode behavior of an already established crack.

The topographic model is established without any additional model parameters or calibrations; however, the inclusion of the topography increases the computational demands. Therefore, in addition to the topographic model a simplified model, where the topographic description is omitted, is presented. The simple model is fitted against the experiments and it is thereby able to capture the mixed mode characteristics. However, the simplification entails some limitations. The mechanical foundation of the model is hidden in the fitting and the model will only be able to capture the mixed mode behavior under constant opening conditions.

Together with **Paper II** this chapter presents the constitutive mixed mode modeling of cracks in concrete. In the following the plasticity frame work of the constitutive model is presented along with its implementation with the topography. Through a series of computations over model variations the capability of the topographic model is illustrated and the model response is compared with the experimental mixed mode results from Chapter 3. The chapter ends with a presentation of the simplified model formulation and the differences between the models are discussed.

## 5.1 Elasto-Plastic Crack Model

The crack behavior in the constitutive crack model is in agreement with the basic principles presented in Section 1.1. Hence, the crack initiation is assumed to take place in Mode I, perpendicular to the largest principal stress $\sigma_I$. Complying with the FCM, the crack is initiated when $\sigma_I$ exceeds the concrete tensile strength $f_t$. This gives the failure criterion

$$\sigma_I = f_t \tag{5.1}$$

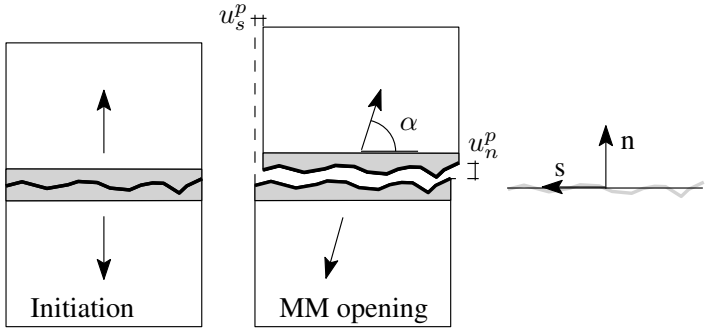


**Figure 5.1***: The crack initiates perpendicular to the largest principal stress. After the initiation, it can open in various mixed mode angles $\alpha$. The crack process zone is grey shaded. Definition of the crack coordinate system* $(\mathbf{n}, \mathbf{s})$.

After the crack initiation the crack can continue the Mode I opening but the opening may also be combined with sliding between the crack faces in a mixed mode opening. Figure 5.1 shows the concept that the crack initiates in Mode I but after the initiation the now establish crack can open with various ratios between pure opening and pure sliding. Because of the rough and jagged crack surface, the cracking takes place in a process zone around the apparent crack. In an idealized model the process zone and the jagged crack are substituted by a plane discontinuity line. The elastic properties of the process zone may then be a part of the surrounding continuum or be ascribed to the plane crack. With the intension to compare the model directly with the mixed mode experiments in Chapter 3, it is convenient to ascribe the elastic properties to the plane crack.

In the experiments the deformations over the crack are measured as the relative displacement $\Delta\mathbf{u}$ between the reference points for the clip gauges rail. In the discrete crack model the deformations are considered as a displacement jump $[\![\mathbf{u}]\!]$ over the discontinuity line. For the crack the tractions and displacements are described by a normal component and a shear component. The engineering notation is used and the tractions are given by $\mathbf{t} = [t_n, t_s]^T$ while the displacements are given by $[\![\mathbf{u}]\!] = [u_n, u_s]^T$. The $(\mathbf{n}, \mathbf{s})$-crack coordinate system is defined in Figure 5.1. The ratio between the incremental opening and sliding defines the mixed mode angle $\alpha = \tan(\frac{\dot{u}_n}{\dot{u}_s})$.

For a given displacement increment $[\![\dot{\mathbf{u}}]\!]$ it is desired to find the matching traction increment $\dot{\mathbf{t}}$ for the crack. In the plastic domain the relation is described by the elasto-plastic flexibility matrix $\mathbf{C}^{\mathbf{ep}}$

$$[\![\dot{\mathbf{u}}]\!] = \mathbf{C}^{\mathbf{ep}}\dot{\mathbf{t}} \tag{5.2}$$

In the actual material state described by the hardening parameters $\boldsymbol{\kappa}$ the elasto-plastic flexibility $\mathbf{C}^{\mathbf{ep}}$ describes the constitutive relations. The traditional plasticity theory (Chen and Han, 1988) establishes the framework for $\mathbf{C}^{\mathbf{ep}}$.

The strain split assumption used on the displacement jump $[\![\mathbf{u}]\!]$ gives that the total displacements $[\![\mathbf{u}]\!]$ can be divided into an elastic $[\![\mathbf{u}]\!]^e$ and a plastic $[\![\mathbf{u}]\!]^p$ contribution.

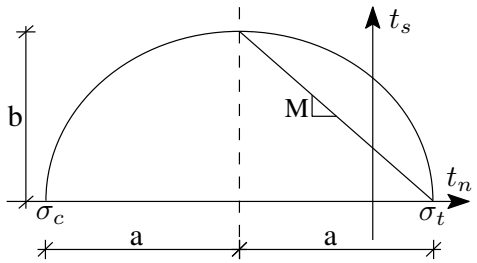


**Figure 5.2**: *Upper part of the elliptic yield surface and M-line. Semi-axes a and b shown.*

In incremental form the strain split assumption is given by

$$[\![\dot{\mathbf{u}}]\!] = [\![\dot{\mathbf{u}}]\!]^e + [\![\dot{\mathbf{u}}]\!]^p \tag{5.3}$$

Hookes law gives the relation between the elastic displacements and the tractions

$$\dot{\mathbf{t}} = \mathbf{D^e}[\![\dot{\mathbf{u}}]\!]^e \;\Leftrightarrow\; [\![\dot{\mathbf{u}}]\!]^e = \mathbf{C^e}\dot{\mathbf{t}} \tag{5.4}$$

where $\mathbf{D^e} = \mathbf{C^{e^{-1}}}$ is the elastic stiffness and $\mathbf{C^e}$ is the elastic flexibility of the crack.

### 5.1.1 Yield Surface and Basic Plasticity Framework

Expressed in tractions the elastic domain is limited by the yield surface $f(\mathbf{t}, \boldsymbol{\kappa})$. For $f < 0$ the state is elastic and for $f = 0$ the state becomes plastic. The elliptic yield surface is shaped by a critical state line with the inclination $t_s/t_n = M$ and is controlled by the intersections with the abscissa $\sigma_c$ and $\sigma_t$, see Figure 5.2. The inclination of the critical state line can be interpreted as an equivalent to the friction coefficient in a Coulomb-like sense. The model is associated, so the plastic flow is proportional to the yield surface normal. The yield surface is given by the ellipse

$$\frac{(t_n - t_{n0})^2}{a^2} + \frac{(t_s - t_{s0})^2}{b^2} = 1 \tag{5.5}$$

where $(t_{n0}, t_{s0}) = (\frac{\sigma_t+\sigma_c}{2}, 0)$ is the center of the ellipse, and $a = \frac{\sigma_t-\sigma_c}{2}$ and $b = aM$ are the semi-axes. Introducing the center of the ellipse and the major and minor axes in Eq. (5.5), the yield surface can be expressed as:

$$f(\mathbf{t}, \boldsymbol{\kappa}) = t_s^2 + M^2 t_n (t_n - \sigma_t - \sigma_c) + M^2 \sigma_t \sigma_c \tag{5.6}$$

For an associated plasticity model, the outward normal to the yield surface in the actual traction point $\mathbf{t}$ dictates the direction of the plastic displacement increment. For a traction point on the yield surface the plastic displacements are given by the flow rule

$$[\![\dot{\mathbf{u}}]\!]^p = \dot{\lambda}^p \frac{\partial f(\mathbf{t}, \boldsymbol{\kappa})}{\partial \mathbf{t}} \tag{5.7}$$

Here $\dot{\lambda}^p \geq 0$ is the plastic multiplier which must be non-negative. The plastic potential normal denoted $\mathbf{a}$ is equivalent with the elliptic yield surface normal

$$\mathbf{a} = \frac{\partial f}{\partial \mathbf{t}} = \begin{bmatrix} M^2 \left(2t_n - \sigma_t - \sigma_c\right) \\ 2t_s \end{bmatrix} \tag{5.8}$$

The evolution of the yield surface is described through the hardening functions $\mathbf{h}(\mathbf{t}, \boldsymbol{\kappa})$ and their relation to the hardening parameters $\boldsymbol{\kappa}$ are defined as

$$\dot{\boldsymbol{\kappa}} = \dot{\lambda}^p \mathbf{h}(\mathbf{t}, \boldsymbol{\kappa}) \tag{5.9}$$

In the model the hardening parameters are the intersections with the abscissa $\sigma_c$ and $\sigma_t$, i.e. $\boldsymbol{\kappa} = [\sigma_t, \sigma_c]^T$. For a given plastic deformation state $\sigma_t$ and $\sigma_c$ are the actual uniaxial tensile and compressive strengths of the material, respectively. The initial surface is given by $M$ and the hardening state $\boldsymbol{\kappa} = [f_t, f_c]^T$, where $f_t$ is the uniaxial tensile strength and $f_c$ is the uniaxial compressive strength of the concrete.

Summarized, a given state is described by the tractions $\mathbf{t} = [t_n, t_s]^T$, the displacements $[\![\mathbf{u}]\!] = [u_n, u_s]^T$ and the hardening state $\boldsymbol{\kappa} = [\sigma_t, \sigma_c]^T$.

### Elasto-Plastic Flexibility Matrix

As introduced in Eq. 5.2 the relation between the displacements and the tractions is given by the elasto-plastic flexibility $\mathbf{C^{ep}}$. In an elastic state $\mathbf{C^{ep}}$ is reduced to the elastic flexibility $\mathbf{C^e} = (\mathbf{D^e})^{-1}$. The elastic stiffness $\mathbf{D^e}$ is given as

$$\dot{\mathbf{t}} = \mathbf{D^e}[\![\dot{\mathbf{u}}]\!] \Rightarrow$$

$$\mathbf{D^e} = \begin{bmatrix} D_n & 0 \\ 0 & D_s \end{bmatrix} \tag{5.10}$$

$D_n$ is the elastic normal stiffness and $D_s$ is the elastic shear stiffness of the process zone.

$\mathbf{C^{ep}}$ is derived from a point on the yield surface, $f(\mathbf{t}, \boldsymbol{\kappa}) = 0$. The point is described by the traction state $\mathbf{t}$ in the hardening state $\boldsymbol{\kappa}$. A loading of the yield surface with an infinitesimal traction increment $\dot{\mathbf{t}}$ leads to a new state $f(\mathbf{t} + \dot{\mathbf{t}}, \boldsymbol{\kappa} + \dot{\boldsymbol{\kappa}}) = 0$. The second state can be approximated by a Taylor expansion to first order of the first state. Assuming that both states are on the yield surface this leads to the approximation

$$\left(\frac{\partial f}{\partial \mathbf{t}}\right)^T \dot{\mathbf{t}} + \left(\frac{\partial f}{\partial \boldsymbol{\kappa}}\right)^T \dot{\boldsymbol{\kappa}} = 0 \tag{5.11}$$

Utilizing the expression for the hardening, Eq. (5.9), the plastic multiplier can be derived from Eq. (5.11)

$$\dot{\lambda}^p = \frac{-\left(\frac{\partial f}{\partial \mathbf{t}}\right)^T \dot{\mathbf{t}}}{\left(\frac{\partial f}{\partial \boldsymbol{\kappa}}\right)^T \mathbf{h}(\mathbf{t}, \boldsymbol{\kappa})} \tag{5.12}$$

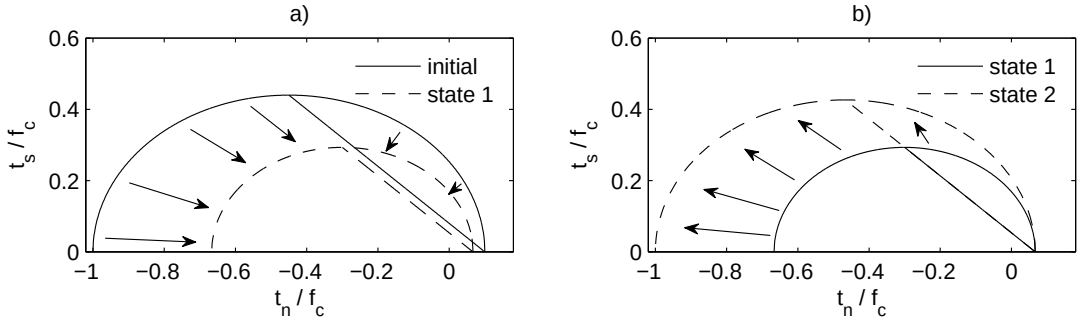


**Figure 5.3***: The two different modes for the yield surface evolution.* ***(a)*** *As a result of either opening or crushing both $\sigma_c$ and $\sigma_t$ soften from the initial state to state 1.* ***(b)*** *As a result of a closure from state 1 only $\sigma_c$ hardens and returns to $\sigma_c = f_c$ in state 2.*

Defining the hardening modulus by,

$$H = -\left(\frac{\partial f}{\partial \boldsymbol{\kappa}}\right)^T \mathbf{h}(\mathbf{t}, \boldsymbol{\kappa}) \tag{5.13}$$

the elasto plastic flexibility matrix, $\mathbf{C^{ep}}$, can be identified from Eq. (5.12) and the split rule Eq. (5.3)

$$\mathbf{C^{ep}} = \mathbf{C^e} + \frac{\dfrac{\partial f}{\partial \mathbf{t}}\left(\dfrac{\partial f}{\partial \mathbf{t}}\right)^T}{H} = \mathbf{C^e} + \frac{\mathbf{a}\mathbf{a}^T}{H} \tag{5.14}$$

where the plastic potential normal $\mathbf{a}$, Eq. (5.8), is introduced. An expression for the plastic multiplier can be obtained from Eq. (5.3) with Eq. (5.7) inserted and multiplied by the yield surface normal $\mathbf{a}^T$

$$\dot{\lambda}^p = \frac{\mathbf{a}^T[\![\dot{\mathbf{u}}]\!] - \mathbf{a}^T\mathbf{C^e}\dot{\mathbf{t}}}{\mathbf{a^T a}} \tag{5.15}$$

### 5.1.2 Hardening Functions

The hardening functions describe the change in the hardening parameters $\boldsymbol{\kappa} = [\sigma_t, \sigma_c]^T$ and thereby the yield surface evolution. As illustrated in Figure 5.3 the yield surface can either soften or harden. In the softening both $\sigma_c$ and $\sigma_t$ soften whereas in the hardening $\sigma_t$ is kept constant and only $\sigma_c$ hardens. Initially the yield surface is limited by the uniaxial strengths $\boldsymbol{\kappa} = [f_t, f_c]^T$ in tension and compression, respectively. The hardening/softening is assumed to be divided into three different cases distinguished by whether there is a crack opening or a closure, and in the case of a closure whether the compressive hardening parameter, $\sigma_c$, has exceeded the compressive strength, $f_c$. The direction of the plastic normal opening $u_n^p$ is used to distinguish whether there is opening or closure. The direction of $u_n^p$ is equivalent to the normal projection (projection on $\mathbf{n}$) of the yield surface normal, $\mathbf{a}_1$. The yield surface evolution is divided into the following three cases:

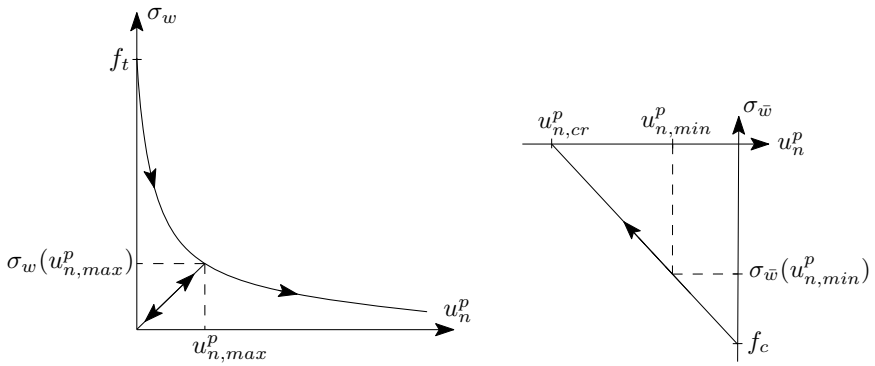


(a) $\sigma_w$-curve. (b) $\sigma_{\bar{w}}$-curve.

**Figure 5.4**: *Basis for the yield surface evolution.* ***(a)*** *$\sigma_w$-curve. $f_t$ is the tensile strength. Indications of the central unloading path with the inclination $D_{\sigma_w} = \sigma_w(u^p_{n,max})/u^p_{n,max}$.* ***(b)*** *$\sigma_{\bar{w}}$-curve. $f_c$ is the compressive strength, $u^p_{n,cr}$ is the plastic normal deformation at crushing failure.*

- **$a_1 > 0$:** The cohesion vanishes according to a typical $\sigma_w$-curve. The $\sigma_w$-curve describes the relation between the normal stress over the crack $\sigma_w$ and the inelastic, normal opening of the crack $u^p_n$ for a Mode I opening of the crack, see Figure 5.4(a). In the model $\sigma_w$ is dependent on the maximal plastic opening $u^p_{n,max}$ and the softening is incorporated as a softening of the hardening parameter in tension $\sigma_t$ and a proportional softening of the hardening parameter in compression $\sigma_c$ with the proportionality factor $\sigma_c/\sigma_t$, see Figure 5.3. In the case of a Mode I opening the proportionality factor ensures that the compressive strength vanishes at the same time as the tensile strength, i.e. that for a large opening the material is exhausted.

- **$a_1 < 0$ and $\sigma_c$ has not exceeded $f_c$:** For instance if the loading state changes from an opening to a closure of the crack, the hardening parameter in compression $\sigma_c$ can harden until it reaches $f_c$. As illustrated in Figure 5.3, in the hardening case only $\sigma_c$ hardens, while the cohesion represented by the hardening parameter in tension $\sigma_t$ is irreversible.

- **$a_1 < 0$ and $\sigma_c$ reaches $f_c$:** The compression resistance diminishes according to a $\sigma_{\bar{w}}$-curve. The $\sigma_{\bar{w}}$-curve describes the Mode I closure where the crushing of concrete may be seen as a localized phenomenon, Jansen and Shah (1997). $\sigma_{\bar{w}}$ is the compressive normal stress corresponding to the postpeak inelastic crushing. Based on the test results by Jansen and Shah (1997) the softening caused by crushing can be linearly represented as shown in Figure 5.4(b). The postpeak inelastic crushing is in the model represented by the lowest attained value of the plastic compression after crushing, $u^p_{n,min}$. The softening due to a compression is in the model expressed as a softening of the hardening parameter in compression $\sigma_c$ and a proportional softening of the hardening parameter in tension $\sigma_t$ with the proportionality factor $\sigma_t/\sigma_c$.

The uniaxial tensile and compressive behaviors are incorporated in the hardening functions as follows. The hardening modulus is defined in Eq. (5.13) and the yield surface dependence on the hardening is given by

$$\frac{\partial f}{\partial \boldsymbol{\kappa}} = \begin{bmatrix} M^2 (\sigma_c - t_n) \\ M^2 (\sigma_t - t_n) \end{bmatrix} \tag{5.16}$$

The model has two hardening functions $\mathbf{h} = [h_t, h_c]^T$ related to $\sigma_t$ and $\sigma_c$, respectively. Together with Eq. (5.16), the hardening modulus is then given by

$$H(\mathbf{t}, \boldsymbol{\kappa}) = -h_t M^2 (\sigma_c - t_n) - h_c M^2 (\sigma_t - t_n) \tag{5.17}$$

In a pure opening the plasticity model follows the normal opening relation $\sigma_w$ with the tangent stiffness $\dot{\sigma}_w$. This means that the plastic normal component of the elasto-plastic normal flexibility matrix $\mathbf{C^{ep}}$ in Eq. (5.14) has to be equal to the flexibility $\frac{1}{\dot{\sigma}_w}$ given by the normal opening relation, leading to the relation

$$H(\mathbf{t}, \boldsymbol{\kappa}) = \dot{\sigma}_w \left(\mathbf{a}\mathbf{a}^T\right)_{(1,1)} \tag{5.18}$$

In pure tension the traction state is $(t_n, t_s) = (\sigma_t, 0)$ and the yield surface normal is $\mathbf{a} = [M^2(\sigma_t - \sigma_c), 0]^T$. For the given traction state, the hardening modulus in Eq. (5.17) can be rewritten to

$$H(\mathbf{t}, \boldsymbol{\kappa}) = -h_t M^2 (\sigma_c - \sigma_t) \tag{5.19}$$

Using Eq. (5.18) together with Eq. (5.19) the hardening function for the tensile capacity can be found as

$$h_t(\mathbf{t}, \boldsymbol{\kappa}) = M^2 (\sigma_t - \sigma_c) \dot{\sigma}_w \tag{5.20}$$

Similarly for a pure Mode I closure, if the normal traction $t_n$ reaches the compressive strength, $f_c$, the plasticity model follows the $\sigma_{\bar{w}}$-curve with the tangent stiffness $\dot{\sigma}_{\bar{w}}$. This means that the plastic normal component of the elasto-plastic flexibility matrix $\mathbf{C^{ep}}$ in Eq. (5.14) has to be equal to the flexibility $\frac{1}{\dot{\sigma}_{\bar{w}}}$ given by the $\sigma_{\bar{w}}$-curve. Using the same arguments as for the opening, the closure leads to the hardening function

$$h_c(\mathbf{t}, \boldsymbol{\kappa}) = M^2 (\sigma_c - \sigma_t) \dot{\sigma}_{\bar{w}} \tag{5.21}$$

After initiation the crack may open or close. If closure starts, the state will normally change from plastic to elastic. Experiments with cracked concrete have shown that unloading is associated with a reduced stiffness, see e.g. Gopalaratnam and Shah (1985) and Madsen (2009). In the model this is included by applying central unloading, see Figure 5.4(a). In the case of central unloading the normal stiffness consists of a contribution from the elastic normal stiffness $D_n$ and a contribution from the unloading stiffness from the $\sigma_w$-curve $D_{\sigma_w} = \frac{\sigma_w(u^p_{n,max})}{u^p_{n,max}}$. As long as $u^p_n > 0$ the elastic normal stiffness can be found from the equation

$$\frac{1}{D^*_n} = \frac{1}{D_n} + \frac{1}{D_{\sigma_w}} \tag{5.22}$$

During the elastic unloading the elastic stiffness matrix $\mathbf{D^e}$ is reduced by the same ratio: $\mathbf{D^{e*}} = \mathbf{D^e} \frac{D^*_n}{D_n}$. When $u_n < 0$ the stiffness returns to the original elastic stiffness, $\mathbf{D^e}$.

**Table 5.1**: *Material parameters.*

| Parameter | value |
|---|---|
| $f_t$ | 3.3 MPa |
| $f_c$ | -41 MPa |
| $E$ | 31 GPa |
| $\nu$ | 0.22 |
| $D_n$ | 570 GPa/m |
| $D_s$ | 380 GPa/m |
| $M$ | 0.8 |
| $u^p_{n,cr}$ | 1.2 mm |

An opening followed by a closure may soften the yield surface to a new hardening state $\boldsymbol{\kappa} = [\sigma_t, \sigma_c]^T$ and bring the traction state into the elastic region. For a continued compression the elastic state can change into a plastic state. If that is the case $\sigma_c$ can harden until it reaches the compressive strength $f_c$ and crushing starts according to Eq. (5.21). During the compressive hardening there is no change in the tensile strength, $\dot{\sigma}_t = 0$. The $\sigma_c$-hardening is in fact assumed to be pseudo-elastic, which means that for a hardening, the state has to be plastic, but the change in tractions corresponds to an elastic increment $\dot{\mathbf{t}} = \mathbf{D^e}[\![\dot{\mathbf{u}}]\!]$ and the hardening does not introduce any plastic displacements, $\dot{\lambda}^p = 0$. The hardening increment $\dot{\boldsymbol{\kappa}}$ is determined from the new state $f(\mathbf{t} + \dot{\mathbf{t}}, \boldsymbol{\kappa} + \dot{\boldsymbol{\kappa}}) = 0$. Since $\dot{\sigma}_t = 0$, the change in the compressive hardening parameter $\dot{\sigma}_c$ is the only unknown in the equation $f(\mathbf{t} + \dot{\mathbf{t}}, \boldsymbol{\kappa} + \dot{\boldsymbol{\kappa}}) = 0$, and it can be found as

$$\dot{\sigma}_c = \frac{(t_s + \dot{t}_s)^2 + M^2(t_n + \dot{t}_n)^2 - M^2(t_n + \dot{t}_n)\sigma_t}{M^2(t_n + \dot{t}_n) - M^2\sigma_t} - \sigma_c \tag{5.23}$$

### 5.1.3 Material Parameters

The constitutive model is compared to and validated against the experiments presented in Chapter 3. The used material parameters for the concrete are listed in Table 5.1. The tensile strength $f_t$, the compressive strength $f_c$ and the youngs modulus $E$ are together with a multi linear $\sigma_w$-curve based on the experimental results. $\nu$ is assumed characteristic for concrete while $M$ corresponds to a friction angle of 39° in a Coulomb friction model. In Figure 5.5 the yield surface from the present elasto-plastic model is compared to a modified Coulomb model, Nielsen (1999), with a 37° friction angle and same $f_t$ and $f_c$. The two yield surfaces almost coincide, and the effect of the different descriptions of the yield surface have not been further investigated. The elliptic description is used in the modeling. The $M$-variation for the model is investigated in Section 5.2.2. The maximum compressive plastic displacement after crushing $u^p_{n,cr}$ is for a linear softening curve estimated from Jansen and Shah (1997). Finally, the elastic normal and shear stiffnesses, $D_n$ and $D_s$ respectively, are determined through the inverse analysis for the test specimen presented in Section 3.3.1.

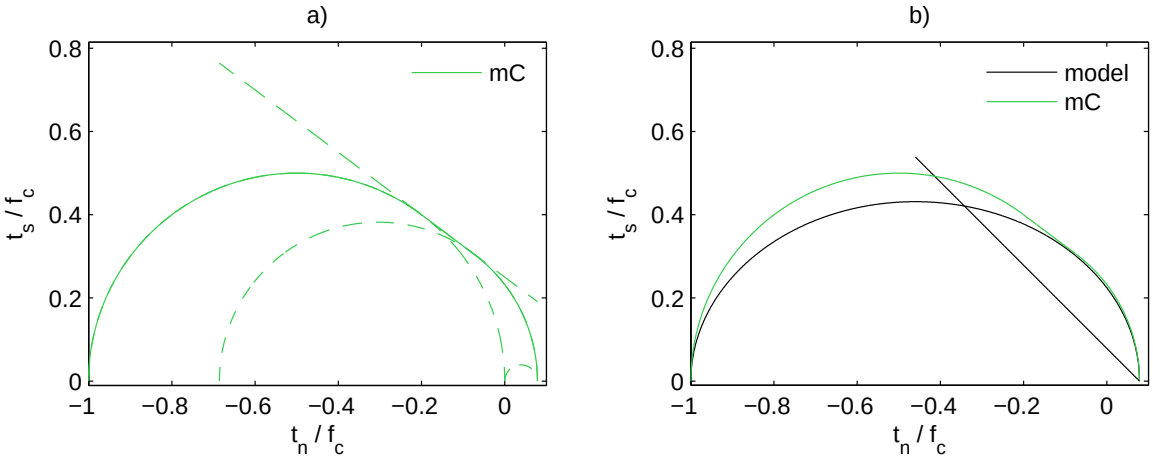


**Figure 5.5**: *Comparison between the modified Coulomb (mC) and the elliptic yield surface from the elasto-plastic model (model).* ***(a)*** *The components of the modified Coulomb model with a friction angle of* $\phi = 37°$. ***(b)*** *The elasto-plastic model with* $M = 0.8$ *and the yield surface for mC with* $\phi = 37°$.

### 5.1.4 Capabilities of the Plasticity Model

The results from the experiments are interpreted as the material data for a material point in a crack in concrete. The capabilities of the constitutive model can thereby be evaluated through a direct comparison. As in the experiments the computational model is displacement controlled and divided into two steps. The first step is the initiation of the crack in a pure Mode I opening until a certain initial opening is reached $(u_n, u_s) = (u_{n,ini}, 0)$. The second step is a mixed mode opening, with a fixed mixed mode angle $\alpha = \frac{\dot{u}_n}{\dot{u}_s}$. The computational scheme is presented in Table 5.2 and commented in the next section. The hardening functions ensure that the model gives the exact response in the case of a Mode I opening and Mode I crushing. Of more interest are the capabilities of the model during a mixed mode opening.

Figure 5.6 shows the model response for an initial opening of $u_{n,ini} = 0.025$ mm followed by five different fixed $\alpha$ values and compared with the experiments. The experimental curves corresponds to Figure 3.17. In Figure 5.6(c) the initial opening of $(u_{n,ini}, u_s) = (0.025,\ 0)$ mm is recognized and after the opening the results from the five different mixed mode angles can be read from the figure. As it appears the model response has a lack of flexibility and also the peak levels for the tractions are too low. In spite of the low traction level, the behavior in Figure 5.6(b) has some of the right trends and the lack of traction and flexibility could in a model sense just be a matter of a correct scaling. The yield surface evolution during the $\alpha = 40°$ computation is displayed in Figure 5.7. During the initial opening the traction states reaches $f_t$. In the remaining computation the traction point is located at the yield surface. In the mixed mode displacement the traction state moves to the location on the yield surface where the direction of the yield surface normal is equivalent to the direction of the prescribed displacement increment. For the $\alpha = 40°$ mixed mode displacement this entails that throughout the entire computation the traction state is located at the tensile softening

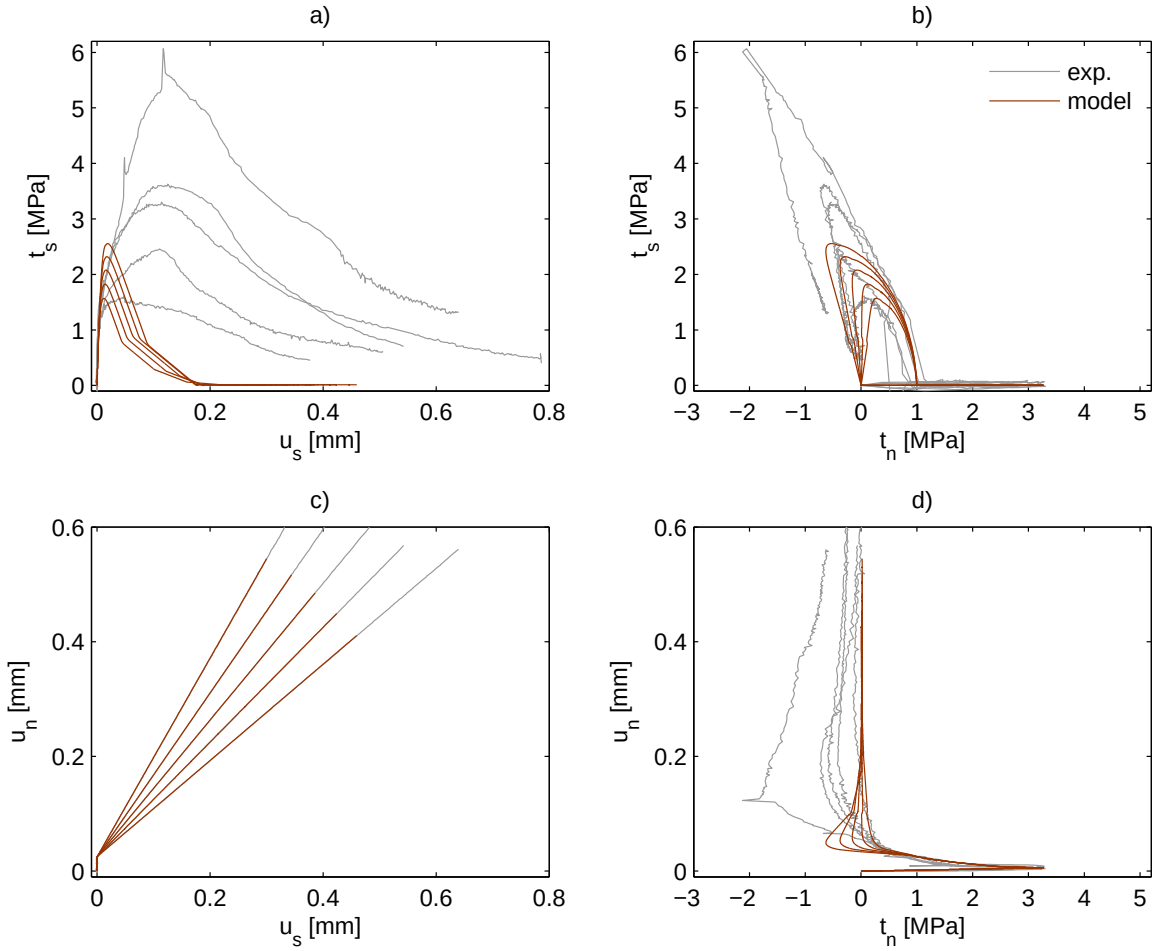


**Figure 5.6**: *Response from the elasto-plastic model for $u_{n,ini} = 0.025$ mm and five different mixed mode angles $\alpha = [40°, 45°, 50°, 55°, 60°]$ compared with experiments (exp.). The four plots show the relation between shear traction $t_s$, sliding $u_s$, normal traction $t_n$ and normal opening $u_n$. The largest tractions are obtained for the lowest $\alpha$.*

side of the yield surface. Hence, it is obvious that the basic crack model based entirely on the plasticity functions is not able to activate all the crack mechanisms. In general, the friction level is too low while the crushing for the given mixed mode openings is not at all activated.

## 5.2 Topographic Model

The plasticity model is together with the crack topography used to describe the crack behavior under mixed mode displacements. As explained in Chapter 4 the plasticity functions is used with the local displacements which are related to the average contour lines. A given global displacement increment over the crack is transformed into a local displacement for each of the average contour lines, see Figure 4.10 for definition of

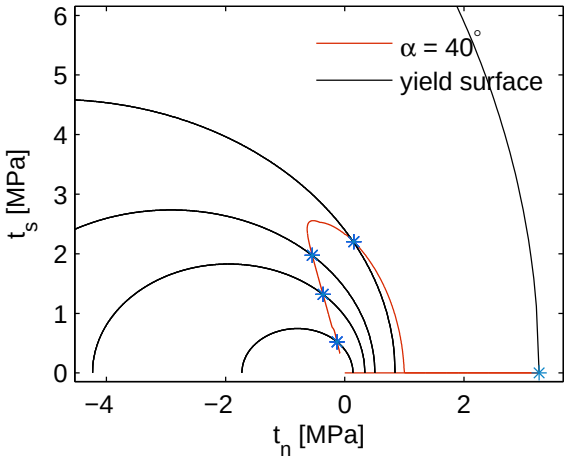


**Figure 5.7**: *Illustration of the yield surface evolution for* $u_{n,ini} = 0.025$ *mm and* $\alpha = 40°$*. From the initial state* $(t_n, t_s) = (0, 0)$ *both the initial opening and the mixed mode opening result in softening and thereby a shrinkage of the yield surface.*

the local coordinate system. For each of the average contour lines the local traction response is determined using the plasticity model. The weighted result is transformed back to global scale and added together with the global results from the other average contour lines.

For each step in the plasticity model the state is controlled by the yield function. In an elastic step, if the increment changes the state from elastic to plastic, the next iteration will be treated as plastic or vice-versa. A direct iteration scheme is used, see Table 5.2. The direct iteration is simple and effective for a sufficiently small deformation step. However, for each plastic increment, a small error is accumulated, so the traction state moves away from the yield surface. To reduce the error on the overall result the plastic state for a few of the increments is corrected by moving the traction state back to the yield surface. During a complete opening history less than 1% of the increments are corrected. The applied increment step size has been chosen sufficiently small to achieve convergence with respect to a smaller increment step size.

Normally this procedure results in a well-conditioned numerical problem. However, it has been observed that under special circumstances the equation system $\dot{\mathbf{t}} = (\mathbf{C}^{\mathbf{ep}})^{-1}[\![\dot{\mathbf{u}}]\!]$ becomes ill conditioned, i.e. $\det(\mathbf{C}^{\mathbf{ep}}) \approx 0$. In these very rare cases, the change in traction and hardening state has been restricted. It turns out that in the succeeding increment the system returns to being well conditioned.

At the top of the yield surface, there is a dramatic change in the hardening which changes from tensile softening to compressive hardening/softening or vice-versa. In order to avoid alternation in the numerical analysis between the hardening states, the hardening state is made continuous by a linearization for a narrow interval around the yield surface top. The interval is defined by the inclination of the yield surface normal with respect to a vertical surface normal, corresponding to the yield surface top. The

**Table 5.2**: *Computational scheme.*

| | |
|---|---|
| Constants | $D_n, D_s, f_t, f_c, M$ |
| Relations | $\sigma_w, \sigma_{\bar{w}}$ |
| State $i$ | $\mathbf{t}_i, \boldsymbol{\kappa}_i, [\![\mathbf{u}]\!]_i, [\![\dot{\mathbf{u}}]\!]$ |
| Iteration<br>if $f < 0$ | $\dot{\mathbf{t}} = \mathbf{D^e}[\![\dot{\mathbf{u}}]\!]$<br>$\dot{\boldsymbol{\kappa}} = 0$ |
| if $f \geq 0$ | $H = -\dfrac{\partial f\left(\mathbf{t}_i, \boldsymbol{\kappa}_i\right)^T}{\partial \boldsymbol{\kappa}} \mathbf{h}\left(\mathbf{t}_i, \boldsymbol{\kappa}_i, \sigma_w, \sigma_{\bar{w}}, [\![\dot{\mathbf{u}}]\!]\right)$<br>$\mathbf{a} = \dfrac{\partial f(\mathbf{t}_i, \boldsymbol{\kappa}_i)}{\partial \mathbf{t}}$<br>$\mathbf{C^{ep}} = \mathbf{C^e} + \dfrac{\mathbf{a}\mathbf{a^T}}{H}$<br>$\dot{\mathbf{t}} = (\mathbf{C^{ep}})^{-1}[\![\dot{\mathbf{u}}]\!]$<br>$\dot{\lambda}^p = \dfrac{\mathbf{a}^T[\![\dot{\mathbf{u}}]\!] - \mathbf{a}^T\mathbf{C^e}\dot{\mathbf{t}}}{\mathbf{a^T a}}$<br>$\dot{\boldsymbol{\kappa}} = \dot{\lambda}^p \mathbf{h}$ |
| Update | $\mathbf{t}_{i+1} = \mathbf{t}_i + \dot{\mathbf{t}}$<br>$\boldsymbol{\kappa}_{i+1} = \boldsymbol{\kappa}_i + \dot{\boldsymbol{\kappa}}$<br>$[\![\mathbf{u}]\!]_{i+1} = [\![\mathbf{u}]\!]_i + [\![\dot{\mathbf{u}}]\!]$ |
| Control | $f(\mathbf{t}_{i+1}, \boldsymbol{\kappa}_{i+1})$ |

linearization takes places within a variation of this inclination of $\pm 2°$.

The capabilities of the topographic crack model are presented in the following. The model is tested in Mode I opening and in mixed mode for varying mixed mode angles and varying initial openings. The dependency on $M$ is investigated together with the topographic description both in relation to the spacing, the weight and the number of average contour lines.

### 5.2.1 Mode I and Mixed Mode Results

The topographic model is based on the measuring of specimen $90_3^d$ with the dense 0.08 mm spacing, see Section 4.1. The angle interval is divided into 40 smaller start inclinations giving 40 average contour lines and thereby 40 independent computations for a given global mixed mode displacement. The model response to the mixed mode displacement is then the sum of the weighted results from the 40 average contour line based computations.

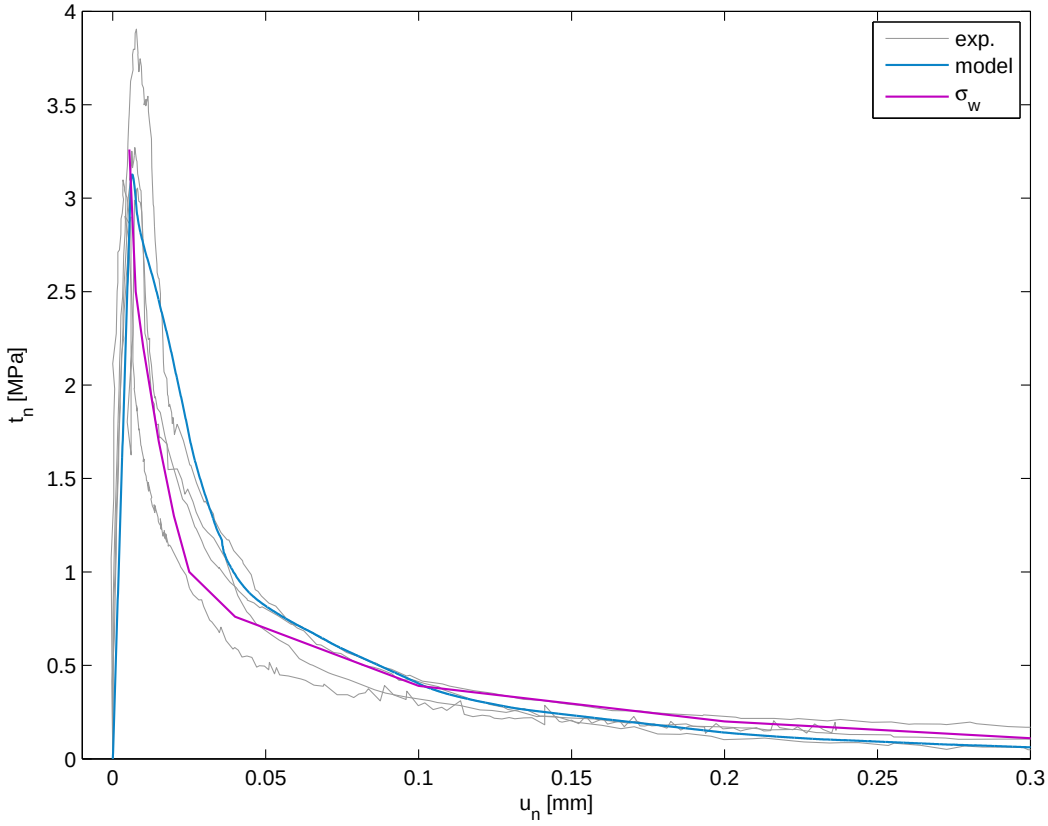


**Figure 5.8**: *Mode I model response from the topographic crack model compared with results from four experiments and the used multi linear $\sigma_w$-curve. Normal traction $t_n$ plotted as function of the opening displacement $u_n$.*

The Mode I opening response for the topographic model is illustrated in Figure 5.8. The response is displayed together with the applied multi linear $\sigma_w$-curve and the experimental Mode I test results presented in Section 3.3. Compared with the $\sigma_w$-curve the inclusion of the crack topography gives a more flexible response for $u_n < 0.1$ mm and a more stiff response for $u_n > 0.1$ mm. The difference is a consequence of the determination of tractions at local level, where some of the average contour lines e.g. for a global Mode I opening locally will experience a significant amount of friction. If the model response should give a better fit to the $\sigma_w$-curve a transformation of material data from global to local level is needed. However, in these computations the transformation is omitted. Even though the opening curve does not converge with the $\sigma_w$-curve the response is still reasonable and well within the range of the opening experiments.

Figure 5.9 shows the mixed mode response for varying mixed mode angle and an initial opening of $u_{n,ini} = 0.025$ mm. The highest shear and compressive normal traction levels are reached for a low mixed mode angle, i.e. for a relatively higher amount of sliding. Compared with the plasticity model without the crack topography in Figure 5.6, the inclusion of the topography has resulted in significantly larger normal and

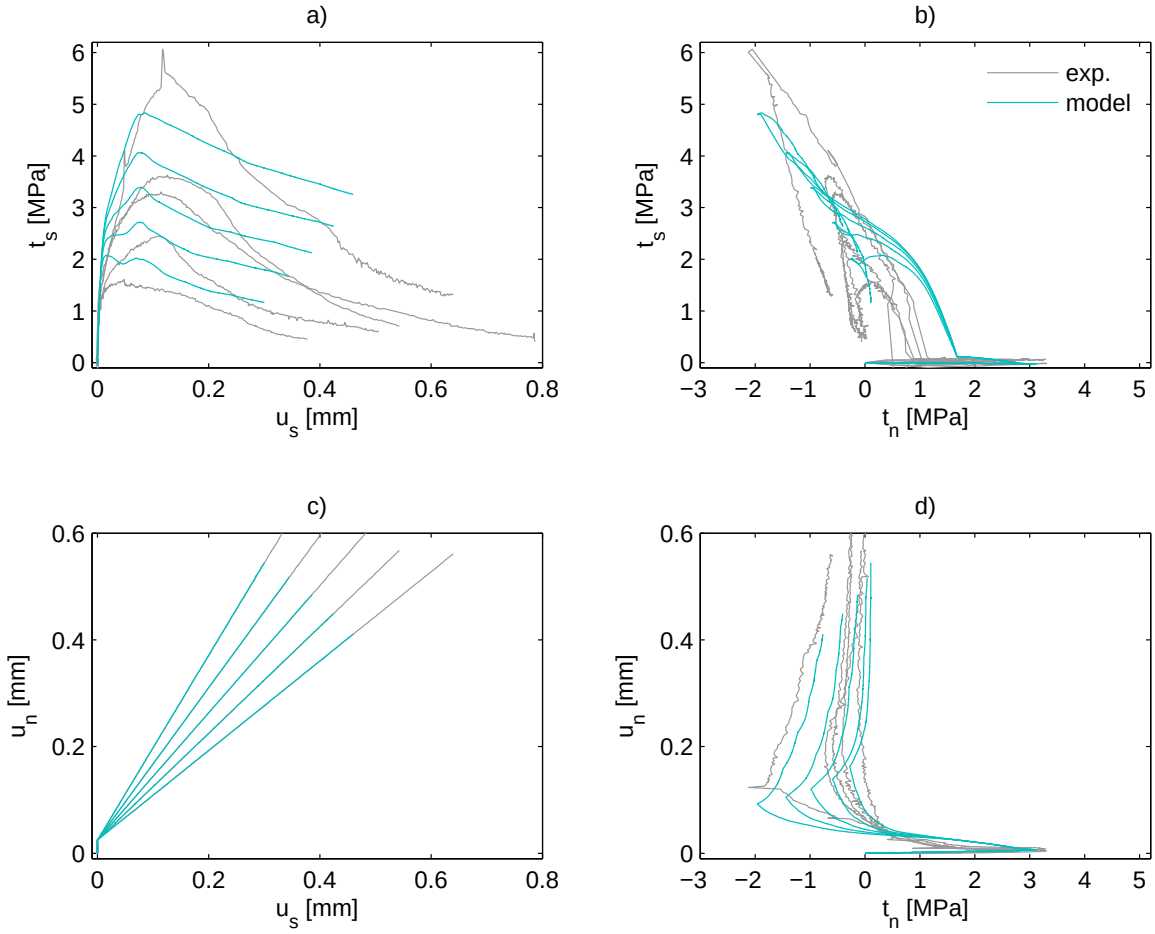


**Figure 5.9**: *Response from the constitutive model for an initial opening of* $u_{n,ini} = 0.025$ *mm followed by five different mixed mode angles* $\alpha = [40°, 45°, 50°, 55°, 60°]$ *compared with the experiments.*

shear traction levels together with a more flexible response. In fact the model overestimates the flexibility and the extreme traction levels, but both traction responses have some of the correct characteristics. For some of the mixed mode angles the model has a looped response in the $(t_n, t_s)$-plot, which cannot be rediscovered in the experiments. The appearance of these loops suggests that the displacement levels in the model response at maximum shear and minimum normal traction are a bit out of sync. The sharp bend on especially the normal traction curves is caused by the kink on the average contour lines for $u_s = 0.08$ mm whereas the bend on the shear traction curves is caused by the shift from compressive hardening to crushing softening. Two of the experiments have a similar sharp shift in the shear traction curves in Figure 5.9(a), while the other experiments have a more smooth transition around maximum shear. For small openings the $\sigma_w$-response is a bit more flexible than in the experiments, seen at the end of the initial opening in the $(t_n, t_s)$-plot. Though, as mentioned in the case of the Mode I opening this only affects the very start of the mixed mode response, and as seen in Figure 5.8 the $\sigma_w$-response fits well for larger initial openings.

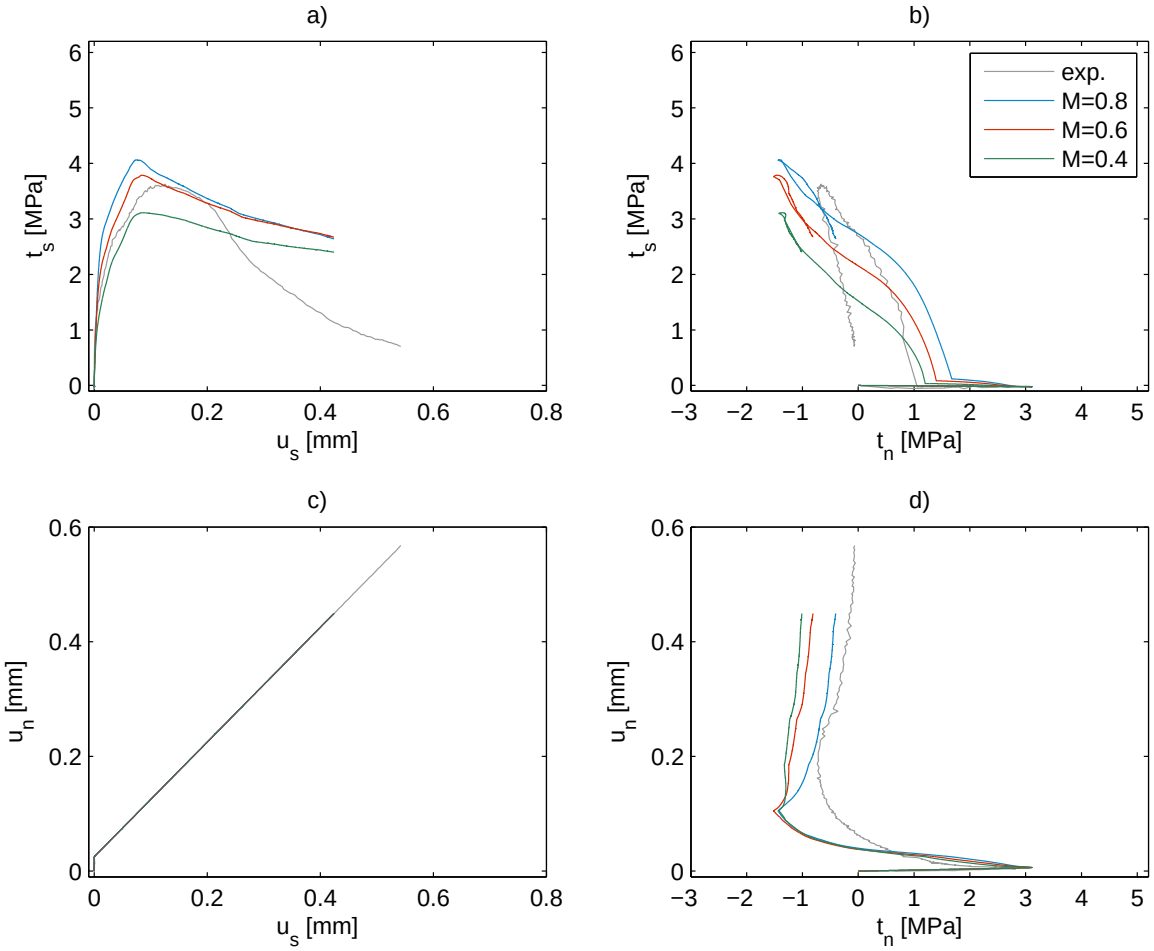


**Figure 5.10**: *Variation of the material parameter $M$ for $u_{n,ini} = 0.025$ mm and $\alpha = 45°$. The results are displayed together with the mixed mode test result for $u_{n,ini} = 0.025$ mm and $\alpha = 45°$.*

### 5.2.2 Model Variations

Besides being the inclination of the critical state line for the elliptic yield surface, the effect of the material parameter $M$ may be a bit unclear. In the presentation of the material parameters in Section 5.1.3 $M$ is compared to a friction angle in a Coulomb friction model interpreted as a inner angle in the material. Figure 5.10 reveals the influence of $M$, where it is varied from $M = 0.4$ to $M = 0.8$ for a mixed mode example with an $u_{n,ini} = 0.025$ mm initial opening followed by a $\alpha = 45°$ mixed mode opening. In terms of a Coulomb friction model the variation corresponds to a variation of the friction angle from 22° to 39°. The reduction of the height of the elliptic yield surface as a consequence of a reduced $M$ gives a lower shear traction level. For the steeper start inclinations of the average contour lines global shear locally corresponds to compression/tension. Therefore, for the given mixed mode angle their results are not that dependent on $M$. $M$ is part of the hardening functions, Equations (5.20), (5.21) and

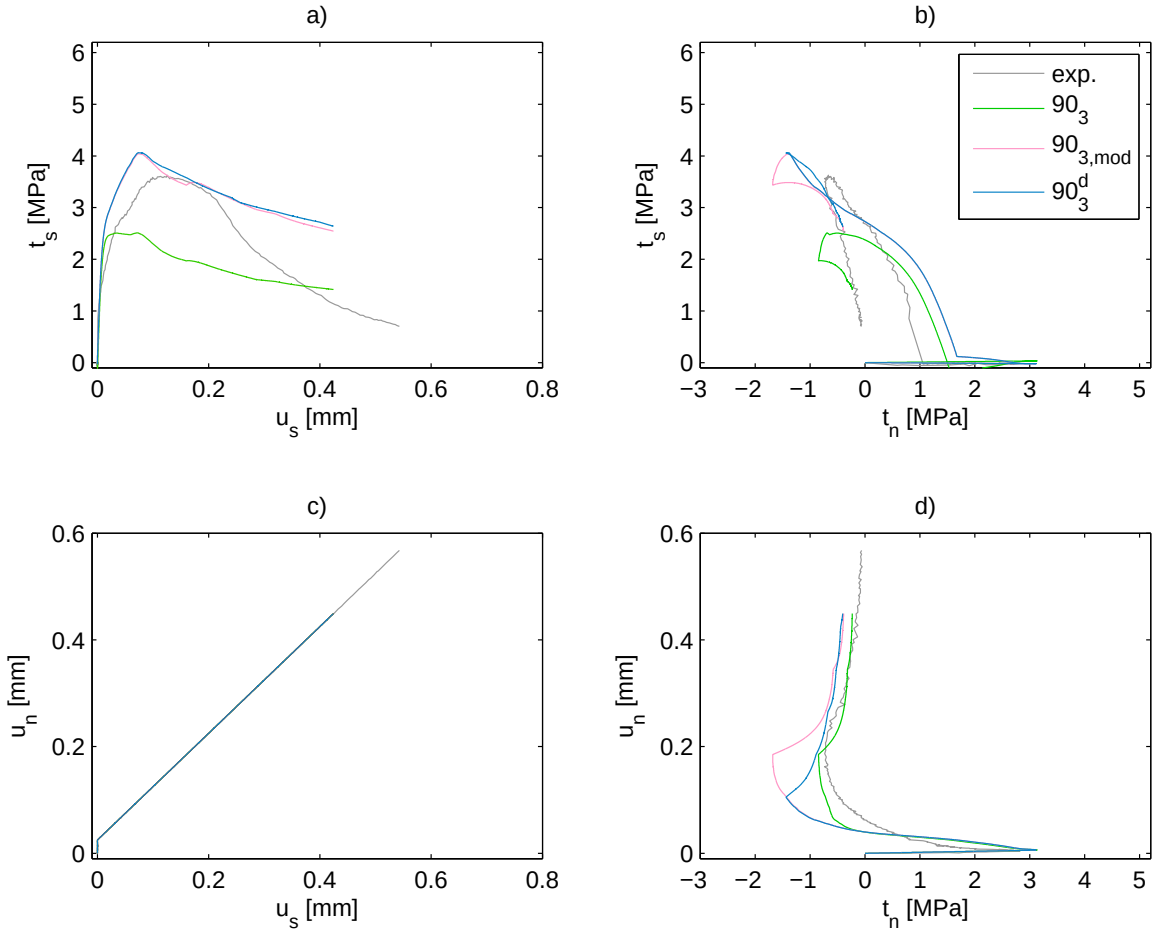


**Figure 5.11**: *Mixed mode test result for* $u_{n,ini} = 0.025$ *mm and* $\alpha = 45°$. *Computations for different spacing* $90_3$, $90_3^d$ *and for a modified weight of representation* $90_{3,mod}$.

(5.23), which explains the reduced softening for lowered $M$ seen both for the shear tractions and for the compressive normal tractions in Figure 5.10.

So far all the computations are based on the topographic description of specimen $90_3^d$ with the dense spacing. As seen in Chapter 4 the spacing influences the shape of the average contour lines as well as the matching weight of representation. Figure 5.11 displays the same $u_{n,ini} = 0.025$ mm and $\alpha = 45°$ computation based on 40 average contour lines for the two different topographic measures $90_3$ and $90_3^d$. The measures are based on the same specimen, but the spacing is different; 0.16 mm for $90_3$ and 0.08 for $90_3^d$. The larger 0.16 mm spacing in $90_3$ results in a lowered shear traction level and the peak is obtained for a smaller sliding but the path is similar to $90_3^d$. A similar picture is given for the normal tractions where $90_3$ in fact is closer to the experiment. In the traction plot in Figure 5.11(b) the path is more open and round with $90_3$, but as mentioned, the shear tractions are too low. Since the topographic descriptions $90_3$ and $90_3^d$ originates from the same specimen, it should be possible to obtain almost identical results from the two descriptions. However, as seen in Figure 4.9 the progress of the average contour lines are not similar and $90_3^d$ has a higher representation of contour

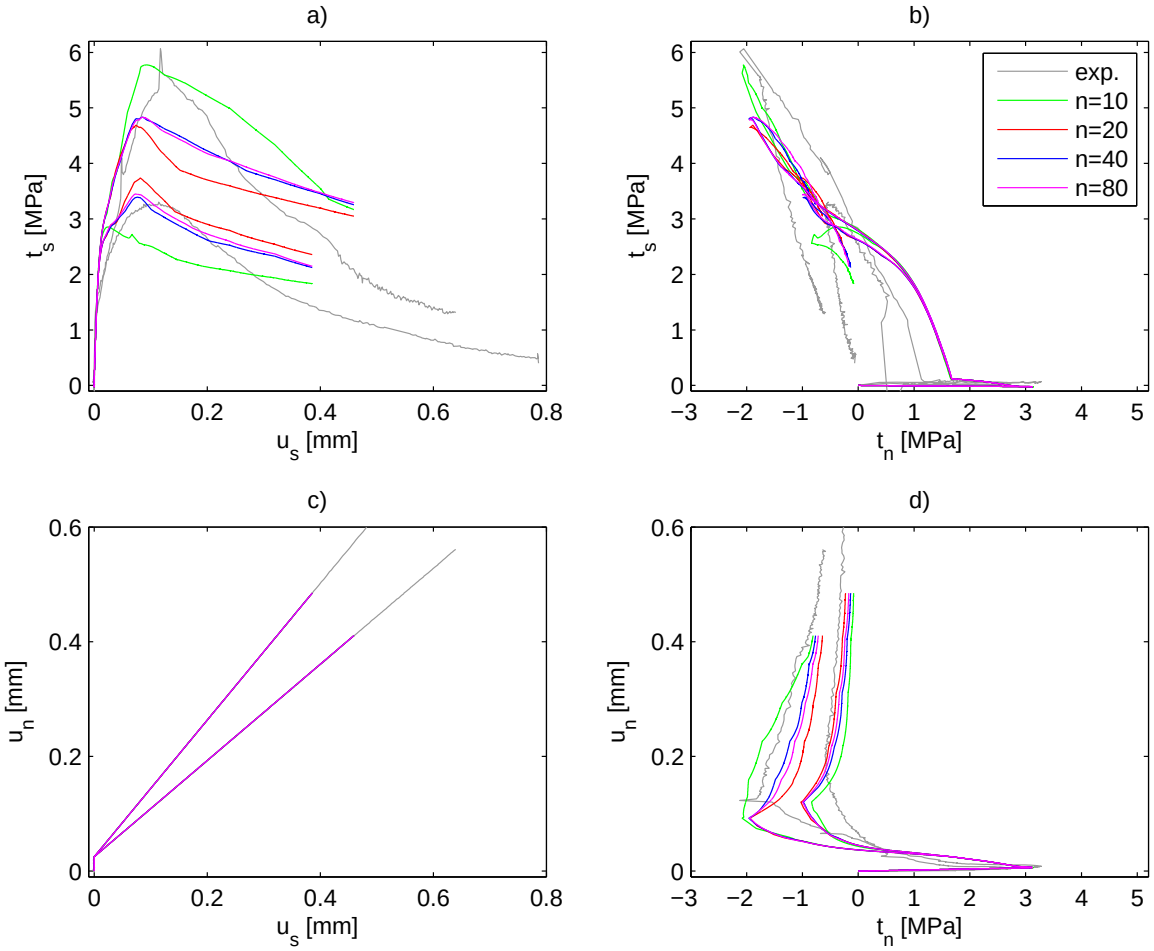


**Figure 5.12**: *Mixed mode test results for* $u_{n,ini} = 0.025$ *mm and* $\alpha = 40°$ *and* $\alpha = 50°$. *Computations for varying numbers,* $n$*, of contour lines used to describe the crack topography.*

lines with a steeper start inclination. Nevertheless, with the weight from $90_3^d$ used together with the contour lines of $90_3$ it is possible to obtain almost identical results. In Figure 5.11 this computation is named $90_{3,mod}$. $90_{3,mod}$ is almost coinciding with $90_3^d$ both in respect to tractions and displacements. Only in the normal traction plot, the later break during compression illustrates the larger spacing for $90_{3,mod}$. A similar break at a similar opening takes place for $90_3$ and the breaks are directly related to the 0.16 mm spacing. For $90_3^d$ the break occurs 0.08 mm earlier. Based on the comparison in Figure 5.11 it may be stated that the obtained weight of representation between the contour lines has an influence on the results. However, the overall mixed mode response is identifiable even for a changed spacing and weight.

Figure 5.12 displays the result from a convergence analysis over the number, $n$, of average contour lines representing the crack topography of specimen $90_3^d$. Results from two mixed mode experiments with $u_{n,ini} = 0.025$ mm and $\alpha = 40°$ and $\alpha = 50°$ are shown together with the model results for computations with $n = [10; 20; 40; 80]$ average contour lines. The coarse subdivisions with $n = 10$ and $n = 20$ differs from

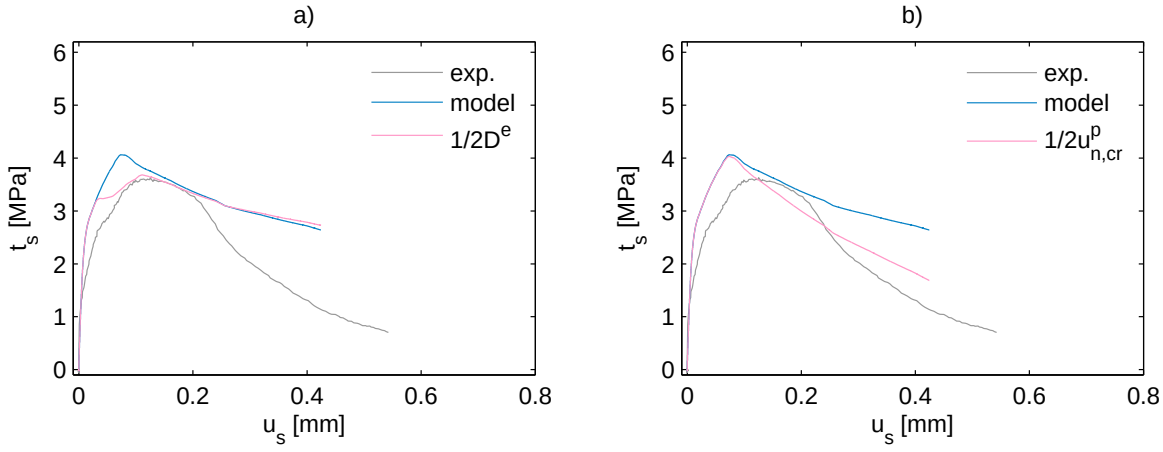


**Figure 5.13**: *Model variation for $u_{n,ini} = 0.025$ mm and $\alpha = 45°$ compared with the similar experiment. Shear traction $t_s$ as function of the sliding $u_s$.* ***(a)*** *The elastic stiffness for the compressive hardening is reduced, $\frac{1}{2}\mathbf{D^e}$.* ***(b)*** *The crushing softening is made more brittle, $\frac{1}{2}u^p_{n,cr}$.*

the finer with $n = 40$ and $n = 80$, and the results converge for $n \geq 40$. Therefore a topographic description consisting of 40 average contour lines is adequate.

The model is simple and uses some easily obtained material parameters and material relations between tractions and displacements. Since the parameters and the relations in the experiments are obtained at global level it introduces some uncertainty when they are used at local level in the material description. There is also some uncertainty about the pre and post cracking material description. For instance, instead of having a fully elastic compressive hardening the introduction of tensile micro cracks could reduce the elastic stiffness. Or the tensile micro cracks could affect the crushing softening response to be more brittle. The consequences of these two variations are illustrated in Figure 5.13. The reduced elastic stiffness for the compressive hardening, $\frac{1}{2}\mathbf{D^e}$, gives a more smooth response around maximum shear traction, whereas the more brittle crushing softening, $\frac{1}{2}u^p_{n,cr}$, makes the total mixed mode softening response more brittle.

Figure 5.14 compares the model response for two different initial mixed mode openings, $u_{n,ini} = 0.025$ mm and $u_{n,ini} = 0.100$ mm, with matching experiments. The shape of the responses are the same as seen in Figure 5.9, and as in the experiments the traction levels drop for increased initial opening. For larger displacements the responses in both the experiments and the model tend to be the same regardless of the initial opening. This suggests that the initial opening mostly affects the initial cracking whereas the cracking changes to a more general behavior for larger displacements. Figure 5.14 also illustrates the combined effect of the two variations presented in Figure 5.13. The changed parameters give a better traction-displacement response while the $(t_n, t_s)$-responses still show looped tendencies.

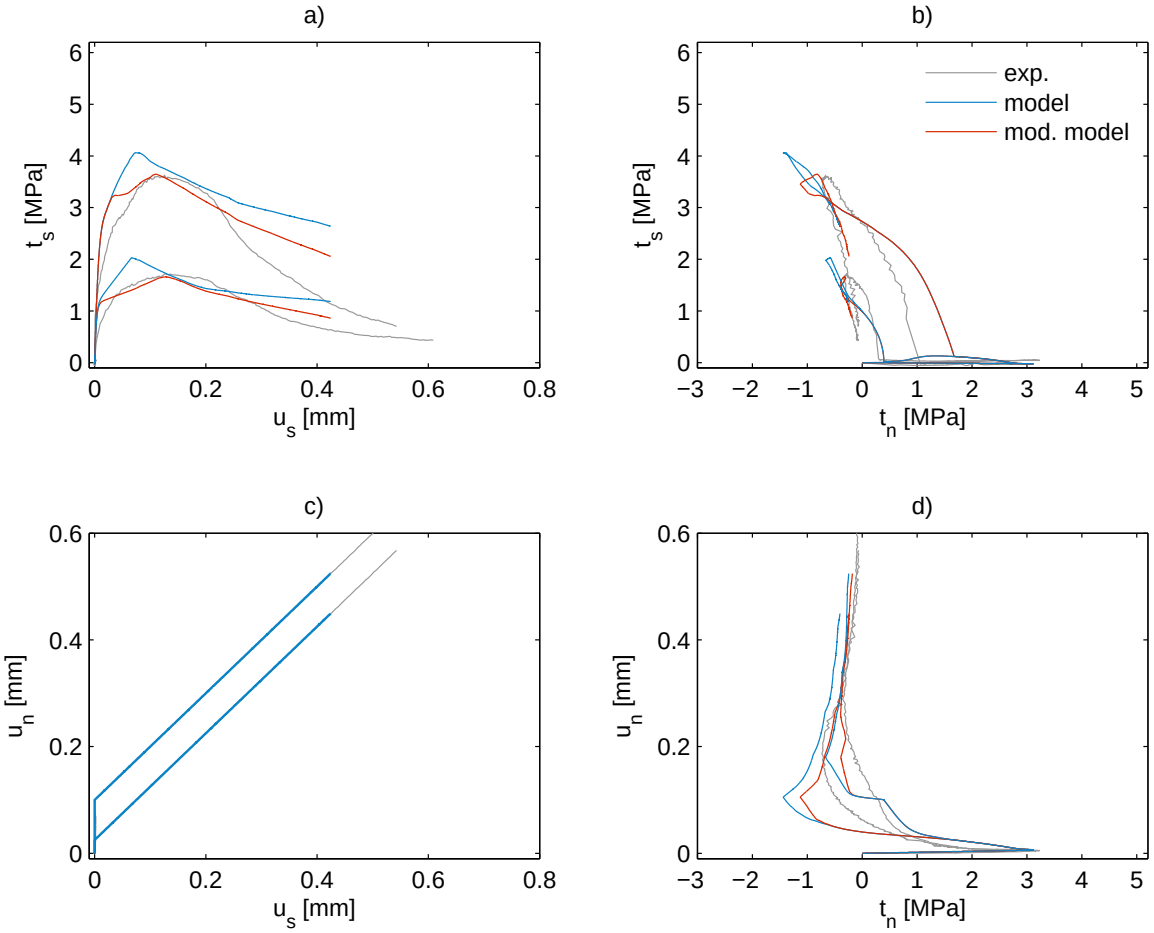


**Figure 5.14**: *The response from the constitutive model (model) and for the model with modified material parameters (mod. model) for* $\alpha = 45°$ *and two different initials openings* $u_{n,ini} = 0.025$ *mm and* $u_{n,ini} = 0.100$ *mm compared with the matching experiments. Smallest initial opening gives the largest tractions.*

## 5.3 Simplified Constitutive Model

The topographic model presented in the previous section is established without any additional fit parameters or calibrations. The inclusion of the crack surface topography facilitates a mechanical interpretation of the mixed mode behavior, and the model may be used to describe both opening and closure under various mixed mode ratios. The model is simply based on easily obtained material parameters; however, since some special equipment is needed for the measuring it is not trivial to obtain the crack surface topography. And since the global traction response for a global displacement increment consists of the sum of local contributions, the topographic model is demanding in relation to computational power. For instance, to obtain the global response from a single displacement increment in the previous examples 40 local computations are accomplished. It is possible to establish a simpler model formulation where the topography is omitted. The exclusion has some drawbacks, though; along with the omission the mechanical foundation fades and the range and the capabilities of the simplified

**Table 5.3**: *Material parameters used in the simplified formulation.*

| Parameter | value |
|---|---|
| $f_t$ | 3.3 MPa |
| $f_c$ | -41 MPa |
| $D_n$ | 570 GPa/m |
| $D_s$ | 90 GPa/m |
| $M$ | 1.0 |
| $k_1$ | $-2 \cdot 10^3$ /m |

model are constraint to the investigated mixed mode ratios. Still, a simplified model can assist to understand the qualitative mechanisms behind the mixed mode cracking.

The simplified model is entirely based on the plasticity model presented in Section 5.1.1 with modified hardening functions $\mathbf{h} = [h_t, h_c]^T$, a changed $M$ and a lowered shear stiffness $D_s$. This means that the plasticity model is associated and, like illustrated in Figure 5.2, it has an elliptic yield surface and the hardening parameters $\boldsymbol{\kappa} = [\sigma_t, \sigma_c]^T$. The initial state is described by the initial tensile and compressive strength of the concrete, thus, in the initial state $\boldsymbol{\kappa} = [f_t, f_c]^T$. The model is only intended to describe mixed mode under continuous opening and the hardening is therefore limited to the case of softening as a consequence of crack openings. The hardening is divided in two conceptual different cases, the Mode I opening and the mixed mode opening, respectively. In Mode I the hardening is directly related to the concrete tensile softening curve ($\sigma_w$-curve), and the hardening function can thereby be obtained directly from Equation (5.20) as

$$\begin{aligned} h_t &= M^2(\sigma_t - \sigma_c)\dot{\sigma}_w \\ h_c &= \frac{f_c}{f_t} M^2(\sigma_t - \sigma_c)\dot{\sigma}_w \end{aligned} \tag{5.24}$$

where $\dot{\sigma}_w$ is the incremental inclination of the $\sigma_w$-curve. The hardening functions in mixed mode are very alike. Instead of $\dot{\sigma}_w$ they are based on the inclination of a similar "mixed mode softening curve". The hardening functions in mixed mode are

$$\begin{aligned} h_t &= M^2(\sigma_t - \sigma_c)\sigma_t k_1 \\ h_c &= \frac{f_c}{f_t} M^2(\sigma_t - \sigma_c)\sigma_t k_1 \end{aligned} \tag{5.25}$$

$\sigma_t k_1$ is the inclination of the mixed mode softening curve, where the softening parameter $k_1$ is introduced. Using $\sigma_t$ to describe the softening ensures that the obtained softening is high for a large $\sigma_t$ and decreases as $\sigma_t$ decreases.

The simplified model is fitted against the experiments which entail that $M$ is raised from 0.8 to 1.0 and that the shear stiffness $D_s$ is significantly reduced from 380 GPa/m to 90 GPa/m. The used material parameters are listed in Table 5.3. Figure 5.15 shows the model capabilities in relation to the experiments for an initial opening of $u_{n,ini} =$ 0.025 mm and followed by five different mixed mode angles. Qualitatively the response

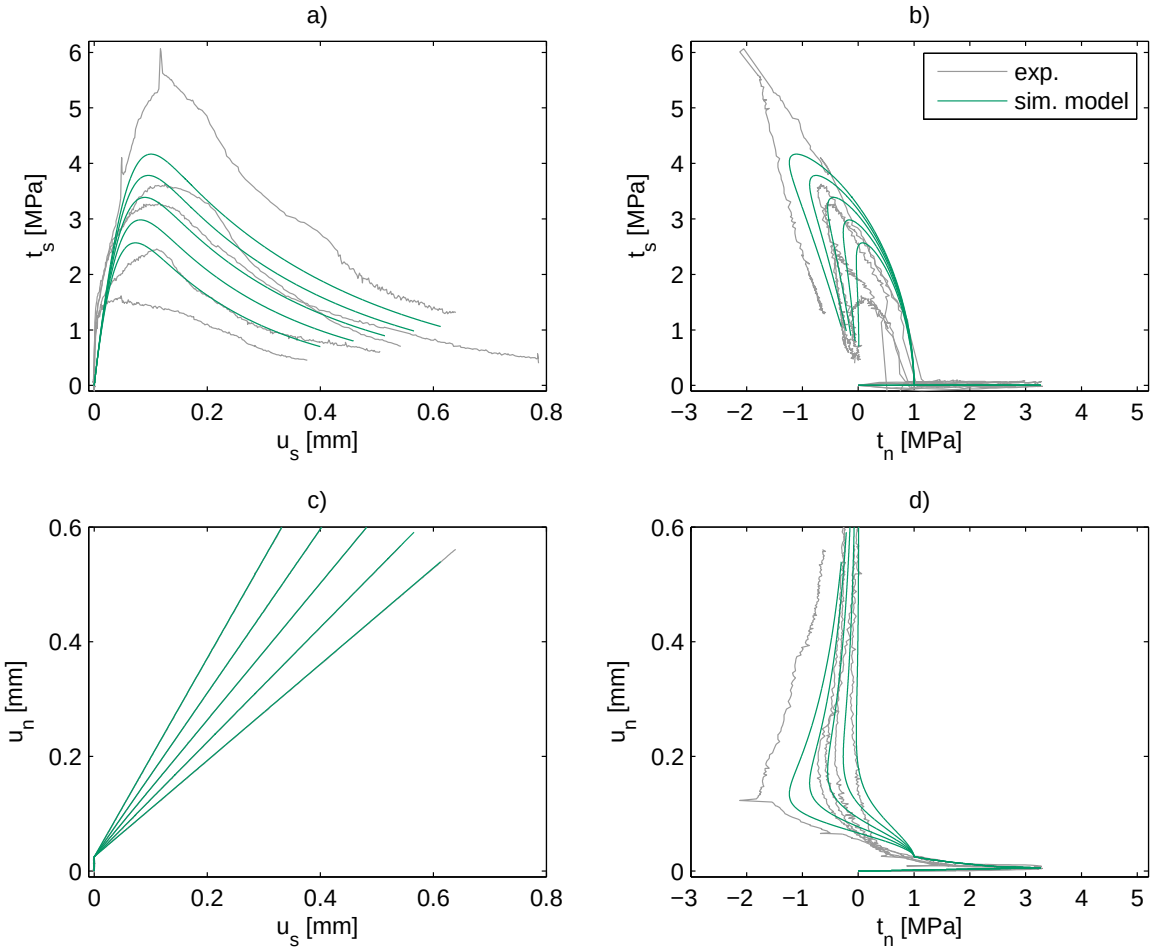


**Figure 5.15**: *Response from the simplified constitutive model for an initial opening of* $u_{n,ini} = 0.025$ *mm followed by five different mixed mode angles* $\alpha = [40°, 45°, 50°, 55°, 60°]$ *compared with the experiments.*

from the simplified model is a good reproduction of the mixed mode experiments. Compared to the original plasticity model, tested in Figure 5.6, the interchange of $\dot{\sigma}_w$ with $\sigma_t k_1$ in mixed mode slows down the softening. The higher $M$ entails a higher shear traction level and the lowered $D_s$ gives a more ductile response both for the normal and the shear tractions. Quantitatively the model response has a too small difference between the different mixed mode angles especially in the shear traction plot and from the normal traction plot the transition between Mode I and mixed mode seems to happen too sudden.

The model is simple but gives a good representation of the mixed mode behavior. It can be shown that the model gives a similar fair representation for a changed initial opening and by simple means it can be enhanced with a better transition between Mode I and mixed mode. However, by the simplified formulation the mechanical interpretation of the mixed mode behavior is now hidden in the $\sigma_t k_1$-relation together with the lowered shear stiffness. And the parameter fit together with the applied hardening

functions only ensure that the model is able to reproduce the mixed mode behavior under constant opening.

## 5.4 Discussion

To begin with the end, the simplified constitutive model in Section 5.3 exemplifies that the mixed mode cracking under constant opening can be treated as two conceptually different hardening cases. One hardening case during Mode I opening and a different and lighter hardening case during mixed mode opening. The model and the material parameters in the simplified model are almost identical to the plasticity model included in the topographic model in Section 5.2. Only the two material parameters $M$ and $D_s$ are changed, and the change only affects the mixed mode response. If the concrete mixed mode behavior should be represented solely by a plasticity model, the constitutive relation must be given through the elasto-plastic flexibility matrix $\mathbf{C^{ep}}$, Eq. (5.14). $\mathbf{C^{ep}}$ may be divided into an elastic part $\mathbf{C^{e}}$ and a plastic part $\mathbf{C^{p}}$. Assuming that the elastic part can be interpreted from the elastic stiffnesses/flexibilities, the inelastic cracking behavior may be evident from $\mathbf{C^{p}}$. $\mathbf{C^{ep}}$ is given as

$$\mathbf{C^{ep}} = \mathbf{C^{e}} + \begin{bmatrix} C^p_{11} & C^p_{12} \\ C^p_{21} & C^p_{22} \end{bmatrix} \tag{5.26}$$

Provided with a satisfactorily tensile softening relation the inelastic Mode I opening behavior can be described entirely through $C^p_{11}$ as demonstrated in Section 5.1.2. Comparable, the Mode II behavior should be described by $C^p_{22}$, though, because of the crack roughness and the related dilatational effects a sliding relation similar to the $\sigma_w$-curve might be difficult to obtain. Likewise this might start a new discussion about Mode II fracture energy, however, the sliding relation should describe the shear traction-sliding displacement relation for an already establish crack. Maybe the relation could be obtained for a crack at an opening level where the cohesion is exhausted. Though, the sliding would introduce dilation and the sliding displacement would thereby introduce either normal opening or compressive normal tractions. Finally, all four quantities in $\mathbf{C^{ep}}$ should describe the mixed mode behavior with an endless combination between crack displacements and tractions. As demonstrated with the simplified model it is possible to set a simple mixed mode plasticity model. The model can be expanded to cover a larger spectrum of the mixed mode cracking, but the model parameters will properly hide the mechanical interpretation of the cracking mechanisms.

The direct topographic link to the crack mechanisms is the unique quality of the topographic model. In the model the mixed mode behavior is related to the different cracking mechanisms like opening, sliding and crushing. The model is simply based on easily obtained material parameters, and provided with a surface description for a given concrete, the model can most likely be used for concrete mixtures with similar

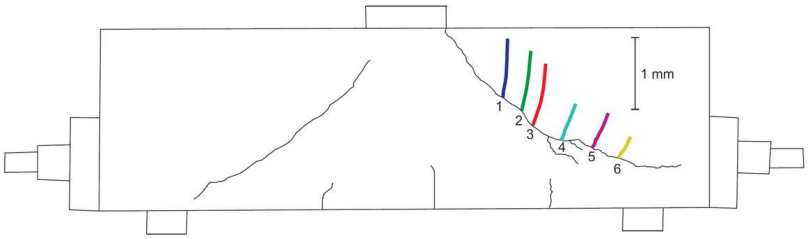


**Figure 5.16***: Three-point bending beam without shear reinforcement. Relative displacements for different parts of the shear crack. After Kragh-Poulsen (2009).*

characteristics. The topographic model is used in the context of a material point investigation. Further validation may include an implementation in a FEM context with the objective to model structural members. In Mougaard et al. (2010) the constitutive model by Nielsen et al. (2010) is used together with XFEM to model the specimen and the experiments presented in Chapter 3. The FEM model of the specimen may be used as an indirect confirmation of the applied material parameters. However, the modeling is rather close to a material point investigation. Three- and four-point bending beams are used to induce mixed loading conditions on a crack, but as long as the beams are simply supported, the crack opens entirely in Mode I. If a beam test for mixed mode crack testing should be successful, the expected dilation from a sliding crack should be prevented. A completely or partially clamped supported beam may provide as a suited test specimen. Or for instance the over-reinforced beam without shear reinforcement in a three point bending set-up presented in Figure 5.16 (Kragh-Poulsen, 2009). Here the over-reinforcement ensures that the beam fails due to a sliding failure in the diagonal cracks. In the figure the relative displacement between the crack faces for one of the shear cracks has been measured and illustrated. After the crack initiation, the relative displacement between the crack faces is inclined with respect to the crack orientation, indicating that the crack is opened in a mixed mode displacement.

The topographic model still needs some verification. For instance the normal traction levels are too high. Both the yield surface in the plasticity model and the topography introduce dilation in the model, which seems reasonable since there are dilatational effects on the various size scales. Dependent on the resolution in the topographic measure, though, the dilation might be accounted for twice in the model. Also the use of global material parameters at local level needs some verification. However, considering the model response the assumption seems reasonable. Despite these uncertainties the topographic model without calibration gives a good crack representation and illustrates the mechanisms behind the mixed mode cracking.

# Chapter 6

# Conclusion

The constitutive mixed mode behavior of cracks in concrete is investigated both through mixed mode experiments and by materials modeling of the crack. A biaxial experimental set-up with a closed control loop is established and used to examine both the Mode I and the mixed mode behavior. The same mixed mode behavior is modeled by a new elasto-plastic material model. The material model is based on the uniaxial tensile opening behavior and the uniaxial compressive crushing behavior for a crack. Combined with a topographic description of a concrete crack surface and without any additional model parameters the model is able to describe the mixed mode behavior.

The biaxial test set-up consisting of a 5 MN universal testing machine and a built-in second axis has been applied to the mixed mode measurements. The relative opening and sliding of the crack is used as the control signals in a new enhanced closed control loop. The opening and the sliding of the crack are measured by clip gauges using a pair of custom made orthogonal gauge rails mounted on the specimen. The tests of the double notch specimen are divided into two steps. A pure Mode I opening step, where a macro crack is initiated between the notches. The initial opening is followed by the mixed mode opening step, where the cracked region is displaced in combined opening and sliding. Together with a photogrammetric registration of the crack development, the experiments provide information about the crack behavior under various ratios between opening and sliding and for various initial openings.

Earlier reported biaxial set-ups have a lack of stiffness and to achieve the actual mixed mode material behavior the results often need to be analyzed through an inverse analysis. In Mode I, the present stiff set-up together with the closed control loop is capable of capturing the crack initiation and the crack development. The precise orthogonal gauge rails entail a direct interpretation of the mixed mode crack opening process, ensuring that the achieved response over the ligament is equal to the prescribed mixed mode displacement. A number a mixed mode experiments are conducted and presented, all under continuous opening conditions. In the experiments there is a clear tendency that the shear level and the compression level raise for both decreasing initial opening and for decreasing mixed mode angle.

In a number of the experiments the crack development is recorded by a photogrammetric system. Despite the occurrence of a few local secondary cracks during the mixed mode fracture development, the crack pattern consists of a distinct primary crack. The fracture localization is supported by a subsequent optical laser measure of the crack topography. By a resolution in the order of 0.1 mm the laser scan provides a detailed registration of the topography. The topography measure reveals that the height fluctuation over the fracture surface is in the same order as the 8 mm maximum aggregate size. The even crack surface is a result of the specimen design and the biaxial set-up design, and the surface is governed by material aspects like aggregate size and concrete strength rather than structural effects. The obtained results from the mixed mode tests are considered representative of a single crack under mixed mode displacement, and the results are well suited as a direct determined basis for the model development of a mixed mode material model.

Besides the qualitative evaluation of the even crack surface the measure of the topography is the basis in a characterization of the surface. The characterization consists of a series of average contour lines describing the average trends of the topography. Based on the average contour lines and provided with information about the inclination of the surface in a given direction in a given point on a surface, it is possible to predict the most plausible curvature of the succeeding path of the surface. In the plasticity model the average contour lines describe the relation between global displacements and local displacements at the crack surface. For a global displacement increment the constitutive equations are solved at local level and the total model response is assembled at global level. To some extent crack mechanisms like the cohesion, the dilatational effect, the stiffness degradation and the friction are related to the irregular and rough crack surface. The average contour lines couple the local ratio between opening, friction and crushing, and thereby the surface roughness, to the global crack behavior.

The elasto-plastic material model is an associated plasticity model and is based on easily obtained material parameters. The elliptic yield surface is controlled by two hardening parameters, which represent the actual compressive and tensile strength of the concrete, respectively. Besides the elastic normal and shear stiffness and the initial compressive and tensile strengths for the concrete, the constitutive behavior is based on the relation between normal opening and normal traction. For an opening of the crack the material softens, for a closure the material hardens, and for a large closure the material crushes described as a softening. The constitutive model is implemented in a material point investigation.

Compared with experiments and without any tuning the constitutive model based on the plasticity model and the topographic description gives a convincing description of both Mode I opening, crushing and mixed mode cracking. Overall, the experimental investigations, and the topographic description together with the constitutive model provide an interpretation of the mixed mode crack behavior.

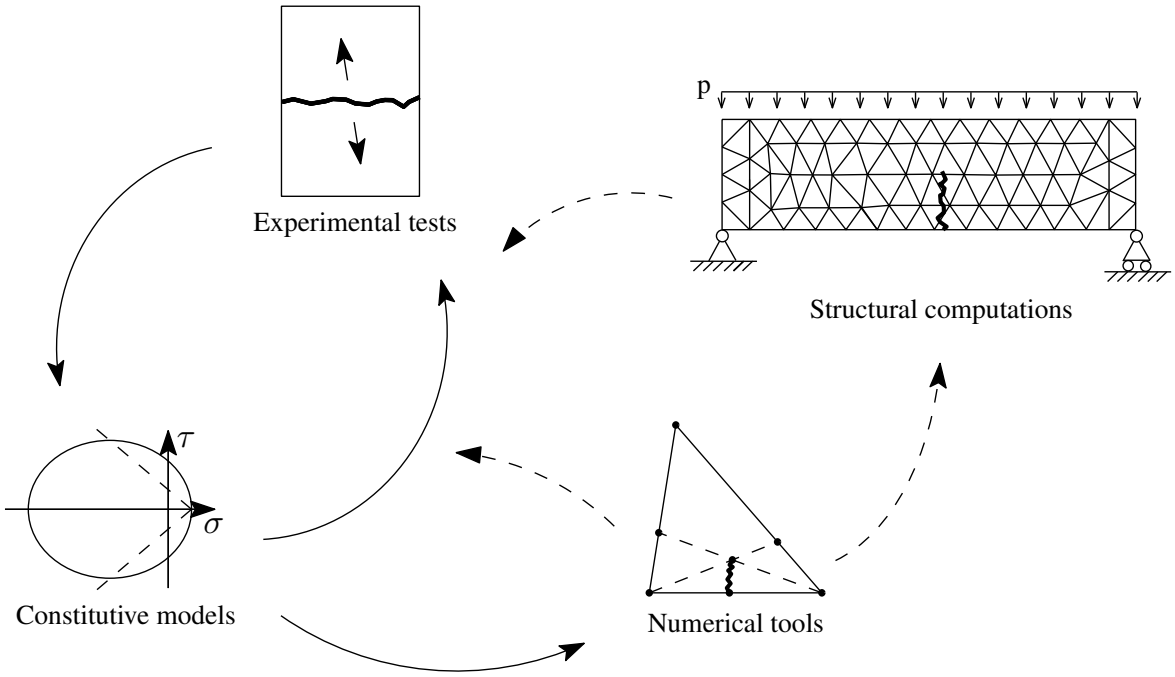


**Figure 6.1***: The process in the formulation of a detailed computational structural model and the relation between experiments, theory and numerical tools. (Identical to Figure 1.4)*

## 6.1 Outlook

The formulation process of the constitutive model presented in this thesis is consistent with the process emphasized in Figure 6.1. The sparse experimental basis for the mixed mode behavior of an already established crack was the outset for the present experimental work. With the enhanced biaxial set-up and a test program focused on the mixed mode crack behavior the experiments provide a basis for the constitutive modeling. The elasto-plastic model behaves qualitative correct in mixed mode, but it gives too low tractions and a too brittle response. Instead of adding tuning parameters the topographic description is included. To obtain the topographic description new experimental investigations were needed, this time with the optical laser scanner. In a material point modeling, the constitutive model consisting of the elasto-plastic model and the topographic description is capable of reproducing the mixed mode experiments. And the first iterations in the formulation process are thereby at an end.

Next the constitutive model may be included in an XFEM context and used to model structural members. Besides modeling the mixed mode experiments, suitable structural computations of reinforced beams may be conducted. The important aspect in the selection of a structural member for the mixed mode modeling is to choose a member, where the crack in fact is exposed in mixed mode. A mixed loading condition must be induced and the dilation of the crack must be prevented to some extent. Modeling shear cracks in a reinforced beam would be suitable.

However, even though the model demonstrate a consistent mixed mode behavior the model is not effective. For each update in the constitutive points in a XFEM-model, 40 sub-calculations have to be accomplished. The computation of the sub-calculations may be optimized. Alternatively a simplified model can be introduced. To avoid tuning and model parameters without a consistent mechanical interpretation, additional experiments may be conducted. The present model is based on the opening behavior, and it could be informative to investigate the crack behavior under sliding conditions. An experiment could be conducted with a large initial opening followed by a sliding displacement between the crack faces, or it could be sliding of a crack under confinement. The only restriction to the displacement path is that a secondary cracking failure ought to be avoided. If a secondary cracking failure is obtained the experiment is no longer a direct material point investigation and the crack behavior has to be interpreted through an inverse analysis.

Probably the structural computations would give rise to new experimental material point investigations. Load cycles could be introduced as experiments exposed to open-closure combined with mixed mode. A change of the material properties could as well provide new useful information to the mixed mode behavior. For instance the influence of the size of the maximum aggregate size could be detected. In this way the formulation process in Figure 6.1 would start again, however, not from scratch. The new process would extent from the basis provided by the research presented in this thesis and the related former research within the field.

# Bibliography


Alfano, G. and Sacco, E. (2006). Combining interface damage and friction in a cohesive-zone model. *International Journal for Numerical Methods in Engineering*, 68(5):542–582.

Asferg, J. L., Poulsen, P. N., and Nielsen, L. O. (2007). A consistent partly cracked XFEM element for cohesive crack growth. *International Journal for Numerical Methods in Engineering*, 72(4):464–485.

Barenblatt, G. I. (1962). The mathematical theory of equilibrium cracks in brittle fracture. *Advances in Applied Mechanics*, 7:55–129.

Bažant, Z. P. and Oh, B. H. (1983). Crack band theory for fracture of concrete. *Materials and Structures*, 16(3):155–177.

Bažant, Z. P. and Pfeiffer, P. A. (1986). Shear fracture tests of concrete. *Materials and Structures*, 19(2):111–121.

Belytschko, T. and Black, T. (1999). Elastic crack growth in finite elements with minimal remeshing. *International Journal for Numerical Methods in Engineering*, 45(5):601–620.

Bocca, P., Carpinteri, A., and Valente, S. (1991). Mixed-mode fracture of concrete. *International Journal of Solids and Structures*, 27(9):1139–1153.

Brühwiler, E. and Wittmann, F. H. (1990). The wedge splitting test, a new method of performing stable fracture mechanics tests. *Engineering Fracture Mechanics*, 35(1-3):117–125.

Britannica, E. (2012). Concrete and reinforced concrete - encyclopædia britannica online academic edition.

Carol, I., López, C. M., and Roa, O. (2001). Micromechanical analysis of quasi-brittle materials using fracture-based interface elements. *International Journal for Numerical Methods in Engineering*, 52:193–215.

Carol, I., Prat, P. C., and López, C. M. (1997). Normal/shear cracking model: Application to discrete crack analysis. *Journal of Engineering Mechanics*, 123(8):765–773.

Carpinteri, A. and Brighenti, R. (2010). Fracture behaviour of plain and fiber-reinforced concrete with different water content under mixed mode loading. *Materials & Design*, 31(4):2032 – 2042.

Carpinteri, A., Valente, S., Ferrara, G., and Melchiorri, G. (1993). Is Mode-II fracture energy a real material property? *Computers & Structures*, 48(3):397–413.

Cendón, D. A., Gálvez, J. C., Elices, M., and Planas, J. (2000). Modelling the fracture of concrete under mixed loading. *International Journal of Fracture*, 103(3):293–310.

Chen, W. F. and Han, D. J. (1988). *Plasticity for Structural Engineering*. Springer-Verlag New York.

Cornelissen, H. A. W., Hordijk, D. A., and Reinhardt, H. W. (1986). Experimental determination of crack softening characteristics of normalweight and lightweight concrete. *HERON*, 31(2):45–56.

Cox, B. N. and Marshall, D. B. (1991). Stable and unstable solutions for bridged cracks in various specimens. *Acta Metallurgica Et Materialia*, 39(4):579–589.

Cox, B. N. and Marshall, D. B. (1994). Concepts for bridged cracks in fracture and fatigue. *Acta Metallurgica Et Materialia*, 42(2):341–363.

de Borst, R. and Groen, A. E. (2000). *Modeling in Geomechanics*. John Wiley & Sons, Ltd.

de Borst, R. and Nauta, P. (1985). Non-orthogonal cracks in a smeared finite element model. *Engineering Computations*, 2(1):35–46.

Dick-Nielsen, L. (2007). *Modeling of ECC Materials using Numerical Formulations based on Plasticity*. PhD thesis, Department of Civil Engineering, Technical University of Denmark, Lyngby, Denmark.

Dugdale, D. S. (1960). Yielding of steel sheets containing slits. *Journal of the Mechanics and Physics of Solids*, 8(2):100–104.

Gettu, R., Mobasher, B., Carmona, S., and Jansen, D. C. (1996). Testing of concrete under closed-loop control. *Advanced Cement Based Materials*, 3(2):54–71.

Gálvez, J. C., Elices, M., Guinea, G. V., and Planas, J. (1998). Mixed mode fracture of concrete under proportional and nonproportional loading. *International Journal of Fracture*, 94(3):267–284.

GOM (2005). *Aramis User Manual (4M) v5.4.1*. GOM mbH.

Gopalaratnam, V. S. and Shah, S. P. (1985). Softening response of plain concrete in direct tension. *Journal of The American Concrete Institute*, 82(3):310–323.

Griffith, A. A. (1921). The phenomena of rupture and flow in solids. *Philosophical Transactions of the Royal Society of London. Series A, Containing Papers of a Mathematical or Physical Character*, 221:163–198.

Hassanzadeh, M. (1990). Determination of Fracture Zone Properties in Mixed Mode I and II. *Engineering Fracture Mechanics*, 35:845–863.

Hassanzadeh, M. (1992). *Behaviour of Fracture Process zones in Concrete Influenced by Simultaneously Applied Normal and Shear Displacements*. PhD thesis, Lund Institute of Technology. Report TVBM-1010.

Hawk (2000). *Nextec Hawk User Manual version 2.0*.

Högberg, J. L. (2006). Mixed mode cohesive law. *International Journal of Fracture*, 141(3-4):549–559.

Hillerborg, A., Modéer, M., and Petersson, P.-E. (1976). Analysis of crack formation and crack growth in concrete by means of fracture mechanics and finite elements. *Cement and Concrete Research*, 6(6):773–781.

Inglis, C. E. (1913). Stresses in a plate due to the presence of cracks and sharp corners. *Transactions of the Institution of Naval Architects*, 55:219–230.

Irwin, G. R. (1957). Analysis of stresses and strains near the end of a crack traversing a plate. *Journal of Applied Mechanics*, 24:361–364.

Jacobsen, J. S., Poulsen, P. N., and Olesen, J. F. (2010). Measurement and characterization of mixed mode fracture in concrete. In et al., B., editor, *Fracture Mechanics of Concrete and Concrete Structures - Recent Advances in Fracture Mechanics of Concrete*, pages 717–723. Korea Concrete Institute, Seoul.

Jacobsen, J. S., Poulsen, P. N., and Olesen, J. F. (2012a). Characterization of mixed mode crack opening in concrete. *Materials and Structures*, 45(1-2):107–122.

Jacobsen, J. S., Poulsen, P. N., Olesen, J. F., and Krabbenhoft, K. (2012b). Constitutive mixed mode model for cracks in concrete. *submitted to Engineering Fracture Mechanics*, –:–.

Jansen, D. C. and Shah, S. P. (1997). Effect of length on compressive strain softening of concrete. *Journal of Engineering Mechanics*, 123(1):25–35.

Jessen, J. C. (2006). Mixed mode fracture in concrete structures. Master's thesis, Department of Civil Engineering. Technical University of Denmark.

Jirásek, M. (2000). Comparative study on finite elements with embedded discontinuities. *Computer Methods in Applied Mechanics and Engineering*, 188(1-3):307–330.

Karihaloo, B. L. (1995). *Fracture mechanics and structural concrete*. Longman Scientific and Technical, Harlow.

Kragh-Poulsen, J.-C. (2009). Forskydningsbæreevnen af fiberarmerede betonbjælker. Master's thesis, Department of Civil Engineering, Technical University of Denmark.

Lens, L. N., Bittencourt, E., and d'Avila, V. M. R. (2009). Constitutive models for cohesive zones in mixed-mode fracture of plain concrete. *Engineering Fracture Mechanics*, 76(114):2281–2297.

Lourenço, P. B. and Rots, J. G. (1997). Multisurface interface model for analysis of masonry structures. *Journal of Engineering Mechanincs*, 123(7):660–668.

López, C. M., Carol, I., and Aguado, A. (2008a). Meso-structural study of concrete fracture using interface elements. I: numerical model and tensile behavior. *Materials and Structures*, 41(3):583–599.

López, C. M., Carol, I., and Aguado, A. (2008b). Meso-structural study of concrete fracture using interface elements. II: compression, biaxial and Brazilian test. *Materials and Structures*, 41(3):601–620.

Madsen, A. (2009). Cracks in concrete under repetitive load; experiments and modeling. Master's thesis, Department of Civil Engineering, Technical University of Denmark.

Mihai, I. C. and Jefferson, A. D. (2011). A material model for cementitious composite materials with an exterior point eshelby microcrack initiation criterion. *International Journal of Solids and Structures*, 48(24):3312–3325.

Montenegro, O. I., Carol, I., and Sfer, D. (2007). Characterization of confined mixed-mode fracture in concrete. In Carpinteri, A; Gambarova, P. F. G. P. G., editor, *Fracture Mechanics of Concrete and Concrete Structures (FraMCoS 6)*, volume 1-3, pages 257–261.

Moës, N., Dolbow, J., and Belytschko, T. (1999). A finite element method for crack growth without remeshing. *International Journal for Numerical Methods in Engineering*, 46(1):131–150.

Mougaard, J. F., Poulsen, P. N., and Nielsen, L. O. (2010). Modelling concrete structures applying xfem with a mixed mode constitutive model. In et al., B., editor, *Fracture Mechanics of Concrete and Concrete Structures : Recent Advances in Fracture Mechanics of Concrete*, pages 614–619. Korea Concrete Institute, Seoul.

Needleman, A. (1990). An analysis of tensile decohesion along an interface. *Journal of the Mechanics and Physics of Solids*, 38(3):289–324.

Nielsen, L. O., Mougaard, J. F., Jacobsen, J. S., and Poulsen, P. N. (2010). A mixed mode model for fracture in concrete. In et al., B., editor, *Fracture Mechanics of Concrete and Concrete Structures - Recent Advances in Fracture Mechanics of Concrete*, pages 231–237. Korea Concrete Institute, Seoul.

Nielsen, M. P. (1999). *Limit analysis and concrete plasticity.* CRC Press.

Nooru-Muhamed, M. B. (1992). *Mixed Mode Fracture of Concrete: An Experimental Approach.* PhD thesis, Delft University.

Petersen, R. B. (2008). Fracture mechanical analysis of reinforced concrete. Master's thesis, Department of Civil Engineering, Technical University of Denmark. Project no. 07-062.

Petersson, P.-E. (1981). *Crack Growth and Development of Fracture Zones in Plain Concrete and Similar Materials*. Report tvbm - 1006, Division of Building Materials, Lund Institute of Technology, Sweden.

Prandtl, L. (1933). A thought model for the fracture of brittle solids. *Zeitschrift für angewandte Mathematik und Mechanik*, 13:129–133. Translated by W.G. Knauss, June 2011, Caltech 105-50.

Reinhardt, H. W., Ozbolt, J., Xu, S., and Dinku, A. (1997). Shear of Structural Concrete Members and Pure Mode II Testing. *Advanced Cement Based Materials*, 5(3-4):75–85.

Reinhardt, H. W. and Xu, S. (2000). A practical testing approach to determine mode II fracture energy $G_{IIF}$ for concrete. *International Journal of Fracture*, 105(2):107–125.

RILEM (1985). Determination of the fracture energy of mortar and concrete by means of three-point bend tests on notched beams. *Materials and Structures*, 18(4):287–290. Prepared by TC50-FMC.

Roscoe, K. H. and Burland, J. B. (1968). On the generalized behavior of 'wet' clay. In *Engineering Plasticity (J. Heyman and F.A. Leckie, eds.), Cambridge University Press, Cambridge*.

Sanford, R. J. (2003). *Principles of fracture mechanics*. Prentice Hall, Upper Saddle River, NJ.

Spada, A., Giambanco, G., and Rizzo, P. (2009). Damage and plasticity at the interfaces in composite materials and structures. *Computer Methods in Applied Mechanics and Engineering*, 198(49-52):3884–3901.

Stang, H., Olesen, J. F., Poulsen, P. N., and Dick-Nielsen, L. (2007). On the application of cohesive crack modeling in cementitious materials. *Materials and Structures*, 40(4):365–374.

Østergaard, L. (2003). *Early-Age Fracture Mechanics and Cracking of Concrete, Experiments and Modelling*. PhD thesis, Department of Civil Engineering, Technical University of Denmark, Lyngby, Denmark.

Østergaard, L., Olesen, J. F., and Poulsen, P. N. (2007). Biaxial testing machine for mixed mode cracking of concrete. In *Fracture Mechanics of Concrete and Concrete Structures: New Trends in Fracture Mechanics of Concretes.*

Tada, H., Paris, P. C., and Irwin, G. R. (2000). *The Stress Analysis of Cracks Handbook, Third Edition*. ASME Press, New York, NY, 3 edition.

THK (2008). *THK General Catalog*, catalog no. 400-1e edition.

Walraven, J. C. and Reinhardt, H. W. (1981). Theory and experiments on the mechanical behavior of cracks in plain and reinforced concrete subjected to shear loading. *Heron*, 26(1).

Walter, R. and Olesen, J. F. (2008). Cohesive mixed mode fracture modelling and experiments. *Engineering Fracture Mechanics*, 75(18):5163–5176.

Wood, D. M. (1990). *Soil Behaviour and Critical State Soil Mechanics*. Cambridge University Press.

Yang, Z. J. and Chen, J. (2005). Finite element modelling of multiple cohesive discrete crack propagation in reinforced concrete beams. *Engineering Fracture Mechanics*, 72(14):2280–2297.

# Appended Papers

# Paper I

*Characterization of Mixed Mode Crack Opening in Concrete*

J.S. Jacobsen, P.N. Poulsen & J. F. Olesen

Published in: *Materials & Structures, 2012*

Materials and Structures (2012) 45:107–122
DOI 10.1617/s11527-011-9754-5

ORIGINAL ARTICLE

# Characterization of mixed mode crack opening in concrete

**J. S. Jacobsen · P. N. Poulsen · J. F. Olesen**

Received: 16 September 2010 / Accepted: 17 May 2011 / Published online: 24 June 2011


**Abstract** In real concrete structures cracks often open in mixed mode after their initiation. To capture the direct material behavior of a mixed mode crack opening a stiff biaxial testing machine, capable of imposing both normal and shear loads on a given crack area, has been applied. The opening and sliding components of the mixed mode displacement are measured using a custom made orthogonal gauge, and the measurements are used directly as the closed loop control signals. A double notch, concrete specimen is used for the crack investigation. The tests are divided into two steps, a pure Mode I opening step, where a macro crack is initiated in the specimen followed by the mixed mode opening step. The high stiffness of the set-up together with the closed control loop ensures a stable crack initiation followed by a controllable mixed mode opening. The deep notches result in a plane crack, only influenced by material aspects such as the aggregate size and concrete strength. Despite the occurrence of a few, local, secondary cracks during the mixed mode crack opening, the results can be treated as the mixed mode material point behavior of a crack in concrete. Results are reported for a range of mixed mode angles and for varying initial Mode I openings of the crack.

J. S. Jacobsen · P. N. Poulsen (✉) · J. F. Olesen
Department of Civil Engineering, Technical University of Denmark, Kongens Lyngby, Denmark
e-mail: pnp@byg.dtu.dk

**Keywords** Biaxial loading · Concrete · Mixed mode fracture · Constitutive behavior

## 1 Introduction

When the stresses in reinforced concrete structures exceed the concrete tensile capacity and thereby activate the reinforcement, cracks will initiate and propagate in the concrete and between concrete and reinforcement. In general the cracks will open in mixed mode after the initiation, i.e. a combined opening and sliding between the crack faces in an already established crack. For a realistic model of the general structural behavior or the detailed deterioration conditions concerning the structure, the modeling of the mixed mode crack opening is crucial. Thus, it is important to have consistent models for the crack behavior both in the concrete and in the interface between concrete and reinforcement.

The initial loading results in micro cracks in the concrete. For increasing load the micro cracks will start to coalesce and finally lead to the formation of macro cracks. As proposed by Hillerborg et al. [7] with the fictitious crack model, cracks in concrete can be simplified as a single crack in a concrete block. This idealized crack is then ascribed some constitutive behavior covering e.g. the geometric effects of the crack and the influence from the surrounding

micro cracking. Thus the cracking in concrete can be modeled at different scales. At the micro level, modeling aggregates, mortar and interlayer, geometric effects such as the roughness are included in the model. Thus, a constitutive Coulomb-like relation including cohesion, but without dilation, can be used. However, modeling at the micro scale is very demanding in terms of computational resources. So, modeling real size structures, it is advantageous to use a macro scale model where the micro cracking effects are included in the larger cracks through the constitutive crack model.

The crack initiation and the Mode I opening behavior are well described in the fictitious model by Hillerborg et al. [7]. The crack initiation is assumed to take place in pure Mode I, perpendicular to the largest principal stress. After the crack has been initiated there is nothing that prevents the crack faces from undergoing sliding as well, i.e. opening in mixed mode. A softening elastoplastic model for the opening-sliding mode has been proposed by Carol et al. [1]. The model is Coulomb-like and uses a fracture energy based damage parameter as control variable for the yield surface contraction, however, the model lacks reversible frictional behavior. The reversible frictional behavior is included in the model by Nielsen et al. [9] which is based on a new Coulomb-like yield surface. The model is elastoplastic with damage and has a cohesional and a frictional part. The frictional part includes deformation state dependency, where the friction decreases with crack opening and is restored with crack closure.

Experimental results from a direct determination of the mixed mode behavior form an essential basis for constitutive model development and verification. Previously significant biaxial set-ups have been presented by Nooru-Muhamed [10] and Hassanzadeh [5]. Nooru-Muhamed developed a setup in which three frames were used to induce the mixed mode loading condition. The stiffness of the set-up is not reported and the crack patterns reported by Nooru-Muhamed consist of cracks which initiate from each notch and propagate in a curved pattern without joining into a single crack. Such a crack pattern may only form an indirect basis for the determination of the mixed mode behavior. Hassanzadeh developed a set-up suited for mounting in a standard testing machine, and the mixed mode loading condition was established with a separate second axis. Hassanzadeh introduced a crack under Mode I opening followed by a mixed mode opening, which lead to a more direct determination of the mixed mode behavior. However, the crack patterns reported include some secondary cracking undermining the direct determination of the crack behavior. Again the stiffness of the set-up is not documented and there are humps on the descending branch, which normally are associated with insufficient stiffness, see e.g. Hillerborg [6].

Another biaxial set-up was presented by Østergaard et al. [14] and consists of a stiff support structure and a separate second axis. The mixed mode loading condition is established by mounting both the support structure and the second axis in a standard testing machine. Østergaard et al. tried two different shaped concrete specimens. First they used a dog bone shaped specimen, but the geometry lead to multiple cracks and an initial cracking, which was very difficult to control. The second specimen was a double notch concrete block which had a side length of 150 mm and a depth of 100 mm. The relatively high specimen introduced a large amount of elastic energy in the set-up, and the larger elastic energy made the fracture initiation unstable and extremely difficult to control. Therefore, according to the stiffness considerations, the specimen dimensions were reduced by Petersen [11] to the dimensions $150 \times 80 \times 75$ mm$^3$ with a notch depth of 37.5 mm, see Fig. 1. The significant lower height reduced the amount of elastic energy. Both Østergaard et al. and Petersen used the piston displacements as the control signal. According to Petersen this resulted in a large deviation between the prescribed ratio between opening and sliding, i.e. the mixed mode angle, and the actual angle achieved. The large deviation made it

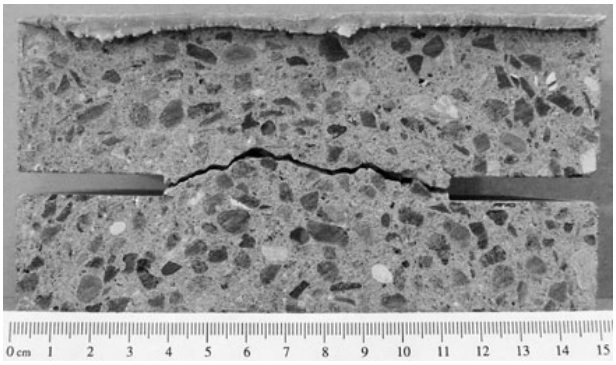


**Fig. 1** Test specimen in the configuration with short notches. Curved crack path between notches

difficult to control the test and made an inverse analysis of the test results necessary.

Another type of specimen partly concrete, partly steel has also been used to investigate the mixed mode behavior, Walter and Olesen [16]. The specimen is inserted in a standard uniaxial testing machine, and the level of mixed mode is prescribed by the inclination of the separation between the two materials with respect to the loading direction. However, for larger mixed mode angles the simple uniaxial set-up results in long specimens with low stiffness and thereby an unstable testing. Pre-notched beams in 3 point bending have also been used to characterize cracks in concrete under mixed mode loading, see e.g. Carpinteri and Brighenti [2]. The level of mixed mode is dictated by the position of the notch with respect to the three supports/loadings. The beam test gives the beam response to the applied loading but it is very difficult to interpret the mixed mode material behavior of the crack, and the test can only provide an indirect crack interpretation. Reinhardt et al. [12] and Reinhardt and Xu [13] suggest a method for Mode II testing in pure concrete. A shear stress state is establish by loading one side of a double notch specimen in compression, parallel to the notch direction, while the other side is unsupported. The method investigates the Mode II fracture toughness, however, since the specimen is not pre-cracked the mixed mode behavior of a crack is not revealed.

In order to capture the direct material behavior of mixed mode fracture, a biaxial testing machine, which is capable of imposing both normal and shear loads on a given crack area, is needed. This paper presents such a set-up and a series of mixed mode results for an already established crack in a double notch, concrete specimen. The present set-up is an enhancement of the set-up by Østergaard et al. [14], where the control is changed such that the vertical and the horizontal axis can be controlled independently in a closed control loop. Referring to Gettu et al. [3], a more stable and robust fracture control is obtained by using the actual opening and sliding over the ligament in the control. The measurements of the opening and sliding are obtained by using a custom made gauge rail mounted on the specimen.

For small initial openings followed by a mixed mode loading, the specimen dimensions by Petersen [11] clearly result in structural like response with either a curved crack path, as in Fig. 1, or a secondary failure in a new inclined crack, running away from the ligament area. By sawing the notches deeper to the present depth of 55 mm, each test results in a single, primary crack between the two notches and a reduced amount of secondary cracks. Further, the deeper notches reduce the structural effects and result in a plane crack, allowing for a more direct material interpretation. Altogether the present set-up gives reliable material tests for a direct characterization of mixed mode fracture in concrete.

The following section presents the test set-up in the new configuration, the specimen and the applied concrete, the orthogonal gauge rails used for mounting the clip gauges in a close vicinity of the crack and the test procedure.

Characteristic results from mixed mode tests, displaying relevant mixed mode ratios between opening and sliding for a single crack, are presented and analyzed.

## 2 Test set-up

The idea with the set-up is to measure the material point behavior for a single crack in a pure concrete specimen. It is believed that the crack initiation takes places in pure Mode I, perpendicular to the largest principal stress. But after the initiation the crack can be exposed to both opening and sliding, i.e. mixed mode. In the fictitious crack model by Hillerborg et al. [7] the initiated crack, or the macro crack, is assumed to be formed when the largest principal stress over the crack area reaches the tensile capacity. Hillerborg et al. states that actually the crack is still an accumulation of micro cracks and that the coalescence of micro cracks into a macro crack happens once the cohesion is exhausted. Though the macro crack is observed by Østergaard et al. [14] to be formed before the cohesion is exhausted. Østergaard et al. report that the initial crack band between the notches, i.e. the macro crack, is established when the tension load has decreased to around 50–70 % of the maximum tensile capacity. So, to make a proper mixed mode crack test of and already established crack, the test must be divided in to two steps, see Fig. 2. The first step is the crack initiation in a pure Mode I opening until the macro crack is fully initiated, followed by the second step, the mixed mode opening.

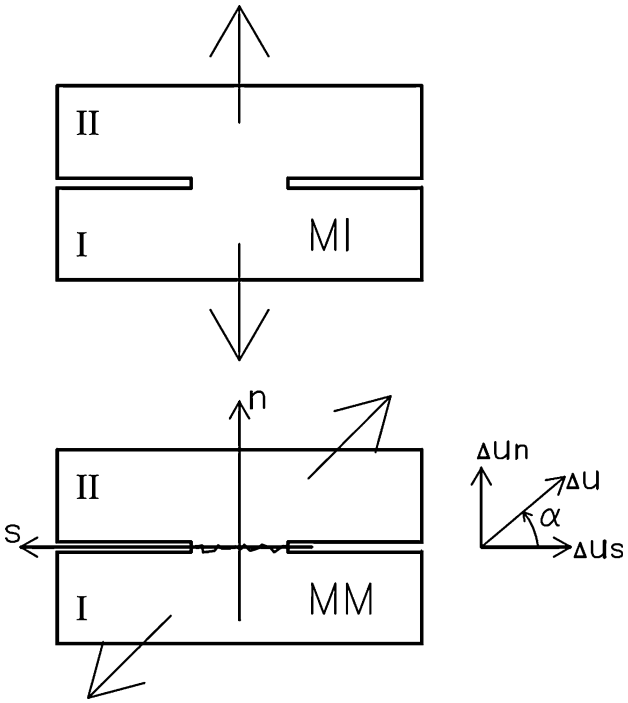


**Fig. 2** The two test steps, the Mode I opening step, MI, and the mixed mode step, MM. At the mixed mode step the local (*n,s*)-coordinate system and direction of positive relative displacements between the two specimen parts, I and II, are indicated and the mixed mode angle $\alpha$ is defined

The biaxial setup by Østergaard et al. [14] has been enhanced with a new improved closed control loop and is modified to the new specimen

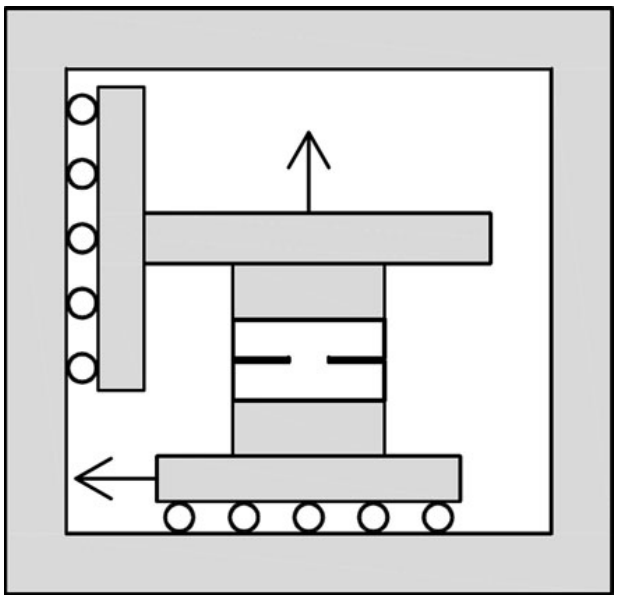

**Fig. 3** The principle idea of the set-up with the stiff frame supporting the motions of the two axes. Displacement directions are indicated

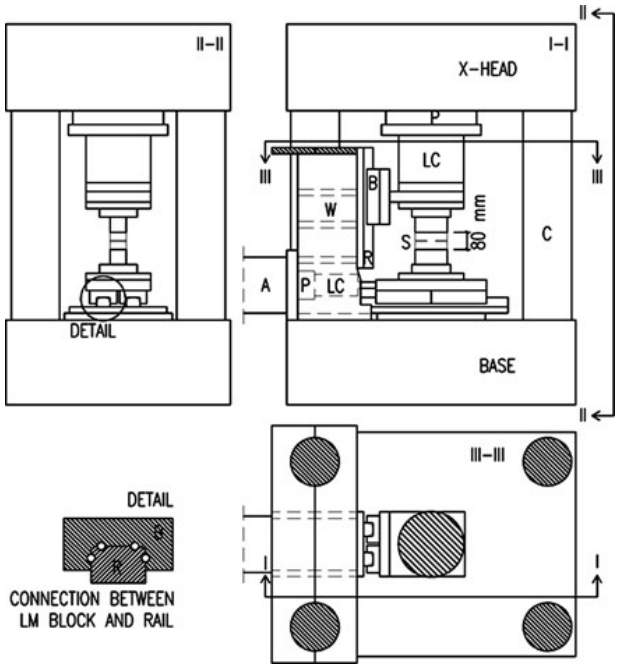


**Fig. 4** Sketch of biaxial set-up. *A* actuator, *P* piston, *LC* load cell, *S* specimen, *C* column, *B* linear motion block (LM block), *R* Rail, *W* web. Some background details are left out for clarity

dimensions, but the principle build up is the same. The set-up consists of a four column 5 MN universal testing machine and then a built in second axis. The four column 5 MN testing machine ensures a stiff frame for the set-up as illustrated on Fig. 3, and supports the motions in the two perpendicular directions. The support structure ensures that the two axes are geometrically independent, and the set-up has separate control valves for the hydraulic supply for the two axes.

## 2.1 Testing machine

Figure 4 shows the overall structure of the machine. The machine consists of two independent actuators and is controlled by a multi-axial Instron 8800 control unit. A four column Instron 5 MN universal testing machine is the basis of the set-up, giving a very stiff and full functional vertical axis of loading. The horizontal axis is designed especially for the set-up and built into a very stiff support structure, such that the shear load is carried from the actuator through the specimen and back to the actuator through compression in the support structure. Thereby this custom made bi-axial hydraulic testing machine has a considerable rotational stiffness. The

stiffness was measured by Østergaard et al. [14] and is given as the translational stiffness $K_{m,t} = 500$ kN/mm and the rotational stiffness as $K_{m,r} = 8000$ kNm/rad. Compared to the actual maximum load used in the test, which is between 10–20 kN, the stiffness is considerable. Further, keeping in mind that the set-up has a closed control loop, the measuring length and thereby the impact from the elasticity of the set-up is negligible.

The motions of the test specimen are conducted through two slides, a horizontal and a vertical. The slides, which can be seen in Fig. 5, are constructed from low friction and high precision THK linear motion systems with oversized balls in the closed ball bearings [15]. All bolted connections in the set-up are pre-stressed such that no slip between the steel plates can occur during the experiment. The specimen is glued into the set-up using sandblasted steel blocks. During the gluing process the set-up is in load control, avoiding that stresses arise in the specimen during the hardening.

**Fig. 5** Test set-up showing a glued in test specimen, vertical load cell, support structure and the slides in both vertical and horizontal direction

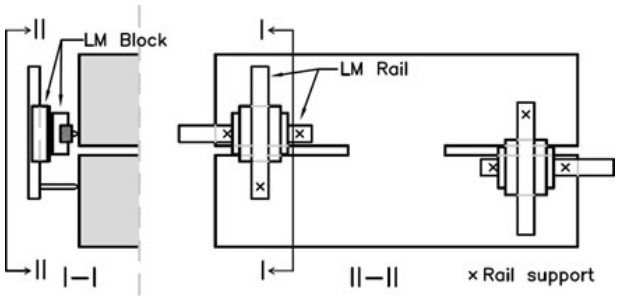


**Fig. 6** Principle sketch of gauges rails with Linear Motion (LM) rails, LM blocks and indication of rail supports

The control in the present set-up is improved such that the vertical and the horizontal axes can be controlled independently by separate closed loop controls. Measurements of the opening and sliding are obtained by using specially designed gauge rails mounted on the specimen, see Fig. 6. In the vertical direction the load is measured using the load cell from the four column testing machine, while the horizontal load is measured by a load cell placed in immediate continuation of the horizontal slide, see Fig. 4. The set-up has been designed for 500 kN in the vertical direction and 250 kN in the horizontal direction. In the present set-up however, the load cells limit the capacity to 100 and 50 kN in the vertical and horizontal direction, respectively, giving a better load resolution at lower loads. The testing machine is capable of imposing both normal and shear loads on a given crack area and together with the closed control loop, the set-up has proven to give an accurate determination of the mixed mode behavior in concrete.

## 2.2 Test specimen

In Fig. 5 the test specimen is shown in place in the testing machine. The double notch test specimen has a width of 150 mm, a height of 80 mm and a depth of 75 mm. The notches are cut from the side and have a depth of 55 mm. Thereby the ligament area is $40 \times 75$ mm$^2$. The specimens are cut from a beam with a cross section of $150 \times 150$ mm$^2$ and a length of 600 mm. The deep notches ensure that a single, fairly plane crack develops between the two notches, ensuring that results can be considered as material point information.

The concrete has a maximum aggregate size of 8 mm and a predicted 28 days strength of 30 MPa,

**Table 1** Mix design

| Mix | kg/m$^3$ |
|---|---|
| Cement (portland basis) | 290 |
| Water | 184 |
| Sand, 00–04 mm | 933.8 |
| Aggregates, 04–08 mm | 928.5 |

the mix design is shown in Table 1. The beams were de-molded after 24 h and then cured in 100 % humidity at 20°C for 40 days. The testing was carried out in between 45 and 65 days from the mixing day, and the compression strength was measured in a standard cylinder test to 41 MPa, 42 days after the mixing.

### 2.3 Gauge rails

A local $(n,s)$-coordinate system is introduced according to Fig. 2. Fracture in the ligament divides the specimen in two parts, I and II, respectively. Relative displacements between the two parts, $\Delta u_n$ and $\Delta u_s$ in the $n$ and the negative $s$ direction, respectively, are defined as

$$\begin{aligned} \Delta u_n &= u_n^{II} - u_n^I \\ \Delta u_s &= u_s^I - u_s^{II} \end{aligned} \tag{1}$$

In the test the relative displacement $\Delta u$ is assumed to be constant along the ligament. The relative displacements are measured by four Clip Gauges (CGs) mounted on the specimen using two custom made orthogonal gauge rails placed across the two notches. In pair the CGs measure the deformation in vertical and horizontal direction, respectively. The CGs allow for independent control of the vertical and horizontal axis in a closed control loop using the mean signal in respective directions as the response signal.

Figure 6 shows the principle structure of the orthogonal gauge rails, and Fig. 7 shows gauge rails and CGs in use. Two small, high precision THK miniature Type LM Guides, [15], are used in each orthogonal gauge rail. Low friction oversized ball bearings together with the CGs allow for the determination of displacements smaller than 1 μm. The rails are assembled orthogonally through the blocks top on top, and a specially designed house around the blocks together with modified end blocks enables the attachment of CGs. At the front of the specimen the

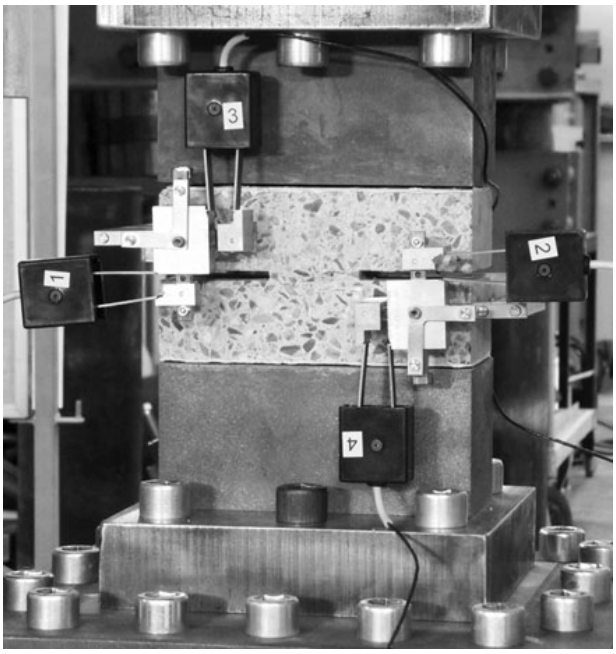


**Fig. 7** Close view of test specimen, gauges rails and clip gauges

gauge rail has three supports, two at one side of the notch supporting the horizontal rail and one at the opposite side supporting the vertical rail. The two horizontal supports and the vertical support can move independently, allowing for the measuring of the relative displacement in both directions between the two parts of the specimen. The gauge rail is kept in place by an aluminum arm clamping around the specimen. At the back, the aluminum arm's point support is placed close to the centre of the triangle defined by the three front supports.

As illustrated by Madsen [8], who used a pair of CGs mounted directly on the specimen, the test set-up is fully capable of performing full uniaxial opening histories and cyclic loading histories on the actual concrete specimens. Further, with the gauge rails the following illustrates that the set-up enables stable closed loop controlled mixed mode testing.

### 2.4 Test procedure

Initially a crack is introduced between the notches by a pure Mode I opening, $\Delta u_s = 0$, and the crack is opened to a specified crack opening measured by the CGs. After the initiation of the crack the specimen can be exposed to both Mode I and II opening introducing a mixed mode opening of the crack.

The mixed mode opening angle, $\alpha$ in Fig. 2, is defined as the angle between the horizontal plane and the relative displacement, i.e.

$$\tan(\alpha) = \frac{\Delta u_n}{\Delta u_s} \quad (2)$$

The initial, vertical displacement velocity is 0.1 μm/s, while the mixed mode opening pace is gradually increased to a final opening pace of 2.0 μm/s. Displacement velocity is set such that the peak load corresponding to $f_t$ is captured in around 60 s and the test in total is finished in around 600 s. Slow opening pace ensures a more stable crack initiation, while the total time is limited in an attempt to limit the influence of viscoelastic effects.

### 2.5 Aramis

Along with the CG signals the displacements are recorded by the high-resolution digital image correlation system Aramis by GOM mbH [4]. The Aramis system is a 3D photometric equipment and uses digital stereo photographing and subsequent triangulation to determine 3D displacements on the observed surface of the specimen. The system enables determination of the displacement field in a close vicinity of the crack. The four megapixels picture, with side lengths h × h, is divided into small regions called facets, which here consist of 15 × 15 pixels. During the analysis the movement and deformation of the facets is registered and assembled. This analysis gives a displacement field of the surface, which e.g. can be post-processed into a strain field. Figure 9a–e show typical results from the Aramis system. The displacement resolution is approximately $h \times 10^{-5}$ and in the present case $h = 120$ mm. The strain calculation is based on the engineering strain determined from the relative displacement between the facets.

## 3 Results

### 3.1 Load opening displacement

At first the test specimen is loaded in pure tension with respect to the ligament between the two notches. This Mode I loading initiates a crack between the notches and results in a characteristic opening-displacement response shown in Fig. 8. The normal stress $\sigma$, defined as the measured normal load divided by the ligament area, is plotted as function of the opening displacement $\Delta u_n$ for different test specimens. During the loading in the elastic domain, the different tests almost coincide, while their maximum points are scattered over an interval of 0.5 MPa. After the maximum point the same scatter interval continues during the fracture initiation. The scatter is most likely caused by the natural variation of concrete properties. In four of the five cases the test set-up is able to capture the softening branch and in the last case, for an additional opening, the softening branch is recaptured. These opening curves prove the sufficient stiffness of the test set-up. Starting the mixed mode at an opening of $\Delta u_n = 0.025$ mm clearly results in a drop in the normal stress but also some more noise caused by the combined loading in mixed mode. Further, it is shown that starting the mixed mode displacement at an opening of $\Delta u_n = 0.025$ mm corresponds to a load level of 30–40 % of $f_t$.

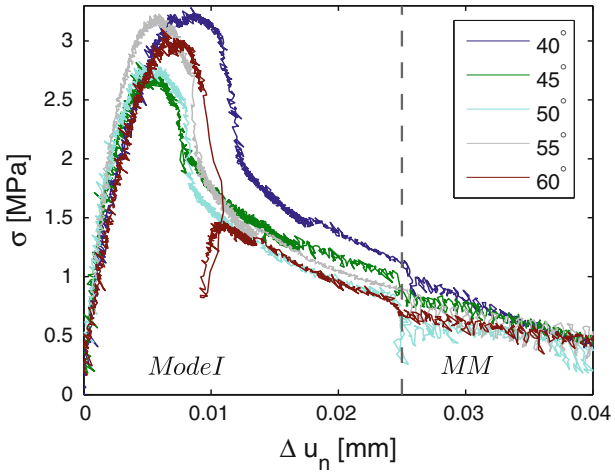


**Fig. 8** Initial load opening displacement curves for five different mixed mode angles. The *dashed line* indicates the start of mixed mode displacement (MM)

The nature of the crack surface introduces some scatter. At a given opening, the surface has a certain shear capacity. At a larger opening or caused by some damage in the crack surface, e.g. a rotating grain, the shear capacity may be exceeded. Exceeding the shear capacity introduces a sudden but limited drop in the load level, and thereby some scatter in the results. The scatter is most distinct in the mixed mode phase, however, since the crack is not completely plane, the

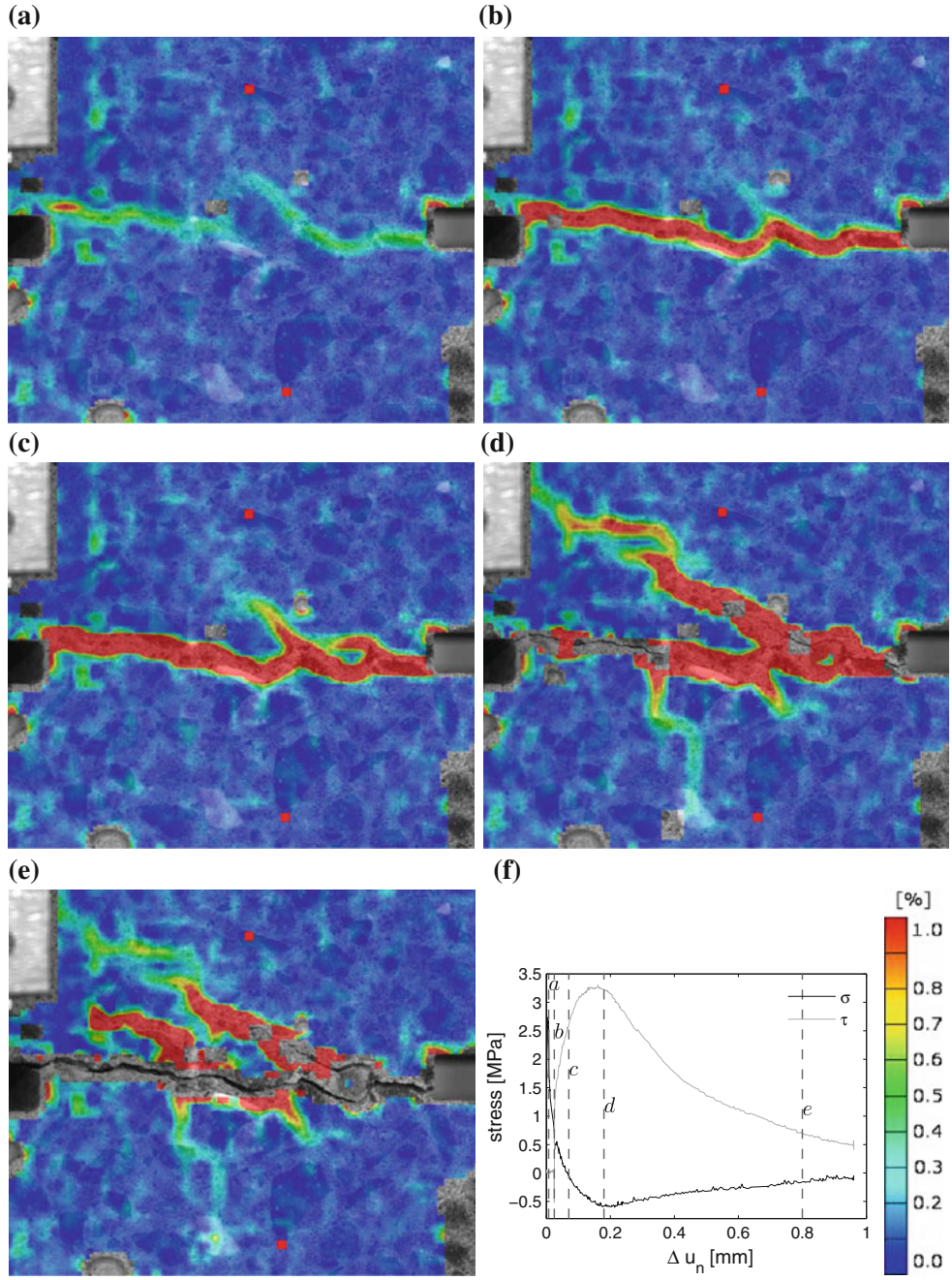


**Fig. 9** Crack initiation and mixed mode opening for the initial opening $\Delta u_n = 0.025$ mm and the mixed mode angle $\alpha = 50°$. **a** Crack initiation for mixed mode angle of $\alpha = 50°$. Maximum tension, crack not fully initiated. **b** Start mixed mode, crack fully localized. **c** Normal stress changing from tension to compression, initiation of secondary cracks. **d** Maximum compression and shear. Propagating secondary cracks and visible opening crack. **e** Final crack pattern with clear primary crack and some secondary fracture primary localized at the right notch. **f** Stress opening relation indicating test progress for the different Aramis pictures, **a**–**e**. The strain scale for Aramis pictures is made transparent, which makes it possible to see the location of aggregates

frictional scatter is also present in the Mode I. The noise in the load-displacement curves in Fig. 8 is very limited during the Mode I opening, while the mixed mode opening increases the amount of scatter.

Besides the frictionally related scatter some electronic noise may also occur in the results. The two axes are hydraulically independent and connected only through the specimen. Noise recognized is

primarily caused by tuning difficulties with the closed loop control. Stiffness of the specimen changes remarkably during the test, which makes it difficult to find a single tuning level for the entire test, and some noise is expected. The noise is reduced after the peak by an increase in displacement rate and thereby an indirect change in the tuning of the closed control loop signal. Figure 8 shows the original test data while the following mixed mode results have been filtered to emphasize the overall mixed mode behavior. The filtering is based on a running mean method, where the maximum shear load in an interval is found. The interval length corresponds to 20 data records of raw data, approximately equal to 2 s of testing time. These 20 data records are reduced to the one representing the maximum shear load.

### 3.2 Aramis example

The photometric system Aramis is used to locate the crack pattern at the specimen surface, see Sect. 2.5 for details about Aramis. Figure 9 shows the fracture propagation during a mixed mode test. The discrete cracking is illustrated by the use of the largest principal strain registered on the surface. The notion of strain is normally not valid in combination with localized cracking, and the strain measure is only for visualization purposes. After the crack initiation the specimen is displaced in a mixed mode angle of $\alpha = 50°$, giving a bit more opening than shear. Figure 9f shows the normal stress $\sigma$ and the shear stress $\tau$ plotted as functions of the opening displacement $\Delta u_n$. Stress stages for the matching pictures are indicated. The average stresses $\sigma$ and $\tau$ are defined as the measured normal and shear load divided by the ligament area, respectively.

The first picture, Fig. 9a, shows the fracture development at peak load and clearly indicates that the macro crack between the notches is not fully established. Same observation is made by Petersen [11] and by Østergaard et al. [14], who state that a clear crack establishment is not obtained until the load has decreased by 20–50% of the peak load. As shown in Fig. 8, the load, at the beginning of mixed mode displacement, is reduced to 30–40% of the peak load. At this displacement level clear crack localization is obtained, see Fig. 9b. The test is displacement controlled, so after some mixed mode loading the dilational effects will shift the normal load from tension to compression and thereby build up some confinement over the ligament area. Figure 9c is snapped directly at this transition and despite a clear, primary crack some secondary cracks tend to grow in crack planes inclined with respect to the ligament area. At maximum compression multiple secondary cracks have formed, see Fig. 9d, but for the fracture propagation a clear primary crack between the two notches is still seen. The last picture, Fig. 9e, shows the final fracture development for loads returning to zero, and a clear fracture area is localized representing some secondary cracks and a distinct primary opening crack.

As seen in Fig. 9 the crack between the notches is not completely straight and the crack pattern also includes some secondary cracking. The crack path is influenced by the aggregates and the current stress state. The sliding introduces some secondary cracks in one or more crack planes located outside the ligament area. If the sliding is dominant compared to the opening, one or more of the secondary cracks may end up being the primary one and the specimen may fail due to a secondary fracture. In this case the test has failed. But if the end state consists of a primary crack between the two notches, possibly with some local secondary cracking, the results are considered as the material information for a single, plane crack.

### 3.3 Crack morphology

The test specimens are cast from a concrete with varying aggregate size up to 8 mm, and the concrete as a material is far from being homogenous. Therefore a completely straight crack path will not be possible. However, the crack path in the present tests is almost straight, with a variation smaller than or equal to the notch height of 4 mm, see e.g. Fig. 9e for 50° mixed mode and Fig. 10 for 40° mixed mode. This fracture localization between the notches is a characteristic of the new test specimen, and structural effects obtained with the old test specimen by Petersen [11], see Fig. 1, are avoided by the new deeper notches. Having a closer view of the crack surface, see Fig. 11 from the 40° mixed mode test, it is clear that the fracture is localized in between the aggregates. Thereby the crack surface is influenced by the aggregate size but without the earlier reported structural effects. This plane fracture localization ensures that results may be considered as material point information.

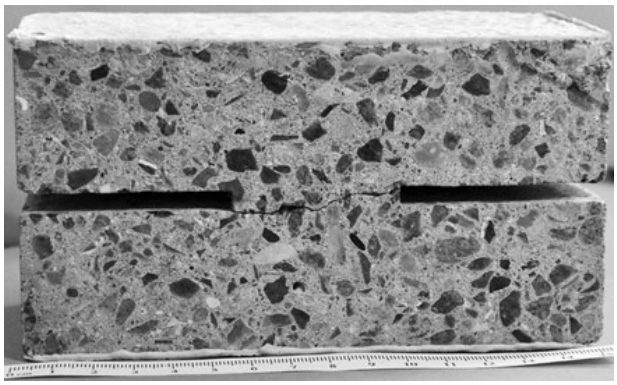

**Fig. 10** Final crack path for the 40° mixed mode test

**Fig. 11** Close view of the crack surface for the 40° mixed mode test

### 3.4 Mixed mode behavior

The test combinations of initial openings and mixed mode angles are listed in Table 2. The combinations cover results ranging from an almost pure Mode I opening, $(\Delta u_n, \alpha) = (0.100\ \text{mm}, 50°)$, to an ending failure in one of the secondary cracks, $(\Delta u_n, \alpha) = (0.015, 60°)$. The secondary failure results in a new inclined primary crack, running away from the ligament area. For a larger initial opening the specimen can be displaced in a smaller mixed mode angle without introducing secondary cracks, while a smaller initial opening needs a larger mixed mode angle to avoid the secondary failure. The different tests indicate a band for combinations of interest, i.e. combinations where the mixed mode angle for the given initial opening is small enough to introduce some shear stresses and still high enough to avoid a secondary failure. The combinations (0.015, 60°), (0.020, 55°) and (0.025, 45°) almost result in a secondary failure with (0.015, 60°) actually changing from a ligament crack to a secondary fracture during the test. In the other end the dilation caused by the sliding is balanced by the simultaneous crack opening, so the combinations (0.025, 60°), (0.040, 55°) and (0.100, 50°) almost do not encounter any build up of compressive stresses.

**Table 2** Mixed mode test program, initial opening $\Delta u_n$ and mixed mode angle $\alpha$

| $\Delta u_n$ [mm] | | | | | |
|---|---|---|---|---|---|
| $\alpha$ | 0.015 | 0.020 | 0.025 | 0.040 | 0.100 |
| 40° | | | ⊣ | ⊣ | ⊣ |
| 45° | | | ⊣ | ⊣ | ⊣ |
| 50° | | ⊣ | ⊣ | ⊣ | — |
| 55° | | ⊣ | ⊣ | — | |
| 60° | ⊣ | ⊣ | — | | |

— plane crack, ⊣ plane crack with local secondary cracking, ⊣ dominant secondary crack

Figures 12 and 13 show the mixed mode behavior for different combinations of initial opening and mixed mode angle, in Fig. 12 for constant initial opening of $\Delta u_n = 0.025$ mm and in Fig. 13 for constant mixed mode angle of $\alpha = 50°$. Together with the results listed in the Appendix A the figures represent the results for the combinations in Table 2.

In Fig. 12 the mixed mode behavior is presented for five specimens opened at five different mixed mode angles from 40° to 60° dictated by the closed control loop. In Fig. 12c the initial opening of$(\Delta u_n, \Delta u_s) = (0.025, 0)$ mm in each test is recognized and after the opening the five different mixed mode angles can be read from the figure. Deformations in Fig. 12c are measured by the CG and are the actual responses to the demand, and even before the filtering they were almost without any noise. Figure 12d is the load opening displacement similar to Fig. 8 but with interchanged axes and a considerable larger range of opening. The natural variation of the concrete is reflected in the variation in the tension strength in Fig. 8. So it is expected to see a scatter in both the compression stresses and the shear stresses. But for the normal stress, there is a clear correlation between the level of compression and the size of the mixed mode angle. Lowered mixed mode angle is equal to a higher level of sliding and thereby intensified dilational effects, which in the displacement controlled test result in more compression.

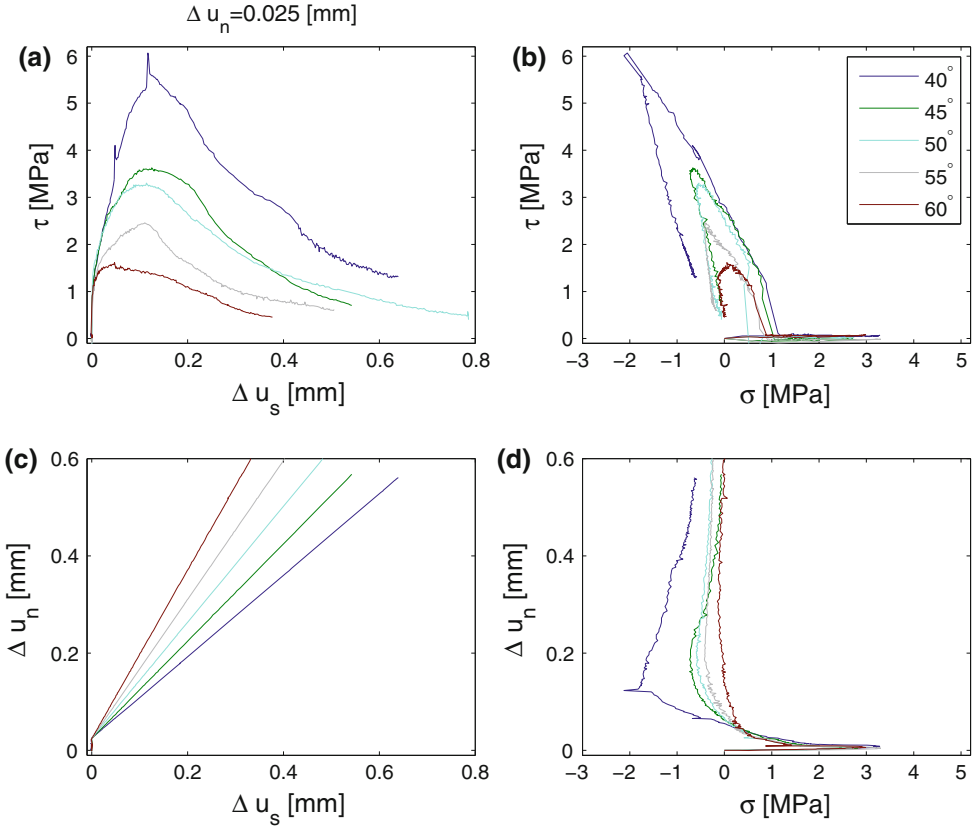


**Fig. 12** Mixed mode test results for five different mixed mode angles with the same initial opening of $\Delta u_n = 0.025$ mm

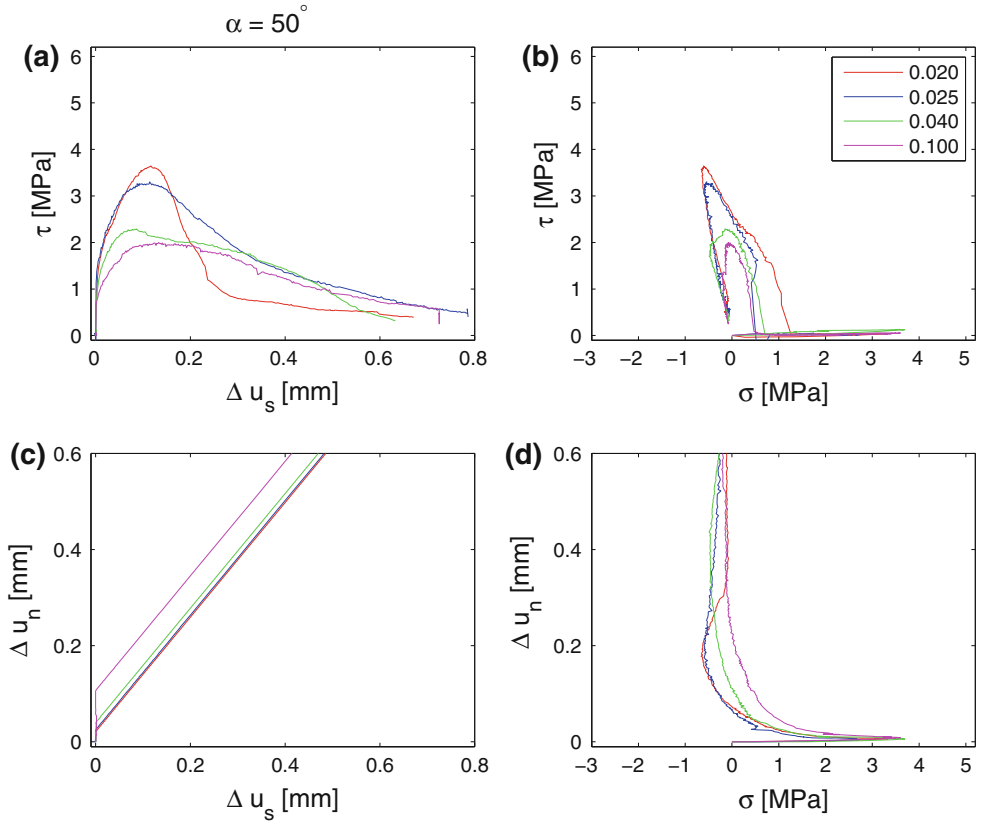


**Fig. 13** Mixed mode test results for four different initial openings and the same mixed mode angle of 50°

The 40° has the most compression followed by 45°, 50° and 55° while the 60° test has a compression level at almost zero. Responses for 45° and 50° are roughly identical, which probably is an effect of the natural variation of concrete properties. The spike for 40° at maximum compression is caused by a change of fracture from a beginning shear crack away from the ligament to a more significant opening crack. Similar to Fig. 12d for normal stress, the shear stress level, shown together with the shear displacement in Fig. 12a, increases for lowered mixed mode angle where the sliding starts to dominate. The displacement controlled test introduces some confinement over the ligament and the ligament can thereby transfer a considerable amount of shear stresses, in these tests up to twice as high as the tensile strength. Figure 12b combines the results from the three other plots and shows the shear stress, $\tau$, as function of the normal stress, $\sigma$. Despite the few tests there is a clear tendency in the mixed mode behavior, with almost straight lines in both loading and unloading before and after the peak in the stress-plot, respectively.

In Fig. 13 the mixed mode behavior is presented for four specimens with varying initial opening from $\Delta u_n = 0.020$ mm to $\Delta u_n = 0.100$mm dictated by the closed control loop. The different initial openings together with the constant mixed mode opening of 50°, can be recognized from Fig. 13c. From Fig. 13a and d it is clear that the highest level of shear and compression is obtained for the smallest initial opening, and that the stress level drops for increasing initial opening, with almost no compression for $\Delta u_n = 0.100$ mm. The normal stress level in Fig. 13d almost coincides for the two tests $\Delta u_n = 0.020$ mm and $\Delta u_n = 0.025$ mm. Even though the difference between the two initial openings is not large it does represent a significant change of cohesion. Therefore the almost coinciding curves are probably a consequence of the natural variation of concrete properties. In the $\sigma$, $\tau$-plot in Fig. 13b again there is a clear tendency in the mixed mode behavior, despite the few tests. The stress level increases for decreasing initial opening, and again there are almost straight lines in both loading and unloading before and after the peak in the stress-plot, respectively.

For the tests with constant initial opening, the 40° test with the relative large amount of sliding almost results in a shear fracture. The 60° test with a relatively large amount of opening is almost without any mixed mode effects. Similar to the tests with constant mixed mode angle the large initial opening of $\Delta u_n = 0.100$ mm is almost without any mixed mode effects, while it was impossible to conduct the same test for an initial opening of $\Delta u_n = 0.015$ mm. The five tested mixed mode angles for the chosen initial opening, and the four different initial openings for the same mixed mode angle, cover the relevant test area from nearly encountering a shear fracture to an almost pure Mode I opening. In the stress plots in Figs. 12b and 13b the stress paths in mixed mode have almost straight lines in both loading and unloading, a Coulomb-like behavior. Overall there is a clear tendency that the shear level and the compression level raises for both decreasing initial opening and for decreasing mixed mode angle.

## 4 Conclusion

The mixed mode opening behavior of a crack is measured and the results are used to characterize the mixed mode material point behavior of a crack in concrete. The tests are conducted in two steps, a pure Mode I opening step, where a macro crack is initiated in a double notch specimen followed by the mixed mode opening step, i.e. a combined opening and sliding of the crack. A biaxial testing machine consisting of a 5 MN universal testing machine and a built-in second axis has been applied for the mixed mode measurements. The set-up has a new enhanced closed control loop with the relative opening and sliding of the crack as the control signals. The opening and the sliding of the crack are measured by clip gauges using a custom made orthogonal gauge rail mounted on the specimen. The concrete specimens are designed with deep notches and are tested both for varying initial opening and for varying mixed mode angle.

Earlier reported biaxial set-ups have a lack of stiffness and the results often need to be analyzed through an inverse analysis to achieve the actual mixed mode material behavior. In Mode I, the present set-up is sufficiently stiff and, together with the closed control loop, it is capable of determining the crack initiation. The orthogonal gauge rail results in a direct interpretation of the mixed mode crack opening process, ensuring that the achieved response over the ligament is equal to the prescribed mixed mode angle.

As a result of the specimen design and the set-up design, the crack surface is even and governed by material aspects like aggregate size and concrete strength rather than structural effects. Subsequent investigation of the total crack surface supports this interpretation. Despite the occurrence of a few local secondary cracks during the fracture development, the crack determination is representative of a single crack under mixed mode displacement; and the results are considered to be the mixed mode material point behavior of a crack in concrete.

A relative sliding between the two crack surfaces introduces dilational effects, which in the displacement controlled test results in some confinement over the crack. The confinement ensures that a considerable amount of shear stresses can be transferred over the crack, here up to twice as high as the tensile strength. A high level of shear and compression is obtained for a small initial opening and for a small mixed mode angle. The stress paths in mixed mode act in a Coulomb-like behavior with almost straight lines in both loading and unloading. Further, there is a clear tendency that the shear level and the compression level raises for both decreasing initial opening and for decreasing mixed mode angle.

The crack determination from the material tests is considered representative of a single crack in mixed mode loading, and the results are well suited as a direct determined basis for the model development of a mixed mode material model. Based on the straight stress paths in mixed mode, it seems reasonable to represent the results by a Coulomb-like material model. Further, the results can be used to validate and calibrate already existing macro and micro mechanical material models for cracks in concrete.

## 5 Appendix A: Complete mixed mode results

The following figures together with Figs. 12 and 13 show the measured mixed mode behavior.

Figure 14 shows tests for the 40° mixed mode angle at three different initial openings. In the stress

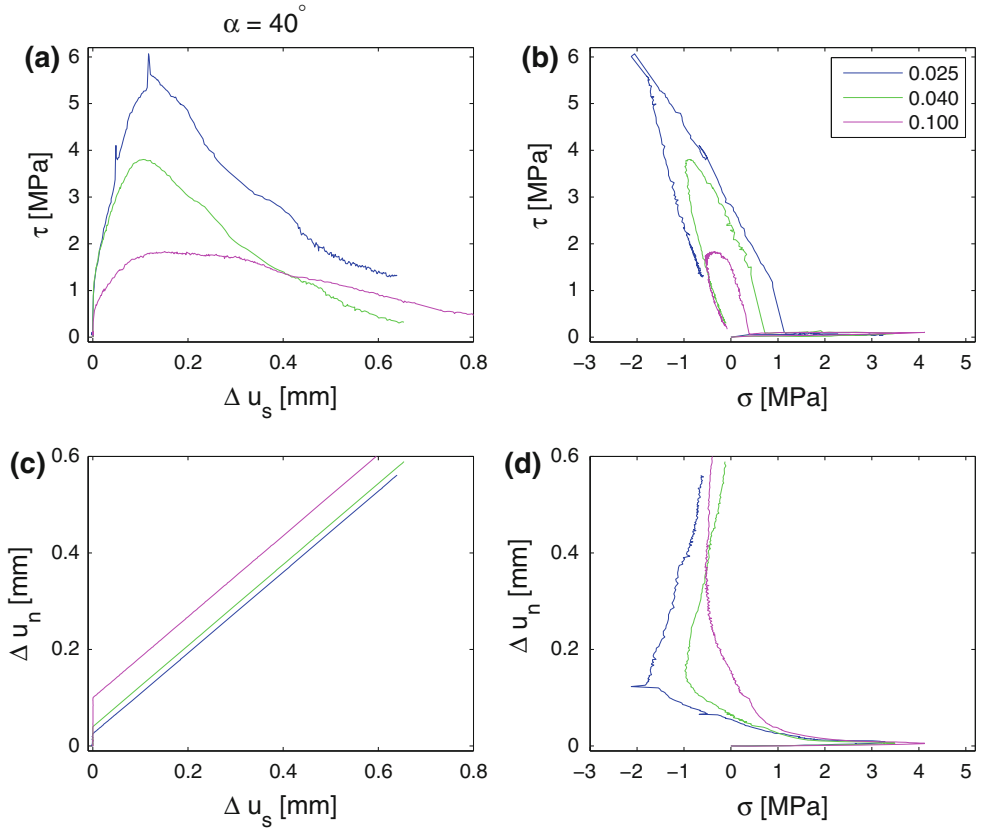


**Fig. 14** Mixed mode test results for three different initial openings at the same mixed mode angle of 40°

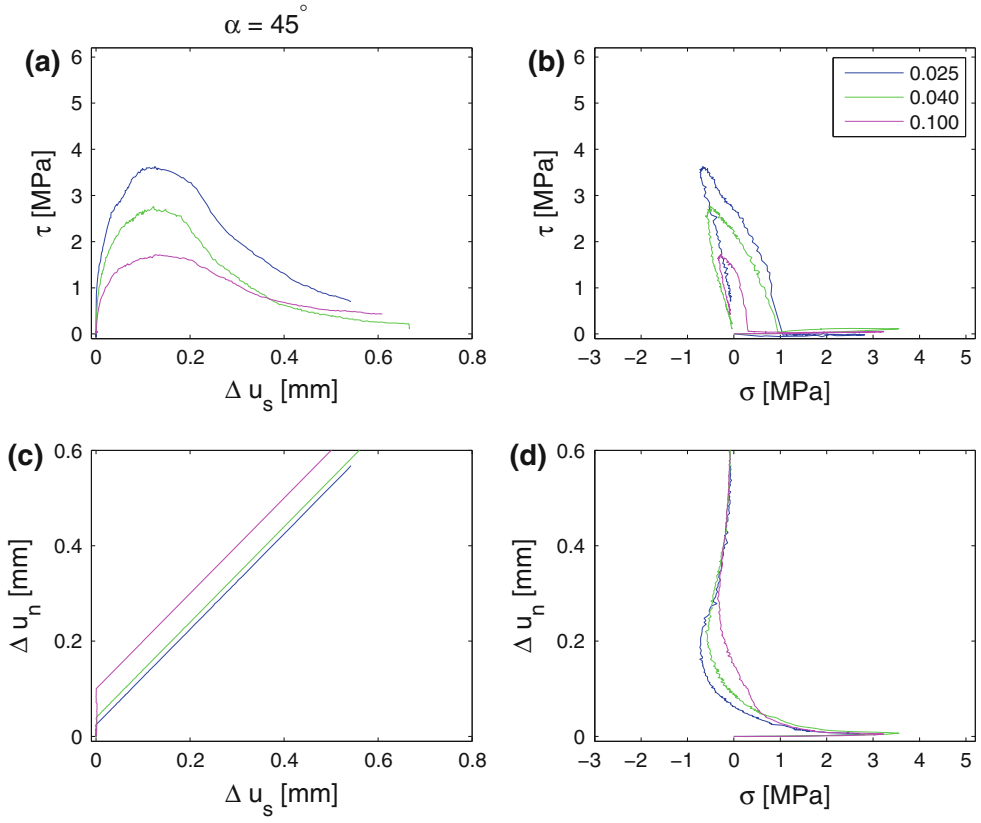


**Fig. 15** Mixed mode test results for three different initial openings at the same mixed mode angle of 45°

**Fig. 16** Mixed mode test results for three different initial openings at the same mixed mode angle of 55°

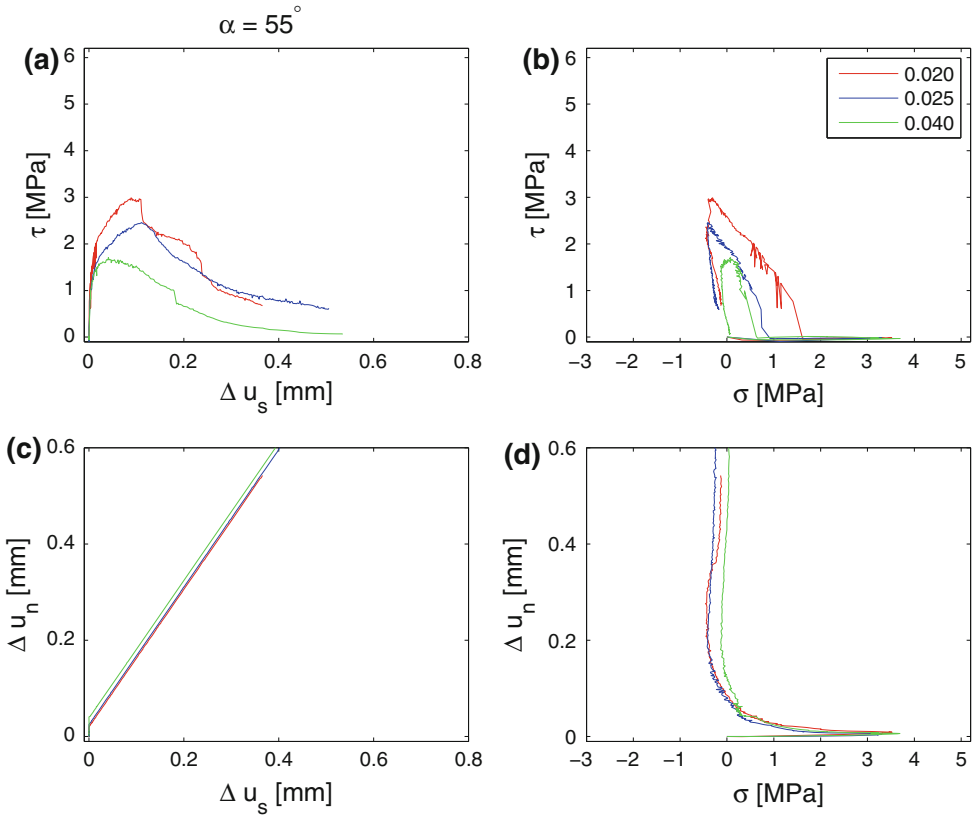

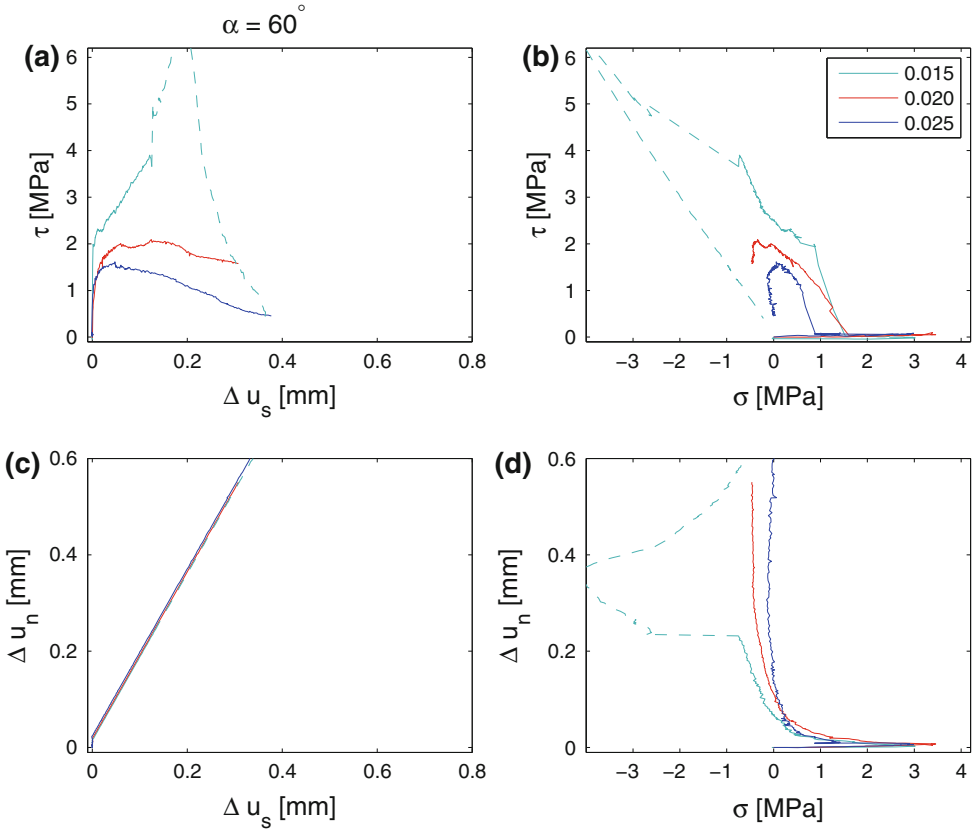


**Fig. 17** Mixed mode test results for three different initial openings at the same mixed mode angle of 60°

plot in Fig. 14b there are almost straight lines in both loading and unloading. The tendency is clear, the compression level and the shear level increases for decreasing initial opening.

Figure 15 shows tests for the 45° mixed mode angle at three different initial openings. The same tendencies are seen as in Fig. 14.

Figure 16 shows tests for the 55° mixed mode angle at three different initial openings. The compression level and the shear level increases for decreasing initial opening. Despite that the results have been filtered some noise is still present for the $\Delta u_n = 0.020$ mm test. This noise is most likely a result of the nature of the crack surface as explained in Sect. 3.1.

Figure 17 shows tests for the 60° mixed mode angle at three different initial openings. The $\Delta u_n = 0.015$ mm changes during the test from a ligament crack to a secondary fracture. In the figure this is illustrated by the line style for the result curve which is changed from solid to dashed when the failure mode changes.

## References

1. Carol I, Prat PC, López CM (1997) Normal/shear cracking model: application to discrete crack analysis. J Eng Mech 123(8):765–773
2. Carpinteri A, Brighenti R (2010) Fracture behaviour of plain and fiber-reinforced concrete with different water content under mixed mode loading. Mater Des 31(4): 2032–2042 Design of nanomaterials and nanostructures
3. Gettu R, Mobasher B, Carmona S, Jansen DC (1996) Testing of concrete under closed-loop control. Adv Cem Based Mater 3(2):54–71
4. GOM (2005) Aramis user manual (4M) v5.4.1. GOM mbH, Germany
5. Hassanzadeh M (1992) Behaviour of fracture process zones in concrete influenced by simultaneously applied normal and shear displacements. Report TVBM-1010. PhD thesis, Lund Institute of Technology
6. Hillerborg A (1989) Stability problems in fracture mechanics testing. In Shah SP et al (eds) Fracture of concrete and rock—recent developments. Elsevier, London, pp 369–378
7. Hillerborg A, Modéer M, Petersson P-E (1976) Analysis of crack formation and crack growth in concrete by means of fracture mechanics and finite elements. Cem Concr Res 6(6):773–781

8. Madsen A (2009) Cracks in concrete under repetitive load; experiments and modeling. Master's thesis, Department of Civil Engineering, Technical University of Denmark
9. Nielsen LO, Mougaard JF, Jacobsen JS, Poulsen PN (2010) A mixed mode model for fracture in concrete. In: Oh BH et al (ed) Fracture mechanics of concrete and concrete structures—recent advances in fracture mechanics of concrete. Korea Concrete Institute, Seoul
10. Nooru-Muhamed MB (1992) Mixed mode fracture of concrete: an experimental approach. PhD thesis, Delft University
11. Petersen RB (2008) Fracture mechanical analysis of reinforced concrete. Master's thesis, Department of Civil Engineering. Technical University of Denmark, Project no. 07-062
12. Reinhardt HW, Ozbolt J, Xu S, Dinku A (1997) Shear of structural concrete members and pure Mode II testing. Adv Cem Based Mater 5(3–4):75–85
13. Reinhardt HW, Xu S (2000) A practical testing approach to determine Mode II fracture energy $G_{IIf}$ for concrete. Int J Fract 105(2):107–125
14. Østergaard L, Olesen JF, Poulsen PN (2007) Biaxial testing machine for mixed mode cracking of concrete. In: Fracture mechanics of concrete and concrete structures: new trends in fracture mechanics of concretes
15. THK (2008) THK General catalog, catalog no. 400-1e edition
16. Walter R, Olesen JF (2008) Cohesive mixed mode fracture modelling and experiments. Eng Fract Mech 75(18): 5163–5176

# Paper II

*"Constitutive Mixed Mode Model for Cracks in Concrete"*

J.S. Jacobsen, P.N. Poulsen, J. F. Olesen & K. Krabbenhoft

Submitted to: *Engineering Fracture Mechanics, 2012*

# Constitutive Mixed Mode Model for Cracks in Concrete

J.S. Jacobsen[a], P.N. Poulsen[a], J.F. Olesen[a], K. Krabbenhoft[b]

[a] *Department of Civil Enginnering, Technical University of Denmark, Brovej Building 118, 2800 Kgs. Lyngby, Denamrk*
[b] *Centre for Geotechnical and Materials Modelling, University of Newcastle, NSW, Australia*

**Abstract**

The scope of the paper is to set up a constitutive mixed mode model for cracks in concrete. The model is formulated at macro level and includes the most important micro scale effects. An associated plasticity model inspired by the modified Cam clay model is established. The hardening parameters are based on the standard Mode I tensile softening response and the response for Mode I crushing. The roughness of the crack is included through a topographic description of the crack surface. The constitutive behavior is based on the integration of local contributions. The local mixed mode ratio is determined from the topographic information and the constitutive model is thereby purely mechanically based. Using the actual topographic description the model is validated against experimental results for mixed mode crack openings.

*Keywords:* Concrete, Constitutive modeling, Fracture Mechanics, Plasticity, Mixed mode fracture

## Nomenclature

$\mathbf{a}$ : yield surface normal
$a$ , $b$ : semi-axes for the elliptic yield surface
$\mathbf{C^e}$ : elastic stiffness matrix
$\mathbf{C^{ep}}$ : elasto-plastic flexibility matrix
$\mathbf{D^e}$ : elastic stiffness matrix
$\mathbf{D^{ep}}$ : elasto-plastic stiffness matrix
$D_n$ : elastic normal stiffness
$D_s$ : elastic shear stiffness

$D_{\sigma_w}$ : unloading stiffness from the $\sigma_w$-relation
$D_n^*$ : normal stiffness during unloading
$D_s^*$ : shear stiffness during unloading
$E$ : Youngs modulus for continuum
$f$ : yield surface function
$f_t$ : initial tensile strength
$f_c$ : initial compressive strength
$H$ : hardening modulus
$\mathbf{h}$ : hardening functions
$h_t$ : softening function for the cohesion
$h_c$ : hardening/softening function for the compressive strength
$k_\theta$ : contour line
$k_{\Delta\theta}$ : average contour line
$M$ : inclination of the critical state line
$\mathbf{n}$ : normal direction to the 2D crack line
$\mathbf{s}$ : tangential direction to the 2D crack line
$\mathbf{t}$ : traction vector
$t_n$ , $t_s$ : normal and tangential components of the traction vector
$t_{n0}$ , $t_{s0}$ : components of center of yield surface
$\mathbf{T}$ : transformation matrix between global and local displacements
$[\![\mathbf{u}]\!]$ : discontinuity jump vector
$[\![\tilde{\mathbf{u}}]\!]$ : modified displacement relative to contour line
$[\![\mathbf{u}]\!]^e$ , $[\![\mathbf{u}]\!]^p$ : elastic and plastic part of the discontinuity jump vector
$u_n$ , $u_s$ : normal and tangential components of the discontinuity jump vector
$u_{n,ini}$ : initial normal opening of the crack
$u_n^p$ : plastic normal opening
$u_{n,max}^p$ : maximum plastic normal opening
$u_{n,min}^p$ : plastic normal displacement for crushing
$u_{n,cr}^p$ : plastic normal displacement at ultimate crushing
$w$ : positive opening displacement for the crack
$\bar{w}$ : negative opening displacement for the crack

$\alpha$ : mixed mode angle
$\Delta\theta_i$ : start inclination angle interval
$\boldsymbol{\epsilon}$ : strain vector
$\boldsymbol{\epsilon^e}$ , $\boldsymbol{\epsilon^p}$ : elastic and plastic part of the strain vector
$\theta$ : start inclination of contour line

$\boldsymbol{\kappa}$ : hardening parameters vector
$\dot{\lambda}^p$ : incremental plastic multiplier
$\nu$ : poison ratio
$\sigma_t$ : hardening parameter for the tensile strength
$\sigma_c$ : hardening parameter for the compressive strength
$\sigma_w$ : stress-crack opening relation
$\sigma_{\bar{w}}$ : stress-postpeak inelastic displacement relation in crushing

$()_g$ : global
$()_l$ : local
$(\dot{})$ : incremental

## 1. Introduction

In order to model the response of reinforced concrete structures to external action it is vital to include the effects of cracks in concrete. In general the modeling of the crack opening and crack sliding is crucial in order to obtain a realistic model for the general structural behavior, in terms of e.g. the stress distribution, the stiffness and crack distributions and crack openings. These are important aspects in structural design covering topics such as static analysis, dynamic analysis or durability analysis including deterioration mechanisms.
Due to the fact that concrete is composed of different sized aggregates, the material is very heterogeneous. Therefore the cracking in concrete may be modeled at different scales. However, with the objective to model real size concrete structures the computational demand is not realistic if the analysis is based on a micro scale model. Therefore the aim is to establish a macro model which includes the most important micro scale effects, thereby making it feasible for computational analysis of real size concrete structures.

Ever since Hillerborg and co-workers,[1], proposed the fictitious crack model for the Mode I crack behavior, this efficient discrete constitutive model has been available for inclusion in finite element models. At the macro level the assumption is that a crack in concrete initiates perpendicular to the largest principal stress, but after the initiation the established crack can open in a combination of crack opening (Mode I) and crack sliding (Mode II), i.e. a mixed mode opening. Experimentally the constitutive relation between

Mode I crack opening and the normal stresses across the crack is well described [2], and for the modeling the relation can be explained in the frame work of the fictitious crack model, whereas in most constitutive crack models the mixed mode effects need an clarification. However, to get a thorough description of the structural consequences as a result of concrete cracking, it is important to include the mixed mode effects. These effects are strongly related to the topography of the crack surface, which as a consequence of the varying aggregate sizes may be characterized as rough or jagged. Due to the jagged crack surface a crack with a small opening is capable of transferring shear stresses across the crack. In order to model the shear transfer and an actual sliding between the crack faces together with the Mode I opening, the fictitious crack model is not sufficient and must be extended.
The mechanical behavior of the jagged surface is crucial for the structural performance. For instance the dilation which is a result of sliding between the crack faces can be attributed to the jagged surface. A general and detailed constitutive crack model must be capable of describing mixed mode behavior including dilatational effects.
Experimentally the mixed mode crack behavior has been investigated in various ways. A biaxial set-up used together with double notched specimens has proven to give the most direct mixed mode behavior of the crack. Such experimental set-ups have been used in the work of Nooru-Mohamed et al. [3], Hassanzadeh [4] and Jacobsen et al. [5]. In [5], the experiments are interpreted as material point information, and the results may be used directly as the constitutive mixed mode crack behavior. For more details on mixed mode experiments see [5].

Some simple mixed mode models are based on a tensile and a frictional softening curve with associated fracture energies and a coupled expression for normal and sliding displacements for a given combination of Mode I and II fracture, see Högberg [6] and Walter and Olesen [7]. For mixed mode fracture, the models are not able to determine all the cracking mechanisms and the Mode II fracture energy is difficult to conceive. The definition of a Mode II fracture energy in concrete needs to be clarified and it is questionable if it is possible in a simple form to describe the crack mechanisms in mixed mode by a quantity related to Mode I and another related to Mode II. A confinement-shear model, Cusatis et al. [8], has been used together with a particle model to model mixed mode displacement of a double notched specimen, see Skoček [9]. The model gives a good prediction of the mixed mode

behavior but the material data needed are difficult to obtain and the model has high computational demands. Another modeling approach at micro scale based on the constitutive model presented by Carol et al. [10] has e.g. been reported in the two accompanying papers [11] and [12]. Here interface elements modeling interfaces between elements for aggregates and mortar are used together with a softening elasto-plastic constitutive model for the mixed mode behavior, [10]. The constitutive model is Coulomb-like and uses a fracture energy-based damage parameter as the control variable for the yield surface contraction. A modified version of the model with an added compression limitation of the elastic region is presented in Dick-Nielsen [13]. The model is partly based on a Mode II fracture energy which is difficult to measure directly. In Lens et al. [14] another elasto-plastic mixed model is presented. It is based on a similar Coulomb-like yield surface and a non-associated plastic potential as in [10]. The surface evolution is described by the actual tensile and cohesive strengths, both controlled by a tensile-softening-like response. The inelastic opening and sliding is coupled through a coupling factor which lacks a physical interpretation and is fitted against experiments.
A macro elasto-plastic constitutive model by Lourenço and Rots [15] is able to describe both tension softening, slipping and crushing, all desirable effects in a model for concrete cracking. The model requires a number of parameters, which are experimentally hard to determine. Two elasto-plastic damage interface models are presented by Spada et al. [16] and Alfano and Sacco [17]. The first one has a rather extensive thermodynamical formulation, the second one lacks dilatational effects and both lack a compressive failure cut off. The model by Nielsen et al. [18] is based on a new Coulomb-like yield surface. The model is elasto-plastic with damage and has a cohesional and a frictional part. The frictional part includes deformation state dependency, where the friction decreases with crack opening and is restored with crack closure. In Mougaard et al. [19] the model by Nielsen et al. [18] is used together with an XFEM crack element. Compared with the experiments by Jacobsen et al. [5] the model response presented in [18] reproduces some of the proper crack behavior but the shear stress level is too low and the model response is too stiff.
The above mentioned models have either a high demand for computational resources, difficult obtainable material parameters or lacking features regarding concrete cracking. Here a simple, macro level constitutive crack model covering Mode I opening, crushing and mixed mode opening is presented.

The constitutive mixed mode crack model presented here is based on an associated plasticity model with an elliptic yield surface. The model is inspired by the modified Cam clay model for clay and sand originally described in Roscoe and Burland [20], [21]. Compared with the modified Cam clay model the mixed mode crack model has a modified formulation of the yield surface which includes cohesion and the hardening functions are completely new. Thereby is the constitutive behavior, which mainly is described through the hardening functions, completely new. For an opening of the crack the material softens, for a closure the material hardens, and for a large closure the material crushes described as a softening. For the crack the initiation takes place perpendicular to the largest principal stress when this exceeds the tensile capacity. The model is capable of representing both the crack initiation, the evolution in Mode I and the mixed mode behavior of an already established crack. The model input for the hardening functions and the rest of the material data are obtained from normal sized concrete specimens like the compression cylinder.
Besides these mechanical aspects the crack behavior is also affected by the crack topography. A crack surface is measured to give a characteristic topographic description of the surface resulting in a number of characteristic opening paths, which in total give rise to the crack response.
The response from the constitutive crack model is compared to a series of mixed mode tests. The model is able to explain the different crack mechanisms which are present in a crack in concrete, both for Mode I opening and for mixed mode opening of the crack.

## 2. Constitutive Mixed Mode Model for Cracks in Concrete

In concrete the crack initiation is assumed to take place in Mode I, perpendicular to the largest principal stress. After the crack has been initiated the crack can continue the pure opening but the opening can also be combined with sliding between the crack faces. The crack then opens in mixed mode. Figure 1 shows the concept that the crack initiates in Mode I but after the initiation the now establish crack can open with various ratios between pure opening and pure sliding. Because of the jagged crack surface, the cracking takes place in a process zone around the apparent crack. In an idealized model the process zone and the jagged crack are substituted by a plane dis-

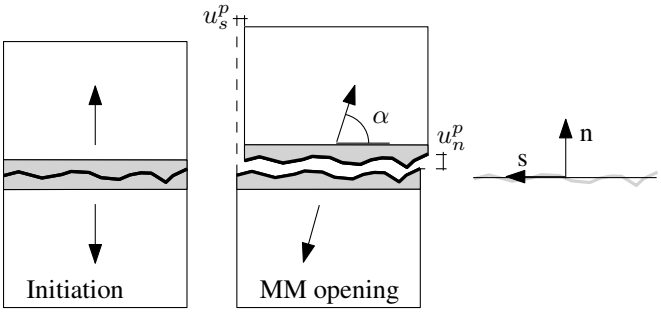


Figure 1: The crack initiates perpendicular to the largest principal stress. After the initiation, it can open in various mixed mode angles $\alpha$. The crack process zone is grey shaded. Definition of the crack coordinate system $(\mathbf{n}, \mathbf{s})$.

continuity line, which therefore can be ascribed some elastic properties.
Tractions and displacements in the crack are described by a normal component and a shear component. The engineering notation is used and the tractions are given by $\mathbf{t} = [t_n, t_s]^T$ while the displacements are given by $[\![\mathbf{u}]\!] = [u_n, u_s]^T$. The $(\mathbf{n}, \mathbf{s})$-crack coordinate system is defined in Figure 1. The ratio between the increment of pure opening and pure sliding defines the mixed mode angle $\alpha = \tan(\frac{\dot{u}_n}{\dot{u}_s})$.
At first the plasticity framework of the constitutive model is presented and followed by the model description. The derivation of the plasticity functions follows a traditional plasticity framework as given in [22]. The implementation of the model is explained and the material parameters used for a crack in concrete are presented. The section ends with a computation illustrating the capabilities of the model.

### *2.1. Plasticity Framework*

For a given displacement increment $[\![\dot{\mathbf{u}}]\!]$ it is desired to find the matching traction increment $\dot{\mathbf{t}}$ for the crack. In the plastic domain the relation is described by the elasto-plastic stiffness matrix $\mathbf{D^{ep}}$

$$\dot{\mathbf{t}} = \mathbf{D^{ep}}[\![\dot{\mathbf{u}}]\!] \;\Leftrightarrow\; [\![\dot{\mathbf{u}}]\!] = \mathbf{C^{ep}}\dot{\mathbf{t}} \tag{1}$$

where the elasto-plastic flexibility matrix $\mathbf{C^{ep}} = (\mathbf{D^{ep}})^{-1}$ has been introduced. The plasticity theory can establish the frame work for $\mathbf{C^{ep}}$ and can through the hardening parameters $\boldsymbol{\kappa}$ describe the actual material state.
The strain split assumption gives that the total strains $\boldsymbol{\epsilon}$ can be divided into

an elastic $\boldsymbol{\epsilon}^{\boldsymbol{e}}$ and a plastic $\boldsymbol{\epsilon}^{\boldsymbol{p}}$ contribution. In the presentation the generalized strains are represented by the displacement jump between the crack faces, $[\![\mathbf{u}]\!]$. Thereby has the stiffness matrix $\mathbf{D}^{\mathbf{ep}}$ the unit stiffness per length. In incremental form the strain split assumption is given by

$$[\![\dot{\mathbf{u}}]\!] = [\![\dot{\mathbf{u}}]\!]^e + [\![\dot{\mathbf{u}}]\!]^p \tag{2}$$

Hookes law gives the relation between the elastic displacements and the tractions

$$\dot{\mathbf{t}} = \mathbf{D}^{\mathbf{e}}[\![\dot{\mathbf{u}}]\!]^e \;\Leftrightarrow\; [\![\dot{\mathbf{u}}]\!]^e = \mathbf{C}^{\mathbf{e}}\dot{\mathbf{t}} \tag{3}$$

where $\mathbf{D}^{\mathbf{e}} = \mathbf{C}^{\mathbf{e}-1}$ is the elastic stiffness and $\mathbf{C}^{\mathbf{e}}$ is the elastic flexibility of the crack.

*2.1.1. Yield Surface, Flow Rule and Hardening*

Expressed in tractions the elastic domain is limited by the yield surface $f(\mathbf{t}, \boldsymbol{\kappa})$. For $f < 0$ the state is elastic and for $f = 0$ the state becomes plastic. For an associated plasticity model, the outward normal to the yield surface in the actual traction point $\mathbf{t}$ dictates the direction of the plastic displacement increment. For a traction point on the yield surface the plastic displacements are given by the flow rule

$$[\![\dot{\mathbf{u}}]\!]^p = \dot{\lambda}^p \frac{\partial f(\mathbf{t}, \boldsymbol{\kappa})}{\partial \mathbf{t}} \tag{4}$$

Here $\dot{\lambda}^p \geq 0$ is the plastic multiplier which must be non-negative. The displacement increment in Eq. (2) can together with Hookes Law, Eq. (3), and the plastic displacements, Eq. (4), be described as

$$[\![\dot{\mathbf{u}}]\!] = \mathbf{C}^{\mathbf{e}}\dot{\mathbf{t}} + \dot{\lambda}^p \frac{\partial f(\mathbf{t}, \boldsymbol{\kappa})}{\partial \mathbf{t}} \tag{5}$$

The evolution of the yield surface is described through the hardening functions $\mathbf{h}(\mathbf{t}, \boldsymbol{\kappa})$ and their relation to the hardening parameters $\boldsymbol{\kappa}$ are defined as

$$\dot{\boldsymbol{\kappa}} = \dot{\lambda}^p \mathbf{h}(\mathbf{t}, \boldsymbol{\kappa}) \tag{6}$$

*2.1.2. Elasto-Plastic Flexibility Matrix*

A traction state $\mathbf{t}$ in the hardening state $\boldsymbol{\kappa}$ is placed on the yield surface, $f(\mathbf{t}, \boldsymbol{\kappa}) = 0$. A loading of the yield surface with an infinitesimal traction

increment $\dot{\mathbf{t}}$ leads to a new state $f(\mathbf{t}+\dot{\mathbf{t}}, \boldsymbol{\kappa}+\dot{\boldsymbol{\kappa}}) = 0$. The second state can be approximated by a Taylor expansion to first order of the first state, and assuming that both states are on the yield surface this leads to the approximation

$$\left(\frac{\partial f}{\partial \mathbf{t}}\right)^T \dot{\mathbf{t}} + \left(\frac{\partial f}{\partial \boldsymbol{\kappa}}\right)^T \dot{\boldsymbol{\kappa}} = 0 \tag{7}$$

Utilizing the expression for the hardening, Eq. (6), the plastic multiplier can be derived from Eq. (7)

$$\dot{\lambda}^p = \frac{-\left(\frac{\partial f}{\partial \mathbf{t}}\right)^T \dot{\mathbf{t}}}{\left(\frac{\partial f}{\partial \boldsymbol{\kappa}}\right)^T \mathbf{h}(\mathbf{t}, \boldsymbol{\kappa})} \tag{8}$$

Defining the hardening modulus by,

$$H = -\left(\frac{\partial f}{\partial \boldsymbol{\kappa}}\right)^T \mathbf{h}(\mathbf{t}, \boldsymbol{\kappa}) \tag{9}$$

the elasto plastic flexibility matrix, $\mathbf{C^{ep}}$, can be identified from Eq. (8) and the split rule Eq. (5)

$$\mathbf{C^{ep}} = \mathbf{C^e} + \frac{\frac{\partial f}{\partial \mathbf{t}}\left(\frac{\partial f}{\partial \mathbf{t}}\right)^T}{H} = \mathbf{C^e} + \frac{\mathbf{a}\mathbf{a}^T}{H} \tag{10}$$

where the plastic potential normal has been introduced as

$$\mathbf{a} = \frac{\partial f(\mathbf{t}, \boldsymbol{\kappa})}{\partial \mathbf{t}} \tag{11}$$

An expression for the plastic multiplier can be obtained by multiplying Eq.(5) with the yield surface normal $\mathbf{a}^T$

$$\dot{\lambda}^p = \frac{\mathbf{a}^T[\![\dot{\mathbf{u}}]\!] - \mathbf{a}^T\mathbf{C^e}\dot{\mathbf{t}}}{\mathbf{a^T a}} \tag{12}$$

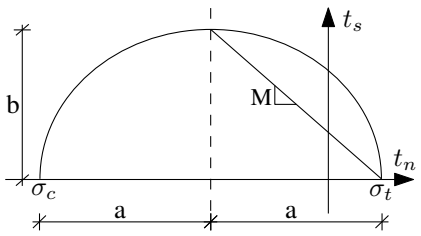


Figure 2: Upper part of the elliptic yield surface and M-line. Semi-axes $a$ and $b$ shown.

*2.2. Yield Surface*

By inspiration from the modified Cam-Clay model, an elliptic yield surface is used to describe the mixed mode crack behavior in concrete. The ellipse is controlled by a critical state line with the inclination $t_s/t_n = M$ and the intersections with the abscissa $\sigma_c$ and $\sigma_t$, see Figure 2. The model is associated, so the plastic flow is proportional to the yield surface normal. The inclination of the critical state line can be interpreted as an equivalent to the friction coefficient in a Coulomb-like sense.

A given state is described by the tractions $\mathbf{t} = [t_n, t_s]^T$, the displacements $[\![\mathbf{u}]\!] = [u_n, u_s]^T$ and the hardening state $\boldsymbol{\kappa} = [\sigma_t, \sigma_c]^T$. For a given plastic deformation state $\sigma_t$ and $\sigma_c$ are the actual uniaxial tensile and compressive strengths of the material, respectively. The initial surface is given by $M$ and the hardening state $\boldsymbol{\kappa} = [f_t, f_c]^T$, where $f_t$ is the uniaxial tensile strength and $f_c$ is the uniaxial compressive strength of the concrete. In the elastic state the stiffness is given by

$$\dot{\mathbf{t}} = \mathbf{D^e}[\![\dot{\mathbf{u}}]\!] \Rightarrow$$

$$\mathbf{D^e} = \begin{bmatrix} D_n & 0 \\ 0 & D_s \end{bmatrix} \tag{13}$$

$D_n$ is the elastic normal stiffness and $D_s$ is the elastic shear stiffness of the process zone. The yield surface separates the elastic domain from the plastic domain and the yield surface is given by the ellipse

$$\frac{(t_n - t_{n0})^2}{a^2} + \frac{(t_s - t_{s0})^2}{b^2} = 1 \tag{14}$$

where $(t_{n0}, t_{s0}) = (\frac{\sigma_t + \sigma_c}{2}, 0)$ is the center of the ellipse, and $a = \frac{\sigma_t - \sigma_c}{2}$ and $b = aM$ are the semi-axes. Introducing the center of the ellipse and the

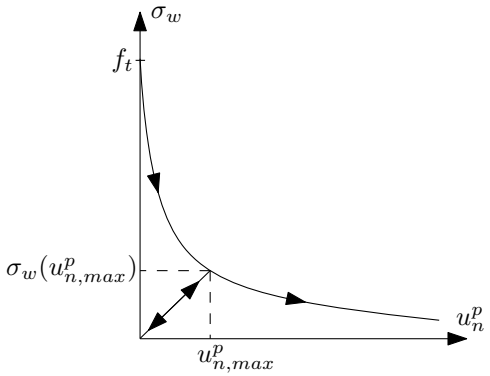


Figure 3: $\sigma_w$-curve. $f_t$ is the tensile strength. Indications of the central unloading path with the inclination $D_{\sigma_w} = \sigma_w(u^p_{n,max})/u^p_{n,max}$.

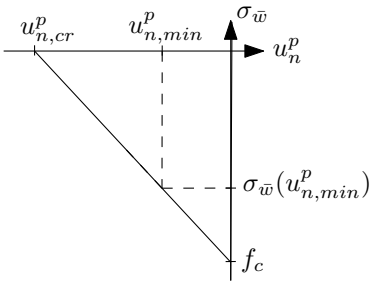


Figure 4: $\sigma_{\bar{w}}$-curve. $f_c$ is the compressive strength, $u^p_{n,cr}$ is the plastic normal deformation at crushing failure. Unloading is not considered.

major and minor axes in Eq. (14), the yield surface can be expressed as:

$$f\left(\mathbf{t}, \boldsymbol{\kappa}\right) = t_s^2 + M^2 t_n \left(t_n - \sigma_t - \sigma_c\right) + M^2 \sigma_t \sigma_c \tag{15}$$

The plastic potential flow is given by the yield surface normal, i.e.

$$\mathbf{a} = \frac{\partial f}{\partial \mathbf{t}} = \begin{bmatrix} M^2 \left(2t_n - \sigma_t - \sigma_c\right) \\ 2t_s \end{bmatrix} \tag{16}$$

*2.3. Hardening Functions*

Following the fictitious crack model by Hillerborg et al. [1] it is widely accepted to describe the Mode I opening of a crack in concrete by a relation between the normal stresses over the crack and the actual inelastic, normal opening of the crack, normally characterized by a $\sigma_w$ stress-crack opening

relationship. The $\sigma_w$-behavior should also appear correctly in the Mode I response from the constitutive mixed mode crack model. Similarly for a Mode I closure where the crushing of concrete may be seen as a localized phenomenon, Jansen and Shah [23]. For Mode I closure, the postpeak behavior can be represented by a $\sigma_{\bar{w}}$-curve, where $\sigma_{\bar{w}}$ is the compressive normal stress corresponding to the postpeak inelastic crushing $\bar{w}$.
In the constitutive mixed mode crack model the displacement parameter for both $\sigma_w$ and $\sigma_{\bar{w}}$ is related to the plastic normal opening $u_n^p$. $\sigma_w$ is dependent on the maximum plastic opening, $u_{n,max}^p$, while $\sigma_{\bar{w}}$ is dependent on the plastic compression after crushing, $u_{n,min}^p$. In Figure 3 a typical $\sigma_w$ relationship for a crack in concrete is shown together with the indication of a central unloading path. Based on the test results by Jansen and Shah [23] the softening caused by crushing can be linearly represented as shown in Figure 4.
The yield surface is limited by the initial uniaxial strengths $\boldsymbol{\kappa} = [f_t, f_c]^T$ in tension and compression, respectively. The yield surface evolution is described by the hardening state. The hardening/softening is assumed to be divided into three different cases distinguished by whether there is a crack opening or a closure, and in the case of a closure whether the compressive hardening parameter, $\sigma_c$, has exceeded the compressive strength, $f_c$. Whether there is opening or closure is determined by the normal projection (projection on $\mathbf{n}$) of the yield surface normal, $\mathbf{a}_1$, which corresponds to the direction of the plastic normal opening, $u_n^p$.

**$\mathbf{a}_1 > 0$:** The cohesion vanishes according to the $\sigma_w$-curve. In the model this is reflected by the softening of the hardening parameter in tension $\sigma_t$ and a proportional softening of the hardening parameter in compression $\sigma_c$ with the proportionality factor $\sigma_c/\sigma_t$, see Figure 5.

**$\mathbf{a}_1 < 0$ and $\sigma_c$ has not exceeded $f_c$:** For instance if the loading state changes from an opening to a closure of the crack, the hardening parameter in compression $\sigma_c$ can harden until it reaches $f_c$, see Figure 5. In the hardening case only $\sigma_c$ hardens, while the cohesion represented by the hardening parameter in tension $\sigma_t$ is irreversible.

**$\mathbf{a}_1 < 0$ and $\sigma_c$ reaches $f_c$:** The compression resistance diminishes according to the $\sigma_{\bar{w}}$-curve. In the model this is reflected by a softening of the hardening parameter in compression $\sigma_c$ and a proportional softening of the hardening parameter in tension $\sigma_t$ with the proportionality factor $\sigma_t/\sigma_c$.

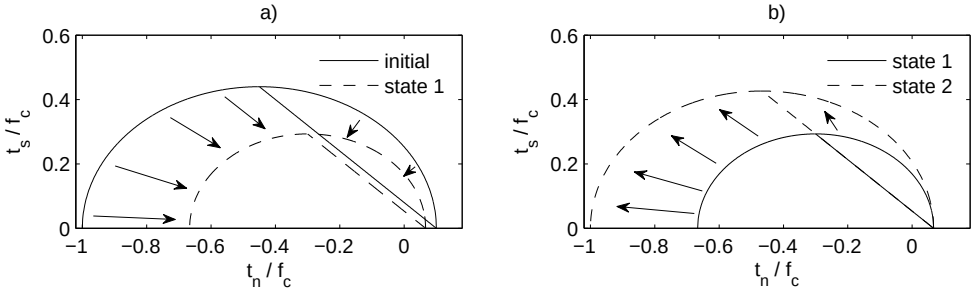


Figure 5: The two different modes for the yield surface evolution. **(a)** As a result of either opening or crushing both $\sigma_c$ and $\sigma_t$ soften from the initial state to state 1. **(b)** As a result of a closure from state 1 only $\sigma_c$ hardens and returns to $\sigma_c = f_c$ in state 2.

The hardening functions are derived in the following. The hardening modulus is defined in Eq. (9) and the yield surface dependence on the hardening is given by

$$\frac{\partial f}{\partial \boldsymbol{\kappa}} = \begin{bmatrix} M^2\left(\sigma_c - t_n\right) \\ M^2\left(\sigma_t - t_n\right) \end{bmatrix} \tag{17}$$

The model has two hardening functions $\mathbf{h} = [h_t, h_c]^T$ related to $\sigma_t$ and $\sigma_c$, respectively. Together with Eq. (17), the hardening modulus, given in Eq. (9), is then given by

$$H\left(\mathbf{t}, \boldsymbol{\kappa}\right) = -h_t M^2\left(\sigma_c - t_n\right) - h_c M^2\left(\sigma_t - t_n\right) \tag{18}$$

In a pure opening the plasticity model has to follow the normal opening relation $\sigma_w$ with the tangent stiffness $\dot{\sigma}_w$. This means that the plastic normal component of the elasto-plastic normal flexibility matrix $\mathbf{C^{ep}}$ in Eq. (10) has to be equal to the flexibility $\frac{1}{\dot{\sigma}_w}$ given by the normal opening relation, leading to the relation

$$H\left(\mathbf{t}, \boldsymbol{\kappa}\right) = \dot{\sigma}_w \left(\mathbf{a}\mathbf{a}^T\right)_{(1,1)} \tag{19}$$

In pure tension the traction state is $(t_n, t_s) = (\sigma_t, 0)$ and the yield surface normal is $\mathbf{a} = [M^2(\sigma_t - \sigma_c), 0]^T$. For the given traction state, the hardening modulus in Eq. (18) can be rewritten to

$$H\left(\mathbf{t}, \boldsymbol{\kappa}\right) = -h_t M^2(\sigma_c - \sigma_t) \tag{20}$$

Using Eq. (19) together with Eq. (20) the hardening function for the tensile capacity can be found as

$$h_t(\mathbf{t}, \boldsymbol{\kappa}) = M^2(\sigma_t - \sigma_c)\dot{\sigma}_w \tag{21}$$

Similarly for a pure Mode I closure, if the normal traction $t_n$ reaches the compressive strength, $f_c$, the plasticity model has to follow the $\sigma_{\bar{w}}$-curve with the tangent stiffness $\dot{\sigma}_{\bar{w}}$. This means that the plastic normal component of the elastoplastic flexibility matrix $\mathbf{C^{ep}}$ in Eq. (10) has to be equal to the flexibility $\frac{1}{\dot{\sigma}_{\bar{w}}}$ given by the $\sigma_{\bar{w}}$-curve. Using the same arguments as for the opening, the closure leads to the hardening function

$$h_c(\mathbf{t}, \boldsymbol{\kappa}) = M^2(\sigma_c - \sigma_t)\dot{\sigma}_{\bar{w}} \tag{22}$$

After initiation the crack may open or close. If closure starts, the state will normally change from plastic to elastic. Experiments with cracked concrete have shown that unloading is associated with a reduced stiffness, see e.g. Gopalaratnam and Shah [24]. In the model this is included by applying central unloading, see Figure 3. In the case of central unloading the normal stiffness consists of a contribution from the elastic normal stiffness $D_n$ and a contribution from the unloading stiffness from the $\sigma_w$-curve $D_{\sigma_w} = \frac{\sigma_w(u^p_{n,max})}{u^p_{n,max}}$. As long as $u^p_n > 0$ the elastic normal stiffness can be found from the equation

$$\frac{1}{D^*_n} = \frac{1}{D_n} + \frac{1}{D_{\sigma_w}} \tag{23}$$

During the elastic unloading the elastic stiffness matrix $\mathbf{D^e}$ is reduced by the same ratio: $\mathbf{D^{e*}} = \mathbf{D^e}\frac{D^*_n}{D_n}$. When $u_n < 0$ the stiffness returns to the original elastic stiffness, $\mathbf{D^e}$. For a continued compression the elastic state can change into a plastic state. If that is the case $\sigma_c$ can harden until it reaches the compressive strength $f_c$ and crushing starts according to Eq. (22). The cohesion is assumed irreversible, so during the compressive hardening there is no change in the tensile strength, $\dot{\sigma}_t = 0$. The $\sigma_c$-hardening is in fact assumed to be pseudo-elastic, which means that for a hardening, the state has to be plastic, but the change in tractions corresponds to an elastic increment $\dot{\mathbf{t}} = \mathbf{D^e}[\![\dot{\mathbf{u}}]\!]$ and the hardening does not introduce any plastic displacements $\dot{\lambda}^p = 0$. The hardening increment $\dot{\boldsymbol{\kappa}}$ is determined from the new state $f(\mathbf{t} + \dot{\mathbf{t}}, \boldsymbol{\kappa} + \dot{\boldsymbol{\kappa}}) = 0$. Since $\dot{\sigma}_t = 0$ the change in the compressive hardening parameter $\dot{\sigma}_c$ is the only unknown in the equation $f(\mathbf{t}+\dot{\mathbf{t}}, \boldsymbol{\kappa}+\dot{\boldsymbol{\kappa}}) =$

0, and can be found as

$$\dot{\sigma}_c = \frac{(t_s + \dot{t}_s)^2 + M^2(t_n + \dot{t}_n)^2 - M^2(t_n + \dot{t}_n)\sigma_t}{M^2(t_n + \dot{t}_n) - M^2\sigma_t} - \sigma_c \tag{24}$$

*2.4. Implementation*

In each step the state is controlled by the yield function. For an elastic step, if the increment changes the state from elastic to plastic, the next iteration will be treated as plastic or vice-versa. A direct iteration scheme is used, see Table 1. The direct iteration is simple and effective for a sufficiently small deformation step. Though for each plastic increment, a small error is accumulated, so the traction state moves away from the yield surface. To reduce the error on the overall result the plastic state for a few of the increments is corrected by moving the traction state back to the yield surface. During a complete opening history less than 1% of the increments are corrected. The applied increment step size has been chosen sufficiently small to achieve convergence with respect to a smaller increment step size. At the top of the yield surface, there is a dramatic change in the hardening which changes from tensile softening to compressive hardening/softening or vice-versa. In order to avoid alternation in the numerical analysis between the hardening states, the hardening state is made continuous by a linearization for a narrow interval around the yield surface top. The interval is defined by the inclination of the yield surface normal with respect to a vertical surface normal, corresponding to the yield surface top. The linearization takes places within a variation of this inclination of $\pm 2^\circ$.

*2.5. Material Parameters*

In Jacobsen et al. [5] a series of characteristic, experimental mixed mode crack opening tests in concrete are presented. The constitutive model is compared to and validated against these experiments. The material parameters used are presented in Table 2. The tensile strength $f_t$ and the youngs modulus $E$, are together with a multi linear $\sigma_w$-curve all non published data from the work of [5]. The compressive strength $f_c$ is referred directly in [5]. $\nu$ is assumed characteristic for concrete while $M$ corresponds to a friction angle of $39^\circ$ in a Coulomb friction model. The $M$ dependence is illustrated in Section 3.2. The maximum compressive plastic displacement after crushing $u^p_{n,cr}$ is for a linear softening curve estimated from Jansen and Shah [23].

Table 1: Computational scheme.

| | |
|---|---|
| Constants | $D_n, D_s, f_t, f_c, M$ |
| Relations | $\sigma_w, \sigma_{\bar{w}}$ |
| State $i$ | $\mathbf{t}_i, \boldsymbol{\kappa}_i, [\![\mathbf{u}]\!]_i, [\![\dot{\mathbf{u}}]\!]$ |
| Iteration | |
| if $f < 0$ | $\dot{\mathbf{t}} = \mathbf{D^e}[\![\dot{\mathbf{u}}]\!]$<br>$\dot{bm}\kappa = 0$ |
| if $f \geq 0$ | $H = -\dfrac{\partial f\left(\mathbf{t}_i, \boldsymbol{\kappa}_i\right)^T}{\partial \boldsymbol{\kappa}} \mathbf{h}\left(\mathbf{t}_i, \boldsymbol{\kappa}_i, \sigma_w, \sigma_{\bar{w}}, [\![\dot{\mathbf{u}}]\!]\right)$<br>$\mathbf{a} = \dfrac{\partial f(\mathbf{t}_i, \boldsymbol{\kappa}_i)}{\partial \mathbf{t}}$<br>$\mathbf{C^{ep}} = \mathbf{C^e} + \dfrac{\mathbf{a}\mathbf{a}^\mathbf{T}}{H}$<br>$\dot{\mathbf{t}} = (\mathbf{C^{ep}})^{-1}[\![\dot{\mathbf{u}}]\!]$<br>$\dot{\lambda}^p = \dfrac{\mathbf{a}^T[\![\dot{\mathbf{u}}]\!] - \mathbf{a}^T\mathbf{C^e}\dot{\mathbf{t}}}{\mathbf{a^T a}}$<br>$\dot{\boldsymbol{\kappa}} = \dot{\lambda}^p \mathbf{h}$ |
| Update | $\mathbf{t}_{i+1} = \mathbf{t}_i + \dot{\mathbf{t}}$<br>$\boldsymbol{\kappa}_{i+1} = \boldsymbol{\kappa}_i + \dot{\boldsymbol{\kappa}}$<br>$[\![\mathbf{u}]\!]_{i+1} = [\![\mathbf{u}]\!]_i + [\![\dot{\mathbf{u}}]\!]$ |
| Control | $f(\mathbf{t}_{i+1}, \boldsymbol{\kappa}_{i+1})$ |

Table 2: Material parameters.

| Parameter | value |
|---|---|
| $f_t$ | 3.3 MPa |
| $f_c$ | -41 MPa |
| $E$ | 31 GPa |
| $\nu$ | 0.22 |
| $D_n$ | 570 GPa/m |
| $D_s$ | 380 GPa/m |
| $M$ | 0.8 |
| $u^p_{n,cr}$ | 1.2 mm |

Finally, the elastic normal and shear stiffnesses, $D_n$ and $D_s$ respectively, are determined through an inverse analysis for the test specimen used by [5]. This analysis was conducted using the commercial finite element program Abaqus where two elastic finite element computations with 46.509 10-node linear strain tetrahedrons were made. The first computation was a pure Mode I displacement of the specimen while the second was a pure Mode II displacement of the specimen.

### *2.6. Basic Model*

The results from experiments by Jacobsen et al. [5] are interpreted as the material data for a material point in a crack in concrete. The capabilities of the constitutive model can thereby be evaluated through a direct comparison. As in the experiments by Jacobsen et al. [5] the computational model is displacement controlled and divided into two steps. The first step is the initiation of the crack in a pure Mode I opening until a certain initial opening is reached $(u_n, u_s) = (u_{n,ini}, 0)$. The second step is a mixed mode opening, with a fixed mixed mode angle $\alpha = \frac{\dot{u}_n}{\dot{u}_s}$.
In the first two tests the Mode I capabilities are tested, both for a pure opening and for a pure crushing failure, see Figure 6. In these two cases the model gives the exact response, which is not surprising since the hardening functions according to Section 2.3 are constructed from either the $\sigma_w$-curve or the $\sigma_{\bar{w}}$-curve. Of more interest are the capabilities of the model during a mixed mode opening. The third computation follows directly a series of experiments, [5]. After an initial opening of $u_{n,ini} = 0.025$ mm where the

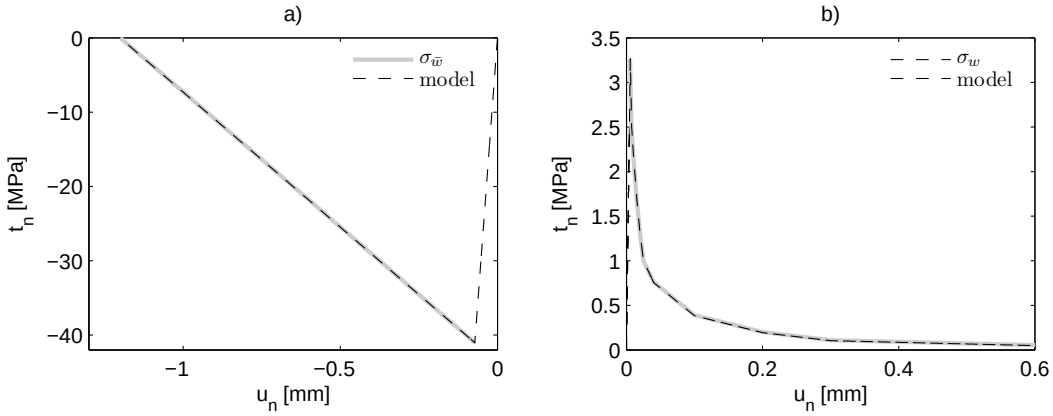


Figure 6: **(a)** The response from the constitutive model for a Mode I crushing compared with the $\sigma_{\bar{w}}$-curve plus elastic displacements. **(b)** The response from the constitutive model for a Mode I opening compared with the $\sigma_w$-curve plus elastic displacements. Normal traction $t_n$ as function of normal opening $u_n$.

crack is initiated the opening is continued by a fixed mixed mode angle $\alpha$. Figure 7 shows the model response for five different $\alpha$ values compared with the experiments. In Figure 7c the initial opening of $(u_{n,ini}, u_s) = (0.025, 0)$ mm is recognized and after the opening the results from five different mixed mode angles can be read from the figure. Figure 7d is the load opening displacement, though with interchanged axes compared with Figure 6. Similar to Figure 7d for normal tractions, the shear traction level is shown together with the shear displacement in Figure 7a. Figure 7b combines the results from the three other plots and shows the shear traction, $t_s$, as function of the normal traction, $t_n$. It is clear that the model response has a lack of flexibility and also the peak levels for the tractions are too low. In spite of the low traction level, the behavior in the $(t_n, t_s)$-plot has some of the right trends and the lack of traction and flexibility could in a model sense just be a matter of a correct scaling. But overall the basic crack model is not able to activate all the crack mechanisms. The friction level is too low while the crushing for the given mixed mode openings is not activated at all.
Summarized, the model is not fully capable of representing mixed mode opening of a crack in concrete. Even though the model with its hardening functions represents reasonable crack features the implementation in a plane crack model is not sufficient. Locally the crack path is mostly affected by the aggregate sizes and can at structural level be considered as plane. However, at

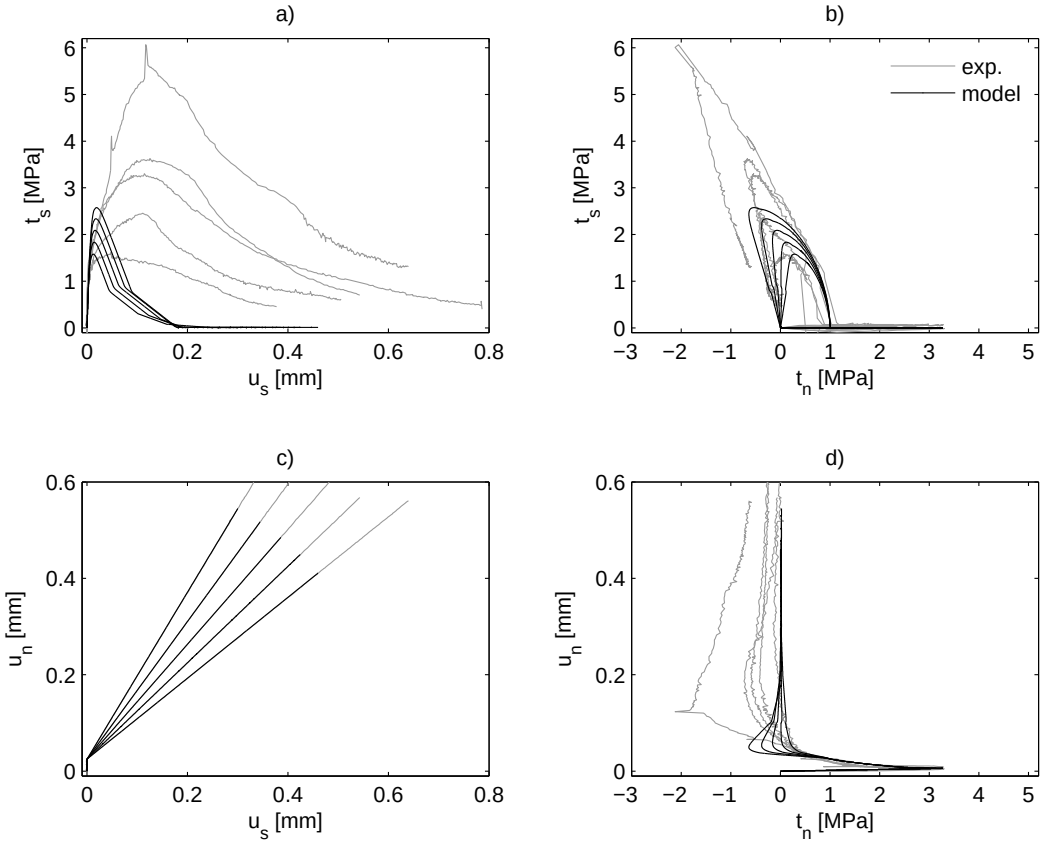


Figure 7: Response from the constitutive model for $u_{n,ini}$=0.025 mm and five different mixed mode angles $\alpha = [40°, 45°, 50°, 55°, 60°]$ compared with experiments (exp.) by Jacobsen et al. [5]. The four plots show the relation between shear traction $t_s$, sliding $u_s$, normal traction $t_n$ and normal opening $u_n$. The largest tractions are obtained for the lowest $\alpha$.

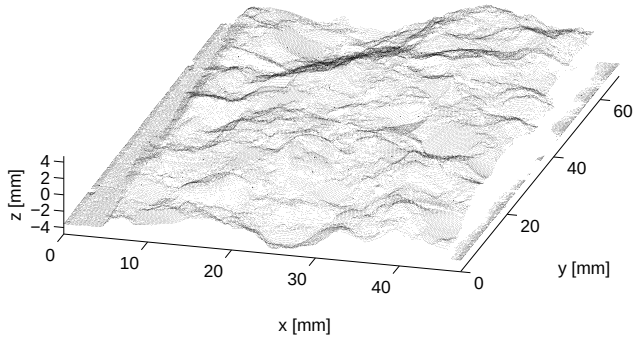


Figure 8: Scan of a concrete crack surface using a Nextec HAWK scanner.

micro level the crack path is far from being plane and for a crack opening the irregular topography of the crack surface locally introduces high friction and crushing. These micro mechanisms affect the overall crack response and should be considered in a crack model. The micro effects can be included in the constitutive model using a topographic description of the crack surface. The method is presented in the following.

## 3. Effects of Crack Topography

For a given global displacement vector the local ratio between opening and sliding is dependent on the actual topography of the surface. For instance, for an inclined path of the crack surface a pure global opening locally results in a combined opening and sliding. From a global displacement, the constitutive model from Section 2 is used with the transformed local displacements to determine the local tractions. To obtain the global response the local tractions are then summed over the surface using an appropriate discretization of the crack topography.

To get a description of a concrete crack surface topography, the crack surface belonging to one of the test specimens by Jacobsen et al. [5] is measured. A non-contact optical laser-scanner is used for the crack surface registration, [25]. As input to the scan a representative, rectangular area of the cracked surface and the spacing in the plane between the points is chosen. For each scanning point at the crack surface the scan gives a $(x, y, z)$-coordinate data set representing latitude, longitude and height, respectively. Figure 8 illus-

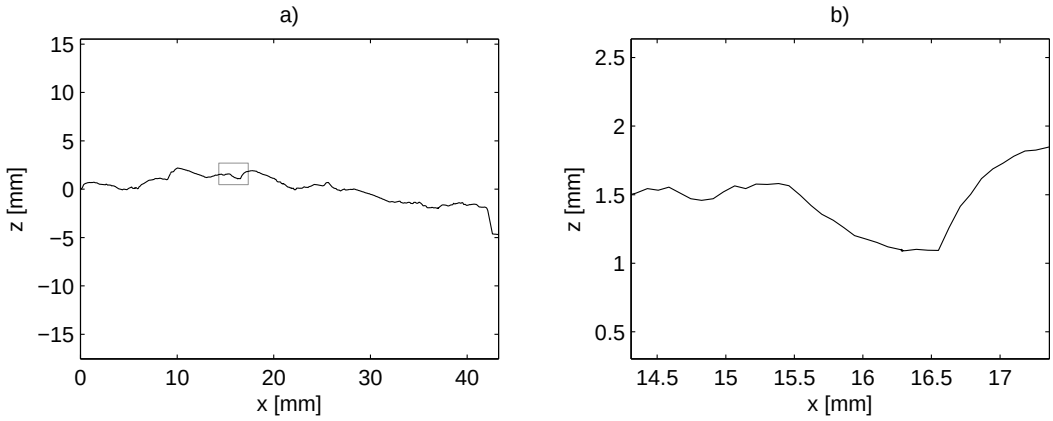


Figure 9: **(a)** A single contour line taken directly from the scan in Figure 8. **(b)** An enlargement of the contour line corresponding to the square in (a).

trates a 3D plot of the rough crack surface. From the scan points and in a given direction the scan provides a number of contour lines. An arbitrary contour line, $k_\theta$, is displayed in Figure 9, representing $x$- and $z$-coordinates for a contour line running across the crack surface. Each contour line can be characterized by its start inclination $\theta$, which is approximated by the inclination between the first and the second data point in the contour line, see Figure 11. A series of average contour lines are established by dividing the total angle interval covered by the start inclinations into a number of intervals, $\Delta\theta_i$. For a given $\Delta\theta_i$ the average contour line, $k_{\Delta\theta_i}$, describes where the successive points in the contour line most likely will be situated with respect to the starting point.

To represent a crack surface for a given direction of motion, a contour line is established for each point in the scan, though neglecting points at the edges. The weight of the interval is given as the number of contour lines in the interval with respect to the total amount of contour lines times $(\cos(\Delta\theta_i))^{-1}$ representing the true length of the given interval. In Figure 10 the crack surface shown in Figure 8 is represented by the average contour lines and the matching weights based on two different scans; one with a 0.08 mm scan spacing and the other with a 0.16 mm scan spacing. For each scan the surface representation consists of 20 average contour lines ordered from lowest to highest start inclination and their weights. The comparison between the fine and the coarse scan in Figure 10 reveals that the fine scan as expected

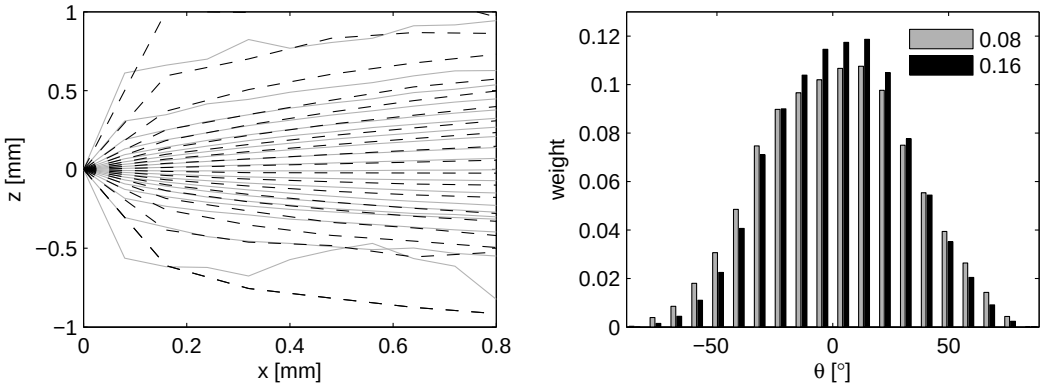


Figure 10: Average contour lines representing the crack surface in Figure 8 ordered from lowest to highest start inclination and their weight. The plot shows the representation from two different scan spacings, 0.08 mm and 0.16 mm.

has a higher representation of the steeper parts. Since the start inclination in the fine scan is followed over a shorter distance the spread of the contour lines is naturally narrower. However, even after the first kink the contour lines from the fine scan are flatter. The differences between the two scans are further studied in Section 3.2.
In total, for the given scan spacing, the average contour lines and their weight characterize the topography of the concrete crack surface for small crack openings. The random contour line in Figure 9 illustrates that for a given mixed mode opening, the surface locally experiences both opening, friction and crushing. However, referring to Figure 10 the very steep paths of the contour line have a very low weight of representation in the overall result.

The topographic effects are included in the model as follows. A given global displacement increment is transformed into a local displacement for each of the average contour lines. The local coordinate system is defined from the start inclination line, see Figure 11. For each of the average contour lines the local traction response is computed according to Table 1 in Section 2.4 and the weighted result is transformed back to global scale and added together with the global results from the other average contour lines. The introduction of the contour lines result in a new measure of the crack opening $\tilde{u}_{ng}$. $\tilde{u}_{ng}$ is given as the opening between the global displacement

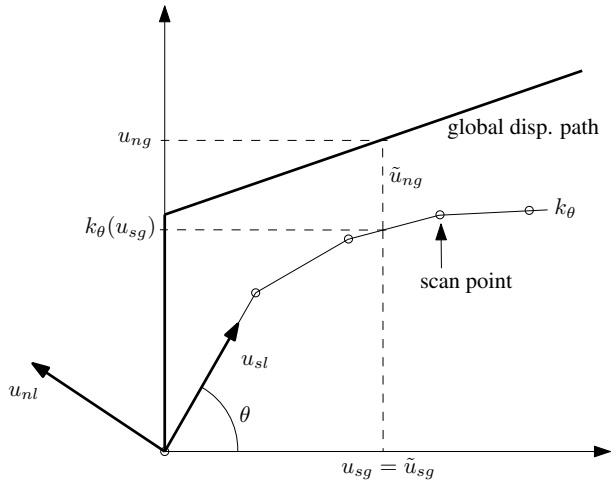


Figure 11: Global and local coordinate system. Indications of the global displacement path, $k_\theta$ and scan points.

and the contour line, see Figure 11. The relations between global and local displacements are summarized as

$$\begin{aligned} \tilde{u}_{ng} &= u_{ng} - k_\theta(u_{sg}) \\ \tilde{u}_{sg} &= u_{sg} \\ [\![\mathbf{u}]\!]_l &= \mathbf{T}[\![\tilde{\mathbf{u}}]\!]_g \end{aligned} \tag{25}$$

where $\mathbf{T}$ gives the transformation between global and local scale.

*3.1. Material Data and Implementation*

The material parameters are the same as presented in Section 2.5. The topography is measured from a test specimen from [5]. Before the measuring the specimen has been deformed and opened in a pure Mode I opening. The entire fracture surface is scanned twice using two different spacing distances. In the first scan a 0.08 mm spacing is used whereas the spacing in the second scan is 0.16 mm. For each scan the spacing is the same in both latitudinal and longitudinal directions. Due to problems with reflection between the equipment and the surface the scan misses minor parts of the surface. Together with an intentional omission of the notched parts this gives a total of around 240.000 scan points for the fine scan and a bit more than 60.000

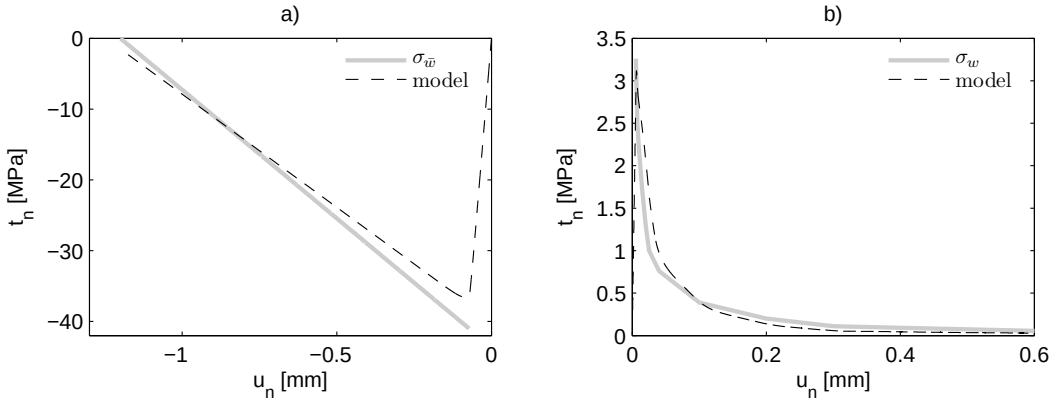


Figure 12: **(a)** The response from the constitutive model for a Mode I crushing compared with the $\sigma_{\bar{w}}$-curve plus elastic displacements. **(b)** The response from the constitutive model for a Mode I opening compared with the $\sigma_w$-curve plus elastic displacements. Normal traction $t_n$ as function of normal opening $u_n$. The dashed line is the model response.

scan points in the coarse scan, still covering a substantial part of the fracture surface.

If nothing else is mentioned the following results are based on the fine 0.08 mm scan spacing. The total angle interval covered by the start inclinations is divided into a number of smaller subintervals described by the average contour lines. The convergence of the number subintervals has been investigated and convergence is obtained for 40 and more subintervals. In the following 40 start inclination intervals are used resulting in 40 independent computations for a given global mixed mode displacement. The model response to the mixed mode displacement is then the sum of the weighted results from the 40 contour line based computations.

Normally this procedure results in a well-conditioned numerical problem, however, it has been observed that under special circumstances the equation system $\dot{\mathbf{t}} = (\mathbf{C^{ep}})^{-1}[\![\dot{\mathbf{u}}]\!]$ becomes ill conditioned, i.e. $\det(\mathbf{C^{ep}}) \approx 0$. In these very rare cases, the change in traction and hardening state has been restricted. It turns out that in the succeeding increment the system returns to being well conditioned.

### *3.2. Computation Including Topographic Effects*

Again the model is compared with the experiments by Jacobsen et al. [5]. In the first two computations the Mode I capabilities are tested, both for a

pure opening and for a pure crushing failure, illustrated in Figure 12. For the modified model, neither the Mode I opening nor the crushing response corresponds directly to the $\sigma_w$ curve and the $\sigma_{\bar{w}}$ curve, respectively. The difference is a consequence of the determination of tractions on local level, where some of the average contour lines e.g. for a global Mode I opening locally will experience a significant amount of friction. If the model response should give a better fit to the $\sigma_w$-curve and the $\sigma_{\bar{w}}$-curve, respectively, a transformation of material data from global to local level is needed. However, in this computation the transformation is omitted.

Figure 13 shows the mixed mode response for varying mixed mode angle and an initial opening of $u_{n,ini} = 0.025$ mm. The highest shear and compressive normal traction levels are reached for a low mixed mode angle, i.e. a relatively higher amount of sliding. Compared with the plane model in Section 2.6, the inclusion of the crack topography has resulted in significantly larger normal and shear traction levels together with a more flexible response. In fact the model overestimates the flexibility and the extreme traction levels, but both traction responses have some of the correct characteristics. For some of the mixed mode angles the model has a looped response in the $(t_n, t_s)$-plot, which cannot be rediscovered in the experiments, suggesting that the displacement levels in the model response at maximum shear and minimum normal traction are a bit out of sync. The sharp bend on both the shear and normal traction curves is most likely caused by the shift from compressive hardening to crushing softening. For two of the experiments this sharp shift is recognized, while the other experiments have a more smooth transition around maximum shear. For small openings the $\sigma_w$-response is a bit more flexible than in the experiments, seen at the end of the initial opening in the $(t_n, t_s)$-plot. This only affects the very start of the mixed mode response, and as seen in Figure 16 the $\sigma_w$-response fits well for larger initial openings.

The model is simple and uses some easily obtained material parameters and material relations between tractions and displacements. However, despite the comparison to a friction coefficient in a Coulomb friction model the influence of the material parameter $M$ may be unclear. In Figure 14 the example with an initial opening $u_{n,ini} = 0.025$ mm followed by a $\alpha = 45°$ mixed mode angle is computed for three different $M$ values varied from 0.4 to 0.8. The variation has two apparent effects. First, the reduced $M$ gives a reduction of

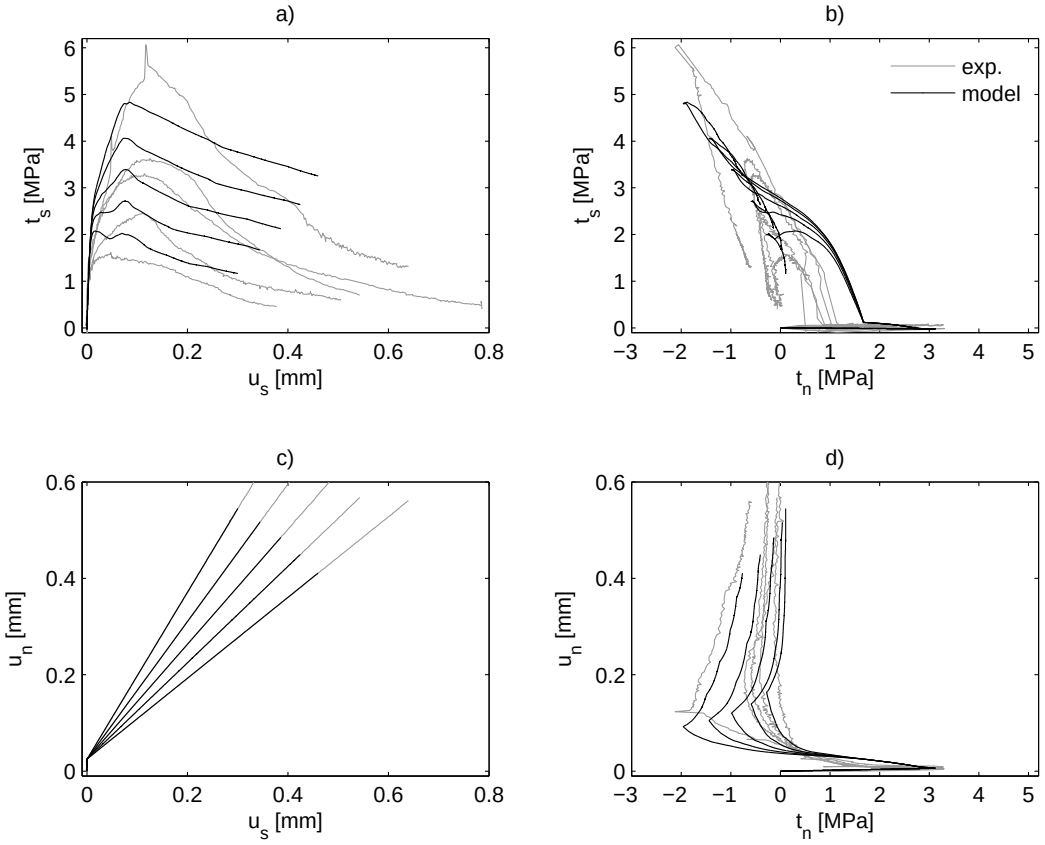


Figure 13: Response from constitutive model for an initial opening of $u_{n,ini} = 0.025$ mm followed by five different mixed mode angles $\alpha = [40°, 45°, 50°, 55°, 60°]$ compared with experiments by [5]. The four plots shows the relation between shear traction $t_s$, sliding $u_s$, normal traction $t_n$ and normal opening $u_n$. The largest tractions are obtained for the lowest $\alpha$.

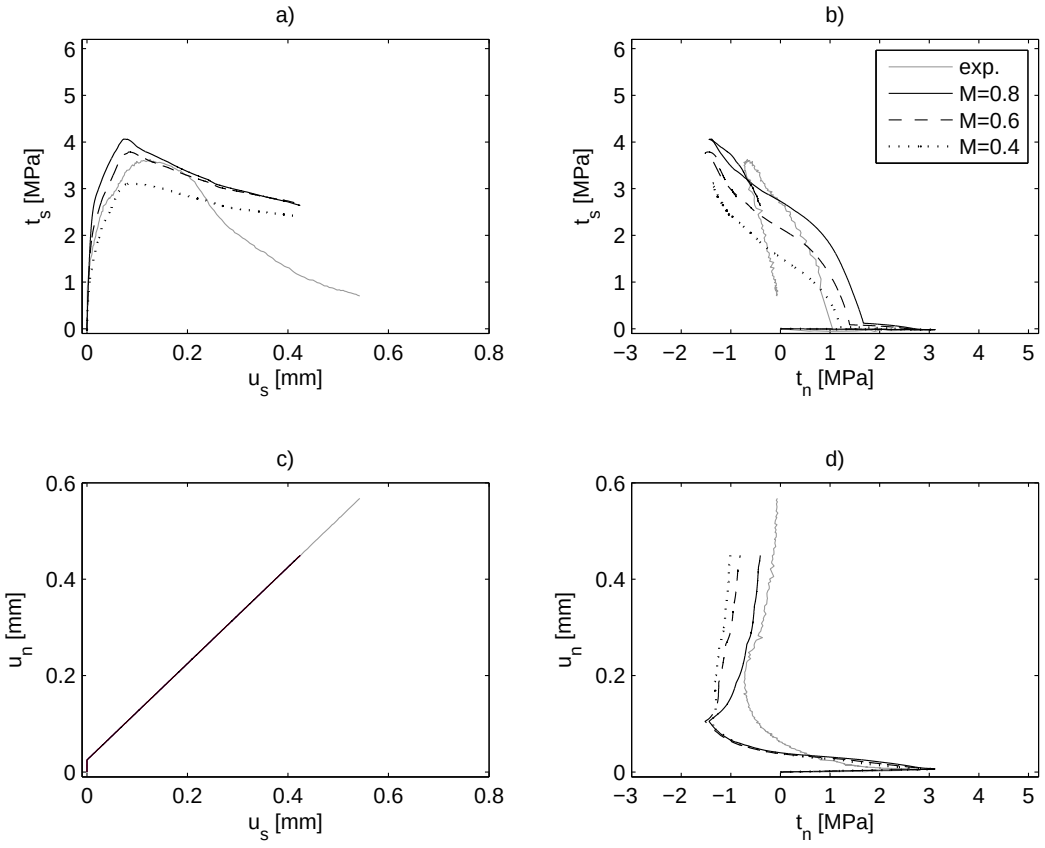


Figure 14: Variation of the material parameter $M$ for $u_{n,ini} = 0.025$ mm and $\alpha = 45°$. The results are displayed together with the matching mixed mode test results.

the shear capacity of the yield surface and thereby a smaller shear traction level. Secondly, since $M$ is part of the hardening functions Equations (21), (22) and (24) the reduced $M$ value gives a reduced softening of both the shear and the compressive normal tractions.

Since the parameters and the relations in the experiments are obtained at global level it introduces some uncertainty when they are used at local level in the material description. There is also some uncertainty about the pre and post cracking material description. For instance, instead of having a fully elastic compressive hardening the introduction of tensile micro cracks could reduce the elastic stiffness. Or the tensile micro cracks could affect the

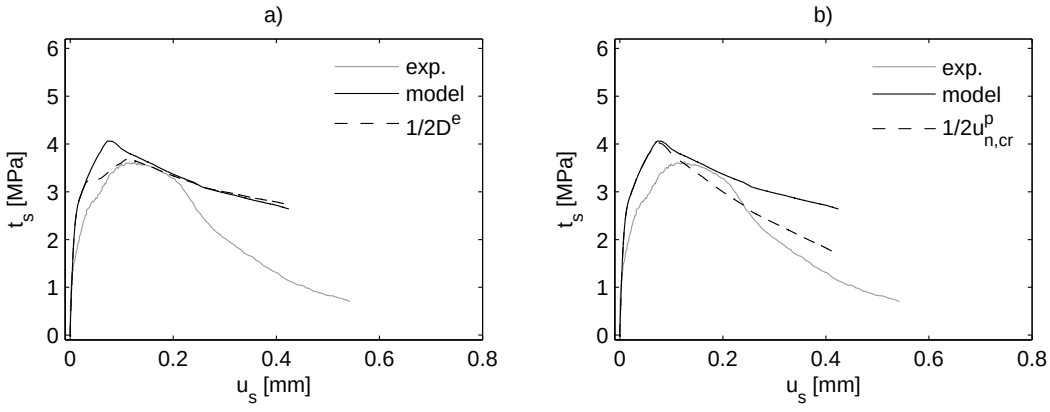


Figure 15: Model variation for $u_{n,ini} = 0.025$ mm and $\alpha = 45°$ compared with the similar experiment by [5]. Shear traction $t_s$ as function of the sliding $u_s$. **(a)** The elastic stiffness for the compressive hardening is reduced, $\frac{1}{2}\mathbf{D^e}$. **(b)** The crushing softening is made more brittle, $\frac{1}{2}u^p_{n,cr}$.

crushing softening response to be more brittle. The consequence of these two variations are illustrated in Figure 15. The reduced elastic stiffness for the compressive hardening, $\frac{1}{2}\mathbf{D^e}$, gives a more smooth response around maximum shear traction, whereas the more brittle crushing softening, $\frac{1}{2}u^p_{n,cr}$, makes the total mixed mode softening response more brittle.
In Figure 16 the model response for two different initial mixed mode openings, $u_{n,ini} = 0.025$ mm and $u_{n,ini} = 0.100$ mm, are compared with the experiments. The shape of the responses are the same as seen in Figure 13, and as in the experiments the traction levels drop for increased initial opening. For larger displacements the responses in both the tests and for the model tend to be the same regardless of the initial opening. This suggests that the initial opening mostly affects the initial cracking whereas the cracking changes to a more general behavior for larger displacements. Figure 16 also illustrates the combined effect of the two variations presented in Figure 15. The changed parameters give a better traction-displacement response while the $(t_n, t_s)$-response still is out of sync.

Figure 17 compares the computed mixed mode responses for the two topographic descriptions based on a 0.08 mm and a 0.16 mm spacing, respectively. The coarse 0.16 mm spacing results in a lowered shear traction level and similarly a lowered level of normal tractions. The two different spacing values

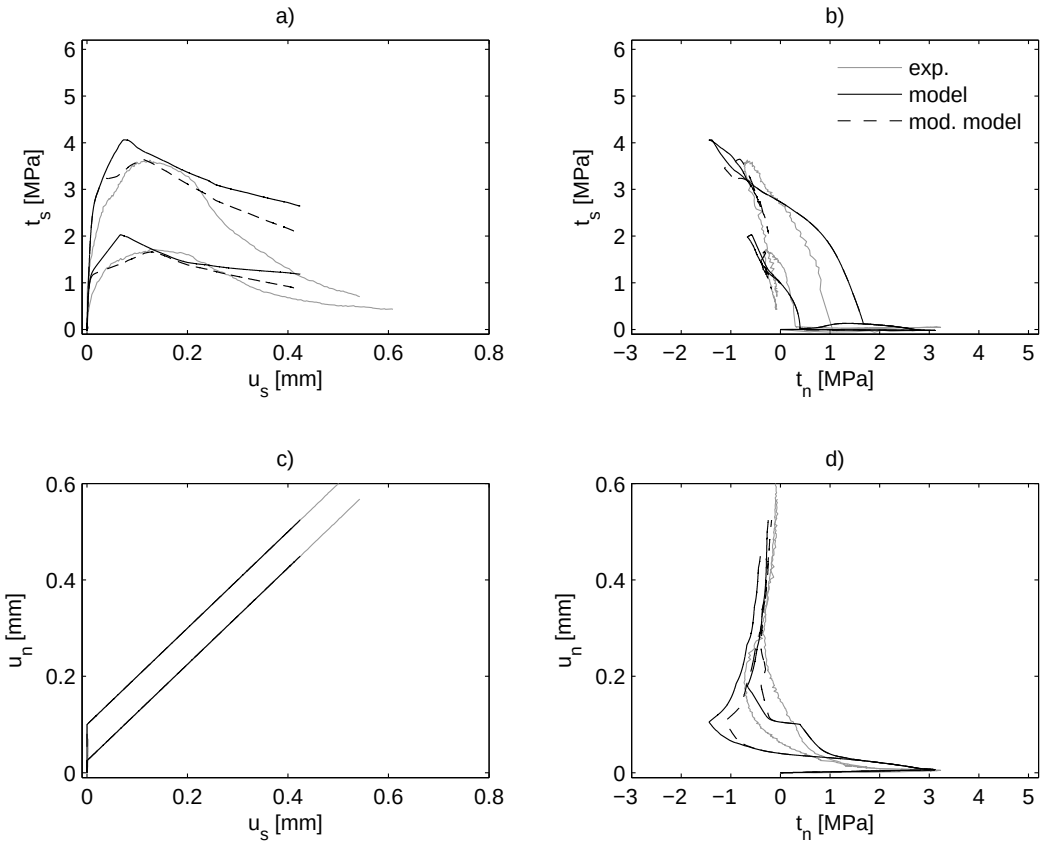


Figure 16: Response from constitutive model and response from modified material parameters (mod. model) for two different initials openings ($u_{n,ini} = 0.025$ mm and $u_{n,ini} = 0.100$ mm) compared with experiments by [5]. Smallest initial opening gives the largest tractions.

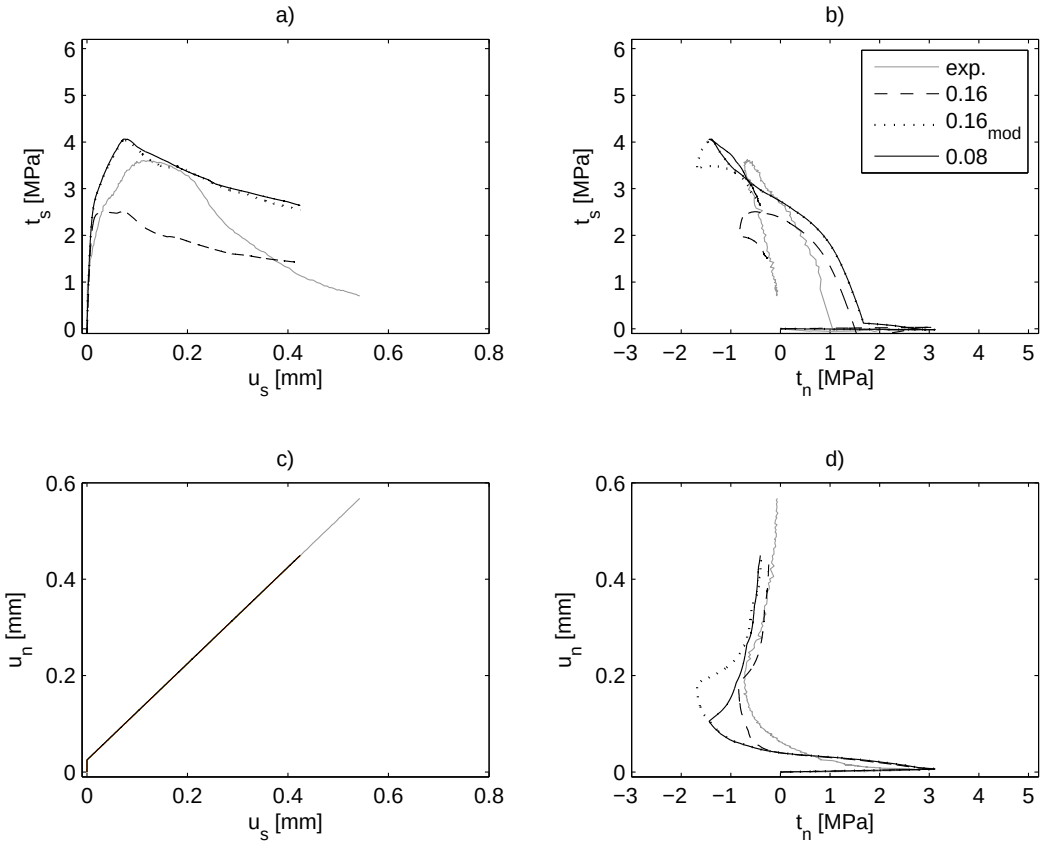


Figure 17: Mixed mode test result for $u_{n,ini} = 0.025$ mm and $\alpha = 45°$. Computations for the two different scan spacing 0.08 mm and 0.16 mm, respectively, and the results for a modified weight for 0.16 mm.

have a direct effect on the normal traction responses where the clear bends on the curves in compression correspond to an opening equal to the first bend on the average contour lines plus the initial opening. Besides these bends on the normal traction curves the difference between the two spacing values is mostly related to the weight of representation of the different average contour lines. This is illustrated by giving the average contour lines related to the coarse 0.16 mm spacing the weight obtained from the fine scan. Here the two topographic measures are almost coinciding and the only apparent difference is on the normal traction curves where the two different spacing values are recognized.

*3.3. Discussion*

The presented model is simply based on easily obtained material parameters. On the other hand, since some special equipment is needed for the measuring it is not trivial to obtain the crack surface topography. But having established the surface description for the given concrete, the description can most likely be used for concrete mixtures with similar characteristics. During the measuring, the spacing between the scan points influences the level of detail and thereby the detail of the micro effects which by the topography can be included in the model. Also the number of angle intervals and thereby the number of average contour lines influences the model response. For instance, too few average contour lines are not able to cover the micro effects related to the crack. Further studies could verify the representation and weight of the average contour lines. In the model, all the contour lines are activated at the same time. Hereby, the effect of redistribution of stresses related to local deformations is neglected. If instead the cracking is considered as a contact problem, the effect of local deformation could be included, but the modeling would then in respect to computational power tend to be a resource demanding micro model.

As seen in the previous section, especially the normal traction levels are too high. Both the yield surface in the plasticity model and the topography introduce dilation in the model, which seems reasonable since there are dilatational effects on the various size scales. Though, dependent on the resolution in the topographic measure, the dilation might be accounted for twice in the model.

The use of global material parameters at local level needs some verification, though considering the model response the assumption seems reasonable. The model is simple and effective with respect to the mixed mode cracking. This simplicity is for instance reflected in the sharp kink around the extremum points. A smoother but also more complicated model could be formulated with transition zones for e.g. the change between compressive hardening and crushing softening.

Despite these uncertainties the simple model without calibration gives a good crack representation and illustrates the mechanisms behind the mixed mode cracking.

## 4. Conclusion

A constitutive mixed mode model for cracks in concrete is established. The model is an associated plasticity model and is based on easily obtained material parameters and a geometric description of a crack surface. A shape parameter and the two hardening parameters representing the actual compressive and tensile strength of the concrete, respectively, control the yield surface. Besides the normal and shear stiffness and the initial compressive and tensile strengths for the concrete, the model is based on the relation between normal opening and normal traction and the relation between crushing deformations and normal tractions. The constitutive behavior is described through the hardening functions. For an opening of the crack the material softens, for a closure the material hardens, and for a large closure the material crushes described as a softening. From the measurements of the crack topography a series of average contour lines are constructed. From a global displacement increment the constitutive equations are solved at local level and the total model response is assembled at global level. The inclusion of the crack topography in the model ensures that some of the important micro scale effects behind the concrete cracking are covered by the model.
Some earlier models have been based on micro mechanical modeling, which computationally makes the modeling very demanding and practically excludes the possibility to model real size structures. Other models lack the dilatational effects, cannot model concrete crushing or are based on one or more material parameters, which are difficult to obtain. The presented plasticity model is simple and physically based. The material parameters and the material relations can be obtained using normal sized concrete specimens like a compressive cylinder. At the crack surface, mechanisms like locally friction and crushing occurs locally as a result of a global mixed mode displacement. The effect of these local mechanisms is included through a topographic description of the irregular crack surface. Compared with experiments and without any tuning the constitutive model based on the plasticity model and the topographic description gives a convincing description of both Mode I opening, crushing and mixed mode cracking.
The inclusion of the crack topography in the model makes the model able to explain some of the important micro mechanical effects of the concrete cracking. And formulated as a constitutive macro model, the model can be used for the modeling of real sized structures. The constitutive model with the topographic crack description is therefore an essential link in the under-

standing of the influence and the importance of micro effects in the macro response of mixed mode concrete cracking.


[1] A. Hillerborg, M. Modéer, P.-E. Petersson, Analysis of crack formation and crack growth in concrete by means of fracture mechanics and finite elements, Cement and Concrete Research 6 (1976) 773–781.

[2] L. Østergaard, Early-Age Fracture Mechanics and Cracking of Concrete, Experiments and Modelling, Ph.D. thesis, Department of Civil Engineering, Technical University of Denmark, Lyngby, Denmark, 2003.

[3] M. B. Nooru-Mohamed, E. Schlangen, J. G. M. van Mier, Experimental and numerical study on the behavior of concrete subjected to biaxial tension and shear, Advanced Cement Based Materials 1 (1993) 22–37.

[4] M. Hassanzadeh, Determination of fracture zone properties in mixed mode i and ii, Engineering Fracture Mechanics 35 (1990) 845–863.

[5] J. S. Jacobsen, P. N. Poulsen, J. F. Olesen, Characterization of mixed mode crack opening in concrete, Materials and Structures 45 (2012) 107–122.

[6] J. L. Högberg, Mixed mode cohesive law, International Journal of Fracture 141 (2006) 549–559.

[7] R. Walter, J. F. Olesen, Cohesive mixed mode fracture modelling and experiments, Engineering Fracture Mechanics 75 (2008) 5163–5176.

[8] G. Cusatis, L. Cedolin, Z. P. Bažant, Confinement-shear lattice model for concrete damage in tension and compression: I. theory, Journal of Engineering Mechanics 129 (2003) 1439–1448.

[9] J. Skoček, Fracture propagation in cementitious materials, Ph.D. thesis, Department of Civil Engineering, Technical University of Denmark, Lyngby, Denmark, 2010.

[10] I. Carol, P. C. Prat, C. M. López, Normal/shear cracking model: Application to discrete crack analysis., Journal of Engineering Mechanics 123 (1997) 765–773.

[11] C. M. López, I. Carol, A. Aguado, Meso-structural study of concrete fracture using interface elements. i: numerical model and tensile behavior, Materials and Structures 41 (2008) 583–599.

[12] C. M. López, I. Carol, A. Aguado, Meso-structural study of concrete fracture using interface elements. ii: compression, biaxial and brazilian test, Materials and Structures 41 (2008) 601–620.

[13] L. Dick-Nielsen, Modeling of ECC Materials using Numerical Formulations based on Plasticity, Ph.D. thesis, Department of Civil Engineering, Technical University of Denmark, Lyngby, Denmark, 2007.

[14] L. N. Lens, E. Bittencourt, V. M. R. d'Avila, Constitutive models for cohesive zones in mixed-mode fracture of plain concrete, Engineering Fracture Mechanics 76 (2009) 2281–2297.

[15] P. B. Lourenço, J. G. Rots, Multisurface interface model for analysis of masonry structures, Journal of Engineering Mechanincs 123 (1997) 660–668.

[16] A. Spada, G. Giambanco, P. Rizzo, Damage and plasticity at the interfaces in composite materials and structures, Computer Methods in Applied Mechanics and Engineering 198 (2009) 3884–3901.

[17] G. Alfano, E. Sacco, Combining interface damage and friction in a cohesive-zone model, International Journal for Numerical Methods in Engineering 68 (2006) 542–582.

[18] L. O. Nielsen, J. F. Mougaard, J. S. Jacobsen, P. N. Poulsen, A mixed mode model for fracture in concrete, in: B. et al. (Ed.), Fracture Mechanics of Concrete and Concrete Structures - Recent Advances in Fracture Mechanics of Concrete, Korea Concrete Institute, Seoul.

[19] J. F. Mougaard, P. N. Poulsen, L. O. Nielsen, Modelling concrete structures applying xfem with a mixed mode constitutive model, in: B. et al. (Ed.), Fracture Mechanics of Concrete and Concrete Structures : Recent Advances in Fracture Mechanics of Concrete, Korea Concrete Institute, Seoul.

[20] K. H. Roscoe, J. B. Burland, On the generalized behavior of 'wet' clay, in: Engineering Plasticity (J. Heyman and F.A. Leckie, eds.), Cambridge University Press, Cambridge.

[21] D. M. Wood, Soil Behaviour and Critical State Soil Mechanics, Cambridge University Press, 1990.

[22] W. F. Chen, D. J. Han, Plasticity for Structural Engineering, Springer-Verlag New York, 1988.

[23] D. C. Jansen, S. P. Shah, Effect of length on compressive strain softening of concrete., Journal of Engineering Mechanics 123 (1997) 25–35.

[24] V. S. Gopalaratnam, S. P. Shah, Softening response of plain concrete in direct tension, Journal of The American Concrete Institute 82 (1985) 310–323.

[25] Nextec Hawk User Manual version 2.0, 2000.

After a crack in concrete is initiated, the crack may open in mixed mode, i.e. a combination of opening and sliding. To get a thorough description of the structural consequences in terms of the stress distribution and the stiffness, it is important to include the stress transferring effects.

A series of new mixed mode experiments are presented. By introducing a crack in a double notch specimen and expose the crack in mixed mode opening, the experiments may be used in a direct interpretation of the mixed mode behavior. A constitutive mixed mode model is established. By a direct inclusion of the actual crack topography, the model gives a consistent and purely mechanical based interpretation of the mixed mode crack behavior.

**DTU Civil Engineering**
**Department of Civil Engineering**
Technical University of Denmark

Brovej, Building 118
2800 Kgs. Lyngby
Telephone 45 25 17 00

www.byg.dtu.dk

**ISBN: 9788778773463**
**ISSN: 1601-2917**